PhD

3rd CYCLE

FCUP
UA
UM
2025

U.PORTO

Optical Fiber Sensors Fabricated by Femtosecond Laser Three-Dimensional Micromachining

Carlos Duarte Rodrigues Viveiros

FC

U.PORTO
FACULDADE DE CIÊNCIAS
UNIVERSIDADE DO PORTO

universidade de aveiro

Universidade do Minho

PhD

Optical Fiber Sensors Fabricated by Femtosecond Laser Three-Dimensional Micromachining

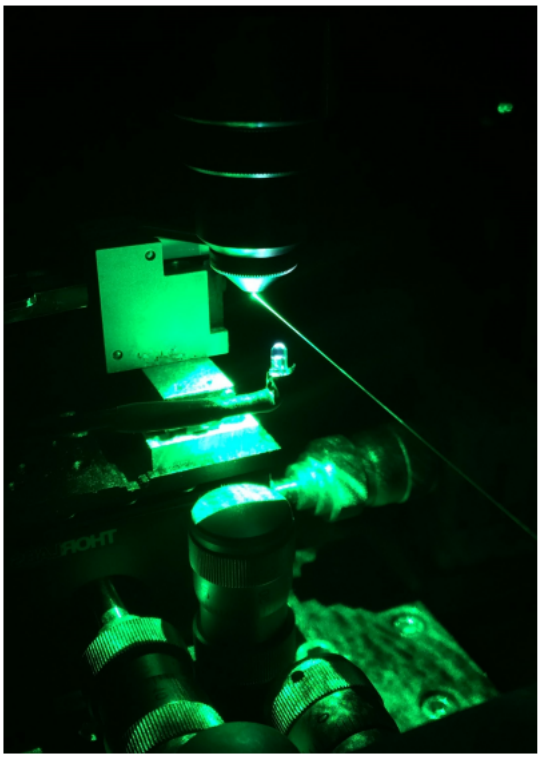
Carlos Duarte Rodrigues Viveiros
Doctoral Program in Physics
Faculty of Sciences of the University of Porto, University of Aveiro and University of Minho
2025

U.PORTO
FACULDADE DE CIÊNCIAS
UNIVERSIDADE DO PORTO

universidade de aveiro

Universidade do Minho

PhD



Optical Fiber Sensors Fabricated by Femtosecond Laser Three-Dimensional Micromachining

Carlos Duarte Rodrigues Viveiros

Thesis carried out as part of the Doctoral Program in Physics
Faculty of Sciences of the University of Porto, University of Aveiro and University of Minho
2025

Supervisor
Paulo Vicente da Silva Marques, Associate Professor, Faculty of Sciences of the University of Porto

Co-supervisor
Pedro Alberto da Silva Jorge, Auxiliary Professor, Faculty of Sciences of the University of Porto

INESCTEC

Institutions (where the work was carried out):





Funding:

This PhD work was supported by the Fundação para a Ciência e a Tecnologia (Portuguese national funding agency for science, research and technology) fellowships SFRH/BD/110035/2015 and 7859/BI_B2-C/2019.











To my loving parents, Catarina, family, and
in loving memory of my grandparents,
for always loving and supporting me.

"The important thing in science is not so much to obtain new facts as to discover new ways of thinking about them."

***Bragg, Sir William Lawrence**,*
Biographical Encyclopedia of Scientists

Acknowledgments

The successful completion of my PhD would not have been possible without the support, guidance, and encouragement of numerous individuals and institutions. I extend my deepest gratitude to all those who have contributed to my academic and personal growth during this journey.

I would like to express my sincere gratitude to my supervisor, Professor Paulo Marques, for his invaluable guidance, constructive feedback, and continuous encouragement throughout this research. His deep knowledge and insightful discussions significantly shaped my work, academic and personal growth. I am equally grateful to my co-supervisor, Professor Pedro Jorge, for the provided critical insights that significantly enriched this work. His constructive feedback and continuous motivation helped me navigate the challenges of this research.

I am also deeply grateful to Professor José Manuel Almeida and Dr. Luís Coelho for their support, motivation, and knowledge shared throughout every stage of my thesis. Their guidance and encouragement were instrumental in keeping my research on track, and their contributions have significantly enriched this work. I would also like to sincerely acknowledge Professor Orlando Frazão and Dra. Susana Silva, whose expertise, insightful discussions, and contributions have greatly enhanced the quality and impact of this research.

I would like to express my heartfelt gratitude to Professor José Luis Santos, Dr. Ireneu Dias, and Professor Carla Rosa for their encouragement, opportunities, and support throughout these years. Their guidance and belief in my potential have been instrumental in my growth as a research scientist.

I would like to express my deepest gratitude to my friends and lab partners, João Maia and Vítor Amorim, who embarked on this journey alongside me, providing support, collaboration, and encouragement every step of the way. Their friendship and dedication have made this experience truly enriching. I also extend my sincere appreciation to my co-authors, whose insightful discussions, shared efforts, and contributions have significantly enhanced both my research and my personal growth throughout this journey.

I would like to express my deepest gratitude to Dr. João Ferreira and Luísa Mendonça, who have not only witnessed my growth but have been integral in shaping me both professionally and personally. Their guidance, and encouragement have played a crucial role in my development, greatly contributing to my achievements and success. I am also grateful to Carlos Gaspar, Pedro Cruz, and Hernâni Marques, whose help and friendship have been truly valuable.

To all the professors of the MAP-fis program, I extend my sincere gratitude for their kindness, guidance, collaboration, and support. Their excellence in teaching and dedication to academic mentorship have greatly enriched my learning experience and research journey. I sincerely thank all the administrative staff at FCUP for their support, kindness and assistance.

I would also like to express my gratitude to my hosts institutions, FCUP and INESC TEC,

particularly the Centre for Applied Photonics, for warmly welcoming me and providing the essential laboratory facilities needed to conduct this research. Additionally, I extend my sincere appreciation to Fundação para a Ciência e a Tecnologia for supporting this work through the doctoral fellowships (SFRH/BD/110035/2015 and 7859/BI_B2-C/2019).

A heartfelt thank you to my colleagues and friends from other research groups and from INESC TEC, partic ularly those from the Centre for Applied Photonics, whose camaraderie, insightful discussions, and support have made this journey enjoyable and enriching. The shared moments of both academic challenges and laughter made my PhD years unforgettable.

I would like to extend a heartfelt thank you to my true friends. Your support, encouragement, and companionship have been invaluable to me over the years. Your belief in me during both challenges and achievements has been a constant source of strength and motivation. I am deeply grateful for your presence, kindness, and the countless moments that have made this journey special.

Dreams do come true. But some dreams are not just our own; they are built on the generosity, belief, and kindness of those who guide us along the way. Today, as I reach this milestone, I cannot help but look back and remember one person whose presence, even in absence, remains a profound part of this journey, my late Master's supervisor, Professor José Manuel Baptista. I am eternally grateful for the doors that Professor José Manuel Baptista opened for me, the knowledge he imparted, the challenges he presented, and, most importantly, the faith he had in my potential. Though he is no longer here to witness the realization of this goal, his impact remains deeply ingrained in my success. I carry forward not only the lessons he taught me but also the inspiration he left behind. It was under his guidance that I had the incredible opportunity to come to Porto, join INESC TEC, and become part of something greater. What began as a step into an academic endeavor soon turned into a transformative chapter of my life, one that introduced me not only to cutting-edge research but also to an extraordinary community of people who have shaped both my professional and personal growth.

My deepest gratitude goes to my family, especially my parents, for their unwavering love, patience, and belief in me. Their endless encouragement and steadfast support have built the foundation of strength that has carried me through every challenge. Their presence has been a constant source of energy, warmth, and resilience, shaping both my personal and professional journey. I also want to honor and thank my late grandparents, whose spirit, pride, and faith in me continue to resonate in my heart. Their energy and legacy have been a guiding force, reminding me of the values, perseverance, and passion they instilled in me. To Catarina, my life companion, and her family, my deepest appreciation for their unconditional support, strength, and encouragement. Their presence has been a pillar of stability and love, providing me with endless motivation and reassurance.

Duarte Viveiros

Resumo

A escrita direta com laser de femtosegundo (fs) surgiu como uma técnica altamente precisa e flexível para o fabrico de sensores avançados de fibras óticas, permitindo a inscrição de micro-estruturas complexas com elevada resolução espacial, independentemente do tipo de fibra. Este trabalho apresenta o desenvolvimento e a otimização de técnicas de fabrico baseadas em laser de fs, centradas em redes de Bragg em fibra (FBGs), redes de fibra de período longo (LPFGs) e interferómetros óticos, nomeadamente interferómetros Mach-Zehnder (MZIs) e interferómetros Fabry-Pérot (FPIs). O objetivo principal é melhorar a precisão, a estabilidade e a versatilidade dos sensores de fibra ótica através do processamento com laser de fs, introduzindo simultaneamente novas metodologias de fabrico e técnicas avançadas de caracterização. Este trabalho dá especial atenção aos FBGs fora do eixo e aos LPFGs de ponto de viragem, que aproveitam o acoplamento de modo assimétrico e as geometrias de grelha concebidas para melhorar a resposta espetral e a sensibilidade às variações do índice de refração, deformação e temperatura. Adicionalmente, são explorados MZIs e FPIs inscritos a laser de fs em fibras SMF-28e padrão para aplicações de deteção de índice de refração e de pressão, respetivamente. Uma análise experimental e teórica sistemática avalia o impacto dos parâmetros de processamento do laser de fs nas propriedades estruturais e ópticas das grelhas e estruturas interferométricas fabricadas. O estudo investiga a sintonização espetral, a estabilidade mecânica e a resistência ambiental, demonstrando a robustez dos sensores fabricados com laser de fs em condições adversas. Além disso, são exploradas abordagens de funcionalização, tais como revestimentos de dióxido de titânio, para melhorar a resposta refratométrica dos sensores baseados em LPFGs. A integração de interferómetros Mach-Zehnder e microcavidades Fabry-Pérot amplia as capacidades de deteção, utilizando interações de campo evanescente e efeitos de ressonância da cavidade, permitindo uma deteção mais eficaz de alterações bioquímicas e ambientais. O fabrico preciso de grelhas e estruturas interferométricas permite um melhor processamento do sinal ótico e a gestão espetral, que são essenciais para as redes de comunicações ópticas de alta velocidade. A capacidade de inscrever microestruturas complexas em fibras de telecomunicações padrão (como a SMF-28e) demonstra a versatilidade do sistema de inscrição com laser de fs desenvolvido no âmbito desta tese para sistemas de comunicação de fibra ótica da próxima geração. Os resultados desta investigação de doutoramento contribuem para o avanço das tecnologias de deteção de fibras ópticas e de telecomunicações baseadas em laser de fs, estabelecendo uma compreensão abrangente da relação entre os parâmetros de inscrição, o desempenho do sensor e a estabilidade operacional.

Palavras-chave: Micromaquinação a laser femtosegundo, redes de Bragg, redes de período longo, interferómetros em fibra ótica, sensores em fibra ótica.

Abstract

Femtosecond (fs) laser direct writing has emerged as a highly precise and flexible technique for fabricating advanced optical fiber sensors, allowing for the inscription of complex microstructures with high spatial resolution, independent of fiber type. This work presents the development and optimization of fs-laser-based fabrication techniques, focusing on fiber Bragg gratings (FBGs), long-period fiber gratings (LPFGs), and optical interferometers, specifically Mach-Zehnder interferometers (MZIs) and Fabry-Pérot interferometers (FPIs). The primary objective is to enhance the precision, stability, and versatility of optical fiber sensors through fs-laser processing, while introducing novel fabrication methodologies and advanced characterization techniques. This work places particular focus on off-axis FBGs and turn-around-point LPFGs, which leverage asymmetric mode coupling and engineered grating geometries to enhance spectral response, improving sensitivity to refractive index, strain, and temperature variations. Additionally, fs-laser-inscribed MZIs and FPIs in standard SMF-28e fibers are explored for refractive index and pressure sensing applications, respectively. A detailed experimental and theoretical analysis evaluates the impact of fs-laser processing parameters on the structural and optical properties of the fabricated gratings and interferometric structures. The study investigates spectral tuning, mechanical stability, and environmental resilience, demonstrating the robustness of fs-laser-fabricated sensors in harsh conditions. Furthermore, functionalization approaches, such as titanium dioxide coatings, are explored to enhance the refractometric response of LPFGs-based sensors. The integration of Mach-Zehnder interferometers and Fabry-Pérot microcavities extends sensing capabilities by utilizing evanescent field interactions and cavity resonance effects, enabling the improved detection of biochemical and environmental changes. The precise fabrication of gratings and interferometric structures allows for enhanced optical signal processing and spectral management, which are essential for high-speed optical communication networks. The ability to inscribe complex microstructures in standard telecommunication fibers (such as SMF-28e) demonstrates the versatility of developed fs-laser inscription system in the framwork of this thesis for next-generation fiber-optic communication systems. The findings of this PhD research contribute to the advancement of fs-laser-based fiber optic sensing and telecommunications technologies by establishing a comprehensive understanding of the relationship between inscription parameters, sensor performance, and operational stability.

Keywords: Femtosecond laser micromachining, fiber Bragg gratings, long period fiber gratings, optical fiber interferometers, optical fiber sensors.

Table of Contents

List of Tables **ix**

List of Figures **xi**

Nomenclature **xvii**

1 Introduction **1**
1.1 Motivation and Objectives . . . 3
1.2 Structure of the Thesis . . . 7
1.3 Main Contributions . . . 8
1.4 Peer-Reviewed Scientific Publications . . . 9

2 Femtosecond Laser Micromachining **15**
2.1 Femtosecond Laser–Material Interaction . . . 15
2.1.1 Regimes of Material Modification . . . 18
2.2 Propagation Conditions and Considerations . . . 20
2.2.1 Writing Geometry . . . 23
2.3 Femtosecond Laser Irradiation Followed by Chemical Etching . . . 25
2.4 Optical Fiber Devices Fabricated by Femtosecond Laser Micromachining . . . 27
2.5 Conclusions . . . 39

3 Fabrication and Characterization Methods **41**
3.1 Femtosecond Laser Direct Writing System . . . 41
3.1.1 Fiber Femtosecond Laser and Power Control Unit . . . 43
3.1.2 Beam Delivery Optics and Motion Stages . . . 44
3.1.3 Femtosecond Laser Direct Writing of Fiber Gratings . . . 47
3.1.4 Hardware Architecture and Application Software . . . 48
3.2 Optical Fiber Preparation and Alignment . . . 50
3.2.1 Focusing Procedure with an Oil Immersion Lens . . . 51
3.2.2 Focusing Procedure with a Dry Aspheric Lens . . . 52
3.3 Optical Characterization Setup . . . 53
3.4 Conclusions . . . 55

4 Development and Optimization of Optical Fiber Sensors **57**
4.1 Fiber Bragg Gratings . . . 57
4.1.1 Theoretical Background . . . 59
4.1.2 Fabrication and Sensitivity Analysis of First- and Second-Order FBGs . . . 61
4.1.3 Fabrication and Sensitivity Analysis of First-Order Off-Axis FBGs . . . 70
4.1.4 Summary . . . 85
4.2 Long Period Fiber Gratings . . . 86
4.2.1 Theoretical Background . . . 88
4.2.2 Characterization of the LPFGs Writing process . . . 91
4.2.3 Sensitivity Analysis of LPFGs . . . 103
4.2.4 Summary . . . 129
4.3 Optical Fiber Interferometers . . . 131
4.3.1 Mach-Zehnder Interferometer . . . 131
4.3.2 Fabry-Perot Interferometer . . . 142
4.3.3 Summary . . . 153
4.4 Conclusions . . . 154

5 Conclusion **157**
5.1 Future Work . . . 159
5.2 Final Remarks . . . 160

References **161**

List of Tables

2.1 Summary of coupling light from SMF core waveguides into fs-laser-formed waveguides. . . . 37

3.1 Objective Lens Specifications. . . . 44
3.2 Motion Stages Specifications. . . . 45
3.3 Optical Fibers Specifications. . . . 50

4.1 Parameters of the femto-inscribed FBGs in an SMF-28e. . . . 65
4.2 Parameters of the FBGs for temperature characterization. . . . 68
4.3 Specification of the fs-laser written FBG before and after the annealing process. . . . 69
4.4 Writing parameters of the fs-laser WGs. . . . 70
4.5 Strain sensitivities of the off-axis FBGs. . . . 77
4.6 Temperature sensitivities of the off-axis FBGs. . . . 78
4.7 Wavelength and Optical Power sensitivities (curvature) of the off-axis FBGs. . . . 81
4.8 Curvature sensitivities of the off-axis FBGs. . . . 83
4.9 Summary of the spectral characteristics of the LPFGs fabricated with different duty cycles. . . . 97
4.10 Summary of the spectral characteristics of the LPFGs fabricated at different positions inside the SMF-28e fiber. . . . 99
4.11 Comparison between a pair of LPFGs. . . . 102
4.12 Main characteristics of two sets of TAP LPFGs fabricated by fs-laser. . . . 103
4.13 Fiber parameters used in the simulation. . . . 111
4.14 Summary of the spectral characteristics of the TiO_2 coated LPFGs operating very close to the TAP. . . . 113
4.15 Wavelength Sensitivity for Uncoated and TiO_2 coated LPFGs in the RI range of Water-based solutions. . . . 117
4.16 RI Resolutions for the uncoated and TiO_2 coated LPFGs operating around TAP. . . . 118
4.17 Comparison between the sensitivity displayed by LPFGs operating around TAP reported in the literature and this work[1]. . . . 119
4.18 RI Resolutions for the cladding mode $LP_{1,6}$ and $LP_{1,7}$. . . . 123
4.19 Summary of the spectral characteristics of the TiO_2 coated LPFGs. . . . 124
4.20 RI Resolutions of the LPFGs, uncoated and coated with 30 nm thick TiO_2 film. . . . 126
4.21 Summary of the spectral characteristics of the first LPFGs of the in-line MZI. . . . 136
4.22 Summary of the spectral characteristics of the in-line MZIs. . . . 136

4.23 Summary of the spectral characteristics of the MZIs, uncoated and coated with 30 nm thick TiO_2 film. 137
4.24 RI Resolutions for the uncoated and TiO_2 coated MZIs. 141
4.25 RI sensitivity of MZIs fabricated by the electric arc technique reported in the literature and this work. 141
4.26 Comparison of FPIs structures 148
4.27 Gas Pressure Sensitivities of the FPIs. 151
4.28 Gas Pressure Resolutions of the FPIs. 152
4.29 Gas pressure sensitivity of FPIs reported in the literature and this work. 153

List of Figures

1.1 Schematic: (a) diagram of an optical fiber sensing system, (b) flowchart summarizing the different classifications of OFS. 2
1.2 Photomontage of remarkable moments of the story of INESC TEC: (a) Research group in the ’80s, (b) Working at project NOSCA, and (c) Optical fiber sensors installation in the D. Luís I Bridge. 5

2.1 Timescale of the physical phenomena associated with the interaction of a fs-laser pulse with transparent materials. 16
2.2 Schematic diagram of the nonlinear photoionization processes underlying fs-laser machining. (a) Multiphoton ionization, (b) tunneling ionization, and (c) Avalanche ionization: free carrier absorption followed by impact ionization. 17
2.3 Schematic diagram of the physical mechanisms in sequential order of the key steps (a), (b), and (c) and microscope images (d) of typical refractive index modulations induced by fs-laser. 19
2.4 Schematics of (a) the interaction between a focused fs-laser beam and an optical fiber, along with a sketch of its Gaussian intensity beam profile, and (b) self-focusing and filamentation of an fs-laser pulse. Optical microscope view (c) of the cross-sections of the fs-laser written waveguides. 22
2.5 Schematic diagrams of the fs-laser direct writing geometries in optical fibers: (a) longitudinal mode and (b) transversal mode. 23
2.6 Schematic diagram of the FLICE technique divided into two steps: (a) fabrication, and (b) chemical Etching. 27
2.7 Micro-hole structured LPFG: (a) Morphology with the grating period of 450 µm; (b) Cross-section view of the grating pitch (i.e. micro-holes); (c) Evolution of the transmission spectrum. 31
2.8 Fiber in-line Michelson interferometer: (a) Optical microscope image; (b) output spectrum with a cavity length of 38 µm. 32
2.9 Schematic diagram of fabrication process of the microfiber with inner air cavity. . . 33
2.10 Fs-laser micromachining of a microfiber in-line Mach-Zehnder interferometer. . . . 34
2.11 Schematic diagram of the fiber in-line Mach-Zehnder interferometer. 35
2.12 Schematic of an optical resonator and access port template embedded within: (a) SMF fiber before HF etching, (b) SMF fiber after HF etching, and (c) coreless fiber. 36
2.13 Fs-laser writing of waveguides in an SMF with an oil-immersion lens. 37

2.14 LIF sensing platform: (a) Schematic, and (b, c, d, and e) Optical micrographs of the LIF sensing elements. 38

3.1 Photomontage showing the facilities where the fs-laser microfabrication system is installed. 42
3.2 Schematic diagram of the fs-laser direct writing system. 43
3.3 Power Calibration: writing laser power after the focusing OL (a) Olympus PLN100XO and (b) Newport 5722-A-H as a function of laser power measured after the power control unit with respective system loss. 46
3.4 Schematic diagram of the burst writing method used in the fs-laser direct writing system. 47
3.5 GUIs of the fs-laser system: (a) Motion, and (b) Gratings Control Panels, respectively. 49
3.6 Recorded images of a SMF-28e fiber (8.2 µm core diameter) as seen through the CCD camera of the fs-laser system. 51
3.7 Recorded images of back-reflected fs-laser beam focused by a 40× objective lens into a SMF-28e. 53
3.8 Experimental setup for measurement of the gratings transmitted and reflected spectrum. 54

4.1 Schematic diagram of a RI modulation induced by fs-laser in the core of an SMF with an oil-immersion lens. 61
4.2 Transmission spectra of femto-inscribed FBG with a wavelength of 1529.82 nm ($\Lambda = 528.60$ nm). 62
4.3 Experimental setup for measurement of the FBGs transmitted spectrum with polarization control. 63
4.4 Transmission spectra of the FBGs fabricated with different duty cycles and measured with polarization control. 63
4.5 Bragg wavelength (a), Grating strength (b), and Birefringence (c) as a function of duty cycle, for FBGs fabricated with parallel polarization. 64
4.6 Fs-laser FBGs inscribed in an SMF-28e: (a) spectra of three first-order FBGs in sequence and (b) sequence of two FBGs fabricated with different orders; (c) and (d) Top-view section images of the first and second order FBGs, respectively. . . . 66
4.7 Fs-laser structures inscribed in a coreless fiber: (a) Schematic diagram, (b) Top-view section image, and (c) End-view optical micrograph. 67
4.8 Femtosecond and UV laser FBGs: (a) Transmission spectra, and (b) Reflection spectra. 67
4.9 Schematic illustration of the FBGs temperature characterization setup. 68
4.10 Spectral evolution of: (a) the UV-inscribed FBG and (b) femto-inscribed FBG during the annealing cycle; (c) decrease of refractive index modulation as a function of temperature and (d) Bragg wavelength as a function of temperature. 69

4.11 Spectral evolution of femto-inscribed FBG Coreless fiber: (a) during the annealing cycle and (b) at room temperature. 70
4.12 Fs-laser written waveguides inside a SMF-28e fiber: (a) cross-section photograph and (b) refractive index profile. 71
4.13 Off-axis FBG with 4.5 µm offset from the core center fabricated with 60 nJ pulse energy (a) top-view image, and (b) reflection spectra. 72
4.14 Top-view images of the off-axis FBGs with an offset of: (a) 3.0 µm, (b) 4.5 µm, and (c) 6.0 µm written with 140 nJ pulse energy (insets: end-view optical micrographs). All gratings were written at 50 µm/s. 72
4.15 Off-axis FBGs: (a) transmission and (b) reflection spectra, and (c) wavelength shift as a function of the grating inscription position from core center. 73
4.16 Simulated mode profiles (electric field norm) at the core/structure for the: (a) $LP_{0,1}$ mode, and (b) $LP_{1,1}$ mode. 74
4.17 (a) Reflection spectra of the off-axis FBG with 4.5 µm offset (measured with polarization control), and (b) birefringence, as a function of the grating inscription position from core center. 75
4.18 Schematic illustration of the off-axis FBGs strain characterization setup. 76
4.19 Off-axis FBG with 6.0 µm offset from the core center: (a) reflection spectra for different strain values and (b) normalized wavelength shift ($\Delta\lambda$) as a function of strain. 76
4.20 Schematic illustration of the off-axis FBGs temperature characterization setup. . . . 77
4.21 Off-axis FBG with 3.0 µm offset: (a) reflection spectra for different temperature values and (b) normalized wavelength shift as a function of temperature; Off-axis FBG with 6.0 µm offset from the core center: (c) and (d) Reflection spectra for different temperature values. 78
4.22 Schematic illustration of the off-axis FBGs curvature characterization setup. 79
4.23 Bragg resonances of the $LP_{1,1}$ mode (λ_1 and λ_2) of the three off-axis FBGs: reflection spectra under different curvature values at a random angle for the: (a) 3.0 µm, (b) 4.5 µm and (c) 6.0 µm off-axis FBGs, respectively. Also shown for the Bragg resonance of the $LP_{1,1}$ mode (λ_1) of each off-axis FBG: (d) the normalized reflected power variation as a function of curvature. 80
4.24 Normalized wavelength shift and normalized reflected power variation as a function of the curvature direction angle (θ) under a curvature equal to 50 m^{-1} for the Off-axis FBGs with: 3.0 µm offset (a), (b), 4.5 µm offset (c), (d), and 6.0 µm offset (e), (f), respectively. 82
4.25 Schematic illustration of the off-axis FBGs twist characterization setup. 84
4.26 4.5 µm off-axis FBG: (a) wavelength shift, (b) normalized reflected power, and (c) twist parameter as a function of the twist rate. 84
4.27 Sketch of the phase-matching curves. 89
4.28 Spectra of fs-laser direct written LPFGs in single mode fiber (SMF-28e). 92

4.29 Experimental setup for characterization of the near-field intensity distribution of several cladding modes excited by the fs-laser gratings inscription. 93
4.30 Fs-laser inscribed LPFG in the SMF-28e fiber with a 8.2 µm core: (a) Optical microscope view of the cross-section, and (b) Near-field intensity distribution. . . . 93
4.31 Fs-laser TAP LPFGs cladding mode $LP_{1,12}$, inscribed in the SMF-28e fiber. 94
4.32 Experimental setup for measurement of the LPFGs transmitted spectrum with polarization control. 95
4.33 Transmission spectra of the TAP LPFG fabricated with a period of 182.7 µm at a depth of 60 µm with pulse energy of 130 nJ, a duty cycle of 50 %, and 19.0 mm long (measured with polarization control). 96
4.34 Transmission spectra of the LPFGs fabricated with different duty cycles and measured with polarization control. 97
4.35 Transmission spectra of the LPFGs fabricated at different positions inside the SMF-28e fiber. 98
4.36 Optical microscope views of the cross-sections of the fs-laser written TAP LPFGs in the SMF-28e fiber (8.2 µm core diameter). 99
4.37 Transmission spectra of the TAP LPFGs fabricated at a depth of 60 µm with pulse energies of 120 nJ and 57 µm with pulse energies of 140 nJ. 100
4.38 Fs-laser TAP LPFGs inscribed with a period of (a) 191.8, and (b) 192.5 µm (numbered from 1 to 12). 102
4.39 Schematic illustration of the temperature characterization setup for LPFGs. 103
4.40 Transmission spectra of the cladding mode $LP_{1,6}$ of a 372.5 µm LPFG at annealing temperature. 104
4.41 Fs-laser LPFG inscribed with a period of 372.5 µm: (a) wavelength shift and (b) strength of the peak attenuation, both measured at the annealing temperature; (c) wavelength shift, and (d) strength of the peak attenuation, both measured at room temperature after annealing the grating at different temperatures. 105
4.42 Fs-laser TAP LPFG inscribed with a period of 182.7 µm: (a) transmission spectra at annealing temperature; (b) normalized wavelength shift and optical power variation as a function of the annealing temperature. 106
4.43 Fs-laser TAP LPFG inscribed with a period of 182.7 µm: (a) transmission spectra at room temperature; (b) transmission spectra immersed in water at room temperature. All measurements were acquired after annealing the grating at different temperatures. 107
4.44 Fs-laser 182.7 µm TAP LPFG: (a) normalized wavelength shift, and (b) normalized optical power variation in air at room temperature; (c) normalized wavelength shift, and (d) normalized optical power variation in water at room temperature. All measurements were acquired after annealing the grating at different temperatures. 107
4.45 Fs-laser TAP LPFG inscribed with a period of 192.5 µm, measured in water at 25 °C: (a) transmission spectra; (b) normalized wavelength shift; and (c) normalized optical power variation. All measurements were acquired after annealing the grating at different temperatures. 109

4.46 Schematic illustration of the LPFGs: (a) coating, and (b) SRI characterization setups.110
4.47 LPFGs mode profiles using the mode analysis of the COMSOL Multiphysics®. . . . 112
4.48 Transmission spectra of LPFGs fabricated with a period of 191.8 and 192.5 µm, (a) and (b) uncoated and, (c) and (d) coated with 10 and 20 nm thick TiO_2 film, respectively for several values of the SRI. 114
4.49 Normalized wavelength shift (a) and (b), and wavelength sensitivity (c) and (d) of the uncoated LPFGs and coated with different TiO_2 films thickness fabricated with a period of 191.8 and 192.5 µm, respectively, as a function of the SRI. 115
4.50 Normalized wavelength shift (a) and (b) for the uncoated LPFGs and coated with different thick TiO_2 films fabricated with a period of 191.8 and 192.5 µm, respectively in the RI range of water-based solutions. Experimental data points were fitted to a linear equation. 116
4.51 Normalized wavelength shift as a function of time when the surrounding medium undertakes step variations for the resonance: (a) and, (b) λ_1 and (c) and, (d) λ_2 of the LPFGs fabricated with a period of 191.8 and 192.5 µm, respectively. 118
4.52 Fs-laser LPFG inscribed with a period of 372.5 µm, measured at room temperature: (a) transmission spectra; (b) wavelength shift. All measurements were acquired after annealing the grating at different temperatures. 121
4.53 Transmission spectra of the LPFG fabricated with a period of 372.5 µm for the (a) $LP_{1,6}$ mode before annealing, and (b) $LP_{1,7}$ mode after annealing; (c) Normalized wavelength shift, and (d) wavelength sensitivity for several values of the SRI. 122
4.54 Normalized wavelength shift as a function of time when the surrounding medium undertakes step variations for the (a) $LP_{1,6}$ and (b) $LP_{1,7}$ cladding modes 122
4.55 Transmission spectra of the LPFGs, uncoated and coated with 30 and 60 nm thick TiO_2 films, in air (RI = 1.0000). 123
4.56 LPFGs transmission spectra ($LP_{1,6}$ and $LP_{1,7}$ cladding modes) for several values of the SRI, for: (a) uncoated, and (b) coated with 30 nm thick TiO_2 film. 124
4.57 LPFGs uncoated, and coated with 30 and 60 nm thick TiO_2 films: (a) normalized wavelength shift, (b) optical power variation; wavelength sensitivity for (c) $LP_{1,6}$ and (d) $LP_{1,7}$ cladding modes, and (e) optical power sensitivity as a function of the SRI. 125
4.58 Normalized wavelength shift as a function of time when the surrounding medium undertakes step variations for the LPFGs fabricated with a period of 372.5 µm, (a) uncoated and (b) coated with 30 nm thick TiO_2 film. 126
4.59 Schematic illustration of the LPFGs strain characterization setup. 127
4.60 Transmission spectra of the LPFG for different strain values (a), normalized wavelength shift (b), and normalized optical power variation as a function of strain (c). . 127
4.61 Transmission spectra of the TAP LPFG for different strain values (a), normalized wavelength shift (b), and normalized optical power variation as a function of strain (c).128
4.62 In-line Mach−Zehnder interferometer based on a matched LPFG pair: (a) Schematic, and (b) and (c) Transmission spectra of the first single LPFG and MZI, respectively. 135

4.63 Transmission spectra of the MZIs, uncoated and coated with 30 nm thick TiO_2 film, in air (RI = 1.0000). 137
4.64 Schematic illustration of the SRI characterization setup for MZIs. 138
4.65 Transmission spectra of an MZI: (a) uncoated and (b) coated with 30 nm thick TiO_2 film, for several values of the SRI. 138
4.66 Normalized wavelength shift as a function of the SRI for MZIs with a cavity of 1.4 cm, uncoated and coated with different TiO_2 films thickness 139
4.67 Normalized wavelength shift for the MZI coated with 50 nm thick TiO_2 film in the RI range of water-based solutions. Experimental data points were fitted to a linear equation. 140
4.68 Normalized wavelength shift as a function of time when the surrounding medium undertakes step variations for the interferometric bands of the MZIs: (a) uncoated and (b) coated with 50 nm thick TiO_2 film. 140
4.69 Schematic of the proposed Fabry-Pérot interferometers in SMF-28e fiber: (a) single FP cavity and, (b) in-line dual FP cavities. 145
4.70 Optical microscopy images of the fabricated structures: (a) and (b) single FP cavity before (on top) and after etching (at the bottom), fabricated with 2 µm and 6 µm separation, respectively; (c) and (d) in-line dual FP cavities before (on top) and after etching (at the bottom), fabricated with 10 µm and 20 µm separation, respectively (top views at the left and side views at the right). 147
4.71 Reflected spectra of the fabricated FPIs structures in air (RI = 1.0000). 148
4.72 Schematic illustration of the FPI experimental setup for gas pressure measurements. 149
4.73 Reflected spectra of the fabricated structures under different CH_4 and N_2 gases pressures, respectively: (a) and (b) single FP cavity; (c) and (d) in-line dual FP cavities. 150
4.74 Normalized wavelength shift as a function of gas pressure increase $\uparrow P$, and decrease $\downarrow P$: (a) single FP cavity and, (b) in-line dual FP cavities. 150
4.75 Normalized wavelength shift of the FPIs resonance peak at approximately 1580 nm as a function of time when the gases (CH_4 and N_2) pressure undertakes step variations: (a) and (b) single FP cavity; (c) and (d) in-line dual FP cavities. 152

Nomenclature

Acronyms/Abbreviations

2D	Two-Dimensional
3D	Three-Dimensional
AOM	Acousto-optic Modulator
BL	Biconvex Lens
BW	Bandwidth
CAP	Centre for Applied Photonics
DM	Dichroic Mirror
EFACEC	Empresa Fabril de Máquinas Eléctricas, SARL
FBGs	Fiber Bragg Gratings
FCUP	Faculty of Sciences of the University of Porto
FLICE	Femtosecond laser irradiation followed by chemical etching
FM	Flip Mirror
FO	Fiber Optic
FPI	Fabry-Perot interferometer
FSR	Free Spectral Range
GPIB	General Purpose Interface Bus
GUI	Graphical User Interface
HAZ	Heat-affected Zone
INESC TEC	Institute for Systems and Computer Engineering, Technology and Science
IPHT	Leibniz Institute of Photonic Technology
ISO	International Organization for Standardization
LbL	Line-by-Line
LIF	Lab-In-Fiber
LPFGs	Long Period Fiber Gratings
M	Mirror
MI	Michelson interferometer
MMI	Multimode Interference
MPI	Multiphoton Ionization
MZI	Mach-Zehnder interferometer
NA	Numerical Aperture
NIR	Near Infrared
OFS	Optical Fiber Sensors
OL	Objective Lens
OPD	Optical Path Difference
OSA	Optical Spectrum Analyzer
P	Brewster type thin film polarizer
p-pol	Transmited p-polarization laser beam
PbP	Point-by-Point
PhD	Doctor of Philosophy
Pl-b-Pl	Plane-by-Plane
PPE	Personal Protective Equipment
R&D	Research and Development
R&D+i	Research, Development and Innovation
RHS	Right-Hand Side
RI	Refractive Index
s-pol	Reflected s-polarization laser beam
SHO	Second Harmonic Output
SI	Sagnac interferometer
SLM	Spatial Light Modulator
SMF	Single Mode Optical Fiber
SRI	Surrounding Refractive Index
TAP	Turn Around Point

TIR Total Internal Reflection

UV Ultraviolet

V Fringe Visibility

WD Working Distance

WG Waveguide

Chemical compounds/elements

Ag Silver

Ge Germanium

HF Hydrofluoric acid

KOH Potassium Hydroxide

SiO_2 Silicon Dioxide

TiO_2 Titanium Dioxide

Units

μm micrometer

dB decibel

fs femtosecond

Hz hertz

mW milliwatt

nm nanometer

CHAPTER 1

Introduction

Optical fiber is currently deployed worldwide, linking people, businesses, communities, countries, and continents. The basic human desire to communicate and problem-solving behavior also led to significant investment in Research and Development (R&D) in the photonics field. Thus, optical fiber communication was born, the union of glass and light, which revolutionized how the world communicates. Indeed, the optical fiber is the backbone of all global communication due to its compatibility with other technologies and nearly unlimited bandwidth capacity. As a result, the 2009 Nobel Prize in Physics[1] was awarded to Charles K. Kao for "groundbreaking achievements concerning the transmission of light in fibers for optical communication".

Currently, optical fibers are revolutionizing distributed and point sensing due to their small size, lightweight, low cost, and fundamentally because glass optical fibers are almost always made from silica (SiO_2), a dielectric material. Thus, optical fibers do not emit electromagnetic radiation, nor are they affected by such radiation. As the Optical Fiber Sensors (OFS) field is complementary to optical communication, it has availed the benefit of advancements on optical fibers and optoelectronic instrumentation [1]. Recent works and exchanging ideas on the latest advances in research and development on optical fiber and photonic sensing are addressed in the International Conference on Optical Fiber Sensors, established in 1983. Currently is acknowledged by the scientific community as one of the world's leading conference on all topics related to photonic sensing technologies. Indeed, optical fiber sensing has become a key enabling technology in many domains, from civil engineering to petrochemical, power cable, and aerospace.

The backbone of the most modern application of fiber optic technology is the single-mode fiber, i.e., a fiber which supports only a single spatial mode. This type of optical fiber comprises a core (typically 8.2 µm in diameter), a cladding (typically 125 µm in diameter), and a coating or buffer (typically 245 µm in diameter). The core (the inner layer) is a cylindrical waveguide made of silica glass containing controlled amounts of doping (e.g., Germanium, Ge), along which light propagates and is guided. The cladding (the exterior layer) made of pure silica glass has a lower refractive index (RI) than the RI of the core, confining the guided mode and minimizing the loss of light from the core, avoiding exposure to the surrounding refractive index (SRI), i.e., air and the scattering loss at the surface of the fiber. The coating or buffer can be composed of a layer of plastic (e.g., simple acrylate or polyimide) or other materials such as carbon and aluminum compounds. This layer is used to absorb all cladding light that is not properly guided and protect the otherwise nacked glass from atmospheric interaction, which can compromise the mechanical

[1] Website: https://www.nobelprize.org/prizes/physics/2009/kao/facts/

strength of the fiber. The principle of transmission of light along optical fibers is based on total internal reflection. The Total Internal Reflection (TIR) occurs when light rays travelling through the fiber meet the core-cladding interface at an incident angle that is equal to or greater than the critical angle. The critical angle relies on the difference in refractive indices between the core and the cladding. Therefore, when the angle of incidence is greater than or equal to the critical angle, the ray is reflected back into the core instead of refracting into the cladding, allowing it to be guided within the core. Snell's law states the relationship between the angles of incidence and refraction according to the refractive indices of the core and cladding [1, 2].

Figure 1.1 (a) illustrates the basic concept of an optical fiber sensing system.

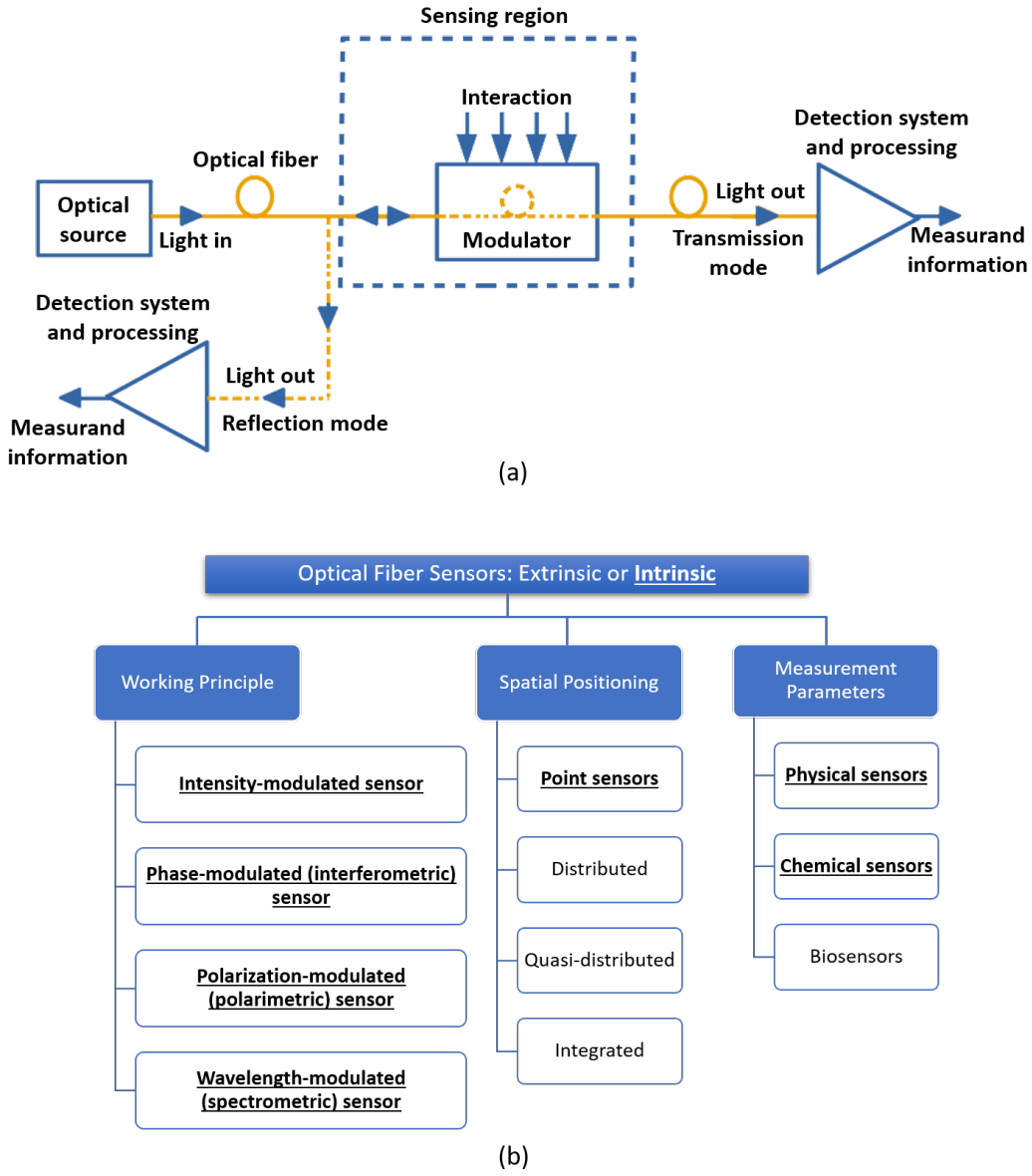


Figure 1.1. *Schematic: (a) diagram of an optical fiber sensing system, and (b) flowchart summarizing the different classifications of OFS.*

In the sensing system, the light travels through the optical fiber, and in the sensing region, the properties of the light are altered by changes in the refractive index, which are caused by variations in the parameters of interest. The optical fiber carries the modulated light signal from the source to the detector [1]. Optical sensing systems must be able to operate flawlessly in harsh environments while meeting demanding operational requirements such as high sensitivity (high signal-to-noise ratio for precision measurement of subtle changes), stability (meaningful results obtained over long periods of time, without the need for recalibration), ruggedness (reliability in a variety of temperature, humidity or vibration conditions), and low size, weight, and power (compact design and energy-efficient for easy field deployment). Furthermore, it must deliver high performance and be cost-effective.

The optical fiber sensors can be classified according to the location where the light is modulated, extrinsic or intrinsic. In the extrinsic sensor types, the optical fiber is used as a means to carry light to an external sensing system, while in the intrinsic type, the light does not have to leave the optical fiber to perform the sensing function. The intrinsic fiber sensor types are more attractive and widely researched as this scheme has many advantages compared to the extrinsic, such as their in-fiber nature and the flexibility in the design of the fiber sensing region [1]. Furthermore, depending on the light property that is modified, optical fiber sensors can be mainly classified in intensity, phase, polarization, and wavelength. The OFSs can also be further classified based on its spatial positioning as well as based on the measurement capabilities. A summary of the different classifications of OFS is shown in Figure 1.1 (b), highlighting the OFSs types explored in this work.

It is anticipated that research on OFS technology will continue to grow, and that the technology will become widespread [1]. New optical fiber sensors are progressively emerging, mainly the fabricated using advanced techniques such as femtosecond (fs) laser[2] micromachining, focused ion beam milling, etc.

1.1 Motivation and Objectives

Gerard Mourou and Donna Strickland were awarded one half of the 2018 Nobel Prize in Physics[3] for “their method of generating high-intensity, ultra-short optical pulses”. A recognized groundbreaking invention in the field of laser physics, which paved the way and enabled new regimes of high-intensity light-matter interactions. In recent years, many research efforts enabled the rapid development of the fs-laser sources, and the breakthrough results achieved in three-dimensional (3D) micro-/nanofabrication make it possible to use the high potential of these fabrication techniques in a wide range of applications including integrated optics, plasmonics, microbiology, and microelectromechanical systems.

In this context, some industrial companies already make efforts to develop and manufacture products (such as high strength Fiber Bragg Gratings (FBGs)) that are supported by fs-laser writ-

[2]The femtosecond laser belongs to the category of ultrafast lasers or ultrashort pulse lasers which emit optical pulses of 1 to 1000 femtoseconds duration.

[3]Website: `https://www.nobelprize.org/prizes/physics/2018/summary/`

ing, with a particular focus on the companies: FBGS[4], Germany/ Belgium based, Translume[5], USA based, and TeraXion[6], Canada based. Furthermore, Newport Corporation[7] offered a micromachining workstation based on laser direct-writing, including Newport's femtoFBG[8], the first commercially available workstation for FBGs manufacturing based on fs-laser direct writing. However, it should be noted that the system is no longer available. Workshop of Photonics, operated by Altechna R&D, is a leading provider of femtosecond laser micromachining solutions for industrial and scientific applications. The company provides a range of integrated services, from feasibility studies and prototyping to turnkey solutions encompassing specialized micromachining services and custom laser workstations. Its portfolio comprises the FemtoFBG Laser workstation for fiber Bragg grating inscription as well as a series of ultra-high precision femtosecond laser micromachining workstations[9] designed to meet both industrial and scientific requirements.

The Centre for Applied Photonics (CAP) at Institute for Systems and Computer Engineering, Technology and Science (INESC TEC[10]) has more than 40 years experience in the design, development, and implementation of different optical sensing devices, going from concept to applications in diverse areas (industrial, environmental, biomedical). The R&D activity is also oriented towards optical fiber sources, optical fiber communication, and microfabrication (thin films and integrated optics). In the early 1980s, INESC TEC started working in the field of optical fiber sensors through the European project NOSCA based on the development of an optical fiber sensor for monitoring pressure in the jet engines of commercial aircrafts. The number of laboratory prototypes grew as the projects increased, with the special focus on the optical fiber sensors installation in the D. Luís I Bridge, in Porto, in 2003, where load tests were performed for the passage of the Metro (Figure 1.2). The low installation and operation costs and a longer life cycle, soon made clear the real potential of these sensors. As a result, FiberSensing was created and pre-incubated at INESC TEC in 2004. Since then, it has become a world leader in supplying systems for measuring and monitoring critical physical assets using optical fiber Bragg gratings. In 2014, a decade later, INESC TEC sold the company to the German instrumentation firm HBM (Hottinger Baldwin Messtechnik), marking a key milestone in the internationalization of Portuguese optical sensing technology. Following its merger with Brüel & Kjær in 2019, HBM became part of HBK (Hottinger Brüel & Kjær), under the Spectris Group[11].

Nowadays, the conventional fabrication of FBGs and LPFGs by using ultraviolet (UV) laser exposure through the phase mask method and the electric arc technique is well-established in the R&D activity of INESC TEC. However, femtosecond written FBGs offer many advantages over conventional UV laser written gratings. Foremost of these is the reduced need for photosensitivity, crucial for UV fabrication. Gratings have been fabricated in sapphire fibers, pure silica photonic

[4]Website: `https://www.fbgs.com/`
[5]Website: `http://www.translume.com/`
[6]Website: `http://www.teraxion.com/`
[7]Website: `https://www.newport.com/`
[8]Website: `https://www.newport.com/f/fiber-bragg-grating-workstation`
[9]Website: `https://wophotonics.com/products/`
[10]Website: `https://www.inesctec.pt/en`
[11]Website: `https://www.hbm.com/en/4584/fibersensing-profile/`

crystal fiber, with refractive index changes close to those obtained by conventional methods.

In 2015, INESC TEC defined the local implementation of an advanced fabrication method based on 3D laser direct writing as a priority to consolidate the knowledge acquired during the last two decades on optical sensors and microfabrication through UV laser exposure. The first works were carried out in cooperation with an international partner (the University of Toronto, Peter Herman Group), allowing learning of the fundamental fs-laser micro/nanofabrication techniques. Thus, it was possible to assemble the first version of the laser direct writing unit developed for planar substrates. Furthermore, from this cooperation resulted, a pioneering work based on the creation of stress relief/induction volumes near the waveguides [3]. The continuity and the application of this work in the development of novel optical fiber devices are explored during this PhD (doctor of philosophy) program.



Figure 1.2. *Photomontage of remarkable moments of the story of INESC TEC: (a) Research group in the '80s, (b) Working at project NOSCA, and (c) Optical fiber sensors installation in the D. Luís I Bridge.*

While the 3D capabilities of fs-laser writing have been quite intensely explored in planar devices, the same effect has not yet been properly explored in optical fibers. Glass cladding in a typical single mode optical fiber (SMF) defines an untapped volume constituting more than 99% of the glass fiber cross-sectional area. Thus, the successful demonstration of devices fabricated in fiber claddings and interacting with the fiber core will eliminate cumbersome work associated with the coupling of optical fibers to planar optical chips, a very relevant practical technological challenge.

Experimental works showed that the existing laser direct writing unit designed for planar substrate exposure in INESC TEC was unsuitable for optical fiber processing. For example, several limitations were identified related to the fiber holder, precise alignment of the focused laser spot, fiber illumination, and image acquisition system, and the absence of a tension control system for writing periodic structures. Thus, assembling a second fs-laser fabrication system dedicated to fiber exposure was important for the R&D activity of the INESC TEC in the field of optical fiber sensors. The available infrastructure and institutional support provide excellent conditions for the development of this PhD work.

In this context, the main focus of this PhD program was the development of a fs-laser based processing system designed for optical fibers. Therefore, the technical backbone of the work will base on three-dimensional (3D) micromachining with a fs-laser. The idea is to use the capabilities of 3D microfabrication for the development and optimization of optical fiber sensors. The choice of this kind of laser, among other processing techniques, stems from its unique characteristics of ultrashort pulse width and extremely high peak intensity. The advantages include suppression of heat-affected zone (HAZ) formation around the irradiated area, high spatial resolution beyond the diffraction limit, and versatility in terms of the materials that can be processed. In this work, the fiber amplified fs-laser Satsuma HP from Amplitude Systèmes is utilized. In the following lines the specific and operational objectives that needed to be met with this PhD work are described:

- Evaluate and determine a cost-effective solution for assembling an fs-laser fabrication system that can process different types of optical fibers. The system should be suitable for fiber positioning, alignment and pre-tensioning during exposure and capable of working with either oil-immersion or dry objective lenses;
- Explore, test, and optimize the fs-laser system features to fabricate optical fiber sensors based on periodic structures, namely FBGs, LPFGs, and optical interferometers. The main effort will be focused on the study of fabrication parameters to optimize the writing process. This will include the evaluation of the effect of the scan velocities, writing power and pulse duration, and beam spot size (focusing optics) to determine the best writing strategy according to the intended structure;
- Investigate the thermal stability of FBGs and LPFGs through different types of pre-conditioning, namely annealing. Assess the thermal annealing conditions for temperature sensors to operate at different temperature ranges. Determine the thermal sensitivity of the sensors and the respective calibration;
- Conceive, design, and characterize new optical fiber sensors for demanding applications. The effort placed in the previous points must give rise to new and improved periodic struc-

tures, capable of acting as sensing elements when different light modulation formats are considered (intensity, wavelength, phase, and polarization);

- Explore the fs-laser irradiation followed by chemical etching technique to fabricate microchannels and cavities in an SMF-28e fiber, which broadens the opportunities to biological, chemical, or biochemical sensing applications (i.e., by enabling sensing of refractive index variation of surrounding medium).

This PhD work is strategic for the research group, allowing an expansion of opportunities and increased potential in what concerns internationalization. Also, the activities proposed provide a good balance between scientific advance and prospects of commercialization and industrial interest.

1.2 Structure of the Thesis

This thesis is organized in five chapters. The first and second chapters clarify the context and focus of the PhD work and review the fundamentals of femtosecond laser micromachining of transparent materials, respectively. Then follow two chapters of results addressing the fs-laser fabrication system and the optical fiber sensors developed; and one final chapter of conclusions and future work.

Chapter 1 provides a brief overview of optical fiber sensors and explains the context of this thesis, including the motivation and objectives. Besides this, the main contributions and the resulting peer-reviewed scientific publications are presented.

Chapter 2 reviews the fundamentals of femtosecond laser micromachining of transparent materials, describing some of the underlying physical mechanisms and technical details of the fabrication process of optical fiber devices. The optical fiber devices fabricated by fs-laser micromachining are also reviewed.

Chapter 3 deals with the fs-laser system developed in the framework of the PhD. Therefore, it describes the methods, tools, and technical details used in the assembling, development of the control software, and final integration of the components of the fs-laser system to fabricate optical fiber sensors. The characterization setups and procedures of the writing process are addressed.

Chapter 4 is dedicated to the optical fiber sensors fabricated by the fs-laser system. It is organized accordingly to the fabricated optical fiber structures: FBGs, LPFGs, and optical fiber interferometers. A brief introduction is presented for each structure, the working principle explained, the fabrication procedures detailed, and the experimental results of the characterization for sensing applications presented.

Chapter 5 presents the main conclusions of the research, development and innovation (R&D+i) activity realized during the PhD, where the main scientific achievements are highlighted, and suggestions for future work addressed.

1.3 Main Contributions

The PhD work resulted in a technological platform for the fabrication of new advanced optical sensors, namely fs-laser inscribed gratings as sensors. The Bragg and long-period gratings inscribed with fs-laser exhibit some features (e.g. robust thermal stability, a relatively large modification of refractive index and, notably controlled placement of the modified RI relative to the fiber axis) that are very useful for sensing applications. The customized fabrication success of these optical fiber sensors led to the collaboration with Fraunhofer Institute for Manufacturing Engineering and Automation, and also with the EFACEC (Empresa Fabril de Máquinas Eléctricas, SARL) company.

The technological platform was also employed in the practical classes of Advanced laboratories of the Integrated Master of Science in Physics Engineering course of the Faculty of Sciences of the University of Porto (FCUP), contributing to training students to:

- Carry out engineering duties, in particular those based on a thorough understanding of the specialized areas in physics engineering such as optics, optoelectronics, lasers, and instrumentation, whether in their fundamental or applied aspects;
- Arrive at full competence and autonomy in the design, fabrication and characterization of Bragg and Long Period gratings;
- Achieve a broad vision of the fundamentals and the role of advanced technology and technological innovation for R&D of optical sensors.

The research, development, and innovation activity realized during the PhD improve the current state-of-the-art of fs-laser inscription in optical fibers and its application to optical fiber sensors (OFS). The main contributions made to the scientific community include:

- The precise production of off-axis first order FBGs in an SMF-28e fiber through fs-laser direct writing. The impact of the fabrication parameters in the number of supported modes and birefringence resulted in novel conclusions, such as determining the minimum offset distance between the grating and core center of 2.5 µm to create a multimode section, which supports two separate fiber modes ($LP_{0,1}$ and $LP_{1,1}$), each split into two degenerate polarization modes. The resulting structure breaks the cylindrical symmetry of the fiber, introducing birefringence ($\sim 10^{-4}$) resulting in a polarization dependent Bragg wavelength for each mode. The potential of the multimode section as sensing head for strain, temperature, curvature and torsion sensing was successfully explored. The relatively low complexity and the robust nature of the fabricated devices opens the possibility of simultaneous detection of multiple parameters in practical applications;
- The entire fabrication process, including thermal annealing to improve the temperature stability, and coating with different TiO_2 film thicknesses of Long Period Fiber Gratings (LPFGs) operating at the turn around point (TAP) in SMF-28e fibers by fs-laser direct writing, is addressed in detail. The main contributions beyond state-of-the-art include a systematic fabrication and characterization study, presenting significant fabrication details such as inscription periods, shape and localization of the refractive index modifications across the core,

and the TiO_2 coating film thickness to obtain LPFGs operating precisely in the TAP condition surrounded by air or water with coupling to the asymmetric cladding modes. The experimental results show that the fabricated LPFGs must be annealed to stabilize their spectra. We demonstrated the fine-tuning of the resonance band's position and thermal stability up to 600 °C. The resonance wavelength sensitivity to the SRI of the uncoated and TiO_2 coated LPFGs operating at the TAP in air and water was evaluated and compared to the literature's reported works, presenting a significant SRI sensitivity enhancement.

1.4 Peer-Reviewed Scientific Publications

The research conducted during the PhD period concerning the 3D microfabrication with a femtosecond laser, in the development of optical devices for sensing applications, resulted in a total of thirty-eight peer-reviewed scientific publications (ORCID iD: `https://orcid.org/0000-0003-0674-9963`). These include twelve articles in international peer-reviewed journals and twenty-six peer-reviewed articles published in the proceedings of international and national conferences.

Since 2013, the PhD candidate has been involved in several research and technology projects related to optical fiber sensing technology. The ECOAL-MGT project work (optical fiber sensors to monitor greenhouse gases emitted from self-combustion coal waste piles at high temperature) that was developed before the PhD project resulted in two other publications during the PhD period. These include an article in a journal and a book chapter.

Several works were presented in international and national scientific conferences. As a result, a total of twenty-sixe peer-reviewed articles, eighteen in the form of oral presentations and eight as poster presentations were presented in international and national communications. Two articles were awarded by the SPIE, the international society for optics and photonics, by the Optical Society (OSA) Student Chapter of the University of Aveiro and Portuguese Society for Optics and Photonics (SPOF), at the IV International Conference on Applications in Optics and Photonics (AOP 2019), which was held in Lisbon.

The peer-reviewed scientific publications are presented in the following sections.

Articles in international peer-reviewed journals

Bibliometric indicators consulted in June 2025, Impact Factor & Quartile: Journal Citation Reports (Clarivate) 2023; SCImago Journal Rank & Quartile: Scimago 2024.

1. **D. Viveiros**, J. M. M. M. de Almeida, L. Coelho, H. Vasconcelos, J. M. Maia, V. A. Amorim, P. A. S. Jorge, P. V. S. Marques, Turn-Around-Point Long-Period Fiber Gratings with Coupling to Asymmetric Cladding Modes Fabricated by a Femtosecond Laser and Coated with Titanium Dioxide, *Journal of Lightwave Technology* 39 (14) (2021) 4784−4793.
   doi:10.1109/JLT.2021.3078257
   Indexing: Web of Science & Scopus. **Journal metrics:** IF 4.1 — Q1; SJR 1.294 — Q1.

2. C. S. Monteiro, A. V. Rodrigues, **D. Viveiros**, C. Linhares, H. Mendes, S. O. Silva, P. V. S. Marques, S. M. O. Tavares, O. Frazão, Optical Fiber Sensors for Structural Monitoring in Power Transformers, *Sensors* 21 (18) (2021) 6127. doi:10.3390/s21186127
Indexing: Web of Science & Scopus. **Journal metrics:** IF 3.5 — Q2; SJR 0.764 — Q1.

3. J. M. Maia, V. A. Amorim, **D. Viveiros**, P. V. S. Marques, Femtosecond Laser Micromachining of an Optofluidics-Based Monolithic Whispering-Gallery-Mode Resonator Coupled to a Suspended Waveguide, *Scientific Reports* 11 (2021) 9128. doi:10.1038/s41598-021-88682-x
Indexing: Web of Science & Scopus. **Journal metrics:** IF 3.8 — Q1; SJR 0.874 — Q1.

4. V. A. Amorim, **D. Viveiros**, J. M. Maia, P. V. S. Marques, Intensity-Modulated Refractometer Based on Mode-Mismatch in Surface Waveguides Inscribed by Femtosecond Laser Direct Writing, *Optics & Laser Technology* 135 (2021) 106723. doi:10.1016/j.optlastec.2020.106723
Indexing: Web of Science & Scopus. **Journal metrics:** IF 4.6 — Q1; SJR 1.000 — Q1.

5. P. Mesonero-Santos, A. Fernández-Medina, L. Coelho, **D. Viveiros**, P. A. S. Jorge, T. Belenguer, R. López Heredero, Effect of Low Doses of Gamma Radiation on Electric-Arc-Induced Long-Period Fiber Gratings, *Sensors* 21 (7) (2021) 2318. doi:10.3390/s21072318
Indexing: Web of Science & Scopus. **Journal metrics:** IF 3.5 — Q2; SJR 0.764 — Q1.

6. V. A. Amorim, J. M. Maia, **D. Viveiros**, P. V. S. Marques, Mach−Zehnder Interferometer-Based Evanescent Refractometer Inscribed at the Surface of Eagle 2000 Glass by Femtosecond-Laser Writing, *IEEE Sensors Journal* 21 (2) (2020) 1603−1608. doi:10.1109/JSEN.2020.3021586
Indexing: Web of Science & Scopus. **Journal metrics:** IF 4.5 — Q1; SJR 1.079 — Q1.

7. **D. Viveiros**, J. M. M. de Almeida, L. Coelho, H. Vasconcelos, J. M. Maia, V. A. Amorim, P. A. S. Jorge, P. V. S. Marques, Temperature Stability and Spectral Tuning of Long-Period Fiber Gratings Fabricated by Femtosecond Laser Direct Writing, *Sensors* 20 (14) (2020) 3898. doi:10.3390/s20143898 **(invited article)**
Indexing: Web of Science & Scopus. **Journal metrics:** IF 3.5 — Q2; SJR 0.764 — Q1.

8. **D. Viveiros**, V. A. Amorim, J. M. Maia, S. Silva, O. Frazão, P. A. S. Jorge, L. A. Fernandes, P. V. S. Marques, Femtosecond Laser Direct-Written Off-Axis Fiber Bragg Gratings for Sensing Applications, *Optics & Laser Technology* 128 (2020) 106227.
doi:10.1016/j.optlastec.2020.106227
Indexing: Web of Science & Scopus. **Journal metrics:** IF 4.6 — Q1; SJR 1.000 — Q1.

9. V. A. Amorim, J. M. Maia, **D. Viveiros**, P. V. S. Marques, Inscription of Surface Waveguides in Glass by Femtosecond Laser Writing for Enhanced Evanescent-Wave Overlap, *Journal of Optics* 22 (8) (2020) 085801. doi:10.1088/2040-8986/aba03f
Indexing: Web of Science & Scopus. **Journal metrics:** IF 2.0 — Q2; SJR 0.572 — Q2.

10. J. M. Maia, V. A. Amorim, **D. Viveiros**, P. V. S. Marques, Magnetic-Field Sensors in Fused Silica Fabricated by Femtosecond Laser Micromachining, *Journal of Physics: Photonics* 2 (1) (2020) 015003. doi:10.1088/2515-7647/ab6711
Indexing: Web of Science & Scopus. **Journal metrics:** IF 4.6 — Q1; SJR 1.576 — Q1.

11. V. A. Amorim, **D. Viveiros**, J. M. Maia, P. V. S. Marques, Mass-Producible Low-Loss Broadband Optical Waveguides in Eagle 2000 Glass by Femtosecond Laser Writing, *IEEE Photonics Technology Letters* 31 (20) (2019) 1658−1661. doi:10.1109/LPT.2019.2942104
Indexing: Web of Science & Scopus. **Journal metrics:** IF 2.3 — Q2; SJR 0.776 — Q2.

12. V. A. Amorim, J. M. Maia, **D. Viveiros**, P. V. S. Marques, Loss Mechanisms of Optical Waveguides Inscribed in Fused Silica by Femtosecond Laser Direct Writing, *Journal of Lightwave Technology* 37 (10) (2019) 2240−2245. doi:10.1109/JLT.2019.2900913
Indexing: Web of Science & Scopus. **Journal metrics:** IF 4.1 — Q1; SJR 1.294 — Q1.

13. J. Ribeiro, **D. Viveiros**, J. Ferreira, A. Lopez-Gil, A. Dominguez-Lopez, H. F. Martins, *et al.* (2017), ECOAL Project - Delivering Solutions for Integrated Monitoring of Coal-Related Fires Supported on Optical Fiber Sensing Technology, *Applied Sciences* 7 (9) (2017) 956. doi:10.3390/app7090956
Indexing: Web of Science & Scopus. **Journal metrics:** IF 3.2 — Q2; SJR 0.521 — Q2.

Book Chapter

1. J. Ribeiro, **D. Viveiros**, J. Ferreira, I. Suárez-Ruiz, J. L. Santos, J. M. Baptista, D. Flores, Volatile organic compounds emitted from self-burning coal waste piles in Spain and Portugal: Environment and human health concerns, in *Progress in Medical Geology* (M. Ibaraki, H. Mori, Eds.), Cambridge Scholars Publishing, Newcastle upon Tyne, UK (2017) 229−247. ISBN 978-1-4438-7319-2

Conference Proceedings Articles

1. **D. Viveiros**, J. M. Maia, J. M. M. M. de Almeida, L. Coelho, V. A. Amorim, P. A. S. Jorge, P. V. S. Marques, Optical fiber interferometers fabricated by femtosecond laser direct writing for sensing applications, in *Proc. SPIE 13639, 29th International Conference on Optical Fiber Sensors* (2025) 13639BD. doi:10.1117/12.3073172 **(post-deadline article)**

2. J. M. Maia, V. A. Amorim, **D. Viveiros**, P. V. S. Marques, Femtosecond laser micromachining of a monolithic whispering-gallery-mode resonator coupled to a suspended waveguide, *EPJ Web of Conferences* 255 (2021) 00001. doi:10.1051/epjconf/202125500001

3. P. V. S. Marques, V. A. Amorim, J. M. Maia, **D. Viveiros**, Loss mechanisms in femtosecond laser written optical waveguides, *Proc. SPIE 11676, Frontiers in Ultrafast Optics: Biomedical, Scientific, and Industrial Applications XXI* (2021) 1167615. doi:10.1117/12.2584493 **(invited article)**

4. **D. Viveiros**, J. M. M. M. de Almeida, L. Coelho, J. M. Maia, V. A. Amorim, P. A. S. Jorge, P. V. S. Marques, Off-axis fiber Bragg grating fabricated by femtosecond laser direct writing for torsion sensing, in *Optical Fiber Sensors Conference 2020 Special Edition*, OSA Technical Digest (2020) paper W4.2. doi:10.1364/OFS.2020.W4.2

5. **D. Viveiros**, J. M. M. M. de Almeida, L. Coelho, H. Vasconcelos, J. M. Maia, V. A. Amorim, P. A. S. Jorge, P. V. S. Marques, Femtosecond laser direct writing of turn-around-point long period fiber gratings coated with titanium dioxide for improved sensitivity, in *Optical Fiber Sensors Conference 2020 Special Edition*, OSA Technical Digest (2020) paper Th3B.5. doi:10.1364/OFS.2020.Th3B.5

6. **D. Viveiros**, H. Vasconcelos, J. M. M. M. de Almeida, L. Coelho, V. A. Amorim, J. M. Maia, P. A. S. Jorge, P. V. S. Marques, Characterization of femtosecond-written Mach−Zehnder interferometers based on titanium dioxide coated long period fiber gratings, in *Optical Fiber Sensors Conference 2020 Special Edition*, OSA Technical Digest (2020) paper W4.18. doi:10.1364/OFS.2020.W4.18

7. **D. Viveiros**, J. M. M. M. de Almeida, L. Coelho, H. Vasconcelos, V. A. Amorim, J. M. Maia, P. A. S. Jorge, P. V. S. Marques, Femtosecond laser-written long period fibre gratings coated with titanium dioxide for improved sensitivity, *Proc. SPIE 11354, Optical Sensing and Detection VI* (2020) 113540C. doi:10.1117/12.2555686

8. **D. Viveiros**, J. M. M. M. de Almeida, L. Coelho, J. M. Maia, V. A. Amorim, H. Vasconcelos, P. A. S. Jorge, P. V. S. Marques, Femtosecond laser micromachining of Fabry−Perot interferometers in SMF-28 fiber for pressure sensing, *Proc. SPIE 11354, Optical Sensing and Detection VI* (2020) 113540R. doi:10.1117/12.2554415

9. H. Vasconcelos, J. M. M. M. de Almeida, C. Saraiva, **D. Viveiros**, P. A. S. Jorge, L. Coelho, Preliminary assessment on the detection of putrescine using long period fiber gratings coated with titanium dioxide and poly(ethylene-co-vinyl acetate), *Proc. SPIE 11354, Optical Sensing and Detection VI* (2020) 113540B. doi:10.1117/12.2555397

10. C. S. Monteiro, A. V. Rodrigues, **D. Viveiros**, C. Linhares, S. M. O. Tavares, H. Mendes, *et al.*, FBG two-dimensional vibration sensor for power transformers, *Proc. SPIE 11199, Seventh European Workshop on Optical Fibre Sensors* (2019) 111990M. doi:10.1117/12.2541132

11. **D. Viveiros**, J. M. Maia, V. A. Amorim, P. A. S. Jorge, P. V. S. Marques, Fabrication of periodic structures in optical fibers by femtosecond laser micromachining, in *Proceedings of the 3rd Doctoral Congress in Engineering − Symposium on Engineering Physics*, Porto, Portugal (2019).

12. J. M. Maia, V. A. Amorim, **D. Viveiros**, P. V. S. Marques, Fabry−Pérot interferometer fabricated in fused silica through femtosecond laser micromachining, in *Proceedings of the 3rd Doctoral Congress in Engineering − Symposium on Engineering Physics*, Porto, Portugal (2019).

13. V. A. Amorim, J. M. Maia, **D. Viveiros**, P. V. S. Marques, Low-loss broadband femtosecond laser written surface waveguides for enhanced evanescent coupling, in *Proceedings of the 3rd Doctoral Congress in Engineering – Symposium on Engineering Physics*, Porto, Portugal (2019).

14. C. S. Monteiro, A. V. Rodrigues, **D. Viveiros**, C. Linhares, S. M. O. Tavares, H. Mendes, S. O. Silva, P. V. S. Marques, O. Frazão, Vibration detection on power transformers using optical fiber sensors, in *Proceedings of the 3rd Doctoral Congress in Engineering – Symposium on Engineering Physics*, Porto, Portugal (2019).

15. **D. Viveiros**, J. M. Maia, V. A. Amorim, P. A. S. Jorge, P. V. S. Marques, Fabrication of periodic structures in optical fibers by femtosecond laser micromachining for sensing applications, *Proc. SPIE 11207, Fourth International Conference on Applications of Optics and Photonics* (2019) 112070W. doi:10.1117/12.2527261 **(best student paper award)**

16. V. A. Amorim, **D. Viveiros**, J. M. Maia, P. V. S. Marques, Spectral characteristics of optical waveguides fabricated in glass by femtosecond laser direct writing, *Proc. SPIE 11207, Fourth International Conference on Applications of Optics and Photonics* (2019) 112071J. doi:10.1117/12.2527400

17. J. M. Maia, V. A. Amorim, **D. Viveiros**, P. V. S. Marques, Femtosecond laser micromachining of Fabry–Pérot interferometers in fused silica for refractive index sensing, *Proc. SPIE 11207, Fourth International Conference on Applications of Optics and Photonics* (2019) 1120712. doi:10.1117/12.2527302

18. C. S. Monteiro, **D. Viveiros**, C. Linhares, S. M. O. Tavares, H. Mendes, S. O. Silva, P. V. S. Marques, O. Frazão, 3D prototyping of a fiber Bragg grating vibration sensor for power transformers, *Proc. SPIE 11207, Fourth International Conference on Applications of Optics and Photonics* (2019) 1120727. doi:10.1117/12.2530084 **(best poster award)**

19. V. A. Amorim, J. M. Maia, **D. Viveiros**, P. V. S. Marques, Addressing the fabrication difficulties of femtosecond laser written surface waveguides for enhanced evanescent coupling, *EPJ Web of Conferences, EOS Optical Technologies* 215 (2019) 15003. doi:10.1051/epjconf/201921515003

20. J. M. Maia, V. A. Amorim, **D. Viveiros**, P. V. S. Marques, Femtosecond laser micromachining of Fabry–Pérot interferometers for magnetic field sensing, *EPJ Web of Conferences, EOS Optical Technologies* 215 (2019) 15001. doi:10.1051/epjconf/201921513001

21. **D. Viveiros**, J. M. M. M. de Almeida, L. Coelho, H. Vasconcelos, V. A. Amorim, J. M. Maia, P. A. S. Jorge, P. V. S. Marques, Spectral tuning of long period fiber gratings fabricated by femtosecond laser micromachining through thermal annealing, in *Proceedings of the 7th International Symposium on Sensor Science* 15 (1) (2019) 4. doi:10.3390/proceedings2019015004

22. P. V. S. Marques, V. A. Amorim, J. M. Maia, **D. Viveiros**, Femtosecond laser fabrication of monolithic low-loss high-quality optical waveguides and microfluidic channels for optical sensing applications, in *Proceedings of the PhotonIcs & Electromagnetics Research Symposium*, Rome, Italy (2019).

23. P. V. S. Marques, V. A. Amorim, J. M. Maia, D. Alexandre, **D. Viveiros**, Fabrication of monolithic add-drop filters in pure silica by femtosecond laser writing, in *20th International Conference on Transparent Optical Networks (ICTON)* (2018) 1–4. doi:10.1109/ICTON.2018.8473735 **(invited article)**

24. V. A. Amorim, J. M. Maia, **D. Viveiros**, P. V. S. Marques, Optical and microfluidic monolithic devices fabricated by femtosecond laser micromachining, in *Optics 2018 – 6th International Symposium in Optics and its Applications*, Trento, Italy (2018).

25. **D. Viveiros**, J. M. Maia, V. A. Amorim, P. A. S. Jorge, P. V. S. Marques, Fabrication of optical sensing devices by 3D laser micromachining, in *JEFFA – 3rd Jornadas em Engenharia Física, Física, Física Médica e Astronomia*, Porto, Portugal (2018).

26. **D. Viveiros**, J. Ferreira, P. A. S. Jorge, P. V. S. Marques, Point-by-point optical fiber Bragg gratings fabricated by femtosecond laser exposure, in *Proceedings of the 2nd Doctoral Congress in Engineering*, Porto, Portugal (2017).

CHAPTER 2

Femtosecond Laser Micromachining

In 1996, a breakthrough was demonstrated by Hirao and co-workers [4]: tightly focused fs-laser pulses could modify in a permanent way the optical properties of a small volume inside the bulk of transparent glass. Correct exposure leads to a permanent refractive index increase within this volume, whereby complex refractive index structures (e.g., diffractive elements, waveguides, and local refractive index modification) could be created by translating the sample. This discovery led to many other research initiatives related to the fs-laser micromachining of optical fibers and their applications in fabricating optical fiber microstructures and sensing devices [5−7].

This chapter reviews the fundamentals of fs-laser micromachining of transparent materials, describing some of the underlying physical mechanisms required to understand the interaction between fs-laser pulses and transparent materials. An overview of the important exposure parameters in fs-laser processing, emphasizing the technical details of the fabrication process of optical fiber devices will be given. A technique for optical fiber machining, based on femtosecond laser exposure followed by anysotropic chemical etching will be reviewed, and some background knowledge to produce an open channel through an optical fiber is provided. The last section of the chapter gives an overview of the optical fiber devices fabricated by fs-laser micromachining.

2.1 Femtosecond Laser–Material Interaction

The fs-laser micromachining results from the laser-induced optical breakdown process. In this process, the optical energy is transferred to the material, ionizing a large number of electrons that, in turn, transfer energy to the lattice. As a result of the fs-laser pulse exposure, the material can undergo a phase or structural modification, giving rise to a localized permanent change in the refractive index or even a void [5−9]. Indeed, the mechanisms of material modification mostly rely on the laser pulse duration. The timescale of the physical processes involved in fs-laser micromachining is shown in Figure 2.1.

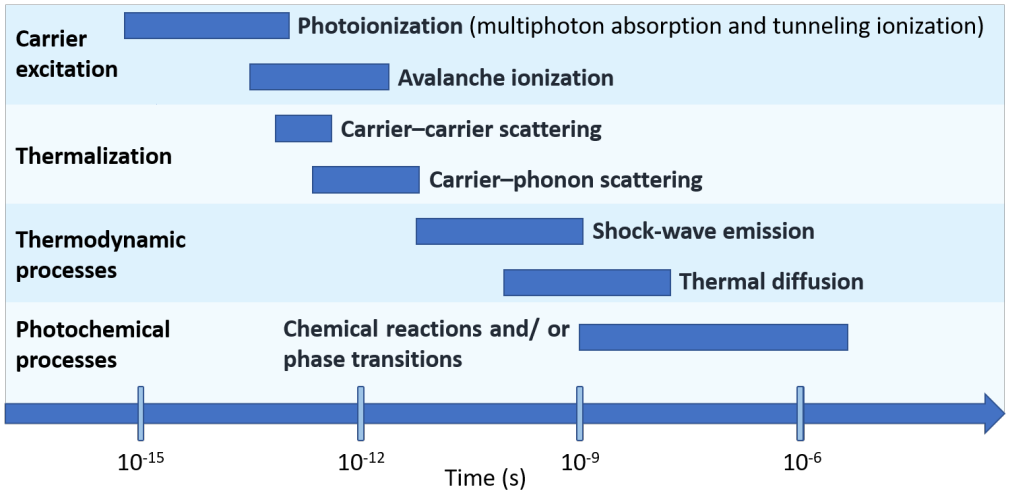


Figure 2.1. *Timescale of the physical phenomena associated with the interaction of a fs-laser pulse with transparent materials. The blue bars represent typical timescales for the relevant process. (Adapted from [8], © 2008, with permission from Springer Nature).*

Focused fs-laser pulses, with wavelengths in the visible or near-infrared spectra, do not possess enough photon energy to be linearly absorbed in glasses. In this case, nonlinear absorption processes such as nonlinear photoionization and avalanche ionization are required to promote valence electrons to the conduction band. Nonlinear photoionization refers to the direct excitation of electrons by the laser field. It can be separated into two different regimes, namely multiphoton ionization (MPI) and/or tunneling photoionization, depending on the laser frequency and intensity [5, 6, 8–10].

Nonlinear Photoionization

Multiphoton absorption occurs due to the simultaneous absorption of multiple photons by an electron in the valence band, as illustrated in Figure 2.2 (a). In this regime, photoionization rate $P_{PI}(I)$ depends strongly on the laser intensity:

$$P_{PI}(I) = \sigma_k I^k, \tag{2.1}$$

where σ_k is the multiphoton absorption coefficient for k photon absorption, and I is the laser intensity [5, 6, 10]. The interband transition takes place when the total absorbed energy of all the k photons that interact with the single electron exceeds the bandgap energy E_g, i.e., $k\hbar\omega \geq E_g$ where $\hbar$ is Planck's constant and ω is the laser frequency [5, 6, 10, 11]. For example, in the fused silica (composition of the fiber cladding), the bandgap energy is 9 eV, while the photon energy at 515 nm wavelength is 2.41 eV. Therefore, at least four photons are required to be absorbed by a single valence electron to drive an interband transition. Typically, multiphoton ionization is the dominant mechanism at low laser intensities and high frequencies (but below that which is needed for single-photon absorption). Whereby, the tunneling ionization (Figure 2.2 (b)) occurs for a high laser intensity and low frequency. In the tunneling ionization, the strong field distorts the band structure and reduces the potential barrier between the valence and conduction bands [5, 6, 10, 11]. Thus, direct band to band transitions may then proceed by quantum tunneling of the electron

from the valence to the conduction band. The transition between the multiphoton and tunneling photoionization can be determined by the Keldysh parameter, γ:

$$\gamma = \frac{\omega}{e}\sqrt{\frac{m_e c n \epsilon_0 E_g}{I}}, \tag{2.2}$$

where e is the fundamental electron charge, m_e is the electron effective mass, c is the speed of light, n is the linear refractive index, and ϵ_0 is the permittivity of free space. When γ is smaller (greater) than 1.5, the tunneling (multiphoton) ionization process dominates the photoionization [5, 6, 10]. For $\gamma \sim 1.5$, photoionization is a combination of tunneling and multiphoton ionization. For waveguide fabrication in dielectrics, typical laser, and material properties result in $\gamma \sim 1$, so that nonlinear ionization is a combination of both processes [5, 6, 10, 11].

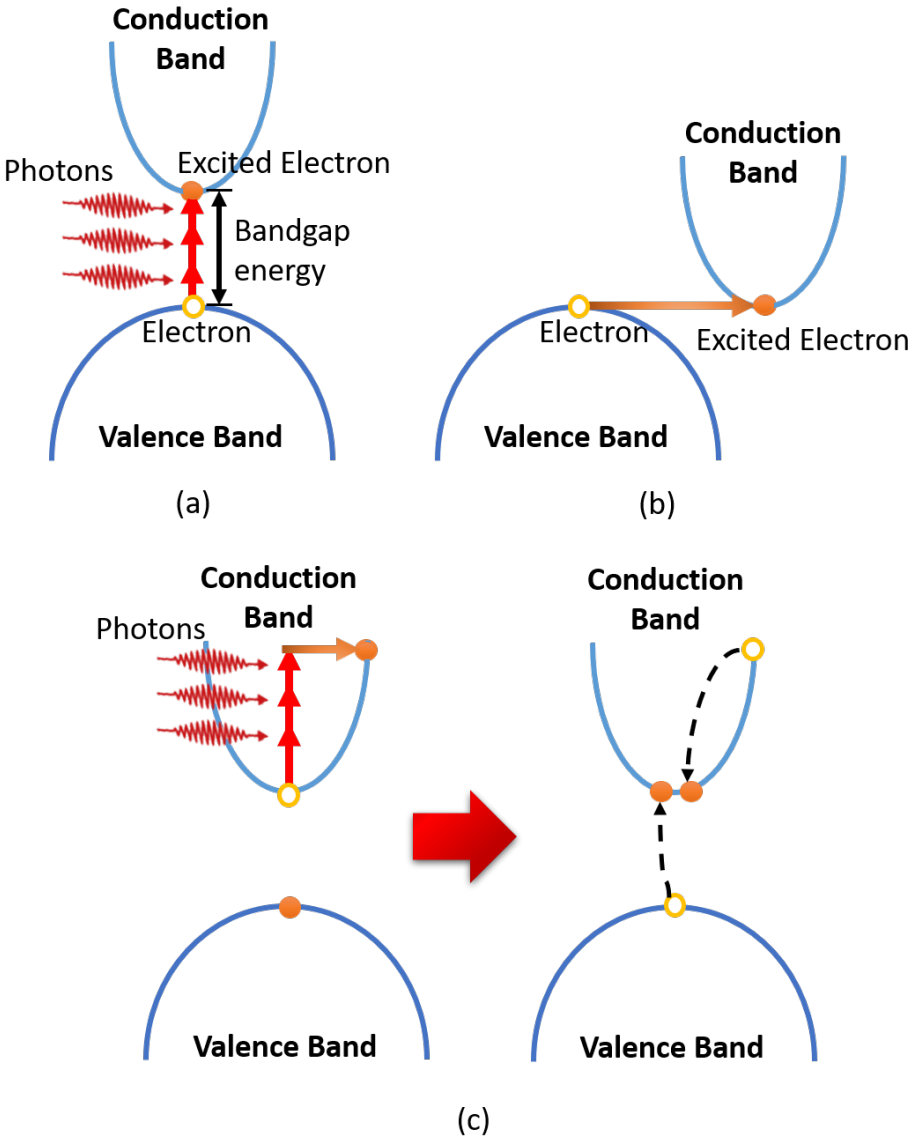


Figure 2.2. *Schematic diagram of the nonlinear photoionization processes underlying fs-laser machining. (a) Multi-photon ionization, (b) Tunneling ionization, and (c) Avalanche ionization: free carrier absorption followed by impact ionization. (Adapted from [11], © 2008, with permission from IEEE).*

Avalanche Photoionization

Avalanche ionization implies free-carrier absorption followed by impact ionization (Figure 2.2 (c)). Electrons present in the conduction band oscillate in the laser's electromagnetic field and gradually gain energy by collisions until the electron energy exceeds that of the bandgap. Therefore, this electron can ionize by collision (impact ionization) another electron from the valence band, resulting in two excited electrons at the conduction band's lowest available energy state. Both electrons can again undergo free carrier absorption and impact ionization. The process can repeat itself as long as the laser field is present and strong enough, giving rise to an electron avalanche. Thus, the avalanche ionization requires sufficient seed electrons in the conduction band, which triggers the process and is more efficient with longer pulse durations. These seed electrons, which rely on the material, may be provided by photoionization (for pure dielectrics and ultrashort pulses) [5, 6, 10, 11].

2.1.1 Regimes of Material Modification

The regime of modification and resulting morphological change rely on exposure parameters (e.g., energy, pulse duration, repetition rate, wavelength, polarization, focal length, and scan speed) and material properties (e.g., bandgap, thermal conductivity, and others) [5, 6, 10−12]. When an fs-laser beam is focused inside the optical fiber through an objective lens, the high fs-laser beam intensity leads to a nonlinear absorption within the focal volume through ionization processes (i.e., multiphoton/tunneling and avalanche photoionization), as shown in Figure 2.3 (a) and (b) [5, 6, 12]. Depending on the pulse energy, fs-laser exposure can induce three regimes of permanent modification in a transparent material (e.g., optical fiber): isotropic refractive index change, anisotropic refractive index change (birefringence), and voids [5, 6, 12]. These regimes are clearly distinguished only for fs-laser pulses shorter than about 200 fs, as shown in Figure 2.3 (c). Following is a description of each regime of modification:

- **Regime 1:** a smooth refractive index change is achieved for low pulse energies, resulting in a positive refractive index change with a very weak selectivity in etching. In this regime, the morphological change is likely due to color center formation, densification (structural change), and thermal treatment (melting) of the glass [5, 6, 12]. For example, optical waveguides devices [13] and FBGs [14] are fabricated inside the optical fiber using design parameters that give rise to this modification regime;
- **Regime 2:** For intermediate pulse energies, the formation of periodic nanostructures occurs in the focal volume, resulting in an anisotropic refractive index change (i.e., birefringence) in the optical fiber. These periodic nanostructures or "nanogratings" consist of periodically distributed oxygen-deficient regions caused by interference of the laser field and the induced electron plasma wave [5, 6, 12]. This regime is suitable to fabricate polarization devices [15] and achieve high etching selectivity of the fs-laser exposed patterns, allowing the fabrication of buried microchannels for microfluidic applications [16];

- **Regime 3:** a Coulomb explosion (microexplosion) occurs in the bulk of the material for high pulse energies, resulting in a region of modification characterized by material damage or void formation. This morphological change is due to the fs-laser induced shockwaves, which generate stresses/pressures greater than Young's modulus (i.e., the internal pressure of the material) within the focal volume. Such shockwaves leave behind a less dense or hollow-core central region termed a void surrounded by a shell of a higher refractive index [5, 6, 12]. Voids are suitable for fabricating optical memory devices, micro-holes, micro-cavities, micro-channels, and type II FBGs [11, 17].

Figure 2.3 (d) shows microscope images of typical refractive index modifications induced by the fs-laser exposure, namely a waveguide [13], a nanograting inscribed with polarization parallel to the scan direction [16], and a micro-void [17]. In addition to pulse energy, these structural changes also depend on repetition rate, which determines whether the modification regime is due to individual pulses or cumulative pulse heating [5, 6, 18].

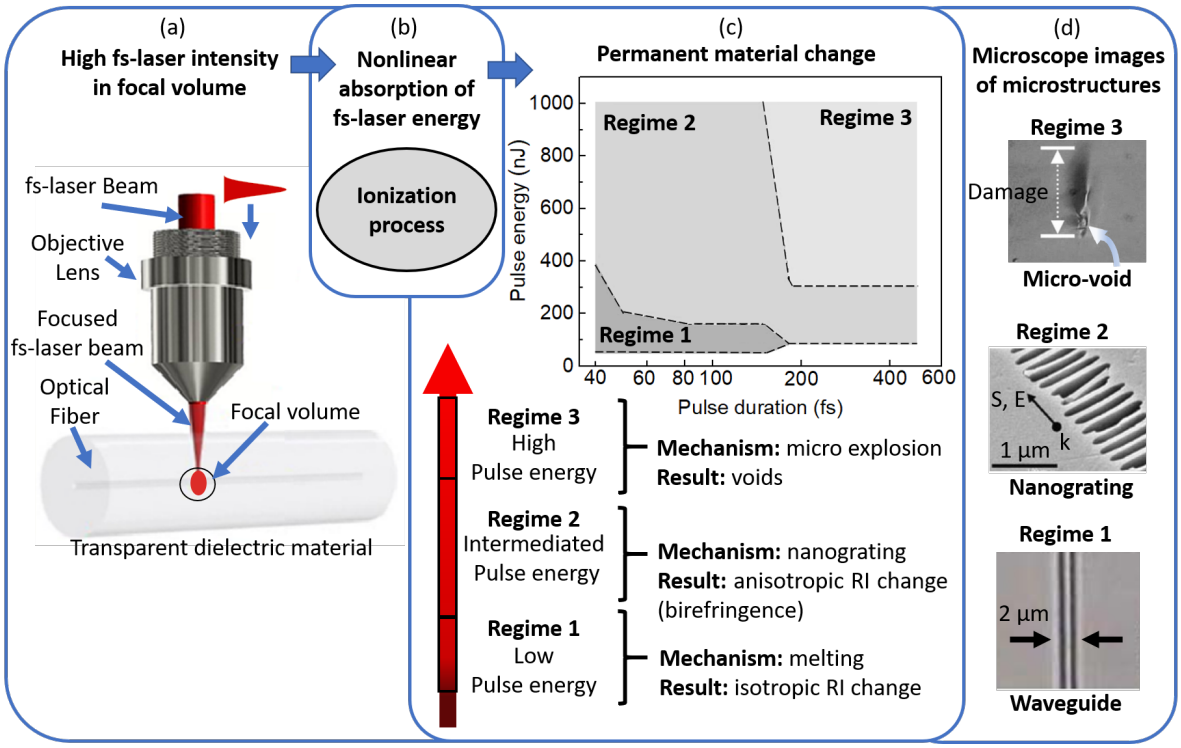


Figure 2.3. *Schematic diagram of the physical mechanisms in sequential order of the key steps (a), (b), and (c) and microscope images (d) of typical refractive index modification induced by fs-laser exposure. Note: the inset image in step (c) was "Adapted from [12], © 2005, with permission from AIP Publishing" , and the insets images in step (d): Waveguide, "Adapted from [13], © 2005, with permission from The Optical Society", Nanograting, "Adapted from [16], © 2006, with permission from Springer Nature", and Micro-void, "Adapted from [17], © 2015, with permission from Elsevier".*

For a low enough repetition rate (i.e., 1 kHz), the generated heat in fused silica is diffused out of the focal volume before the next pulse arrives (i.e., the thermal diffusion time in glass is $\sim$1 µs, which is much shorter than the time between two consecutive pulses, $\sim$1 ms). Thus, the structure is modified pulse by pulse without heat accumulation effect [5, 6, 18]. However, if the repetition rate is high (i.e., >100 kHz), the time between laser pulses is less than the heat diffusion time, resulting

in cumulative heating in the focal volume. When the material is moved, the size of melted volume can be controlled by the effective number of pulses N from laser exposure, i.e., $N = 2w_0R/v$ where $2w_0$ is the spot size diameter (typically, $1/e^2$ of intensity), R is the repetition rate of the laser, and v is the scan speed of the translation stage [5, 6, 18]. Therefore, the morphology of the structural change is dominated by the heating, melting, and cooling dynamics of the material in and around the focal volume [5, 6, 18].

2.2 Propagation Conditions and Considerations

The linear optical effects (i.e., dispersion, diffraction, and aberration) and nonlinear (i.e., self-focusing, plasma defocusing, and energy depletion) influence the propagation behavior of a focused fs-laser beam in dielectrics materials. For a collimated Gaussian beam focused in a dielectric material by a lens, its diffraction-limited minimum waist radius w_0 is given by:

$$w_0 = \frac{M^2\lambda}{\pi \mathrm{NA}}, \tag{2.3}$$

where M^2 is the Gaussian beam propagation factor (beam quality), NA is the numerical aperture of the focusing objective lens, and λ is the free space wavelength [5−7]. The Rayleigh range z_0 (1/2 the depth of focus) inside a transparent dielectric material of refractive index n is given by:

$$z_0 = \frac{M^2\lambda n}{\pi \mathrm{NA}^2}. \tag{2.4}$$

Chromatic and spherical aberrations cause a deviation in the intensity distribution near the focus, making equations 2.3 and 2.4 no longer valid [5−7]. The effect of chromatic aberration is caused by the dispersion characteristics of the objective lens, whereby the lens fails to focus all the wavelengths to the same convergence point. As the name suggests, the spherical aberration comes from the spherical lenses where the light rays parallel to the optic axis but at different distances from the optic axis fail to converge to the same point. These issues can be addressed, employing multiple lenses (i.e., microscope objectives) or an aspheric focusing lens [5−7]. However, additional spherical and astigmatic optical aberrations are also introduced by the index mismatch at the air-glass interface (cylindrical) in the interaction between a focused fs-laser beam and an optical fiber (as depicted in left side of Figure 2.4 (a)). Therefore, oil-immersion objective lenses (where the refractive index of matching oil equals that of the transparent material), or adaptive optics with air objective lenses [19] are imposed to circumvent the beam distortion caused by the spherical and astigmatic optical aberration at the fiber volume [5−7].

In addition to the linear propagation, nonlinear effects can also occur when the laser intensity within the focal point inside the transparent material is extremely high [6]. The main nonlinear effect associated with the focusing of an fs-laser beam inside a transparent dielectric material is the optical Kerr effect. This effect stems from the contribution of the third nonlinear susceptibility

$\chi^{(3)}$ in polarization. The resulting refractive index is defined as:

$$n = \sqrt{1 + \chi^{(1)} + \frac{3}{4}\chi^{(3)}|\mathrm{E}|^2} = n_0 + n_2 I, \tag{2.5}$$

where $\chi^{(1)}$ is the first order susceptibility, E is the electric field vector, $n_0 = \sqrt{1+\chi^{(1)}}$ is the linear refractive index, $n_2 = 3\chi^{(3)}/4\epsilon_0 c n_0^2$ is the nonlinear refractive index, and $I = \frac{1}{2}\epsilon_0 n_0 c|\mathrm{E}|^2$ is the laser intensity [5−7]. Therefore, the Kerr nonlinearity results in an intensity-dependent refractive index change that follows the spatial intensity profile of a Gaussian laser beam, as shown in right side of Figure 2.4 (a). The center of the fs-laser beam induces the highest refractive index modification and its wings the lowest. As a result, the refractive index exhibit a graded profile affecting the beam, such as a positive lens. Thus, self-focusing is a direct cause of the optical Kerr effect. The strength of self-focusing relies on the peak power of the laser, and the critical power for self-focusing is given by:

$$P_{cr} = \frac{3.77\lambda^2}{8\pi n_0 n_2}. \tag{2.6}$$

The factor 3.77 is valid for beams with a Gaussian spatial distribution [5−7]. Therefore, if the peak power (P_p) of the fs-laser pulse exceeds the critical power (P_{cr}) threshold for the medium, the collapse of the pulse to a focal point is predicted and the beam divergence from diffraction is overcome. In addiction, the initial point of self-focusing is determined by:

$$Z_f = \frac{2n_0}{0.61}\frac{w_0}{\lambda}\frac{1}{(P_p/P_{cr})^{1/2}}. \tag{2.7}$$

However, as the beam self-focuses, the intensity at the focal point is high enough to nonlinearly ionize the medium and form a free-electron plasma [5−7]. The resulting refractive index of the plasma is expressed as:

$$n = n_0 - \frac{n(t)}{n_0 n_c(t)}, \tag{2.8}$$

where $n_c(t)$ is the characteristic plasma density for which the plasma frequency equals to the laser frequency [5−7]. The plasma-modified refractive index acts as a diverging lens to the fs-laser beam that counters the Kerr lens self-focusing and leads to a filament formation. The pulse filamentation is essentially a chain of hot plasma spots along the propagation axis that results from a dynamic balance between self-focusing and defocusing mechanisms such as diffraction and plasma defocusing (as depicted by the schematic of Figure 2.4 (b)). For peak powers sufficiently higher than the critical power, the beam cross-section appears as a collection of randomly distributed spots resulting from small-scale multiple self-focusing of the pulse [20]. These spots are identified as small-scale filaments acting as sources of white light. Thus, the white light essentially results from the spatial and spectral transformation of the initial pulse during nonlinear propagation inside the medium [20]. The filamentation process is complete when the energy spent ionizing the medium weakens the pulse, and the self-focusing gradually declines and finishes [5, 6, 20, 21].

Figure 2.4 (c) shows an optical microscope view of the cross-sections of waveguides (dark and

bright regions correspond to index decreases and increases, respectively) fabricated in a single-mode fiber by fs-laser exposure. In this microscope view, it is possible to observe the effect of the astigmatic optical aberrations induced by the index mismatch at the air-glass interface, where the alignment of the waveguides is hampered principally by the optical fiber curvature [5, 6, 21]. These axially elongated refractive index structures are undesirable for waveguide (WG) fabrication. Conversely, with the proper fs-laser writing technique and the spatial and temporal dynamics of such laser filament interaction and material response controlled, the filamentary propagation can be employed to inscribe fiber Bragg gratings as addressed in Section 2.4 [21]. The Kerr self-focusing effect is typically avoided by balancing the laser pulse energy and focusing conditions (i.e., achieving the optical breakdown intensity without exceeding the critical power for self-focusing). This is attained by tightly focusing the fs-laser beam with a low laser pulse energy and employing a high NA objective lens [5, 6, 21].

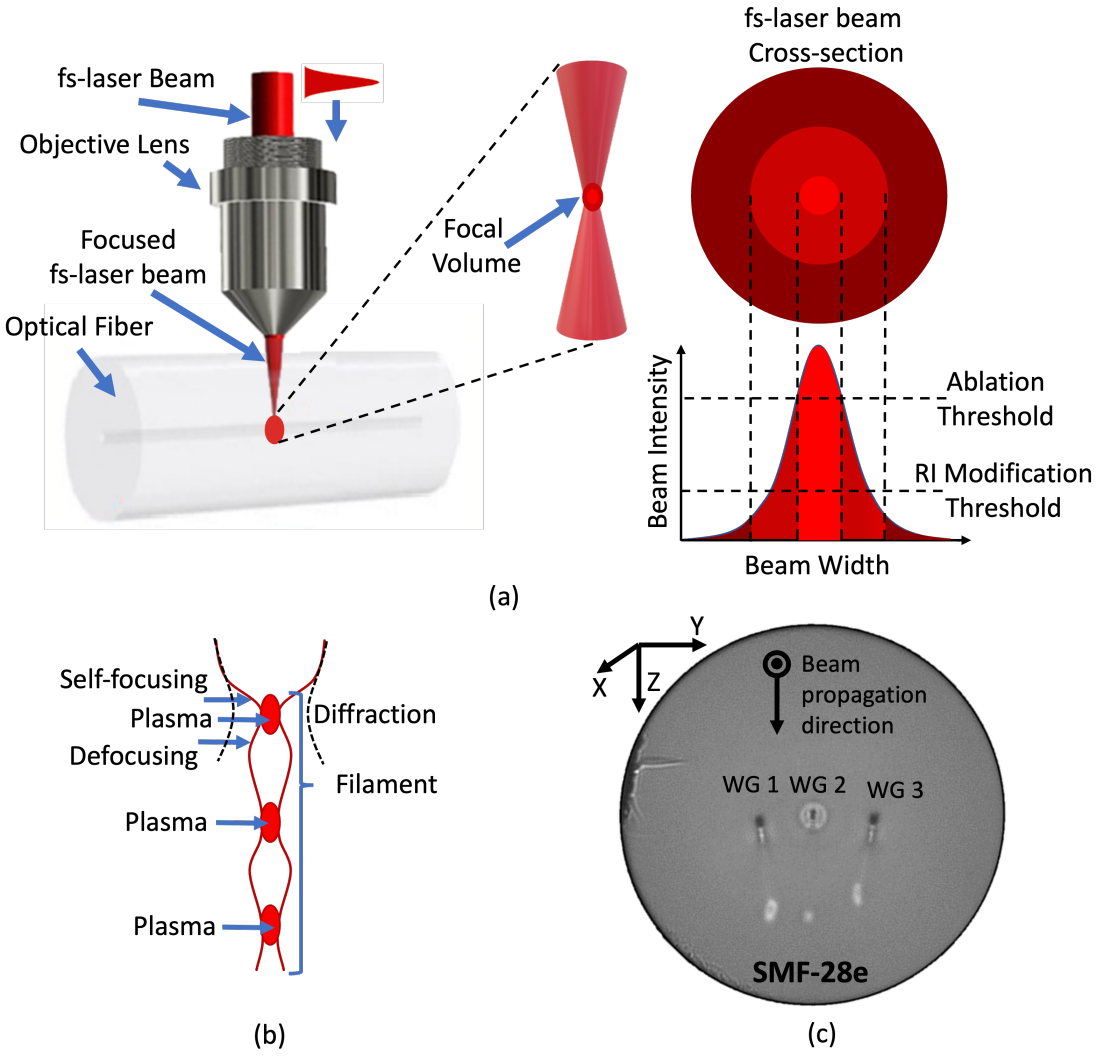


Figure 2.4. *Schematics of (a) the interaction between a focused fs-laser beam and an optical fiber, along with a sketch of its Gaussian intensity beam profile, and (b) self-focusing and filamentation of an fs-laser pulse. Optical microscope view (c) of the cross-sections of the fs-laser written waveguides.*

2.2.1 Writing Geometry

The proper control of the refractive index profile, or cross-section of the fs-laser induced modifications, is important to optimize the optical waveguides performance and the design of grating structures [5]. Indeed, the cross-section directly determines the number of transverse modes supported by the waveguide and the properties of these modes. In addition, the adjustment of the cross-section dimensions allows the inscription of gratings that partially cover the cross-section of the core and gratings with a large cross-section that extends far into the cladding [5, 10, 22]. The dimensions of the gratings' cross-section, underlying the overlap between the grating and the mode, are an important factor governing the efficiency, insertion losses, and radiation mode of the gratings. Thus, the process parameters, namely focusing optics, translation direction, and pulse repetition rate, play the most important role in the inscription process, defining the cross-sections of the structures.

Two standard configurations for the fs-laser direct writing of optical waveguides are possible, including longitudinal mode and transverse mode, as shown in Figure 2.5. Typically, the fs-laser beam stays stationary, and a translation stage is used to displace the optical fiber in three dimensions relative to the focal spot of the beam [5, 10, 22].

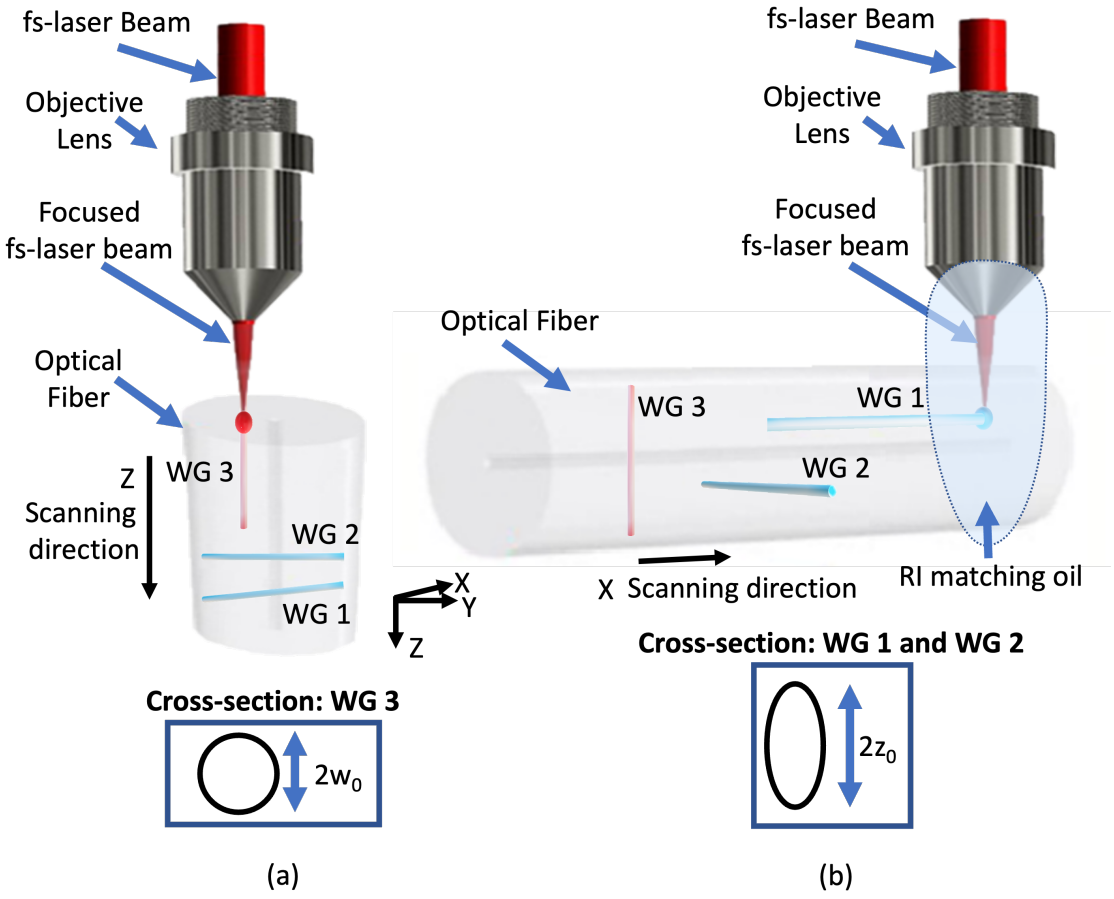


Figure 2.5. *Schematic diagrams of the fs-laser direct writing geometries in optical fibers: (a) longitudinal mode and (b) transversal mode.*

In the longitudinal writing geometry, the optical fiber is translated longitudinally along the direction of propagation of the inscription laser beam. Here, the writing depth is limited by the working distance of the focusing lens and spherical aberrations, which distort the focus. Thus, the resulting waveguide structures have symmetric cylindrical cross-sections and are only a few millimeters long. In addition, the cross-sectional size of the modified region (the waveguide core) is directly related to the beam waist diameter [5, 10, 22].

In the transverse writing geometry, the optical fiber is translated transversely to the direction of propagation of the inscription laser beam. Hence, the working distance (WD) of the lens no longer restricts the waveguide length, although the fiber curvature interface cause beam distortion [5, 10, 22]. In addition, this writing mode allows the implementation of more complex structures over the entire fiber volume, such as bent waveguides and Y splitters [10, 22]. However, the resulting cross-section is asymmetric, presenting an elliptical shape with poor confinement of the guided modes [5, 10, 22]. The size of the WG core in either the x- or y-axis is again directly related to the fs-laser beam waist diameter, but now the size of the WG core along the z-axis is directly related to the confocal parameter (or depth of focus) [5]. The functions defining the beam waist diameter and the confocal parameter are:

$$2w_0 = \frac{2f\lambda}{\pi w(f)} \approx \frac{2\lambda}{\mathrm{NA}\pi}, \qquad (2.9)$$

$$b = 2z_0 = \frac{2\pi n w_0^2}{\lambda}, \qquad (2.10)$$

where w_0 is the beam waist radius, $w(f)$ is the beam radius at the lens, f is the focal length of the lens used to focus the beam, λ is the free space wavelength of the light, n is the refractive index of the medium, NA is the numerical aperture of the lens, b is the confocal parameter and z_0 is the Rayleigh range of the focus [5].

Therefore, for a Gaussian beam, the high degree of asymmetry imposed by the transverse writing geometry is due to the fact that the depth of focus is larger than the spot size by a factor n/NA. This asymmetry vanishes for a beam waist radius close to $\lambda/n\pi$, which can be achieved using a focussing NA close to n. To overcome this focal volume asymmetry, high NA oil-immersion lenses, dry objectives with collars, and special beam shaping methods such as those involving the use of a spatial light modulator (SLM) or slit are required as suggested by several groups [5, 10, 22].

Typically, in optical fibers, the fs-laser transversal writing is the most employed method. Conversely, the fs-laser longitudinal writing is mainly used to inscribe structures at the fiber end-face. However, these writing geometries can be used jointly to inscribe more complex 3D structures [5, 10, 22].

2.3 Femtosecond Laser Irradiation Followed by Chemical Etching

Femtosecond laser irradiation followed by chemical etching (FLICE) has shown to be a promising technique for 3D writing of optical and fluidic devices in bulk fused silica glass and optical fibers. This technique uses the fs-laser direct writing method to engineer 3D structures in the glass (i.e., optical fiber) with great spatial precision. Therefore, a single system based on fs-laser microfabrication can be used to fabricate both optical waveguides and microchannels, integrated with unique 3D arrangements. The 3D integration of these devices, allowing compact geometries, paves the way for the development of new optofluidic microsystems (exploits the synergy of optics and fluidics) [5, 14−16].

The FLICE technique, although it produces channels that are presently limited in length to a few millimeters, has some advantages over the conventional approaches (e.g., photolithography and wet/dry chemical etching), as reported by Osellame et al. [5]:

- it avoids photolithography and clean rooms;
- it creates directly buried channels that do not require sealing with a cover glass;
- it naturally produces channels with a circular cross section, which are not easily obtained by other techniques;
- it allows straightforward fabrication of channels with 3D geometries.

Regarding the fs-laser direct writing, it can be used as a post-processing tool, giving the possibility to add optical and fluidic functionalities to a microfluidic device manufactured by conventional methods.

The fabrication process of optic and fluidic structures employing the FLICE technique consists mainly of two steps:

1. inscription of RI modified regions through fs-laser direct writing method to construct the structure with a tightly focused fs-laser beam;
2. etching the material (e.g., fused silica glass and optical fibers) in a solution (e.g., hydrofluoric acid (HF)) to remove the fs-laser modified regions and form the final structure.

In addition, before the etching process, the thermal annealing of the structures (optional step) is done to smooth the fs-laser induced modifications (less roughness) and improve the acid diffusion throughout the processed region [5, 14, 16].

Without entering into details that can be found in textbooks such as [5] in particular, the FLICE relies on the formation of self-ordered nanograting structures (with a $\sim \lambda/2n$ period, where λ is the fs-laser wavelength and n is the refractive index of the medium), that are perpendicular to the laser polarization direction and highly susceptible to HF or potassium hydroxide (KOH) etching.

The fs-laser modification of Regime 1 (Figure 2.3) can also be used in the first step of the FLICE technique. However, in this regime, a very weak selectivity to etching is achieved. Therefore, the formation of the self-ordered nanograting structures (Regime 2) is most suitable because it enhances the etching rate by up to two orders of magnitude (compared to pristine fused silica), enabling the manufacturing of channels with a high aspect ratio (length-to-diameter ratio) [5, 14, 16].

The FLICE process mainly relies on the cumulative action of multiple fs-laser pulses impinging on the same spot. Consequently, the writing parameters, such as intensity and translation speed, have to be chosen appropriately. Nevertheless, this process also depends on the relationship between the laser inscription and polarization direction. When the polarization and inscription directions are perpendicular, the nanogratings are aligned perpendicular to the laser polarization direction and directed along the channel axis, favoring the diffusion of the etchant. Otherwise, if polarization and inscription directions are parallel, the nanogratings are perpendicular to the channel axis, and the etchant diffusion is blocked [5, 14, 16, 23].

Thus, the FLICE process can be understood as a laser induced etching anisotrophy. Using HF solution, etching of fused silica occurs through the reaction: $SiO_2 + 4HF \rightarrow SiF_4 + 2H_2O$, in which the etching rate is temperature-dependent. However, the etching process is self-terminating, due to the exhaustion of the HF acid in the depth of the etched microchannel and to the difficulty in refreshing it [5, 14, 16, 23]. Therefore, the etch rate gradually decreases, limiting the maximum achievable channel length and leading to the formation of microchannels with conical shapes and a larger radius at the channel entrance than the buried end. One possible solution is using the chemical etching in an ultrasonic bath to promotes acid diffusion and achieves microchannels of greater length and aspect ratio [5, 14, 16]. There is usually a trade-off between the quality of the microchannel and the consumption of time. Indeed, a lower concentration of HF solution results in the formation of microchannels with better quality (higher aspect ratio and less roughness) at the cost of a long etching time (i.e., a decrease of the etch rate) and conversely [5, 14, 16, 23]. In addition, KOH can also be used as an alternative to HF for highly selective etching and avoid the typical saturation behavior observed for the etching of fused silica in HF. However, the chemical etching with KOH implies a rather long etching time [5, 14, 16, 23].

Indeed, in optical fibers, the prevalent etchant used in step 2 of the FLICE technique is HF. As an example, the whole fabrication process of the FLICE technique to produce an open channel through an optical fiber is shown in Figure 2.6.

The oil-immersion objective lenses (as depicted in Figure 2.6), or adaptive optics with air objective lenses [19] are used to circumvent the spherical aberration and beam-focusing distortion in the fiber, as addressed in Section 2.2. Hence, the fs-laser beam focusing spot is freely moved within the fiber without being distorted. In addition, the longitudinal inscription geometry is preferable used to achieve channels with circular cross-sections, although with the writing length being limited by the working distance of the focusing objective [5, 14, 16, 23]. This inscription geometry allows the fabrication of microchannels with a maximum length equal to the diameter of the fiber. However, it is important to remark that the chemical etching also causes a reduction in the fiber cladding diameter. Typically, microchannels with diameters of less than 6 µm and aspect ratios of the order of $20 - 25$ are achieved for etching times of less than one hour with low HF concentrations ($4 -$ 15%) [5, 14, 16, 23].

Regarding microchannels fabricated in standard SMF fibers, the etch rate changes for the different materials, and etching due to faster etching rate in the germanium-doped core than that in the pure fused silica cladding leads to the formation of concave surfaces in the core [5, 14−16,

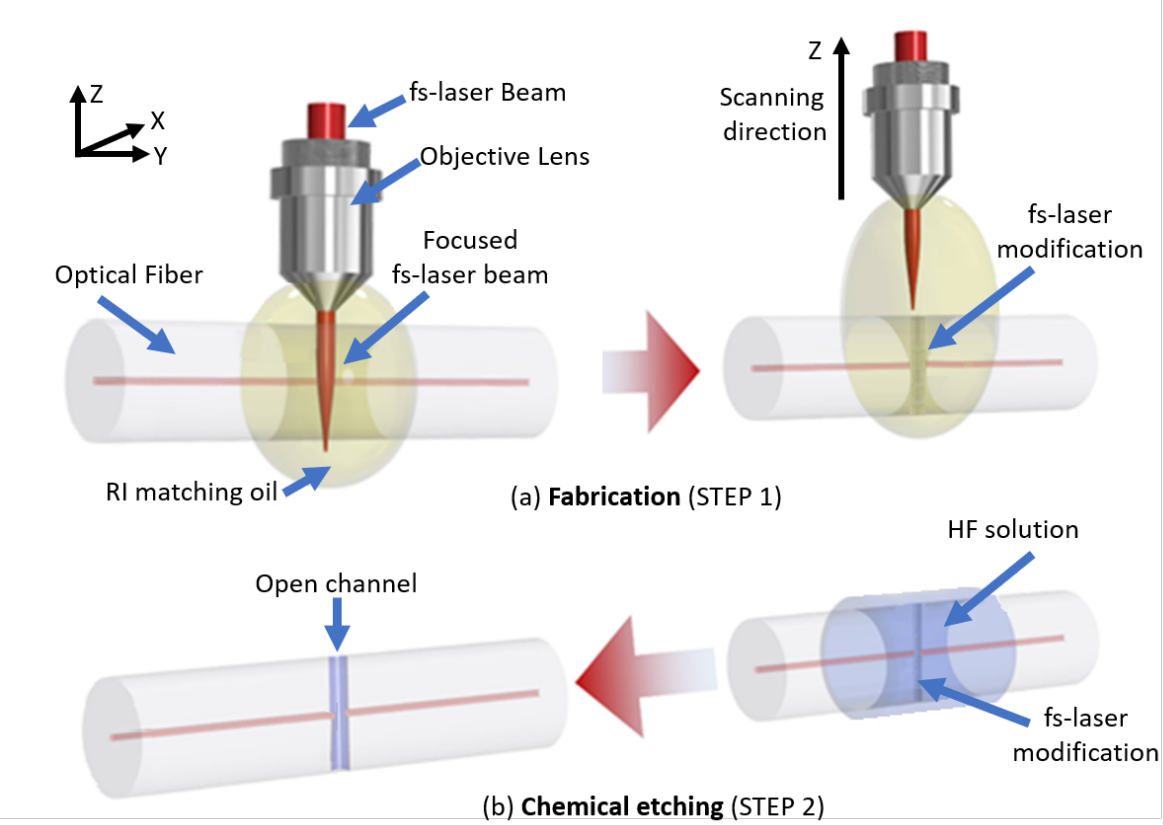


Figure 2.6. *Schematic diagram of the FLICE technique divided into two steps: (a) inscription of permanent RI modified regions by focused fs-laser pulses, and (b) etching of the fs-laser modified regions in a HF solution.*

23, 24]. The concave surface induces a negative lensing effect leading to higher insertion losses. Typically, these issues are circumvented by avoiding the positioning of the structures directly into the germanium-doped SMF core waveguide or fabricating the microchannels on coreless fibers and interrogating the microfluidic channel with fs-laser inscribed waveguides [5, 14–16, 23, 24].

2.4 Optical Fiber Devices Fabricated by Femtosecond Laser Micromachining

Femtosecond laser micromachining has been used to fabricate photonic devices in different kinds of opaque and transparent materials, such as metals, ceramics, soft materials (e.g., polymers and bio-tissues), and even brittle materials (e.g., glasses). Furthermore, this fabrication technique is used for applications such as scribing/ cutting, drilling, surface patterning and texturing, nano-ablation, and micro/nanostructuring that demand high-quality, high-precision surface micro-and nano-machining [25]. Glasses and crystals are commonly used as base materials due to their high purity and large transparency window [8].

The fs-laser technology exhibits excellent capability in performing 3D processing in transparent materials, especially glass, which makes them a powerful tool for micromachining optical fibers [17]. Optical fiber is typically made of silica glass and functions as a waveguide, which is small in

dimension. Hence, the micromachining of optical fibers is difficult to achieve via conventional manufacturing methods. Thus, the fs-laser technology offers high spatial resolution and micro-scale control, essential features to overcome the difficulty mentioned above [17, 26, 27].

In recent years, fs-laser micromachining techniques have been used in a broad range of optical fiber applications, from gratings inscription and waveguides [5, 28] to interferometers fabrication [29], weak reflectors (i.e., scattering dots) [14], and for the creation of microcavities and microchannels inside the optical fiber [14, 30].

Gratings are small perturbations induced in the fiber with a given period that decouples or reflects the light of fundamental mode with a spectral dependence on the inscription period. For periods much higher than the wavelength (i.e., periods of hundreds of microns to a few millimetres), the grating is known as LPFG and couples the light of the fundamental mode to forward propagation cladding modes following the coupled-mode condition; otherwise, when the grating exhibits small periods (i.e., periods of a few hundred nanometres to a few microns) it reflects light at Bragg resonance and is known as Fiber Bragg Gratings (FBG) [7]; in addition, the contrast of the RI modulation is typically around $\sim 10^{-4}$ [22].

Nowadays, conventional FBGs fabricated involving UV lasers are a mature technology relatively simple to produce and replicated. However, the FBGs can only be inscribed in the core of photosensitive fibers. Furthermore, these fabrication methods are not suitable to write in the optical fiber cladding [14, 22, 31]. Indeed, FBG is one of the most widely used OFS due to its compact size, high sensitivity, easiness for multiplexing, and mass production, and is capable of working as filter and mirror [14, 22, 31]. In 2001, Oi et al. reported a novel approach to the inscription of FBGs by fs-laser holographic interferometry based on these well-developed conventional methods [32]. Following, in 2003, research efforts made by Dragomir et al. [33] and Mihailov et al. [34] resulted in the fabrication of FBGs by using UV and near infrared (NIR) fs-laser phase mask methods, respectively. However, it is complex to use one phase mask to fabricate long and complex grating structures with different Bragg resonant wavelengths. Therefore, Becker et al. (in 2008) [35] at Leibniz Institute of Photonic Technology (IPHT) demonstrated the fabrication of FBGs by using an fs-laser source and a Talbot interferometer. Thus it is possible to have high flexibility with an interferometric setup in choosing the Bragg grating wavelength [22, 35]. Nevertheless, the phase masks and other interference-based exposure methods are inflexible in offering only limited wavelength tuning and spectral shaping of the FBG [36]. Studies into FBG fabrication using direct-write methods, namely point-by-point (PbP) inscription were reported in 2004 by Martinez et al. [37], and Wikszak et al. [38]. The direct writing of gratings by fs-laser enables the use of different inscription methods such as point-by-point [14, 37, 39], line-by-line (LbL) [40, 41], and plane-by-plane (Pl-b-Pl) [42, 43]. Following are a description of each inscription method:

- **Point-by-point:** The modification in each period is inscribed by fs-laser pulse or pulses along the optical fiber axis. This is achieved by a stage platform that displaces along the fiber axis with a certain velocity. The period is defined by the ratio of the translation speed of the fiber to the pulse repetition rate of the laser. However, the RI modification cross-section is not uniform and is usually much smaller than the fiber core diameter. As a result, the PBP

inscribed FBGs show relatively high insertion loss, increased coupling to cladding modes, raised grating birefringence and polarization dependent losses [14, 37, 39]. The use of specific adaptive optics arrangements overcome these issues [44]. Furthermore, alternative approaches based on the PbP setup have emerged, such as the fs-laser pulse filamentation, continuous core-scanning and burst writing methods reported by Ahmed et al. [45], Williams et al. [46] and Peter Herman et al. [47], respectively.

The fs-laser pulse filamentation method relies on focusing fs-laser pulses in a very tiny spot to achieve high power density at the focal point and initiate pulse filamentation. Thus, employing a high NA objective lens or a glass medium placed after the objective lens, tight focusing can be achieved to generate submicron width filaments and uniform filament tracks with a high aspect ratio. In addition, the scanning period and speed should be chosen so that the filamentary structures are partially overlapped to form desired RI modulation in the fiber core [31, 36, 45].

The continuous core-scanning method employs a piezo-controlled translation stage to move the optical fiber. The piezo stage was driven by a sine wave, resulting in a sinusoidal inscription across the core. Furthermore, the amplitude of the sine wave is significantly greater than the core diameter, such that the inscribed lines across the core are approximately parallel. The grating period is given by the half-period of the sine-wave track in the fiber [46, 48]. Alternatively, the scanning piezoelectric transducer can also be employed to moves the lens and hence the beam across the core of the fiber to induce a uniform RI change [7].

The burst writing method modulates the fs-laser pulses with an external acousto-optic modulator to produce periodic burst-trains of fs-laser pulses. Here, the acousto-optic modulator (AOM) acts as an accurate on/off beam deflector to prevent overexposure, unwanted exposure, or optical damage during the fs-laser direct writing process. Thus, this method is suitable for inscribing gratings (FBGs and/or LPFGs) during the inscription of a waveguide, as the burst-mode pulses may be synchronized with the translation of the fiber to inscribe a grating [7, 47, 49]. The burst writing method was employed and explored in this PhD work.

- **Line-by-line:** In this method, instead of a single inscription, several lines are inscribed perpendicular to the longitudinal fiber axis, and the space between them determines the grating period. Thus, more core surface interacts with the grating, leading to a more homogeneous index modification that reduces the coupling to the cladding modes. In addition, it allows lower broadband losses, reduces the insertion and polarization-dependent losses. The fabrication of relatively complex structures can be achieved by changing the induced refractive index, length, and roughness of each inscribed lines. However, this inscription method requires a longer fabrication time, e.g., it needs some minutes to write a grating while the PbP method needs a few seconds for the same length [14, 40, 41].
- **Plane-by-plane:** This method consists of a fs-laser inscription of two-dimensional (2D) index planes across the fiber core, controlling both the width and depth of the modified region. This approach reduces the stringent requirements of aligning the fs-laser to the optical fiber's longitudinal axis as demanded by PbP and LbL methods. However, requires proper shaping of the fs-laser beam through a cylindrical lens that induces astigmatism in the focal volume or

by slit beam technique that increases the waist of the focal volume in the transverse direction of the fiber to be employed efficiently. This PI-b-PI method was proven to be an efficient technique for fabricating strong ($\sim$25 dB), low insertion loss ($<$0.02 dB), and complex grating structures in fiber [14, 42, 43].

These direct writing methods allow the fine control of the position, phase, and amplitude of grating's refractive index modulations, facilitating the formation of chirped [48], phase-shifted [41, 50], tilted [51], sampled [31, 52], and apodized [53] periodic structures. Therefore, the restrictions of the phase mask and interferometry methods can be overcome with direct writing methods. However, this flexibility comes at the expense of elaborate alignment procedures and setups. Regarding the stability of the grating period (important for shorter periods), it relies on the precision of the translation stage in terms of relative positioning and velocity stability [22].

The writing of gratings by fs-laser exposure methods has attracted considerable interest due to their high thermal stability withstanding temperatures in the range of 1000 °C [54, 55]. Fiber gratings can be classified by the underlying photosensitivity mechanism and the resulting thermal stability: Type I and Type II fs denotes modifications below and above the damage threshold of the fiber material, respectively. Therefore, the Type I femtosecond RI changes can be attributed to a combination of color centers, densification, and induced stress-fields mechanisms [14, 22, 55]. This type of gratings can resist up to 1000 °C with some erasure, while the UV-FBGs are erased at temperatures in the range of $600 - 800$ °C. The Type II femtosecond modification occurs for high-energy fs-laser pulses (regime 3) where a void is formed. In addiction, this type of FBGs have a local RI change range on the order of 10^{-2}. Thereby, Type II FBGs with enhanced thermal stability can operate up to close to the melting point of glass fiber and are suitable for high-temperature thermal monitoring applications in harsh environments (e.g., nuclear power plants, aerospace, steam turbines, etc.) [7, 14, 22, 56].

The residual stress that exist in the fiber has some negative effects on the fiber reliability and grating quality and, consequently, the thermal stability [54, 56]. Thus, pre-annealing of SMF-28e fibers at high temperatures relaxes residual stresses that result in higher temperature stability of the type II fs FBGs up to 1200 °C for time durations of 20 hours [54−56]. Fs-laser FBGs can also be manufactured in radiation hardened fibers suitable for applications in nuclear radiation environment [57]. Although high thermal stability and radiation resistance have been demonstrated in fs-laser FBGs, it is still necessary to improve their stability before they can be used for high temperature and stress sensing in high radiation environments [57].

Along the last years some works have reported a series of symmetric and asymmetric LPFGs inscribed in photonic crystal fiber (Endlessly Single-Mode fiber from NKT Photonics) [17, 27, 29]. Due to the fast growth of photonic crystal fiber and its special structure property, fs-laser writing of LPFGs is currently attracting much more attention. Fs-laser induced LPFGs are more thermally stable and reveal no degradation of grating performance from 20 to 500 °C [17, 55]. The temperature sensitivity of such LPFG within SMF is of 0.098 nm/°C. This sensitivity value is almost the same as the values of LPFGs fabricated by UV-light exposure in SMFs [17, 55].

The fs-laser writing methods offer flexibility in exploring the entire optical fiber volume and

fabricating FBGs of different periods in several fibers. These features can be highly advantageous from a device design point of view as, for example, it enables the writing of each grating into each core of a multi-core fiber that can be used as a directional bend sensor [58, 59].

The direct processing using fs-laser can be applied to drill the optical fiber (ablation modification), which results in holes. Thus, focusing the fs-laser beam at the optical fiber surface, a single micro-hole can be drilled without moving the laser focus point transversely. The dimensions of the fabricated micro-hole are determined through the single pulse energy and the fs-laser beam exposure time. Typically, larger pulse energy together with longer laser beam exposure time will result in a larger diameter and depth of the micro-hole. The numerical aperture value of the focusing objective will also affect the micro-hole morphology. In this method, micro-holes can be directly drilled in fibers without any chemical etching procedure. However, the holes present a marked conical morphology and a more irregular surface [17, 60]. This fs-laser manufacturing method can be applied to inscribe a strong structural modulated LPFG by periodically drilling multiple micro-holes along the fiber. The air hole structured LPFG introduces a strong and asymmetric structural modulation in the fiber core and cladding [17]. This periodic structure couples light from the fiber core mode to the cladding mode in a relatively efficient way by supporting a small grating dimension. The micro-hole structured LPFG can be formed in different types of optical fibers such as SMF and photonic crystal fibers [17, 29, 61]. Figure 2.7 shows the morphology and the transmission spectrum of the micro-hole structured LPFG in SMF [17]. The depth of the resonance peak at around 1517 nm becomes saturated when 15 grating periods are created, which is over 20 dB with an insertion loss of $\sim$15 dB. The depth would dramatically decay if the number of grating periods were further increased due to over coupling. The resonance peak near 1404 nm is created due to the coupling of the fundamental core mode to another lower order cladding mode [17].

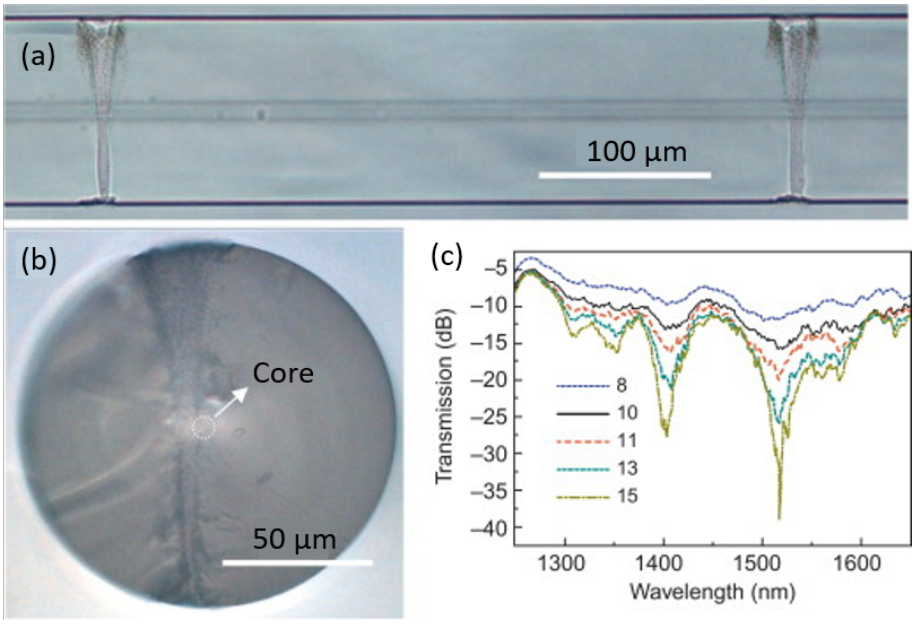


Figure 2.7. *Micro-hole structured LPFG: (a) Morphology with the grating period of 450 µm, (b) Cross-section view of the grating pitch (i.e. micro-holes), and (c) Evolution of the transmission spectrum for several grating periods (Reprinted from [17], © 2015, with permission from Elsevier).*

Fiber in-line interferometers fabricated by fs-laser direct processing have attracted considerable research interest in recent years because of their compactness, ease of construction, and convenient operation in many sensing applications. As a result, typical interferometric sensors using in-fiber microcavities have been demonstrated based on the open air-cavity fabricated by fs-laser drilling in the fiber [17, 25, 27−29, 62]. The interferometer configurations reported are mainly Fabry-Perot interferometer (FPI) [63], Mach-Zehnder interferometer (MZI) [64], and Michelson interferometer (MI) [65]. The open micro-cavity based interferometers are especially attractive for refractive index sensing owing to their high sensitivity, ultra-compact sensing region, small temperature cross-sensitivity and flexible tuning of sensitivity and operating range [65]. Thus, a compact fiber in-line MI tip sensor based on open micro-cavity, fabricated by fs-laser micromachining and thin film coating was reported by Liao et al. in 2012 [65]. The MI consists of a section of SMF, with partially removed fiber core near the fiber end. The light propagates in the fiber core along two paths: one is reflected by the cut end of the removed core and the other traveling along the remaining core is reflected back by the fiber end, thus forming two arms of an MI. A silver (Ag) thin film is deposited on both the cut end of the core and the fiber end to enhance the reflectivity. The optical microscope image of the fiber interferometer and the output spectrum of the fiber in-line MI with a cavity length of $\sim$38 µm in air are shown in Figure 2.8 (the red dotted line represents the calculated spectrum based on two beam interferometry). This MI presented a wavelength sensitivity of $\sim$975 nm/RIU (refractive index unit) at a RI of 1.484. Besides that, it can be operated in the reflection mode, which is attractive in many sensing applications [17]. However, the micro open cavity interferometer is easily cracked due to the laser-induced damage within the fiber.

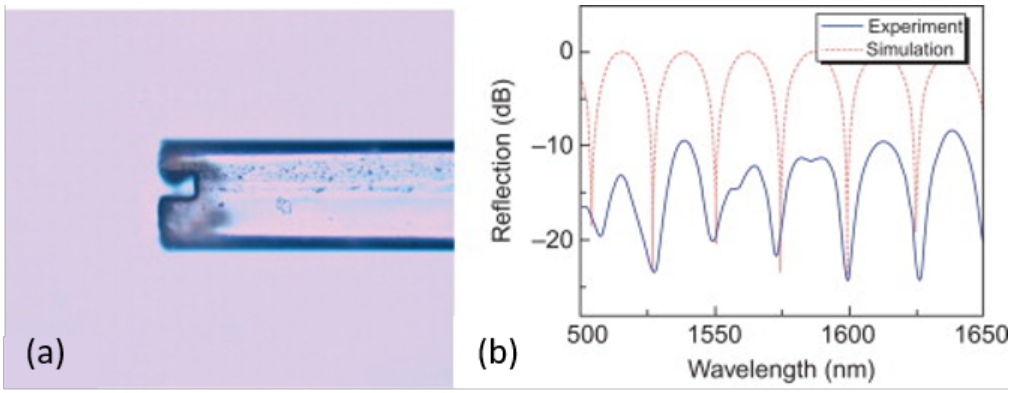


Figure 2.8. *Fiber in-line Michelson interferometer: (a) Optical microscope image, and (b) output spectrum with a cavity length of 38 µm (the red dotted line represents the calculated spectrum based on two-beam interferometry) (Reprinted from [17], © 2015, with permission from Elsevier).*

A wide variety of manufacturing methods, such as chemical etching, special fusion splicers, and fs-laser direct processing, could be used jointly. This approach is useful to overcome the limitations of each method when employed separately in the fabrication of complex OFS. Figure 2.9 (a) − (c) shows a fiber in-line FPI fabricated by fs-laser micromachining and fusion splicing [17]. A hollow-sphere cavity is formed by drilling a micro-hole at the end facet of SMF, followed by fusion splicing. The incident light beam along the SMF is reflected by the two surfaces of the sphere, respectively, and recombined in the fiber core, resulting in an interference spectrum at the output. By using

different initial micro-hole sizes, fusion splicing parameters and flame brushing technique, different sizes of hollow sphere and hence different cavity lengths could be created [17, 27].

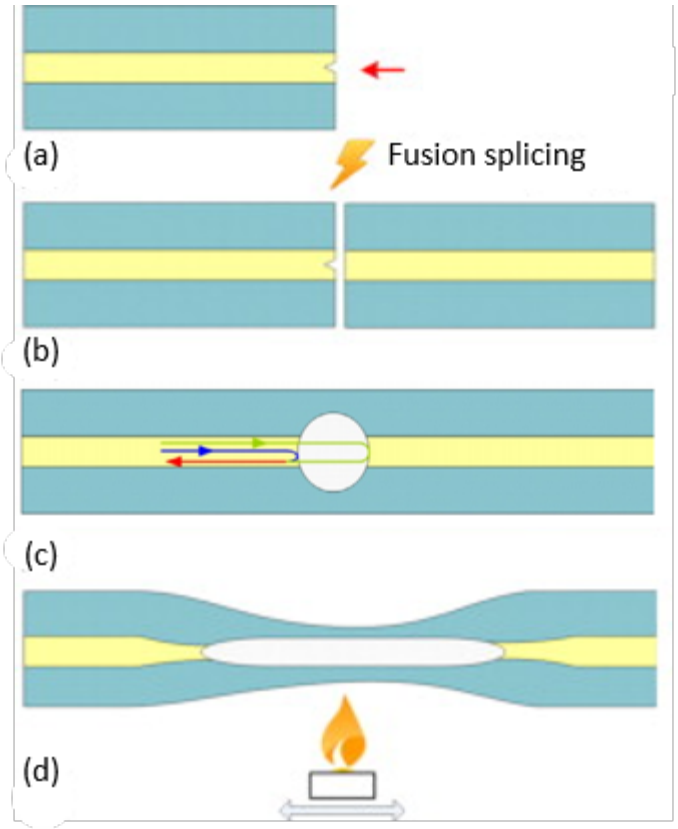


Figure 2.9. *Schematic diagram of the fabrication process of the microfiber with inner air cavity: (a) Micro-hole produced by fs laser, (b) fiber tip with micro-hole spliced together with another cleaved SMF, (c) hollow sphere formed in SMF, and (d) microfiber with inner air cavity produced by flame brushing technique (Reprinted from [17], © 2015, with permission from Elsevier).*

A long-standing goal of optical fiber devices is the development of a miniature and versatile optical fiber component capable of performing multiple functions and allowing a simple integration and efficiency in a system [17, 24, 25, 30]. A promising candidate to achieve miniaturization is to use microfiber. Microfiber has a small size but a large evanescent field for the guiding light, making it easy to manipulate and highly sensitive to the surrounding medium. Such unique and interesting properties help to create novel optical fiber devices. An ultra-compact optical fiber device would be realized if microstructures could be created within microfibers [17, 66]. Indeed, a way of achieving an ultracompact optical fiber in-line Mach−Zehnder interferometer is to create an inner air cavity in a section of a microfiber, as shown in Figure 2.9 (d) [67]. Figure 2.10 shows an ultracompact microfiber in-line MZI based on an inner air cavity, which was fabricated by combining fs-laser micromachining, fusion splicing and flame brushing techniques.

A micro-hole of a few micrometers in diameter at the center of the cleaved fiber end facet was ablated by an fs-laser beam with on-target power of $\sim$5 mW, as shown in Figure 2.10 (a) [67]. Figure 2.10 (b) shown a hollow sphere formed in the SMF, achieved after the fusion splicing with another section of SMF. The inner wall of the air cavity is rather smooth, due to the high

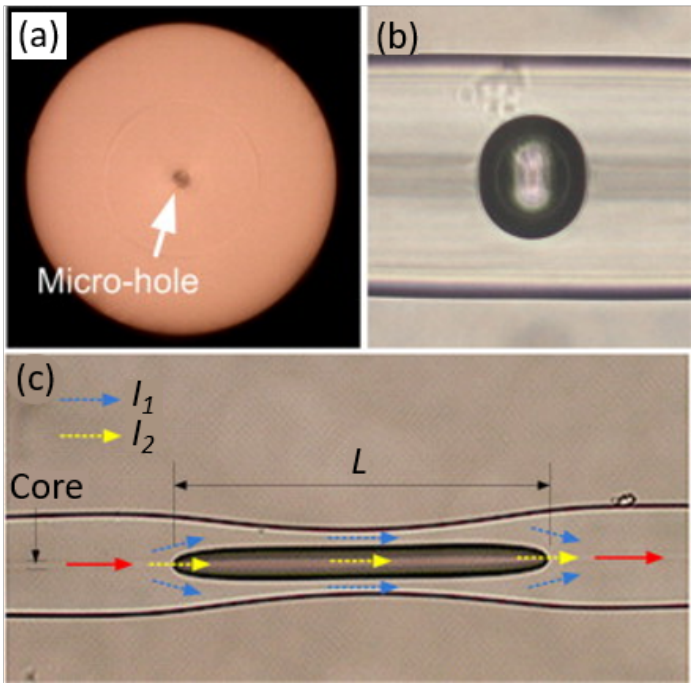


Figure 2.10. *Fs-laser micromachining of a microfiber in-line Mach-Zehnder interferometer: (a) The micro-hole fabricated by femtosecond laser ablation at the center of cleaved SMF end facet, (b) the hollow sphere formed after fusion splicing, and (c) microfiber Mach-Zehnder interferometer with an inner air cavity (Reprinted from [17], © 2015, with permission from Elsevier).*

temperature experienced in the hollow sphere formation. Figure 2.10 (c) presents the microscope image of the tapered microfiber with an inner air cavity which essentially forms a microfiber in-line MZI. In the tapered section, the input light beam is split into two portions denoted by I_1 and I_2, respectively. While I_1 travels along the silica cavity wall, I_2 propagates through the inner air cavity, and the interference takes place when the two output beams recombine at the cavity end [17, 66]. Compared with the conventional microfiber of similar size, the thinner cavity wall supports a larger evanescent field and hence an enhanced light interaction with the surrounding medium. Thus, the microfiber in-line MZI opens a promising way to achieve a miniature, versatile, and highly sensitive optical fiber sensing devices [17].

However, these and other related methods are directed mainly at the core waveguide at the center of the fiber, where light guiding is typically confined to less than 1% of the total cross-sectional fiber area for the case of SMF [15]. There exists a large and relatively unexplored volume in which to consider cladding devices that promise to add significantly more functionality and improve the value of the optical fiber [26, 27, 62].

Several advances have emerged in the direction of fiber cladding devices, as demonstrated by Grenier in 2015 [15]. Therefore, it was demonstrated the surface functionalization of cladding surfaces for label-free chemical, biological, and acoustic sensing [68, 69], acid thinning of fibers for evanescent [70] and interferometric sensing [71, 72], laser writing of long period waveguide gratings to couple and sense from fiber cladding modes [73], and laser drilling of microholes to the core waveguide for sensing [14, 74]. The schematic diagram of a fiber in-line MZI based on

an inner air cavity adjacent to the fiber core is represented in Figure 2.11 as an example of laser drilling of microholes for sensing [17]. The air cavity is fabricated through fs-laser micromachining together with the fusion splicing technique. Light propagating in the fiber core is divided into two portions: one passing through the air cavity and the other traveling along with the fiber core, before recombining at the air cavity end. Such an inner air cavity-based MZI is miniaturized and robust, responds linearly to temperature with high sensitivity ($\sim$43.2 pm/$^{\circ}$C up to 1000 $^{\circ}$C), while being insensitive to the surrounding refractive index variation [17]. Furthermore, employing the manufacturing method such as the FLICE technique, explained in Section 2.3, is possible to obtain holes with a higher aspect ratio and a surface with less roughness.

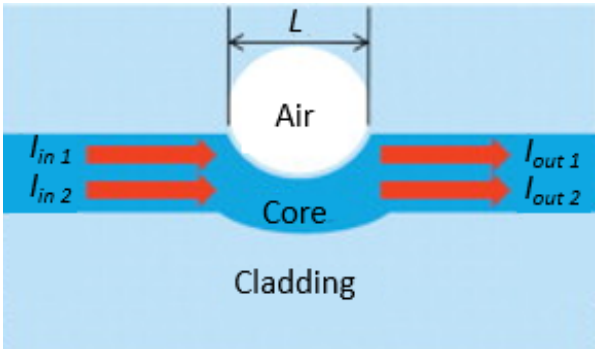


Figure 2.11. *Schematic diagram of the fiber in-line Mach-Zehnder interferometer (Reprinted from [17], © 2015, with permission from Elsevier).*

In recent times, there has been a notable increase in the development of Lab-In-Fiber (LIF) devices by wrapping microfluidic and optical components around the core of a fiber [14, 15, 24, 75]. The fused silica cladding found in most types of standard, multicore, and photonic crystal fiber is highly favorable for biocompatibility and resistance to chemical erosion [17]. Thus, it is a promising LIF platform to bring microfluidic and structural components into even more compact size scales [15, 24]. An ultrasensitive optofluidic detection method to discriminate edible oils from gutter oils (i.e., illegal cooking oils) was demonstrated in [76]. This device is based on a hybrid-waveguide coupler fabricated in an SMF-coreless-ST (pure silica tube)-SMF structure with an sensitivity of $\sim$112.743 nm/RIU [76].

It is noteworthy the contribution of FLICE to fabricate microchannels with different designs [77], LPFGs based on transverse microchannels [78], refractometers based on a micro-slot in a FBG [19], microfluidic reservoirs, optical resonators and other complex 3D structures [15, 23−25].

The fabrication of highly functional LIF components that offer rapid prototyping capabilities into fully integrable 3D optofluidic systems was demonstrated by Haque et al. (2014) [24] and Grenier et al. (2015) [15, 26]. The microfluidic reservoirs and optofluidic resonators are examples of integrated optofluidic structures presented in their works. Also, microfluidic reservoirs and optical resonators could be manufactured with arbitrary shapes and sizes, allowing great flexibility in the desired spectral response. Schematics of an optical resonator design formed by fs-laser writing inside SMF is shown in Figure 2.12 (a) and (b) [26, 27, 62].

Optical resonators may also be embedded within coreless fiber as shown in Figure 2.12 (c),

where probing waveguides were laser written in positions aligned with the cores of spliced fibers [26, 27, 62]. This approach offered facile integration of LIF coreless devices with light sources, spectral analyzers, and other optical devices. Hence, laser writing of both waveguides and resonators into coreless fiber was favored for generating optically smooth resonators without undesired waveguide etching.

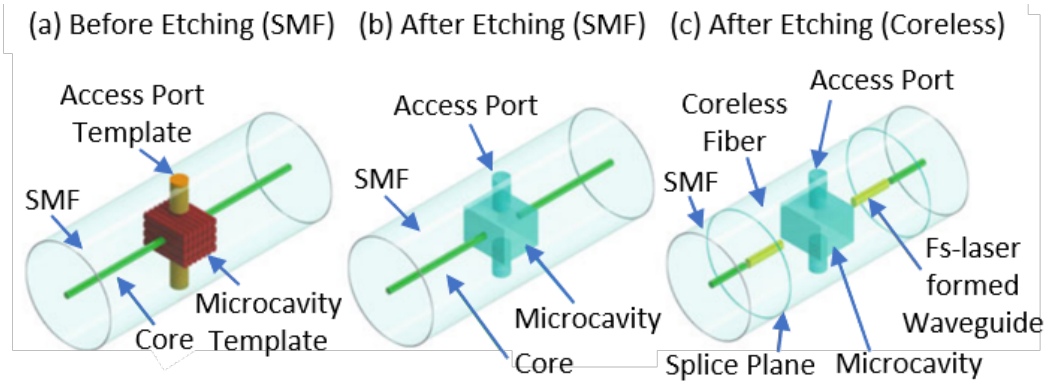


Figure 2.12. *Schematic of an optical resonator and access port template embedded within: (a) SMF fiber before HF etching using 2D arrays of overlapping fs-laser tracks, (b) SMF fiber after HF etching, and (c) coreless fiber and integrated with fs-laser formed waveguides aligned to the optical axes of spliced SMF core waveguides, (Reprinted from [15], © 2015, with permission from Springer Nature).*

The formation of multicore waveguides within a single fiber was also explored in order to increase the performance of optical fiber [15]. Such fibers recently enabled a record 1.05 Petabits/s communication rate while the writing of FBGs into the individual waveguide cores served to define a novel temperature-independent three-axis bend sensor [15]. Here, the core waveguides are independent and isolated from each other and pose significant packaging challenges for efficient light coupling at the fiber facets [15].

Nevertheless, when writing waveguides using an fs-laser in the cladding of a standard optical fiber, the resulting waveguide exhibits different mode fields and propagation constants compared to the core waveguide. Thus, as light tries to transfer between the core and a cladding waveguide, the difference in mode fields and propagation constants leads to a lower coupling efficiency (less than 100%). This represents one fundamental challenge with writing optical circuits in SMF. For this reason, coreless fiber is also introduced as a platform for fs-laser writing of photonic fiber systems [15, 26]. Thus, different approaches of coupling light from an SMF core waveguide into fs-laser-formed waveguides were investigated by using X-couplers (also known as cross couplers), S-bend couplers, and directional couplers as depicted in Figures 2.13 (a) – (c), respectively [15, 26].

X-couplers are formed by two waveguides that intersect at a given crossing angle (θ). Thereby, one of the significant challenges of writing X-couplers in SMF is the accurate alignment required to position the crossing waveguide to intercept the center of the core waveguide. Also, the S-bend coupler shown in Figure 2.13 (b) represents an alternative approach to couple light out of an SMF core waveguide. Therefore, the fs-laser-formed waveguide was inscribed by starting in the core and curving outwards to a distance of 45 µm into the cladding, following along two reversing

circular arcs that terminated into a straight 15 mm long Bragg grating waveguide segment [15, 26]. The 15 mm long Bragg grating waveguide was formed along the spur to create a back reflection for probing the coupler efficiency and determining the polarization axis and birefringence of the waveguide. In this way, polarization-selective taps in SMF and polarization beam splitters in coreless fiber were designed and fabricated [15, 26].

Figure 2.13 (c) shows an asymmetric directional coupler in SMF to guide the SMF core waveguide light into the isolated spur waveguide with strong polarization, and wavelength dependence [15, 26]. Directional couplers transfer optical power via evanescent fields between two or more waveguides positioned close to each other and are widely used in planar lightwave circuits. Thereby, have the advantage of complete energy transfer over coupler lengths predicted by coupled-mode theory; however, they are highly wavelength and polarization-dependent [15, 26].

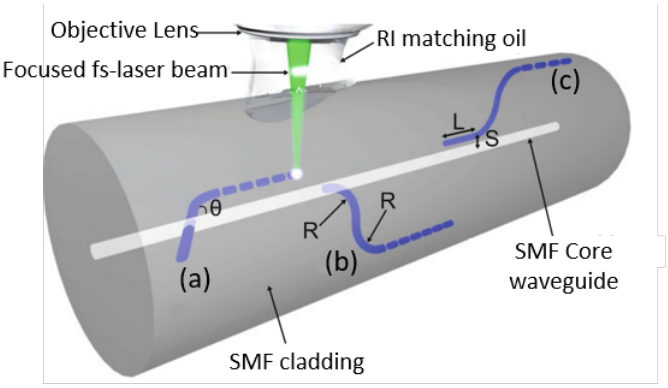


Figure 2.13. *Fs-laser writing of waveguides in an SMF with an oil-immersion lens to form an: (a) X-coupler, (b) S-bend coupler, and (c) directional coupler; Here, θ is the crossing angle, R is the turning radius, S is the separation distance, and L is the straight length of the laser-formed waveguide (Reprinted from [15], © 2015, with permission from Springer Nature).*

Table 2.1 summarizes the coupler losses (not include the propagation loss encountered in guiding the light in the fiber cladding) of the X-, S-bend, and directional couplers [15, 26].

Table 2.1. *Summary of coupling light from SMF core waveguides into fs-laser-formed waveguides (wavelength range from 1250 to 1650 nm), (Reproduced from [15], © 2015, with permission from Springer Nature).*

Coupler type	Coupling ratio	Device bandwidth	Polarization dependence	Coupler loss (dB)
X-coupler SMF	$0-0.76$	>350 nm	Negligible	1.2
S-bend coupler SMF	$0-0.33$	>350 nm	Negligible	$1-1.7$
Directional coupler SMF	$0-0.32$	<0.73 nm[1]	Strong	0.2
Directional coupler (coreless fiber)	$0-0.99$	<175 nm[2]	Strong	0.04

[1]Based on a coupling length of 0.099 mm;
[2]Based on a zero length coupler.

S-bend and X-couplers provided polarization independent coupling while the strong polarization dependent coupling offered by the directional couplers provided new directions for designing in fiber polarization selective taps and polarization beam splitters [15, 26].

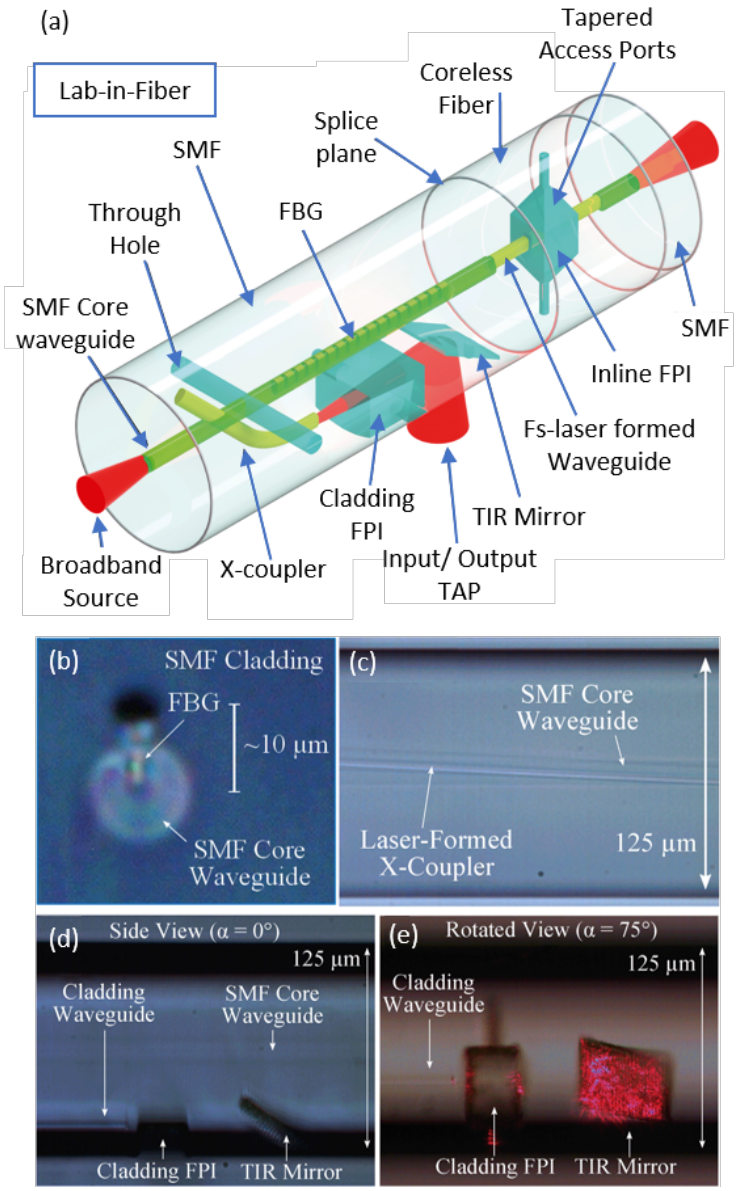


Figure 2.14. *LIF sensing platform: (a) Schematic, and Optical micrographs of the LIF sensing elements: (b) Bragg grating, (c) X-coupler, and (e) cladding FPI and TIR mirror ($\alpha = 0°$) embedded inside the SMF that together form the integrated LIF sensor; (e) a rotated ($\alpha = 75°$) view of (d) showing scattering and ejection of red light that was coupled into the SMF core waveguide, (Adapted from [24], © 2014, with permission from The Royal Society of Chemistry).*

The fs-laser systems' capability to inscribe different patterns in the fiber allows creating microchannels in straight, circular, or arbitrarily complex shapes, increasing the applicability of this type of structure. In this regard, Figure 2.14 shows schematic and optical micrographs of a multiplexed LIF sensing platform. This compact LIF device integrates a through-hole for fluorescence detection or absorption spectroscopy, an FBG for temperature or strain detection, an in-line FPI embedded within a coreless optical fiber for refractive index or pressure sensing, and an X-coupler tap and fs-laser-formed waveguide for probing a cladding FPI for refractive index, pressure, or curvature sensing. Total internal reflection mirrors are used to tap light either into or out of the fiber cladding for an alternative probing method [24]. The overall approach of 3D laser structuring

in optical fibers extends to many more application directions, including through and blind holes, microfluidic networks and reservoirs, micro-optics, in-line Bragg grating waveguide filters, birefringence tuning, interferometers, and polarization selective taps. Thus, fs-laser writing offers a new and attractive opportunity for the dense 3D integration of optical sensors within many general types of optical fibers [26, 27, 62]. This has remarkable advantages for significantly enhancing the functionality of such fibers and paves the way for powerful new research tools, commercial products, and biomedical devices [14, 15, 24, 26, 75].

2.5 Conclusions

The development of ultrashort pulse lasers, namely the fs-lasers, was a key factor in introducing high-resolution three-dimensional micro-machining processes that take advantage of nonlinear light-matter interaction.

In this chapter, an introductory overview of the nonlinear absorption process (i.e., nonlinear photoionization and avalanche ionization) in dielectric materials was presented, providing a basic background to understand the mechanisms of material modification. The regime of modification and resulting morphological change rely on exposure parameters and material properties. According to the writing parameters, three regimes of permanent modification can be induced: isotropic refractive index change, birefringence, and voids. In addition, the repetition rate determines whether the modification regime is due to individual pulses or cumulative pulse heating. Therefore, the morphology of the structural change is dominated by the heating, melting, and cooling dynamics of the material in and around the focal volume.

A fundamental understanding and practical knowledge of the interaction between an fs-laser beam and an optical fiber are required to guide optical fiber sensors and devices fabrication. Thus, the main writing challenges addressed were the beam distortion caused by the spherical and astigmatic optical aberration, Kerr self-focusing effect, the alignment issues hampered principally by the optical fiber curvature, and the high degree of asymmetry imposed by the transverse writing geometry.

The FLICE technique was also addressed and understood as a laser-induced wet etch anisotropy. This technique, along with the fs-laser direct writing method, reveals to be a promising approach for 3D writing optical and fluidic devices in optical fibers.

An overview of the different writing methods and experimental considerations were given to support the development and home-assemble of an fs-laser writing system. Here, it was understood that direct writing methods could overcome the restrictions of the phase mask and interferometry methods. In addition, the burst writing method based on the PbP setup can prevent overexposure, unwanted exposure, or optical damage during the fs-laser direct writing process. According to these features, the burst writing method based on the PbP setup was chosen for this PhD work.

The main focus of this PhD program is to use the capabilities of 3D microfabrication for the development and optimization of optical fiber sensors. Therefore, this chapter also provided a brief review of the optical fiber devices fabricated by fs-laser micromachining.

CHAPTER 3

Fabrication and Characterization Methods

The processing of an optical fiber device by an fs-laser requires a proper system that allows the control of the optical fiber and the laser beam. Typically, an fs-laser writing system comprises the following modules: a laser, pulse controller, focusing optics, vision system, and sample positioning. The workstations or customized solutions for fs-laser direct-write processing, which are available commercially, are expensive. Generally, the laser and the sample precision positioning and displacement are the most costly resources. In addition, the homemade development allows the customization of the system features to optimize the fabrication of optical fiber devices, emphasizing the fs-laser direct writing of FBGs and LPFGs.

This chapter aims to introduce the fs-laser system developed in the framework of the PhD. Therefore, it describes the methods, equipment, and technical details used in the system assembling. Here, a description of the control and measuring software and the final integration of the system components are presented. Then, the fiber gratings fabrication methodologies are described, focused on the fs-laser burst writing method. The optical fiber preparation and alignment are described, along with the focusing procedures using dry and oil immersion objective lenses. The chapter last section addresses the characterization methods of the optical fiber devices during their fabrication.

3.1 Femtosecond Laser Direct Writing System

The developed fs-laser direct writing system is installed at the Microfabrication laboratory located in room 022 at the Department of Physics and Astronomy of the FCUP (Figure 3.1). The laboratory was also equipped with an air conditioning system and a new fabrication apparatus for fs-laser direct writing of planar substrates during the PhD program. The work developed in this laboratory aims to explore traditional top-down microfabrication techniques and non-traditional based on laser direct writing processes to support the activities of other areas. The femtosecond fiber amplified laser (Satsuma HP, from Amplitude Systèmes [79]) employed is a class IV laser equipment and is hazardous for the eye and skin. Therefore, the operator/users must be acquainted with all the safety hazards related to the use of high-power laser beams and strictly follow the safety instructions. The safety instructions and the protective equipment are available in the entry hall of the laboratory.

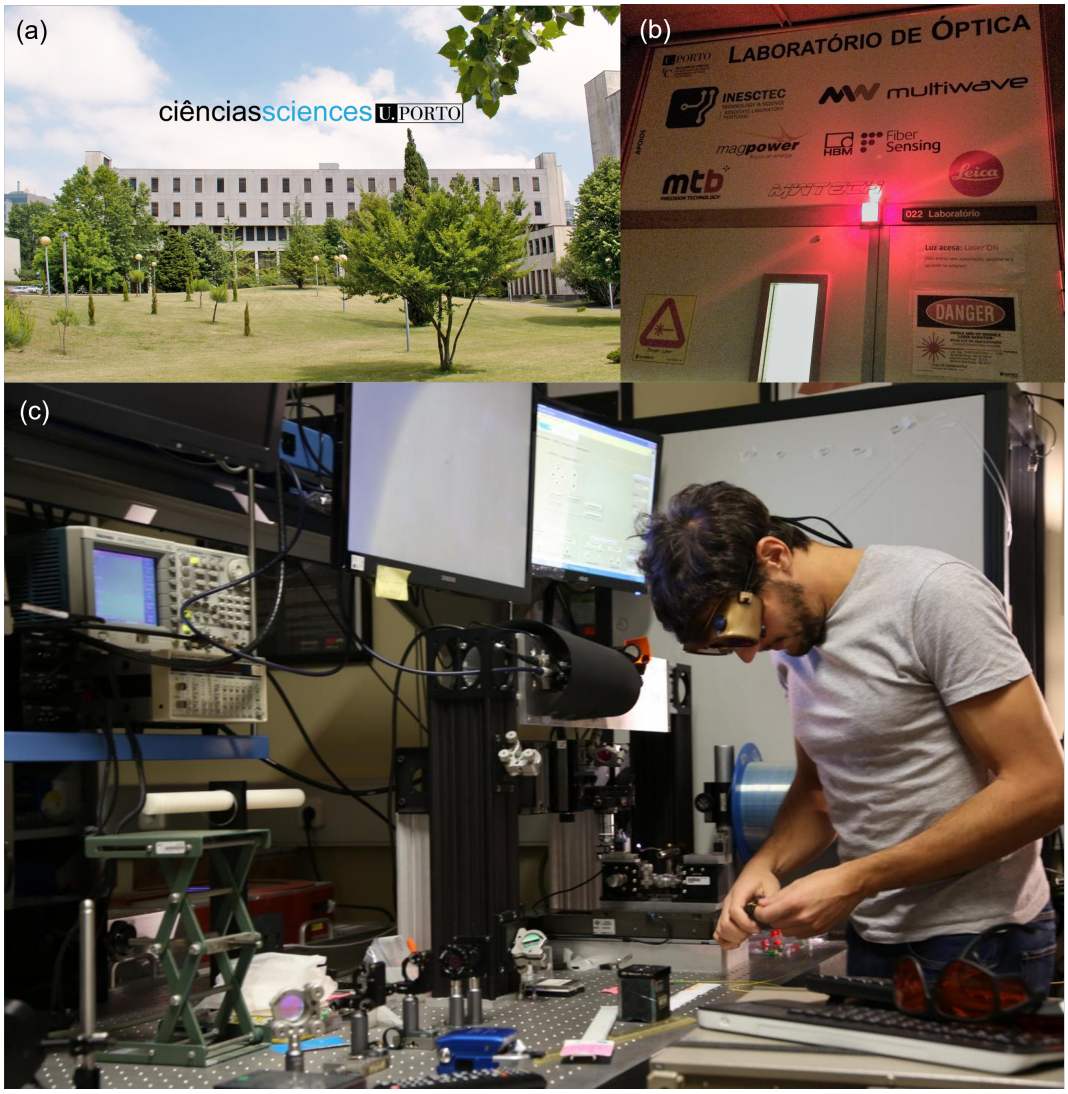


Figure 3.1. *Photomontage showing the facilities where the fs-laser microfabrication system is installed: (a) FCUP building is located in Pole 3 of the University of Porto (Polo Campo Alegre), (b) Microfabrication laboratory located in room 022 at the Department of Physics and Astronomy, and (c) Working at fs-laser microfabrication system.*

Direct laser writing is carried out on a home assembled system that features several components for tuning the power and polarization of the fs-laser beam and for focusing the beam inside the optical fiber. The fs-laser system components (i.e., optics, optomechanical, stages, imaging, and fiber amplified Amplitude Systèmes Satsuma HP laser) were assembled on a Newport optical table with pneumatic isolation, and the system is kept inside an isolated space that provides a safer environment.

The system is fully controlled by a LabVIEW program developed for data acquisition and control of the equipment (precision linear stages, function generator, load cell, charge-coupled device (CCD) camera, and Optical Spectrum Analyzer). The user has control of the experimental parameters, from exposure conditions to complex motion, within an easy-to-use Graphical User Interface (GUI) optimized for the fabrication of FBGs and LPFGs.

The schematic diagram of the fs-laser direct writing system is shown in Figure 3.2.

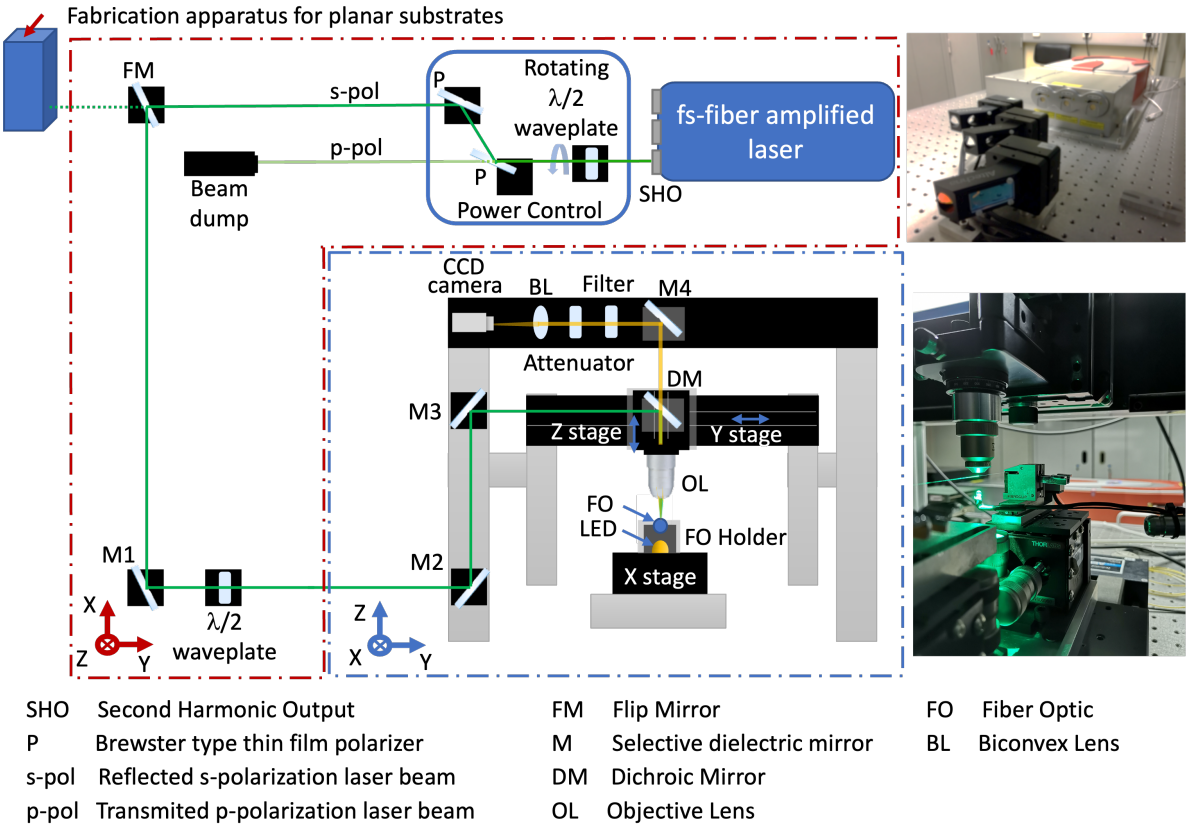


Figure 3.2. *Schematic diagram of the fs-laser direct writing system.*

3.1.1 Fiber Femtosecond Laser and Power Control Unit

The central piece of this writing system is a fiber amplified Amplitude Systèmes Satsuma HP laser, which generates 250 fs long pulses (at a repetition rate of 500 kHz) with a Gaussian mode profile (TEM_{00}) and polarization ratio of 1200:1. The fs-laser pulse has a beam size of $2.35x2.20$ mm^2 and beam quality, $M^2(X,Y)$ of $(1.11, 1.14)$ at a fundamental wavelength of 1030 nm.

The system features a harmonic generation module capable of converting the fundamental wavelength of the laser beam (1030 nm) to either its second (515 nm) or third (343 nm) harmonic wavelengths, with maximum pulse energy of 21 µJ, 11 µJ, and 3.88 µJ, respectively. The second harmonic wavelength is utilized throughout this PhD thesis as it provides a higher photoionization rate for exposure in fused silica than the fundamental wavelength (1030 nm) [13]. In addition, it provides a higher spatial confinement than irradiation at 343 nm due to the higher number of photons involved in the ionization process [80].

The fs-laser pulse energy can be controlled internally through an acousto-optic modulator (the efficiency is set to 50 %). In addition, an external motorized attenuator unit (Altechna Watt Pilot, [81]) is integrated into the fs-laser direct writing system (inset in the top right corner of Figure 3.2) for a simple definition and stable adjustment of the pulse energy. This power control unit is formed by a motor-driven rotating quartz half-wave ($\lambda/2$) plate (set transversal to the propagation direction

of the fs-laser beam) and two thin film polarizers that separate the incident beam into an s-polarized and p-polarized beams in parallel directions. The Brewster thin film polarizers reflect the s-polarized beam while transmitting the p-polarized beam. The intensity ratio of the separated beams can be tuned by rotating the waveplate. In this work, the s-polarization is utilized because it offers a higher purity beam polarization contrast. The p-polarized beam is guided towards a beam dump (p-polarization should be selected for maximum transmission). Following, the s-polarized beam is guided to a flip mirror set at $45°$ from the beam propagation direction and engaged to route it toward the optical path of the fs-laser direct writing system.

3.1.2 Beam Delivery Optics and Motion Stages

The selection and alignment of the beam delivery and conditioning optics are important for maintaining the beam quality, achieving precise focus and maximizing energy delivery. The fs-laser system uses dielectric mirrors with high reflectivity of over 99% at 515 nm for a $45°$ angle of light incidence. The mirrors are assembled in standard kinematic mounts, exhibiting minimal dispersion and a wavefront distortion of $\lambda/8$. A half-wave ($\lambda/2$) plate, which controls the polarization of the writing beam, is also mounted in a standard kinematic mount. Thus, the laser beam is directed through these mirrors and the half-wave ($\lambda/2$) plate into a dichroic mirror that reflects the wavelength of the laser beam (515 nm) into the focusing objective lens. The lenses used in this PhD work are a $100\times$ oil immersion objective lens, [82], and a $40\times$ aspheric lens, [83]. The objective lens specifications are summarized in Table 3.1.

Table 3.1. *Objective Lens Specifications.*

Objective Lens	**Olympus PLN100XO**	**Newport 5722-A-H**
Objective Type	Plan Achromat	Plano-Convex Aspheric
Magnification	100x	40x
Numerical Aperture	1.25	0.55
Working Distance (mm)	0.15	3.08
Immersion Medium	Oil	Air/Dry

The $100\times$ oil-immersion lens provides the high spatial resolution needed for the precise definition of microstructures. It was employed for the fabrication of FBGs, which require submicron-period modulation ($\sim$0.5 μm), and for FPIs, where accurate focusing is required to inscribe the modified regions that define the areas subsequently removed during etching to form the cavities. The oil-immersion objective was employed to minimize spherical and astigmatic aberrations at the fiber surface. The immersion oil, whose refractive index closely matches that of the cladding, reduces refraction at the glass interface and improves the focusing accuracy within the fiber. However, this index matching also removes the refractive-index contrast at the cladding boundary, resulting in strong attenuation of cladding-mode resonances, which are therefore not observed in the transmission spectrum. As a consequence, this configuration is unsuitable for the fabrication of LPFGs. For this reason, a $40\times$ dry aspheric lens was used for LPFGs and MZIs. Although

it introduces higher optical aberrations and provides lower spatial resolution compared to the oil-immersion lens, it preserves the air−cladding interface, allowing cladding-mode resonances to be monitored in real time during the inscription process.

The writing lens is attached to a lens mounting platform, which offers micro-metric precision. This configuration enables the objective entrance to be centred along the XY plane in relation to the fs-laser beam and adjusts the platform's tilt angle. The lens mounting platform is subsequently mounted in a Y (Newport M-ILS150CC) and Z (Newport M-VP-25XA) precision linear stages. The stages are connected to the same XPS-D motion controller with the XPS-DRV driver module. A high-quality air-bearing linear stage (AerotechABL10100-LN) in which the fiber was mounted is used for the X-direction. This motion stage is connected to the A3200 software-based motion controller. The specifications of the motion stages are summarized in Table 3.2. In this system, the X is the scanning direction and is parallel to the fiber axis, Y is the direction transversal to the fiber axis and Z is the beam propagation direction. Thus, the three-axis motion and alignment system provides control on the position of the laser beam. An LED source is assembled in the optical fiber holder to illuminate the optical fiber from below, allowing it to be imaged through the optical components. Therefore, the light from the LED, which is refracted through the optical fiber, passes through the dichroic mirror and is focused on the CCD camera (Watec 902-B).

Table 3.2. *Motion Stages Specifications.*

Stages	**Aerotech ABL10100-LN**	**Newport M-ILS150CC**	**Newport M-VP-25XA**
Axis	**X**	**Y**	**Z**
Travel Range (mm)	100	100	25
Accuracy (µm)	± 0.5	± 0.8	± 2
Resolution (µm)	0.5×10^{-3}	0.5	0.1
Velocity (mm/s)	300	100	25
Acceleration (mm/s^2)	10000	500	100

System Alignment

The alignment protocol is introduced to standardize the alignment and ensure an efficient beam delivery of the fs-laser direct writing system. This protocol consists of the following steps:

- The optical components are inspected for cleanliness and cleaned using compressed air or optic wipes moistened with ether if necessary;
- The fs-laser system should be turned on time for the pulse energy to stabilize;
- The pulse energy of the laser is reduced through the modulator efficiency, kept at 5%;
- Leveling the laser beam to the table surface and orienting its beam so that it travels along a well-defined path. To measure the height, two post-mounted iris diaphragms are placed close to and far from the laser. Matching heights are needed to ensure the path is level with the table's surface. This step is complete when the laser spot is centered on the iris' aperture;
- Verify that the optical fiber holder is orthogonal to the laser beam propagation direction. A mirror is placed over the optical fiber holder, and the position of the dichroic mirror is adjusted

until the paths of the incident and reflected beams coincide;

- Verify that the laser beam propagates parallel to the optical axis of the objective lens. The mirror is placed over the lens holder, and the platform's tilt angle is adjusted until the paths of the incident and reflected beams coincide;
- Verify that the laser beam's polarization is directed along the half-wave ($\lambda/2$) plate fast axes to adjust the laser beam polarization to be parallel to the fiber axis;
- The objective lens is attached to the holder, and the focused laser beam is inspected. The irradiation pattern is observed on a laser viewing card placed below the objective. The optical axis of the objective lens is centred relative to the laser beam when observing a clear pattern that grows symmetrically. This broadening of the irradiation pattern is observed by opening the iris placed before the objective.

The execution of these steps is imperative to properly align the system before assembling the optical fiber into its holder.

Power Calibration

The calibration of the writing laser power is realized by measuring the laser power at different levels after the focusing objective lens. A thermal sensor (LaserPoint 10-BB-D25) with a measurement range between 2 mW and 10 W is connected to a sensor meter (LaserPoint PLUS 2) for the measurements. Figure 3.3 shows the measured writing laser power as a function of the laser power measured after the power control unit. It also shows the respective fitting and system loss for the 100x oil immersion objective lens and 40x aspheric lens.

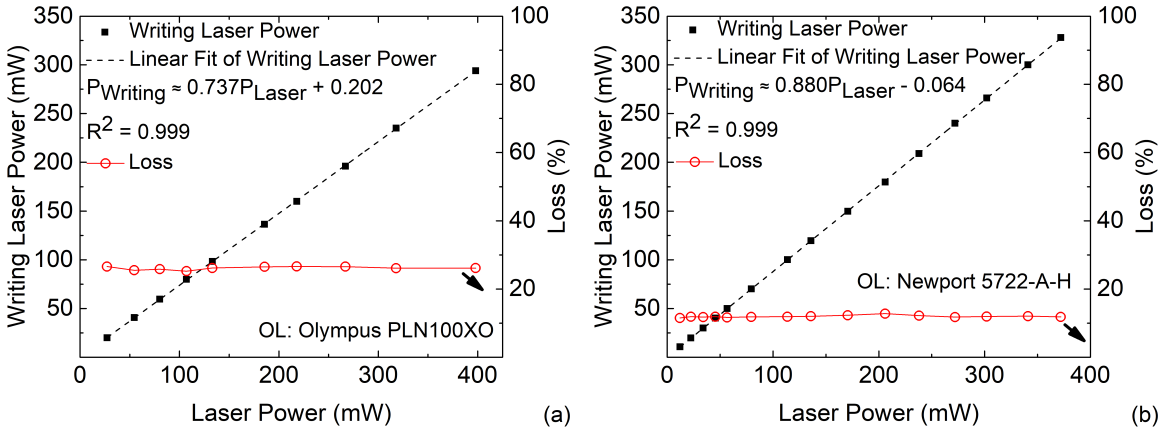


Figure 3.3. *Power Calibration: writing laser power after the focusing OL (a) Olympus PLN100XO and (b) Newport 5722-A-H as a function of laser power measured after the power control unit with respective system loss.*

The laser beam is conditioned to overfill the entrance aperture of the objective lens, allowing the entire numerical aperture of the lens to be utilized. Therefore, the writing numerical aperture corresponds to the nominal NA specified for each objective lens (Table 3.1), which directly affects the focusing spot size and depth of focus. The system losses were determined by measuring the laser power at the output of the power control unit and after the focusing objective lens. This results in 26% and 12% of the incident power being lost through the 100x oil immersion objective lens and

40x aspheric lens, respectively.

The pulse energy (Ep) is calculated from the relation $Ep = P_{Writing}/R$, where $P_{Writing}$ is the measured writing laser power and R is the repetition rate.

3.1.3 Femtosecond Laser Direct Writing of Fiber Gratings

The fabrication of gratings is carried out with the burst writing method, using the second harmonic wavelength (515 nm) of the fs laser with a pulse duration of approximately 250 fs and with the pulse repetition rate set to 500 kHz. The fs-laser beam is modulated through the acousto-optic modulator, controlled by an arbitrary waveform generated by a function generator (AFG3102, Tektronix), and applied to the laser gate. The fiber is then displaced along the X-direction at a constant velocity using a high-quality air-bearing linear stage (Aerotech ABL10100-LN), with the signal modulation turned on to create a refractive index modification over the required length. This modulation results in periodically spaced refractive index modification corresponding to the grating period. Therefore, the grating period can be defined by adjusting the stage velocity, V, and the modulation frequency, f_{mod}. The Bragg wavelength is given by $\lambda_B = 2n_{eff} \times (V/f_{mod})$, where n_{eff} is the effective index of refraction of the guided mode [7, 47, 49]. The schematic diagram of the burst writing method used in the fs-laser direct writing system is shown in Figure 3.4.

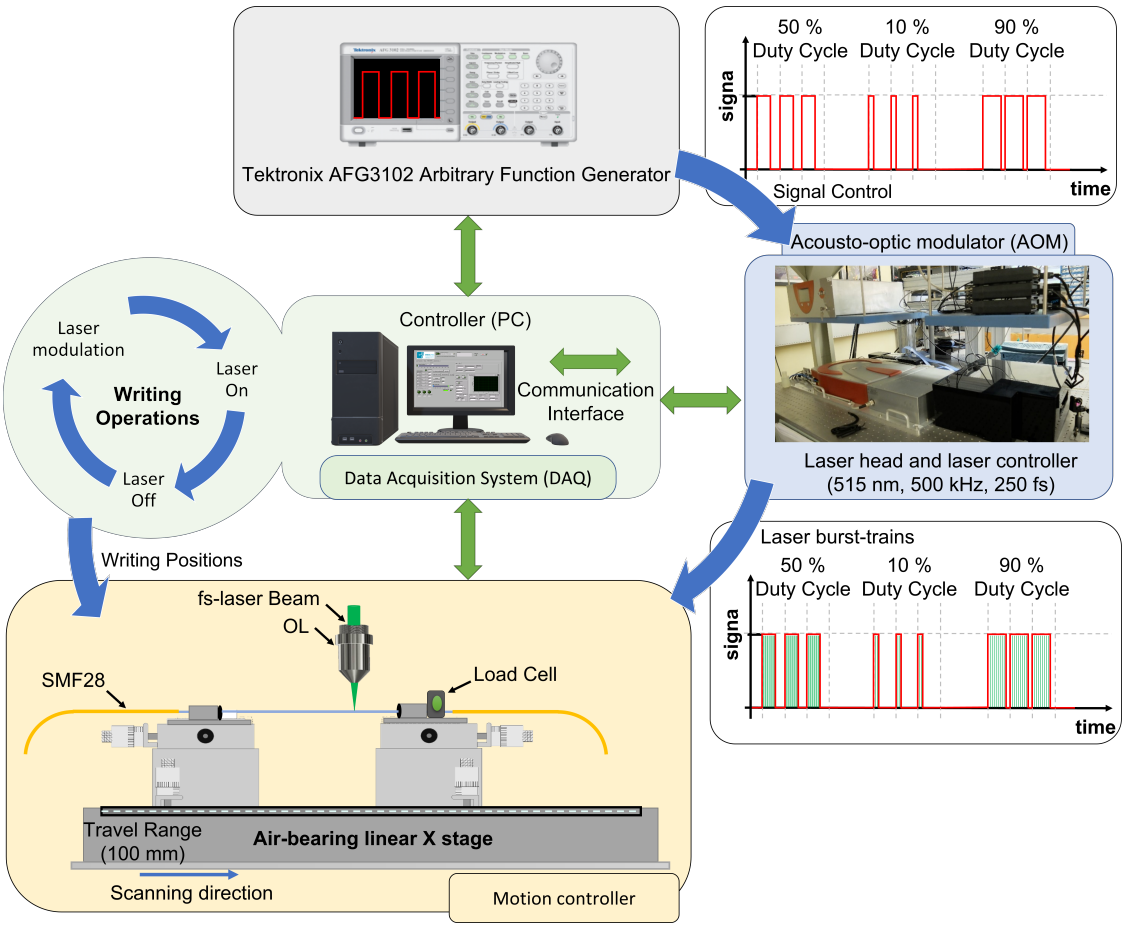


Figure 3.4. *Schematic diagram of the burst writing method used in the fs-laser direct writing system.*

The central control unit ensures communication between the fs-laser, function generator, and the stages. The software reads the positional data and triggers the function generator as the stages move. The function generator produces a periodic square function with a custom duty cycle (e.g., 50%, 10%, and 90%, as depicted in Figure 3.4), which controls the laser gate. Therefore, the laser is controlled by reading the motion stages' positions and dynamically activating the function generator in response to these inputs. This ensures that the laser pulses are synchronized with the fiber movement and the writing section. In addition, acceleration and deceleration margins are provided to ensure that the laser will only switch on or off when the scanning stage reaches the programmed velocity. This prevents overwriting at the beginning or end of the grating.

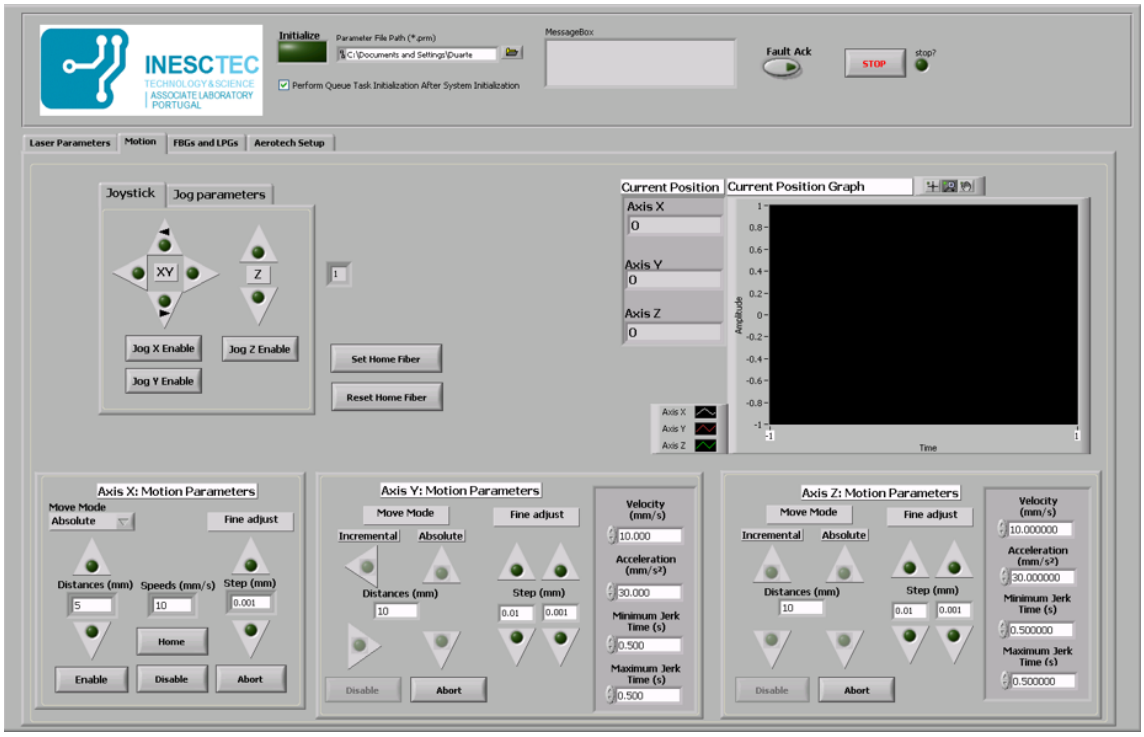
3.1.4 Hardware Architecture and Application Software

The part of the system that concerns the control of all the equipment described above consists of subsystems interconnected by a central control unit. This unit is responsible for the management and integration of the functionalities of each controller. Therefore, it enables communication with these devices, allowing the acquisition of data necessary for the real-time monitoring of the parameters related to the writing process. This is based on an expansion board with PCI slots where an NI PCI-6040 acquisition board and an NI PCI-1409 video acquisition board are connected. The acquisition is controlled by the NI PCI-6040 board, which communicates with the controller of this expansion board through a protocol defined for this purpose. Thus, the NI PCI-6040 board includes the NI-DAQmx driver and configuration utility, simplifying the configuration and delivering data acquisition capabilities. The two motion controllers are also connected to the central unit: the XPS-D motion controller, which communicates with all the Newport stages, and the A3200 software-based motion controller assigned to the high-quality air-bearing linear stage (AerotechABL10100-LN).

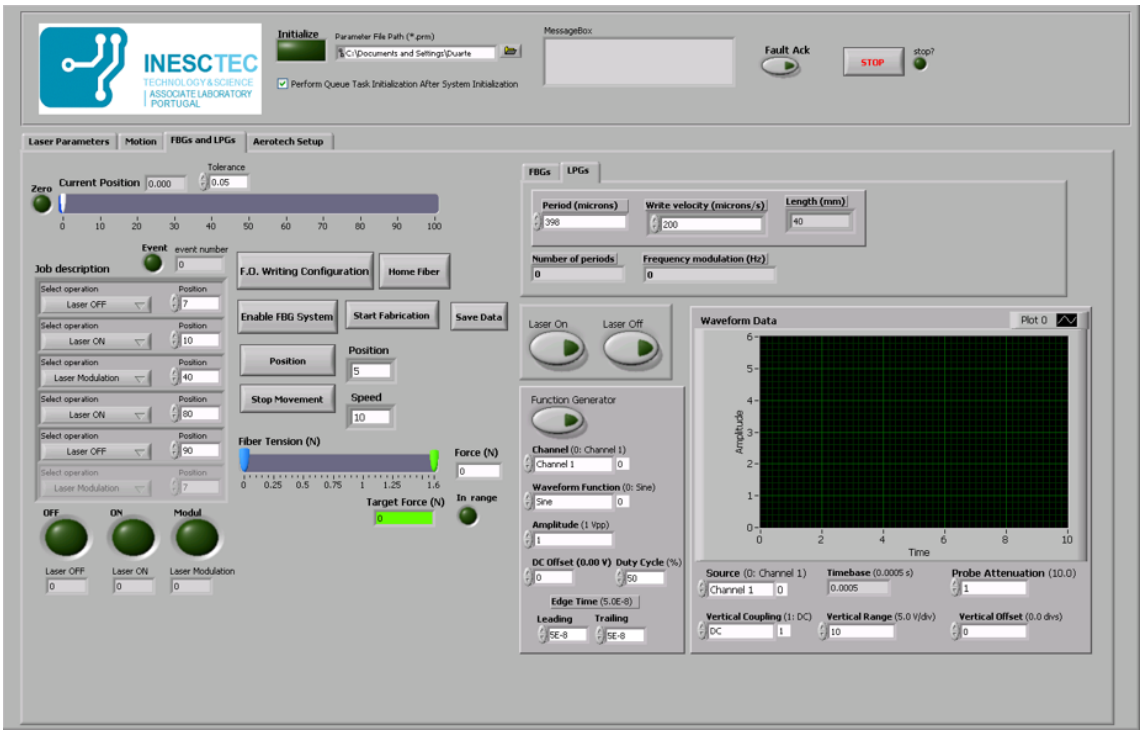
The entire control program was implemented in LabVIEW 2013. Several of the toolkits designed by National Instruments are required to use their sub-VIs (virtual instruments). The graphical user interface was developed to encompass all aspects related to the control of the available hardware. This is achieved by reading the system's inherent parameters and subsequently executing instructions according to the logical progression of the optical fiber devides fabrication process. This interface provides users with the capability to initiate the system as well as to execute, monitor, and record the parameters associated with the fabrication process.

The graphical user interface of the fs-laser system, shown in Figure 3.5, consists of two main panels that facilitate the control and real-time monitoring of the motion stages and grating fabrication parameters. The motion control panel (Figure 3.5 (a)) includes controls for setting the movement modes and the positions of the X, Y, and Z stages. It includes fine-tuning buttons for precise adjustments, as well as a joystick option that provides a more intuitive way to operate the stages. This allows for smooth and accurate movements. This panel also integrates real-time feedback through a graph that continuously displays the current positions of the three stages (X, Y, and Z), enabling the user to monitor and make informed adjustments.

The Gratings control panel (Figure 3.5 (b)) provides buttons, indicators, graphical elements and sliders to introduce and monitor the writing parameters. Two sliders are used, one to monitor



(a) *Motion Control Panel*



(b) *Gratings Control Panel*

Figure 3.5. *GUIs of the fs-laser system: (a) Motion, and (b) Gratings Control Panels, respectively.*

the current position of the writing section, and the other is dedicated to tracking and adjusting the applied tension on the fiber, ensuring the same tension level throughout the operation. The user can define the gratings parameters in a proper section of the panel, labelled according to the grating

type. The optical fiber writing configuration button gives access to the alignment procedure of the fiber, including the CCD camera image. The grating length and the writing position in the optical fiber are defined in the job description menu. In this panel, the users also configure and monitor the settings of the function generator (AFG3102, Tektronix), which is responsible for generating the periodic square wave function used to control the laser gate. The buttons to manually turn the laser on or off are also presented. In addition, three circular green indicators display the laser activation status, i.e., off, on, and modulation. Each indicator turns green at a time to show the active status and verify that the laser is working at the appropriate moment and synchronised with the movement of the stages. After each writing procedure, the software generates an activity file recording information about the motion stage's position, movement corrections, laser writing parameters, grating parameters, the tension applied to the optical fiber, and other adjustments made during the operation.

3.2 Optical Fiber Preparation and Alignment

The optical fibers used in this PhD work are Corning single-mode fiber SMF-28e, [84], and Thorlabs coreless fiber FG125LA, [85]. The optical fibers specifications are summarized in Table 3.3.

Table 3.3. *Optical Fibers Specifications.*

Optical Fiber	**Corning SMF-28e**	**Thorlabs Coreless FG125LA**
Core Diameter	8.2 µm	–
Cladding Diameter	125.0 ± 0.7 µm	125.0 ± 1.0 µm
Core-Cladding Concentricity	≤ 0.5 µm	–
Cladding Non-Circularity	$\leq 0.7\%$	–
Coating	Dual acrylate CPC®	Acrylate
Coating Diameter	245.0 ± 5.0 µm	250.0 ± 12.5 µm
Refractive Index Difference	0.36%	–
Mode Field Diameter ($\lambda = 1550$ nm)	10.4 ± 0.5 µm	–
Attenuation ($\lambda = 1550$ nm)	< 0.20 dB/km	–

In the preparation of the optical fiber, the coating is removed and carefully cleaned using ethanol. The bare fiber is then clamped to two three-axis positioners (MBT616/M, Thorlabs) that are mounted on the X air-bearing linear stage. The real-time monitoring and the adjustment of the fabrication tension are done through a previously calibrated load cell (Interface SML series). The tension is applied by increasing the distance between the two 3-axis positioners, which are connected to the load cell. The fiber is kept under tension (1N) to remove the curvature during the alignment and writing processes and to ensure that remains in position. The precise alignment of the fiber is realized using the CCD camera image, which is acquired through the writing objective lens. This alignment is realized with micrometric precision, involving fine, incremental adjustments to the fiber position along the Y and Z axes via the two positioners. After this fine alignment, the

optical fiber is moved along the X-direction using the air-bearing linear stage to verify the alignment at different points along the fiber. If there is a misalignment, it is necessary to readjust via the two positioners the tilt along the X-Z plane or the X-Y plane. This procedure is carried out iteratively, using real-time imaging from a CCD camera to provide feedback and specific adjustments. The alignment procedure depends on the objective lens used to write the optical fiber devices.

3.2.1 Focusing Procedure with an Oil Immersion Lens

When using the oil immersion lens, the alignment of the writing system is achieved through real-time monitoring of the optical fiber by the CCD camera. To realize this procedure, it is necessary to turn on the LED source integrated into the fiber holder to illuminate the optical fiber, while the laser beam is turned off to prevent unwanted focusing directly within the index matching liquid. The use of an index-matching liquid (Cargille cat#: 19571, RI = 1.4587, and viscosity of 80 centistokes, [86]) is essential for eliminating cylindrical aberrations caused by the fiber's geometry and for compensating for the refractive index mismatch at the fiber surface. The utilization of the index-matching liquid precludes the possibility of performing real time alignment using the laser beam itself.

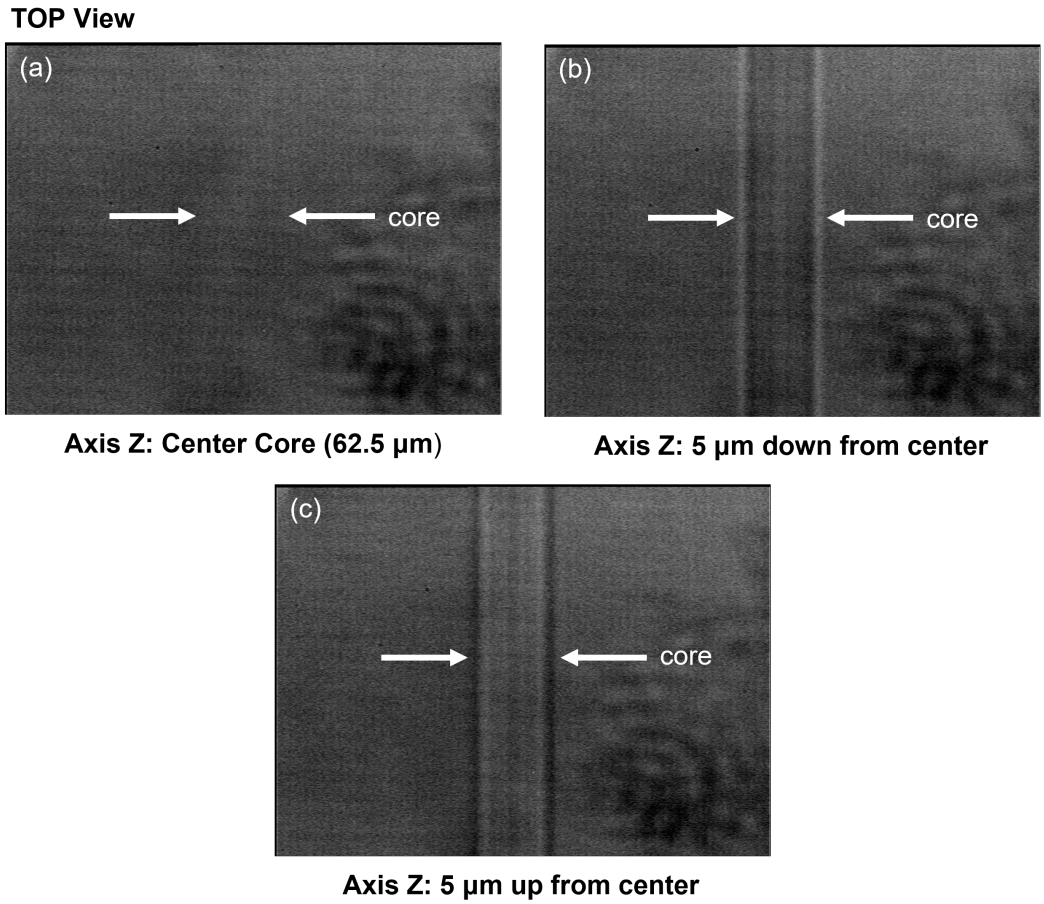


Figure 3.6. *Recorded images of a SMF-28e fiber (8.2 µm core diameter) as seen through the CCD camera of the fs-laser system at different positions the fiber top surface: (a) 62.5 µm (center focus) and slightly off focus (± 5 µm), (b) 67.5 µm and (c) 57.5 µm.*

The index-matching liquid is placed on a coverslip, which is then used to apply the liquid in the optical fiber and the tip of the oil-immersion objective lens, forming a convex meniscus. The meniscus stability relies on the viscosity of the index-matching liquid, 80 centistokes. This viscosity is sufficient to maintain the liquid between the objective lens and the optical fiber at the scanning velocities used in this work (up to 200 µm/s). The inspection of the optical fiber writing region is realized to detect bubbles or dust using the real time visualization system. If bubbles or dust are observed in the image acquired by the CCD camera, it is essential to clean both the fiber and the oil-immersion objective before resuming the application process.

Figure 3.6 shows the recorded images of an SMF-28e fiber immersed in index-matching liquid following the alignment procedure. As the core comes into focus, the boundaries between the core and cladding become indistinct (Figure 3.6 (a)). When the fiber is slightly off focus ($\pm$ 5 µm) the core/cladding boundaries is visible as shows in Figure 3.6 (b) and (c), respectively.

3.2.2 Focusing Procedure with a Dry Aspheric Lens

The alignment is realized through the back-reflected fs-laser beam focused by the Dry Aspheric Lens into the optical fiber and visualized with the CCD camera. Therefore, it is necessary to attenuate the laser to a value of less than 2 mW to keep pristine optical fiber before the writing. The profile of the back-reflected laser beam from the fiber surface at different focal positions after aligning the optical fiber is illustrated in Figure 3.7.

The laser reflected signal is used to identify the position of the fiber surface, tracking a single bright spot when the laser focus is positioned at the top center position of the fiber cladding, Figure 3.7 (a). As the laser focus is adjusted deeper into the fiber, interference fringes start to appear at depths of 10 µm and 50 µm below the top surface, as illustrated in Figure 3.7 (b) and Figure 3.7 (c), respectively. At a focal depth of 62.5 µm, with and without a lateral offset of 5 µm, the cylindrical lensing effect of the fiber resulted in a single line focus, as shown in Figure 3.7 (d) and Figure 3.7 (e). As far as the back-reflected laser spot from the fiber surface is concerned, it remains visible at this depth. When it overlaps with the interference line, the fiber center is achieved as shown in Figure 3.7 (d). Figure 3.7 (f) shown the image of the back-reflected laser light focused into the SMF-28e at 92.2 µm. At this depth, the back-reflected laser spot from the fiber surface is still visible, and the interference line broadened.

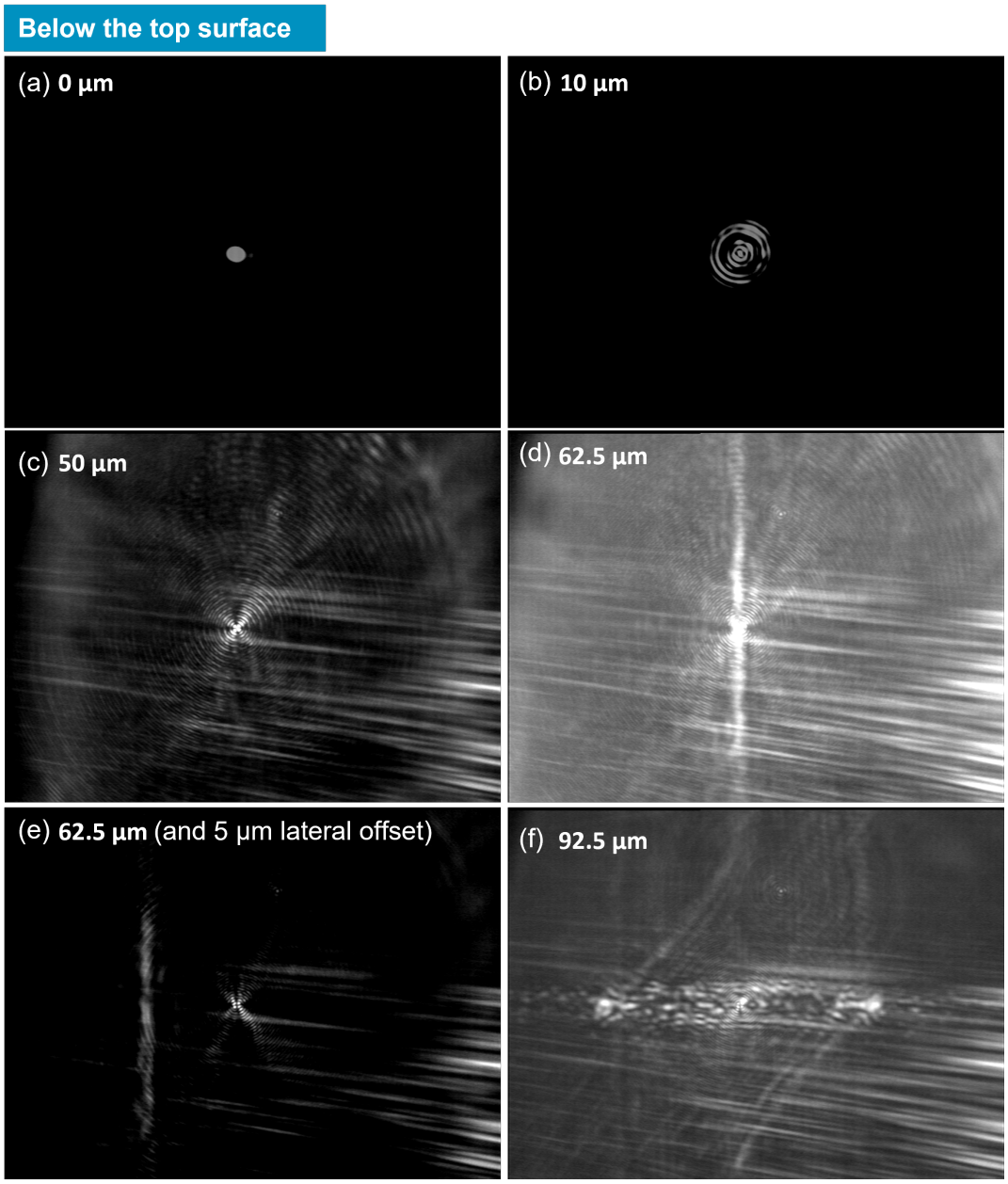


Figure 3.7. *Recorded images of back-reflected fs-laser beam focused by a 40× objective lens into a SMF-28e fiber at (a) 0 µm, (b) 10 µm, (c) 50 µm, (d) 62.5 µm, (e) 62.5 µm (and 5 µm lateral offset), and (f) 92.5 µm below the top surface.*

3.3 Optical Characterization Setup

Monitoring the optical transmission through a device during its fabrication allows a flexible tuning of device properties based on the desired performance specifications, e.g., center wavelength, reflectivity, bandwidth, and length of FBGs and LPFGs. The laser beam is promptly turned off using the AOM modulation signal. Therefore, the optical fiber devices reported throughout this thesis are characterized in real-time during the fabrication by measuring the spectrum in transmission or reflection through the experimental setup shown in Figure 3.8. Regularly, the devices

that compose the experimental setup are cleaned. In particular, the optical fiber is moistened with ethanol and thoroughly cleaned with dry wipes to ensure the nonexistence of contaminants in the sensing region. The optical fiber connectors of the light source, optical detector, or other optical device utilized are cleaned with a one-click fiber cleaner pen. The optical fiber connectors are cleaned with delicate task wipers and inspected with an optical fiber microscope (FAVA FOM400) to check the proper execution of the cleaning task.

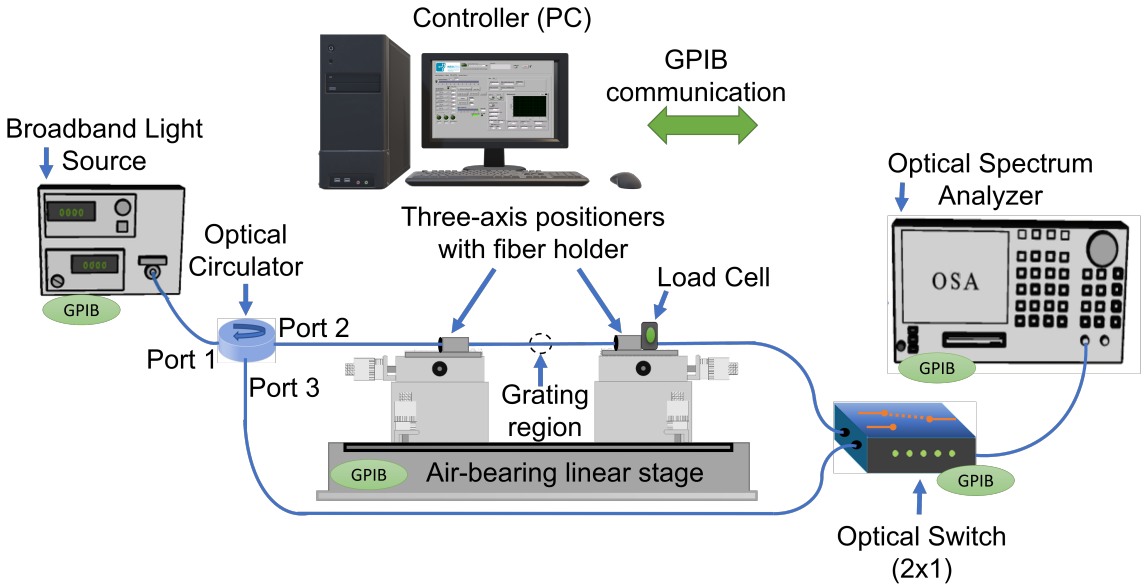


Figure 3.8. *Experimental setup for measurement of the gratings transmitted and reflected spectrum.*

First, the optical source is switched on before any measurement on time to stabilize and prevent any output power variations during the characterization. After that, the light reflected or transmitted from the periodic structures is measured by connecting the radiation source to port 1 of a three-port optical circulator, as shown in Figure 3.8. Therefore, light emitted from the source is transmitted through port 2 to the periodic structure and sequentially to one port of the optical switch. Light reflected from the periodic structure is routed by port 3 of the circulator to another port of the optical switch. Lastly, the optical switch output is connected to the optical detector through an SMF-28e fiber. The transmitted or reflected signals are measured by switching the route of the optical switch through a Labview program developed to control the devices connected to the PC by GPIB (General Purpose Interface Bus) interface. Furthermore, the signal is measured without polarization control, and the recorded spectra were always normalized to the optical spectrum of the radiation source.

Different optical sources and detectors were used throughout this PhD thesis according to the device under test. The post fabrication characterization setups are presented in Chapter 4.

3.4 Conclusions

This chapter introduced the fs-laser system developed in the PhD framework. A description of the components of the fs-laser system was made, focusing on the optics, optomechanical components, stages, imaging, and the fiber amplified Amplitude Systèmes Satsuma HP laser. The homemade development of the fs-laser system presented was achieved by overcoming important steps, including selecting, assembling, integrating, and precisely aligning the components to ensure optimal laser beam delivery. System alignment is imperative in laser systems because it directly affects the laser beam quality and stability. The alignment protocol was implemented to ensure standardized alignment and efficient laser beam delivery. Before each utilization of the fs-laser system, regular checks and adjustments should be made to ensure continued alignment. The preparation and alignment of the optical fiber are fundamental requirements of the fabrication process, which includes the real-time monitoring and adjustment of the fabrication tension. The alignment was realized iteratively, using real-time imaging from a CCD camera to provide feedback and adjustment with micrometric precision, involving fine, incremental adjustments to the fiber position along the axes by two positioners. Therefore, it is necessary that the optical fiber is precisely aligned and positioned to facilitate accurate writing. The burst writing method was implemented to fabricate the gratings. Thus, the fs-laser is controlled by continuously reading the motions stages positions and dynamically enabling the function generator in response to these inputs. This allows the laser pulses to be synchronised with the fiber movement and the writing section. The development of fabrication and characterisation routines involved programming sequences that handle specific tasks, such as focusing procedures, communication between the system components and synchronisation of the laser pulses with the fiber motion and writing section. The GUI features easy-to-use controls and indicators for real-time monitoring and control of the fabrication procedure. Finally, the description of the optical characterization setup was provided. By monitoring optical transmission throughout the fabrication process, it becomes possible to fine-tune the properties of the device to achieve desire performance requirements. This method ensures that parameters such as center wavelength, reflectivity, bandwidth, and the length of the FBGs and the LPFGs are optimized for the desired outcomes. While both FBG and LPFG structures rely on periodic refractive-index modulation, the main difference in spatial scale, spanning sub-micrometer to hundreds of micrometers, imposes different requirements on the laser inscription system. The successful fabrication of fiber gratings and interferometric structures by femtosecond laser inscription depends on the focusing lens, which governs the interaction between the laser beam and the optical fiber. The oil-immersion configuration is preferable for the fabrication of short-period structures, such as the FBGs and FPIs realized in the present work, as it minimizes spherical and astigmatic aberrations at the fiber surface and enables submicron-scale focusing within the fiber. Conversely, the dry aspheric configuration is preferred for LPFGs and MZIs, as it preserves the air-cladding interface, enabling real-time monitoring of grating formation.

CHAPTER 4

Development and Optimization of Optical Fiber Sensors

This chapter is dedicated to the optical fiber sensors fabricated by the fs-laser system, and it is organized according to the fabricated optical fiber structures: FBGs, LPFGs, and optical fiber interferometers. A brief introduction is presented for each structure, and the fabrication procedures are detailed, followed by the characterization data and performance of the sensor devices.

4.1 Fiber Bragg Gratings

Fiber Bragg gratings are important and invaluable passive optical devices in optical communication, sensing, and fiber laser applications [1, 31, 87]. Their most distinguishing feature is the flexibility they offer for achieving specific spectral characteristics, due to the broad range of variation in their physical parameters (refractive index change, length, apodization, period chirp, and fringe tilt) [1, 31, 87, 88]. FBGs can be conventionally photo-inscribed into the core of a photosensitive single mode fiber using UV laser exposure through a phase mask or by holographic methods, which allows the inscription of a single FBG in the fiber core determined by the germanium doping distribution [89, 90].

The fs-laser direct writing method [88, 91, 92] has a few advantages relative to methods that employ a phase mask, either by UV exposure [89, 90] or fs-laser exposure [93, 94]. With the direct writing method, there is no need for a phase mask [37], it can be used to write gratings through the fiber polymer coating [31, 37, 87], and in a variety of optical fibers (including in coreless fibers [15]) without any special treatment for photosensitivity enhancement [88]. It has excellent design flexibility, enabling rapid change of grating parameters, such as length, bandwidth, or Bragg wavelength [26, 31]. High-order gratings (e.g., 2nd, 3rd and 4th order) are fabricated by simply adjusting the writing period [7, 95]. The underlying non-linear light-matter interaction opens the possibility to change the fiber refractive index not only in the core but also in the fiber cladding with high spatial resolution [39]. There are examples in the literature of waveguides arbitrarily located in different cladding positions to create directional couplers [96], and RI modifications placed close to the pre-existing core waveguide of optical fibers to form in-fiber multimode interference (MMI) devices [97] or convert the co-propagating fundamental mode into a counter-propagating higher-order mode [22, 98, 99]. Furthermore, birefringent gratings can be fabricated by inducing a slightly shifted refractive index modulation from the fiber core center, creating an asymmetry in the fiber

cross-section as demonstrated in [92, 100, 101]. In these FBGs, also called eccentric gratings, both the Bragg and cladding modes are excited [92, 98, 101], with a behavior similar to the tilted FBGs [102, 103].

FBGs can be employed as optical sensors to measure physical parameters, such as temperature [104], strain [105], curvature/bending [106, 107], pressure [55], or twist [108, 109] either individually or simultaneously [110], through wavelength monitoring or power detection [111]. Sensing configurations involving the fabrication of birefringent FBGs [100], tilted FBGs [112], FBG arrays [26, 113] or sampled FBGs [52] have already been demonstrated. Similar bending sensors have also been shown in depressed cladding fibers [114], in few-mode fibers [115] and in twin-core few-mode fibers [116], which showcases the versatility of this technique.

Sensing in harsh environments, such as the oil and gas industry, power stations, aircraft engines, and furnaces, requires high operating temperatures from 400 ℃ to above 1000 ℃ [31, 54, 55]. Therefore, it is necessary to anneal the FBGs at elevated temperatures to guarantee their performance at the operating temperature and subject to strain above the measurement range to eliminate relaxation effects over the lifetime of the sensor [117].

One of the issues with common FBG sensing configurations is the low sensitivity to curvature, given that the fiber mode is strongly confined to the core and is only slightly influenced by the external bending. A possible way to solve this is to employ cladding modes [110, 116, 118]. However, when utilizing cladding modes, a suitable coupling mechanism is imposed to recouple the light back into the core, to allow remote interrogation with low loss [105, 111]. This can be done through offset splicing [51], core mismatching or abrupt taper [119] which, nevertheless, brings up issues of low reproducibility (offset splicing), weakened mechanical strength (abrupt taper), and complex fabrication processes [111].

Optical fiber twist sensors have also been topics of research within the optical fiber sensor community [109]. Sagnac interferometers fabricated in low-birefringence SMF [120] and photonic crystal fiber [121], high-birefringence FBGs [122], and corrugated long-period fiber gratings [123] are some examples of proposed devices for twist measurements. However, some of these sensors require complex fabrication processes that turn difficult to implement in practical applications [108, 124].

This section presents the fabrication of periodic structures in optical fibers, including type I first- and second-order FBGs in an SMF-28e through the fs-laser direct writing system. The entire fabrication process and characterization of the FBGs are described. The influence of the writing parameters on the spectral properties were studied to improve the coupling efficiency and achieve high reflectivity and narrow bandwidth FBGs. The polarization dependence of the gratings induced by the larger asymmetric structure formed during the writing process was evaluated. The possibility to write type I first- and second-order Bragg gratings in the same single-mode fiber (SMF-28e), with reflectivities of 99.6% and 59.3%, respectively, is presented. The fabrication of an FBG between two waveguides in a coreless fiber (FG125LA, Thorlabs) was also demonstrated. The FBGs and the device (waveguide-FBG-waveguide in coreless fiber) were characterized in temperature and compared with the traditional UV-inscribed ones to verify their thermal stability,

as fs-laser gratings offer higher thermal stability, withstanding temperatures up to 1000℃ [125]. The fabrication of first-order off-axis FBGs in an SMF-28e through fs-laser direct writing is also demonstrated. The optimization of the fabrication process of off-axis FBGs, and the grating spectra characterization while varying the lateral distance of the grating to the core center are presented in detail. For distances equal or above 2.5 µm, a multimode section in the SMF-28e that can support two-mode ($LP_{0,1}$ and $LP_{1,1}$) FBGs was observed, similarly to what was already observed by others [51, 93, 126] in different types of optical fibers and periodic structures. However, the formation of this type of FBGs when fabricated by fs-laser writing in standard single-mode fibers was not anticipated. The influence of the lateral offset to strain, temperature and curvature sensing was investigated, by fabricating three FBGs, with offsets of 3.0, 4.5 and 6.0 µm. In addition, the polarization proprieties for twist measurement of the 4.5 µm FBG were also evaluated through the reflected intensity ratio, enabling the simultaneous measurement of the twist, and twist direction. The existence of two separate fiber modes, each split into two degenerate polarization modes, induced by the larger asymmetric structure formed during the writing process, also enables simultaneous detection of multiple parameters.

4.1.1 Theoretical Background

The coupled-mode theory is a widely used technique for modeling the optical properties of FBGs [1, 7, 127, 128]. In this thesis, the essential considerations to realize a quantitative analysis of the gratings spectral characteristics are presented without entering into details that can be found in textbooks such as [1, 7, 127]. An FBG consists of a periodic or aperiodic modulation (typically of the order of few hundred nanometers) of the refractive index along the longitudinal axis of the core of a single-mode optical fiber [1, 7, 127, 128]. The FBGs are based on the coupling between the forward and backward propagation (LP_{01}) guided modes in an optical fiber, described by:

$$\Delta\beta = \beta_{0,1(\text{forward})} + \beta_{0,1(\text{backward})} - \frac{2\pi}{\Lambda}, \tag{4.1}$$

where $\Delta\beta$ is the detuning factor, Λ is the grating period, and $\beta_{0,1}$ is the propagation constant of the guided modes [1, 7, 127, 128].

Considering the forward and backward propagation modes have the same propagation constant, under the phase-matching condition ($\Delta\beta = 0$), the Bragg resonant condition, λ_B, is given by:

$$\lambda_B = 2n_{eff}\Lambda, \tag{4.2}$$

where n_{eff} is the effective refractive index of the guided mode [1, 7, 127−131]. When a beam of light passes by the grating region, a narrowband spectral component corresponding to the Bragg resonance wavelength of the grating is reflected, and all other wavelengths outside the narrow reflection band are transmitted [1, 7, 127, 128]. Thus, the grating structure acts as a selective mirror for the wavelength that satisfies the Bragg condition. Typically, an uniform FBG is considered the fundamental grating structure, having a period modulation of the RI that is constant and orthogonal to the longitudinal fiber axis [1, 7, 127, 128].

The grating bandwidth $\Delta\lambda_{BW}$ defined as the wavelength range between the first zeros apart from the Bragg peak is given by [1]:

$$\Delta\lambda_{BW} = \frac{\lambda^2}{2\pi n_{eff} L_g}\sqrt{(kL_g)^2 + \pi^2}, \tag{4.3}$$

where L_g is the length of the grating, and the coupling coefficient of the grating, k, is given as:

$$k = \frac{2\pi n \Delta n \eta}{\lambda_B}, \tag{4.4}$$

in which n is the nominal refractive index of the core, Δn is the magnitude of the refractive index modulation, and η is the overlap integral of the modes ($\eta \approx 1$ for identical modes) [5, 7, 127].

The maximum reflectivity, R, of the grating at the Bragg wavelength for the phase-matching condition ($\Delta\beta = 0$) is given by [5, 7, 127]:

$$R = \tanh^2(kL_g). \tag{4.5}$$

In addition, the reflectivity, r, in % can be determined by [5, 7, 127]:

$$r(\%) = 1 - 10^{\frac{T_{dip}(dB)}{10}}, \tag{4.6}$$

where T_{dip} is the transmission dip in decibels (dB) at the Bragg wavelength, λ_B.

Physical parameters such as temperature and strain are sensed by the FBGs due to their modulation of n_{eff} and/or grating pitch, Λ, [1, 5, 7, 127]. The gratings sensitivity to these parameters are analyzed in the following sections.

Temperature Sensitivity

The Bragg wavelength shift ($\Delta\lambda_B$) at constant strain for a temperature variation (ΔT) is given by:

$$\Delta\lambda_B = \lambda_B(\alpha + \delta)\Delta T. \tag{4.7}$$

Where, $\alpha = \frac{1}{\Lambda}\frac{d\Lambda}{dT}$ is the thermal expansion coefficient of the fiber, and $\delta = \frac{1}{n_{\text{eff}}}\frac{dn_{\text{eff}}}{dT}$ is the thermo-optic coefficient [1, 5, 7, 127]. Therefore, the temperature variation has two effects over the Bragg wavelength shift; the first effect corresponds to the change in the grating period, increasing the resonance wavelength with temperature, while the second reflects the thermo-optic effect, which changes the effective refractive index of the guided mode with temperature [1, 5, 7, 127]. Typical temperature responses of the Bragg resonance wavelength of the grating are 10 pm/℃, and 13 pm/℃ for 1300 nm and 1550 nm band, respectively [1, 5, 7, 127].

Strain Sensitivity

The Bragg wavelength shift under isothermal condition ($\Delta T = 0$) due to longitudinal strain is given by:

$$\frac{\Delta\lambda_B}{\lambda_B} = (1 - P_e)\Delta\varepsilon_z, \tag{4.8}$$

where $P_e = \frac{n_{\text{eff}}^2}{2}(p_{12} - \nu(p_{11} + p_{12}))$, p_{11} and p_{12} are Pockel's coefficients of the strain-optical tensor, "ν" is the material Poisson's ratio of the optical fiber, and $\Delta\varepsilon_z$ is the applied longitudinal strain [1, 5, 7, 127]. Typical strain sensitivity at 1300 nm, and 1550 nm are 1.0 pm/$\mu\varepsilon$, and 1.2 pm/$\mu\varepsilon$, respectively, for a value of germanosilicate optical fiber ($p_{11} = 0.113$, $p_{12} = 0.252$, $\nu = 0.16$, and $n_{eff} = 1.447$) [1, 5, 7, 127]. The strain sensitivities of an FBG depends on the type of photosensitive fiber used to fabricate the FBG [1, 5, 7, 127].

4.1.2 Fabrication and Sensitivity Analysis of First- and Second-Order FBGs

The fabrication of FBGs is carried out with the burst writing method, using the second harmonic (515 nm) of the fiber amplified fs laser (Satsuma HP, from Amplitude Systèmes) with a pulse duration of approximately 250 fs and with the pulse repetition rate set to 500 kHz. The fs-laser beam was modulated through an acousto-optic modulator, controlled by an arbitrary waveform generated by a function generator (AFG3102, Tektronix). In addition, the fs-laser beam was linearly polarized along the scanning direction. The fs-laser direct writing system and inscription process were described in Chapter 3. Succinctly, it consists in focusing the laser beam in the fiber core with a 100× oil immersion lens (Olympus PLN 100XO) with a numerical aperture of 1.25 (Figure 4.1).

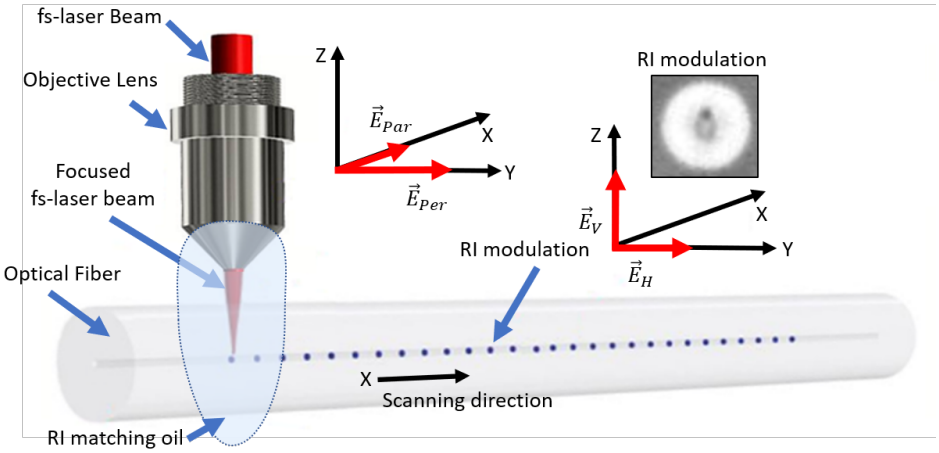


Figure 4.1. *Schematic diagram of a RI modulation induced by fs-laser in the core of an SMF with an oil-immersion lens. An optical micrograph (upper right corner) shows the cross-section of a single-mode fiber core with a RI modification written with the fs-laser beam incident from the top. The $\vec{E}_V$ and $\vec{E}_H$ indicate the electric field orientation for Vertical, V, and Horizontal, H, grating polarization eigenmodes. At the same time, $\vec{E}_{Par}$ and $\vec{E}_{Per}$ represent the parallel and perpendicular polarizations of the writing laser, respectively.*

The fiber is then displaced along the X-direction (which is parallel to the fiber axis) at a constant velocity (v) using a high-quality air-bearing linear stage (Aerotech ABL10100-LN) to create a refractive index modification over the required length. Each focused burst-trains pulses induces

a refractive index modification in a point-like region of the fiber core, as shown in Figure 4.1. The spacing between these points corresponds to the grating period, which can be controlled by the speed of the translation stage and/or the modulation frequency of the acousto-optic modulator. After fabrication, the gratings were characterized according to the procedure described in section 3.3 and with the measurement setup of Figure 3.8. A broadband light source from PolarOnyx, Inc. model ASE 2000 and an optical spectrum analyzer Yokogawa AQ6370D were used as optical source and detector, respectively. The measurements were carried with a resolution of 0.02 nm at room temperature.

Figure 4.2 shows the transmission spectra of a 10.0 mm long FBG with a Bragg wavelength at 1529.82 nm ($\Lambda = 528.60$ nm) written with a pulse energy of 60 nJ, 50 µm/s scan velocity, a fiber tension of 1 N, and with a duty cycle of 50 %.

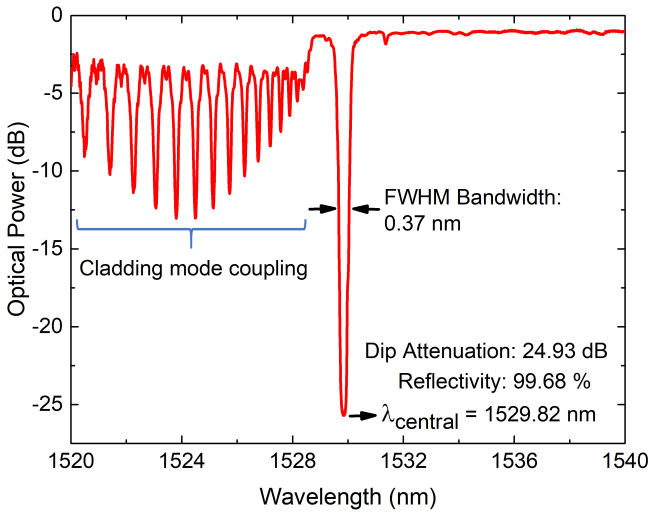


Figure 4.2. *Transmission spectra of femto-inscribed FBG with a wavelength of 1529.82 nm ($\Lambda = 528.60$ nm), 10.0 mm long, a pulse energy of 60.0 nJ, and with a duty cycle of 50 %.*

The fiber Bragg grating exhibits a main resonant peak centered at the Bragg wavelength, which corresponds to the maximum reflectivity of 99.68 %. Beyond the Bragg wavelength, a series of resonances can be observed on the shorter-wavelength side of this central wavelength due to the coupling to forward-propagating cladding modes. The asymmetric refractive index profile, as shown in the optical micrograph in the upper right corner of Figure 4.1, or the offset position of the FBG from the center axis, leads to the coupling to forward propagating cladding modes. Another characteristic of the fs-laser FBGs is their considerable polarization dependence. Birefringence leads to the splitting of the Bragg resonance into two distinct ones. The different Bragg resonance peak associated with each polarization axis can be used as a means to determine the degree of birefringence using the following equation [100, 132, 133]:

$$\Delta n_B = \frac{\lambda_{B_2} - \lambda_{B_1}}{2\Lambda}. \tag{4.9}$$

The FBGs fabricated by the fs-laser direct written system with different duty cycles were explored to assess how changes in duty cycle affect the grating's spectral response, i.e., wavelength,

optical power, and birefringence. The experimental setup shown in Figure 4.3 is used to measure the transmitted spectrum of fiber Bragg gratings with polarization control. In this configuration, the optical source is connected to an in-line polarizer (Thorlabs ILP1550PM-APC) to allow linearly polarized light to pass while blocking the orthogonal polarization from the unpolarized light source. Additionally, the output polarization of the polarization-maintaining fiber is adjusted using a manual paddle fiber polarization controller (Thorlabs FPC564), which modifies the polarization state of the light incident on the FBG.

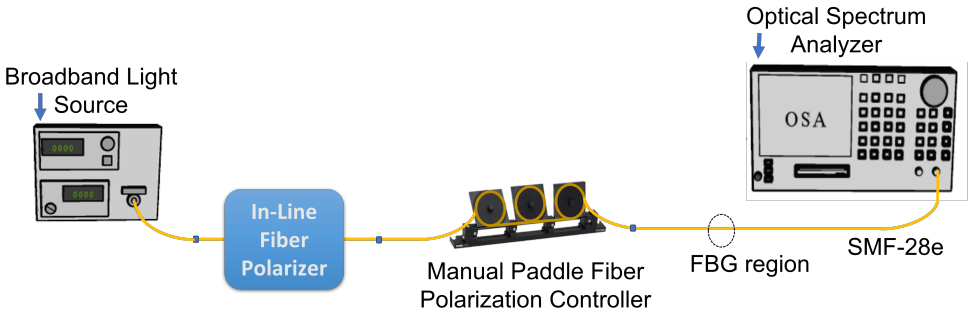


Figure 4.3. *Experimental setup for measurement of the FBGs transmitted spectrum with polarization control.*

Figure 4.4 shown the transmission spectra of the FBGs fabricated with a period of 535.44 nm, 5.0 mm long, a pulse energy of 60.0 nJ, 50 µm/s scan velocity, a fiber tension of 1 N, and with duty cycle of 30 %, 50 %, 70 %, and 90 % (measured with polarization control).

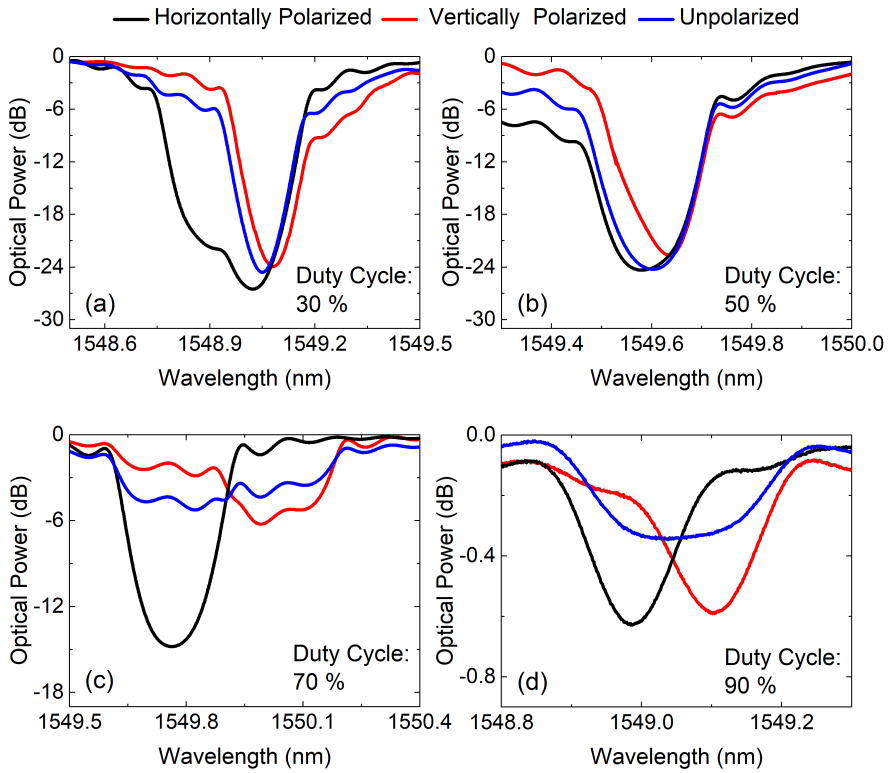


Figure 4.4. *Transmission spectra of the FBGs fabricated with a period of 535.44 nm, 5.0 mm long, a pulse energy of 60.0 nJ, and with a duty cycle of (a) 30 %, (b) 50 %, (c) 70 %, and (d) 90 % (measured with polarization control).*

By analysing the transmission spectrum of the FBGs to different duty cycles, it is observed that for all duty cycles, the Bragg wavelength and amplitude of the FBG, when subjected to polarization control, changes compared to the unpolarized state. When the FBGs are analyzed under horizontal polarization, the Bragg wavelength shifts to shorter wavelengths and the amplitude increases. Conversely, for vertical polarization, the Bragg wavelength shifts to longer wavelengths and a decrease is observed in the amplitude, except an increase in amplitude noted at 70% and 90% duty cycles.

Figure 4.5 illustrates the relationship between key spectral characteristics of fiber Bragg gratings and the duty cycle used during their fabrication with parallel polarization.

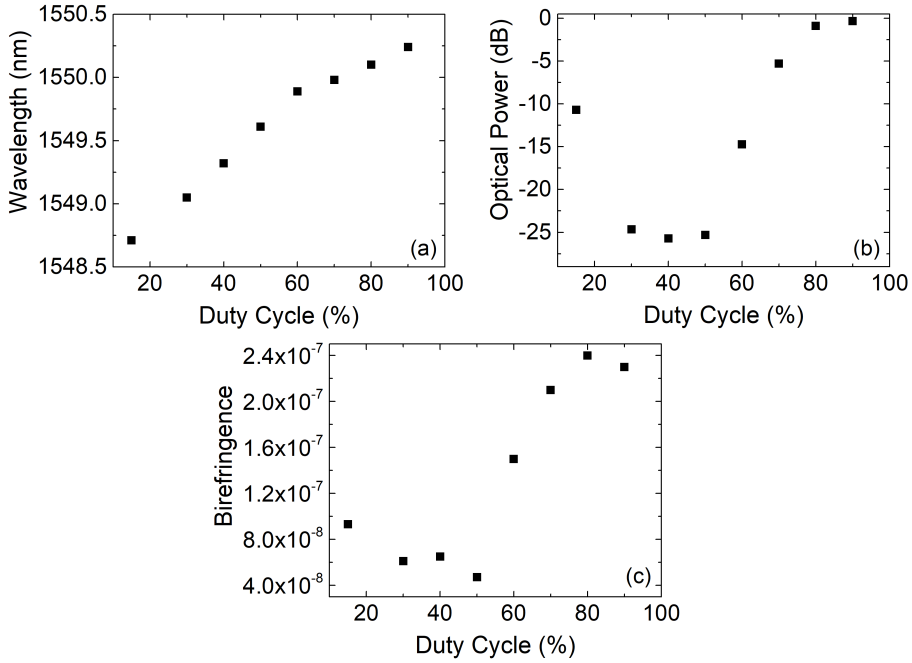


Figure 4.5. *Bragg wavelength (a), Grating strength (b), and Birefringence (c) as a function of duty cycle, for FBGs fabricated with parallel polarization.*

Figure 4.5 (a) shows a shift in the grating's Bragg wavelength as the duty cycle increases. This wavelength change occurs because the increase in the duty cycle leads to an increase in the effective refractive index. Therefore, higher duty cycles result in increased cumulative energy deposition, which increases the effective refractive index. The optical power of the FBG, measured in transmission, showed a dependency on the duty cycle, as illustrated in Figure 4.5 (b). The grating coupling coefficient, which determines the strength of the interaction between the forward and backward propagating modes within the fiber, is influenced by the duty cycle used during fabrication. At duty cycles of 30 %, 40% and 50%, the coupling coefficient increases due to a controlled refractive index modulation, resulting in strong grating strength. However, at duty cycles of 60% and above, the optical power decreases due to the a reduction in the grating coupling coefficient, causing degradation in the transmission spectra. A grating's strength is determined by the modulation depth of the refractive index change. A higher duty cycle generally results in an increase in energy deposition, which enhances the grating's strength to an optimal point prior to

undesirable thermal effects.

The birefringence of the FBGs, influenced by the asymmetrical refractive index profile induced by the fs-laser, was evaluated as a function of the duty cycle, as shown in Figure 4.5 (c). At duty cycles of 30%, 40%, and 50%, birefringence decreases to the order of 10^{-8}, indicating a more uniform refractive index profile across the grating. However, as the duty cycle increases, birefringence rises to the order of 10^{-7}, suggesting that higher duty cycles induce more significant asymmetrical changes in the refractive index. These changes affect the polarization characteristics of the gratings by introducing a stronger birefringence.

Adjusting the duty cycle in fs-laser direct-written FBGs enables precise control over key grating properties, including Bragg wavelength, grating strength, and birefringence. This duty-cycle-dependent birefringence shift is particularly relevant for polarization-sensitive applications, as it directly impacts the stability of the polarization state within the grating. This control level allows for optimising FBGs tailored to applications in sensing and other fields.

Various periodic structures were fabricated with different parameters, which are summarized in Table 4.1, alongside the measured spectral properties: full width at half maximum (FWHM), dip attenuation and reflectivity.

Table 4.1. *Parameters of the femto-inscribed FBGs in an SMF-28e.*

FBG order	Fabrication Parameters				FBG Specifications		
	Pulse Energy (nJ)	Write Velocity (µm/s)	Central Wavelength (nm)	FBG Length (mm)	FWHM Bandwidth (nm)	Dip Attenuation (dB)	Reflectivity (%)
First-order	60.0	50.0	1540.96	4.0	0.21	−14.67	96.6
			1550.82		0.22	−13.22	95.2
			1560.63		0.21	−13.65	95.7
First-order	63.0	50.0	1547.32	10.0	0.17	−24.04	99.6
Second-order			1555.97		0.49	−3.90	59.3
			1556.26				

Three FBGs with the same length (4 mm) and different periods: 531.983, 535.437 and 538.891 nm, respectively were serially inscribed in the core of an SMF-28e fiber and axially separated by 1 mm. The transmission and reflection spectra are shown in Figure 4.6 (a). In this case, all the FBGs inscribed are first-order FBGs, but with the fs-laser system developed in this PhD work it is also possible to inscribed second-order FBGs by just changing the period of the grating. Therefore, first- and second-order Bragg gratings (the latter with a fundamental reflection near to 3110 nm) around 1550 nm with the periods of 533.710 nm and 1074.328 nm, respectively, were fabricated sequentially in the same optical fiber.

The second order FBG also presents higher birefringence, which splits the Bragg resonance into two polarization modes, as observed in Figure 4.6 (b). The two Bragg resonances are separated by 290 pm, yielding a birefringence value equal to 1.35×10^{-4}. Analyzing the top view

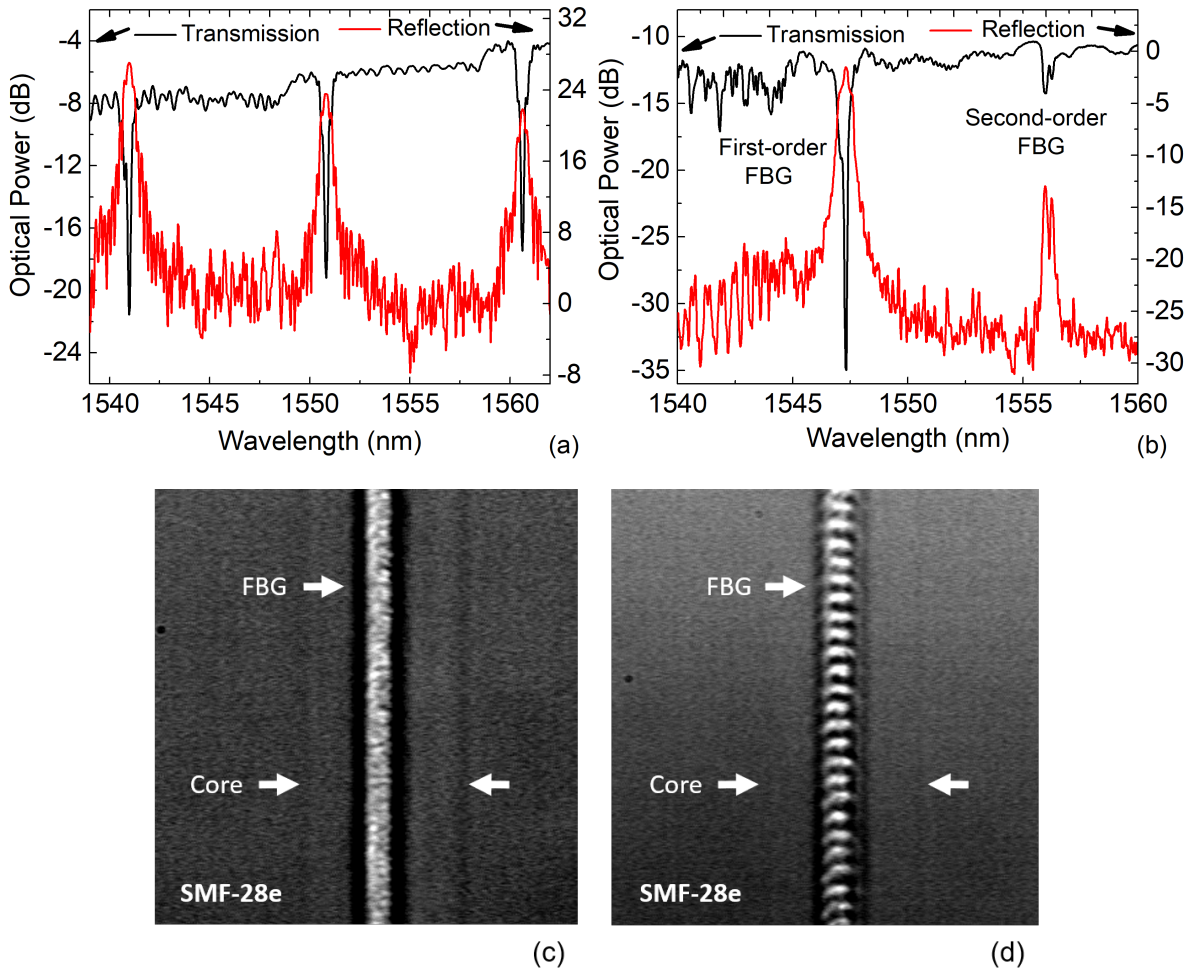


Figure 4.6. *Fs-laser FBGs inscribed in an SMF-28e: (a) spectra of three first-order FBGs in sequence and (b) sequence of two FBGs fabricated with different orders; (c) and (d) Top-view section images of the first and second order FBGs, respectively.*

section images presented in Figure 4.6 (c) and (d), it is possible to verify the increase of the grating period in the refractive index modification for the case of this grating.

In order to fabricate gratings in a coreless fiber, a section of this fiber was spliced between two single-mode fibers forming an SMF-coreless-SMF structure. This structure is considered a multimode interference-based optical device [134]. The fs-laser direct written system was configured to inscribe the device (composed by waveguide-FBG-waveguide) sequentially. Therefore, a configuration on/modulation/on was defined to switch the laser beam according to the desired structure (i.e., waveguide: laser on and FBG: laser modulation on). A pulse energy of 130 nJ was selected to write the waveguides and FBG in the coreless fiber, as found previously to offer a relatively low propagation loss of ≈ 0.5 dB/cm at 1560 nm [49, 132]. As a result, a coreless FBG was fabricated with the single-mode fibers connected by a waveguide with a grating in the middle, as shown in Figure 4.7.

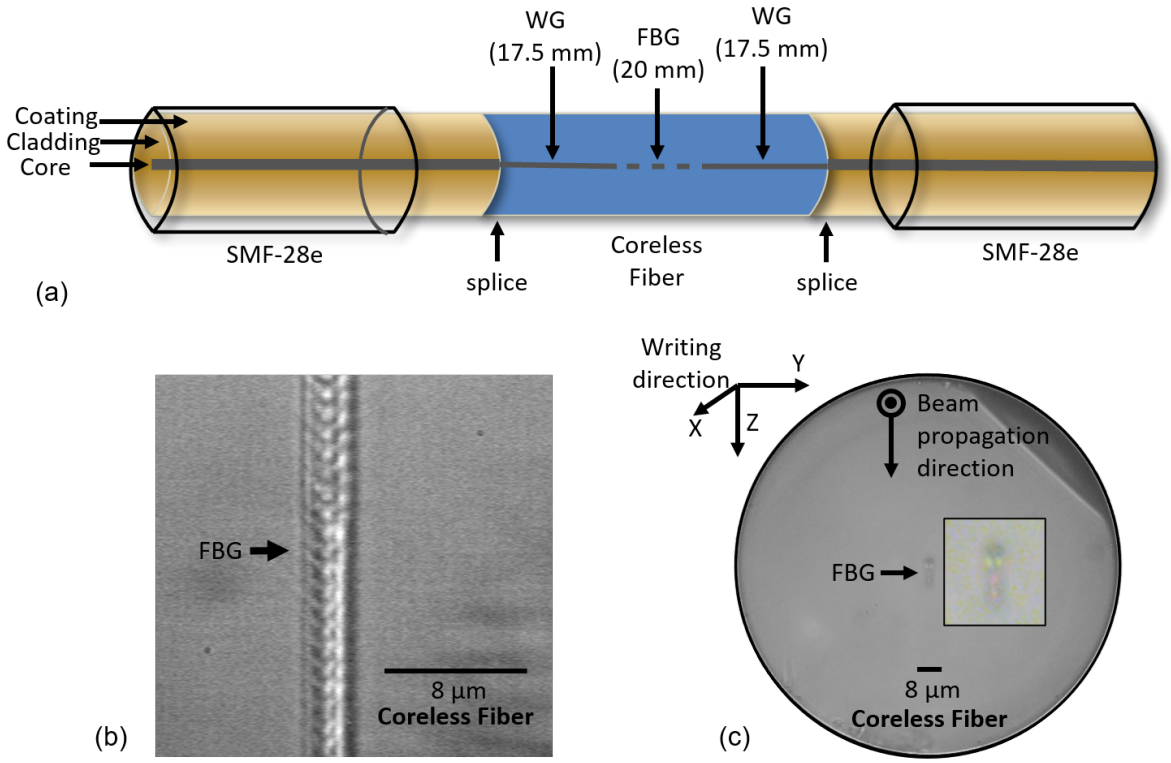


Figure 4.7. *Fs-laser structures inscribed in a coreless fiber: (a) Schematic diagram, (b) Top-view section image, and (c) End-view optical micrograph.*

Figure 4.8 shows the spectra of three different FBGs, one written with a UV-laser on a SMF-28e fiber, and two with the fs-laser direct writing system in a SMF-28e fiber and in a coreless fiber.

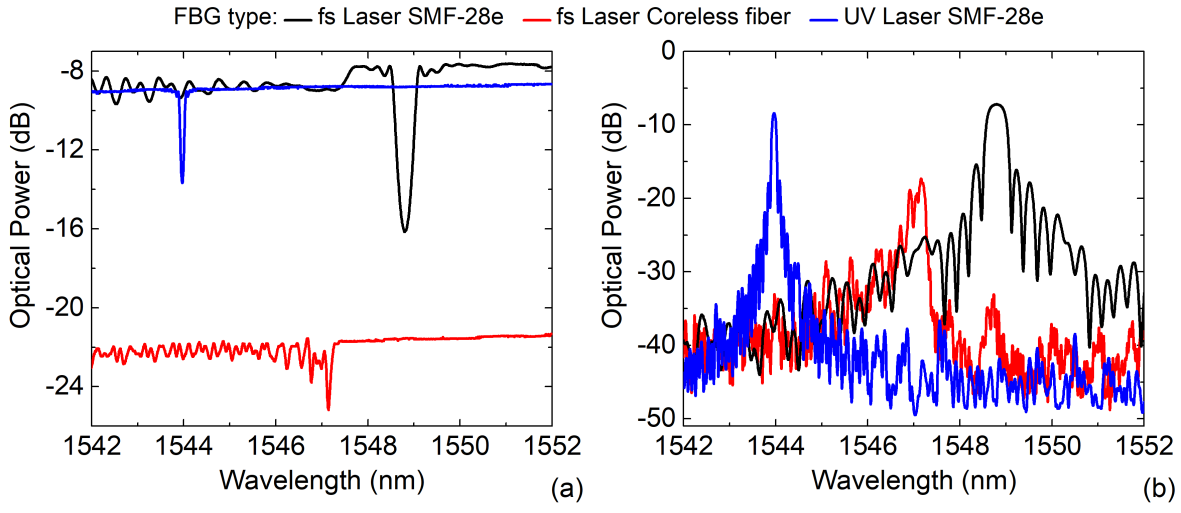


Figure 4.8. *Femtosecond and UV laser FBGs: (a) Transmission spectra, and (b) Reflection spectra.*

The femto-inscribed structure in the coreless fiber presents higher attenuation and the Bragg resonance is not well defined, when compared with the previously mentioned gratings. The fabrication parameters and the measured optical properties, such as the FWHM, dip attenuation and

reflectivity are presented in Table 4.2.

Table 4.2. *Parameters of the FBGs for temperature characterization.*

FBG Type	Fabrication Parameters				FBG Specifications		
	Pulse Energy (nJ)	Write Velocity (µm/s)	Central Wavelength (nm)	FBG Length (mm)	FWHM Bandwidth (nm)	Dip Attenuation (dB)	Reflectivity (%)
fs Laser SMF-28e	60.0	200.0	1548.80	30.0	0.36	−8.42	85.6
fs Laser Coreless fiber	130.0	200.0	1547.14	20.0	0.10	−3.64	56.7
UV Laser SMF-28e	N.A.	N.A.	1543.97	N.A.	0.09	−4.75	66.5

The annealing process leads to modifications in the FBGs spectral response, affecting the dip attenuation and reducing grating reflectivity. The UV-inscribed FBG, the femto-inscribed FBGs in an SMF-28e fiber and in a coreless fiber were placed in an oven and annealed at constant temperatures ranging from 100 to 1000 °C with steps of 100 °C, for a period of 1 h. The grating spectra were monitored every 10 minutes by a continuous swept laser scanning interrogator specifically designed to interrogate FBGs (FS22 HBM BraggMETER) with a resolution of < 0.5 pm (Figure 4.9). After the annealing period, the oven was switched off and the gratings were allowed to cool down to room temperature and the grating spectra was recorded.

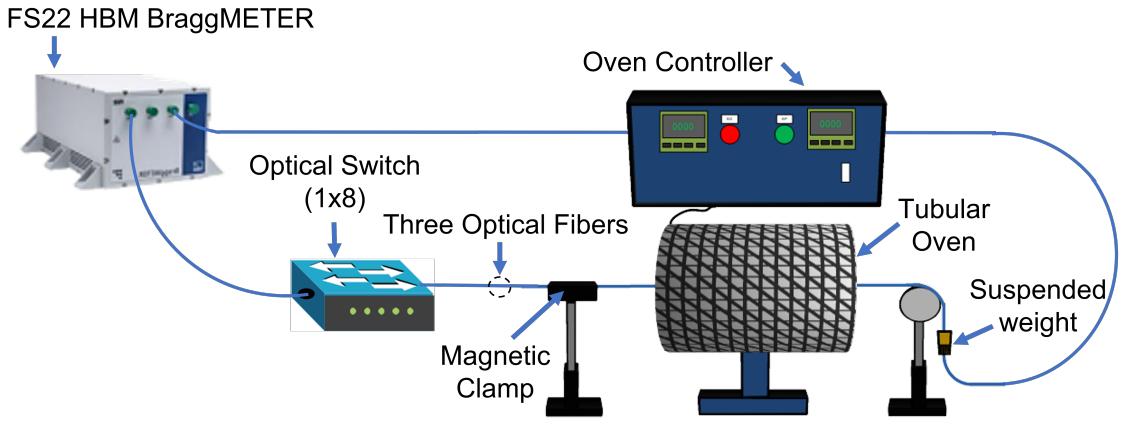


Figure 4.9. *Schematic illustration of the FBGs temperature characterization setup.*

Figure 4.10 represents the evolution of the Bragg wavelength of the above referred gratings as a function of the thermal treatment.

While the UV-inscribed FBG were erased as the temperature exceeded 800 °C, the femto-inscribed FBG were more stable by thermal exposure at temperatures of 800 °C. Above this temperature, a portion of the refractive index change of the femto-inscribed FBG was annealed

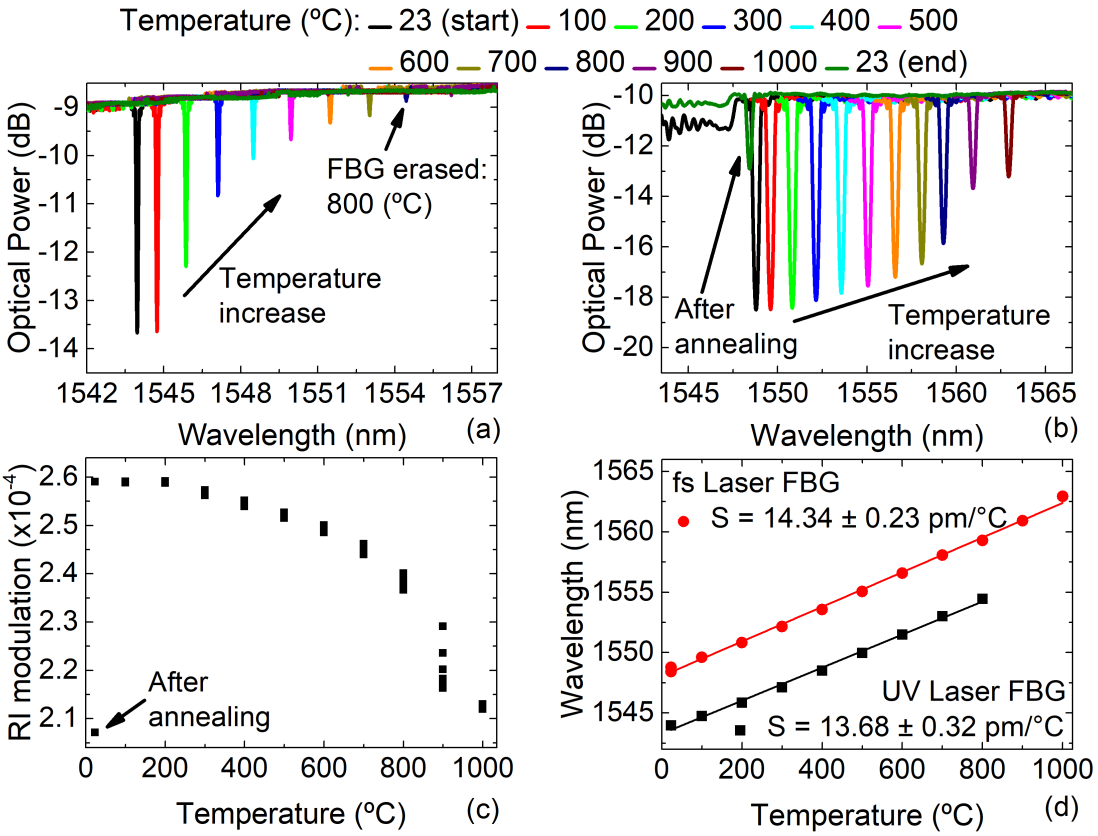


Figure 4.10. *Spectral evolution of: (a) the UV-inscribed FBG and (b) femto-inscribed FBG during the annealing cycle; (c) decrease of refractive index modulation as a function of temperature and (d) Bragg wavelength as a function of temperature.*

out, resulting in a degradation of grating reflectivity as presented in Figure 4.10 (c). A 0.36 nm down shift of the Bragg resonance was detected at the end of the annealing. Table 4.3 summarize the spectral properties of the fs-laser written FBG before and after the annealing process.

Table 4.3. *Specification of the fs-laser written FBG before and after the annealing process.*

FBG Type	Annealing Process	FBG Specifications			
		Central Wavelength (nm)	FWHM Bandwidth (nm)	Dip Attenuation (dB)	Reflectivity (%)
fs Laser SMF-28e	Before	1548.80	0.36	−8.42	85.6
	After	1548.44	0.28	−2.98	49.6

Temperature sensitivities of 14.34 and 13.65 pm/°C were achieved for the fs-laser written FBG and for the UV-laser written FBG, respectively. Comparing the achieved results with those of similar FBGs reported in the literature [7, 14, 17, 22, 55, 125] indicates that our FBGs are of Type I. The classification of Fiber Bragg Gratings (FBGs) as Type I is substantiated by the fact that the refractive index changes induced during their fabrication occur through mechanisms such as the

formation of color centers, densification, and the establishment of induced stress fields, which take place below the damage threshold of the fiber material. This type of gratings can resist up to 1000 °C with some erasure, [14, 22, 55].

Figure 4.11 represents the shift of the femto-inscribed FBG in an coreless fiber spectra after one hour at constant temperatures. It can be seen from Figure 4.11 (a) that, unlike, SMF-28e femto-inscribed FBG which became thermally stable at temperatures of 400 °C, the FBG inscribed in a coreless fiber was almost erased as the temperature exceeded 400 °C. This could be a result of a different refractive index modification. When the FBG is inscribed in the core, the index is further increased compared to the index inscribed in the coreless fiber, resulting in a more thermally stable grating [125]. Figure 4.11 (b) shows the spectra of the structure before and after the annealing, where it can be seen that the grating is erased after annealing.

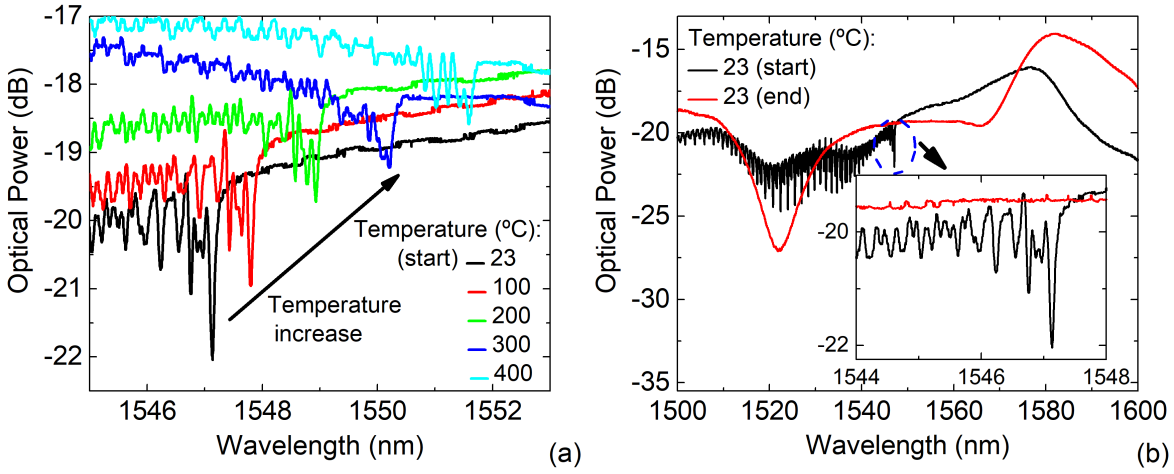


Figure 4.11. *Spectral evolution of femto-inscribed FBG Coreless fiber: (a) during the annealing cycle and (b) at room temperature.*

4.1.3 Fabrication and Sensitivity Analysis of First-Order Off-Axis FBGs

The fabrication of first-order off-axis FBGs in an SMF-28e fiber through fs-laser direct writing is presented in this section. The work starts with the analysis and measurement of the RI modifications induced by the fs-laser of five waveguides written with different pulse energies and scanning velocities, as represented in Table 4.4.

Table 4.4. *Writing parameters of the fs-laser WGs.*

Waveguides (WGs)	**1**	**2**	**3**	**4**	**5**
Pulse energy (nJ)	90	90	90	60	120
Writing Velocity (µm/s)	100	200	200	100	100

Figure 4.12 shows an optical microscope view of the cross-section of the waveguiding structures (a), and the respective refractive index profile (b), which was measured at 980 nm with an

IFA-100 (Interfiber Analysis) interferometric system [135].

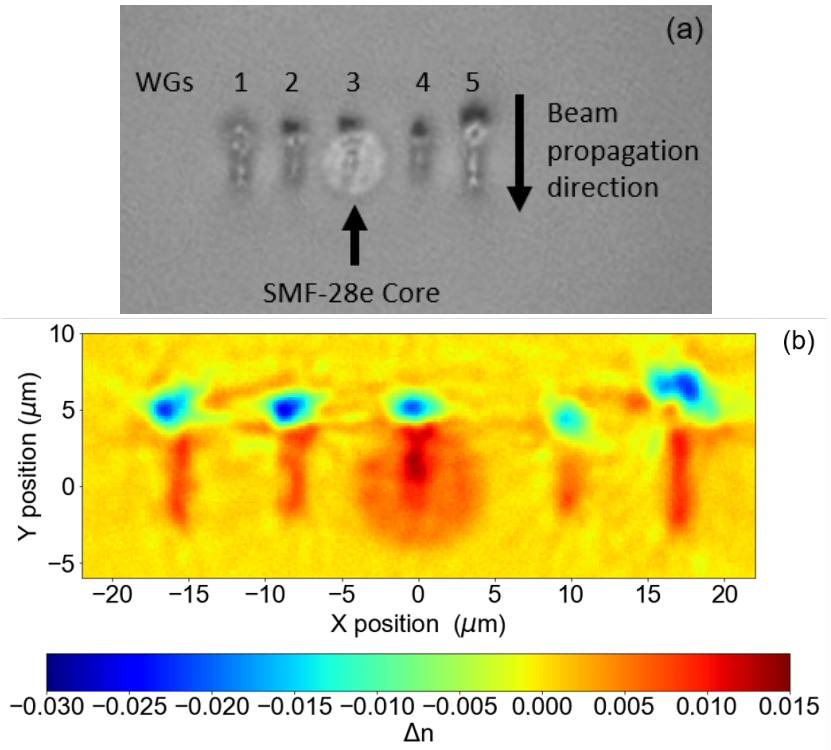


Figure 4.12. *Fs-laser written waveguides inside a SMF-28e fiber: (a) cross-section photograph and (b) refractive index profile.*

The RI modification has an asymmetric shape and is composed by a region of reduced refractive index (shown in blue) located above a region of increased refractive index (shown in red). The RI contrast was seen to increase with pulse energy ranging from 60 to 120 nJ, evolving from $\approx 0.5 \times 10^{-2}$ to $\approx 1.0 \times 10^{-2}$ and from $\approx 1.4 \times 10^{-2}$ to $\approx 2.2 \times 10^{-2}$ for the bottom and top regions, respectively. The contrast achieved inside the optical fiber core is similar to those seen in the cladding. The height of the modification structures grows with the increase of the pulse energy, extending from 7.5 µm to 11 µm, with the width maintaining at $\approx$ 3 µm. Velocities ranging from 100 µm/s to 200 µm/s show no significant impact on the RI modification. The IFA measurements of the refractive index profile suggest that the induced modifications are in the Type-I regime [136].

The fabrication of the FBGs with an offset from the core center was performed by taking advantage of the high precision optical fiber positioning system (Y stage), as proven by Figure 4.12. The grating period and length were defined to be 535.44 nm and 15 mm, respectively. The optimal writing conditions for an FBG centered in the core were found to be 60 nJ of pulse energy, 50 µm/s of scanning velocity, fiber tension of 1 N, and a writing beam polarization aligned with the scanning direction of the fiber. The fabrication of the off-axis FBGs with 1 N of tension introduces birefringence possibly via elastooptic index change [100], as shown in Figure 4.13. The fundamental Bragg resonance splits into two peaks, when relaxing the optical fiber. The optimum pulse energy to write off-axis FBGs was found to be 140 nJ, instead of 60 nJ, as it will improve the $LP_{1,1}$ mode reflectivity.

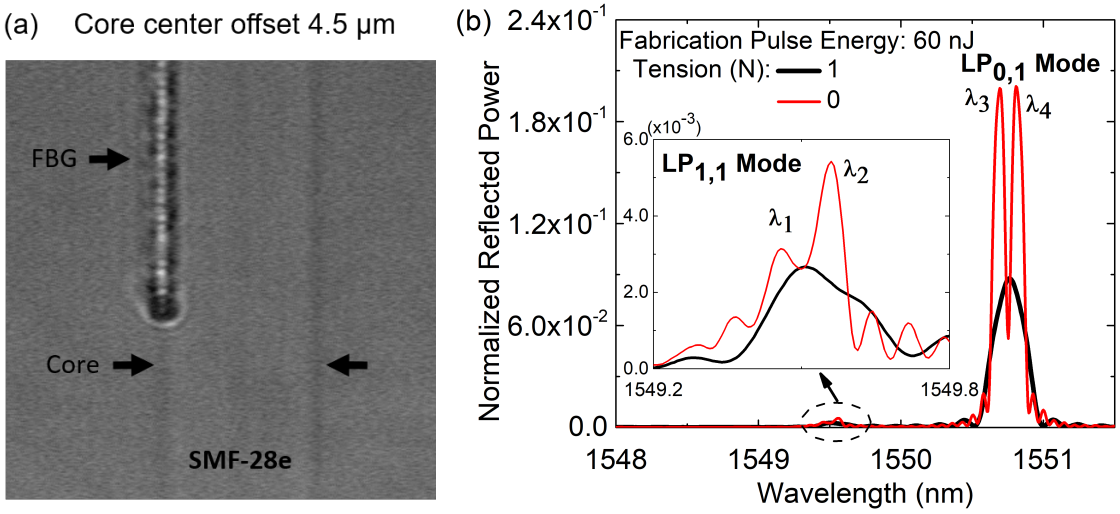


Figure 4.13. *Off-axis FBG with 4.5 µm offset from the core center fabricated with 60 nJ pulse energy (a) top-view image, and (b) reflection spectra under fabrication tension of 1 N and without tension.*

Figure 4.14 shows off-axis FBGs fabricated with 3.0, 4.5 and 6.0 µm offsets from the core center. The fabrication method gives full control of where the grating is inscribed: it can be inscribed totally inside the core, over the core-cladding boundary or totally outside of the fiber core. Analyzing the top and end view section images presented in Figure 4.14, it is possible to verify the increase of the core effective size in the section where the FBG is inscribed.

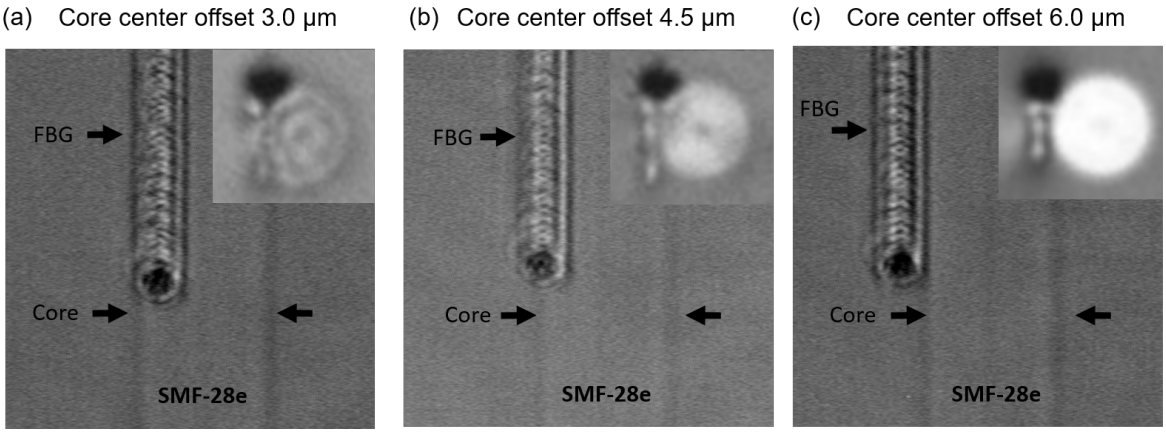


Figure 4.14. *Top-view images of the off-axis FBGs with an offset of: (a) 3.0 µm, (b) 4.5 µm, and (c) 6.0 µm written with 140 nJ pulse energy (insets: end-view optical micrographs). All gratings were written at 50 µm/s.*

Figure 4.15 (a) and (b) shows the transmitted and reflected spectra of the off-axis FBGs written with an offset distance of 3.0, 4.5 and 6.0 µm. The spectrum was measured in either reflection or transmission with an optical spectrum analyzer (OSA, model Yokogawa AQ6370D) with a resolution of 0.02 nm. Also, all spectra are represented in a normalized linear scale. The transmission spectra presented in Figure 4.15 (a) consists of two bands: two Bragg resonance with two peaks, due to birefringence induced by the asymmetric structure, and several cladding mode resonances on the short wavelength side. From the reflection spectra shown in Figure 4.15 (b), the existence of the Bragg resonance associated with the $LP_{1,1}$ mode is clearly visible. Figure 4.15 (c)

shows the wavelength shift of the off-axis FBGs as a function of the offset distance. Here, it is observed that, with the increase of the offset distance, the Bragg wavelength of the $LP_{1,1}$ mode increases, while the Bragg wavelength of the $LP_{0,1}$ mode stays constant. This can be explained by the increase of the core's size with the offset distance (visible in Figure 4.14), which leads to an increase of the V-number and, consequently, of the effective refractive index. For an offset higher than 7.5 µm, the off-axis FBG is undetected in both the transmission and reflection spectra. This means that the overlap between the core mode and the induced modification is negligible, resulting in a very weak Bragg reflected signal.

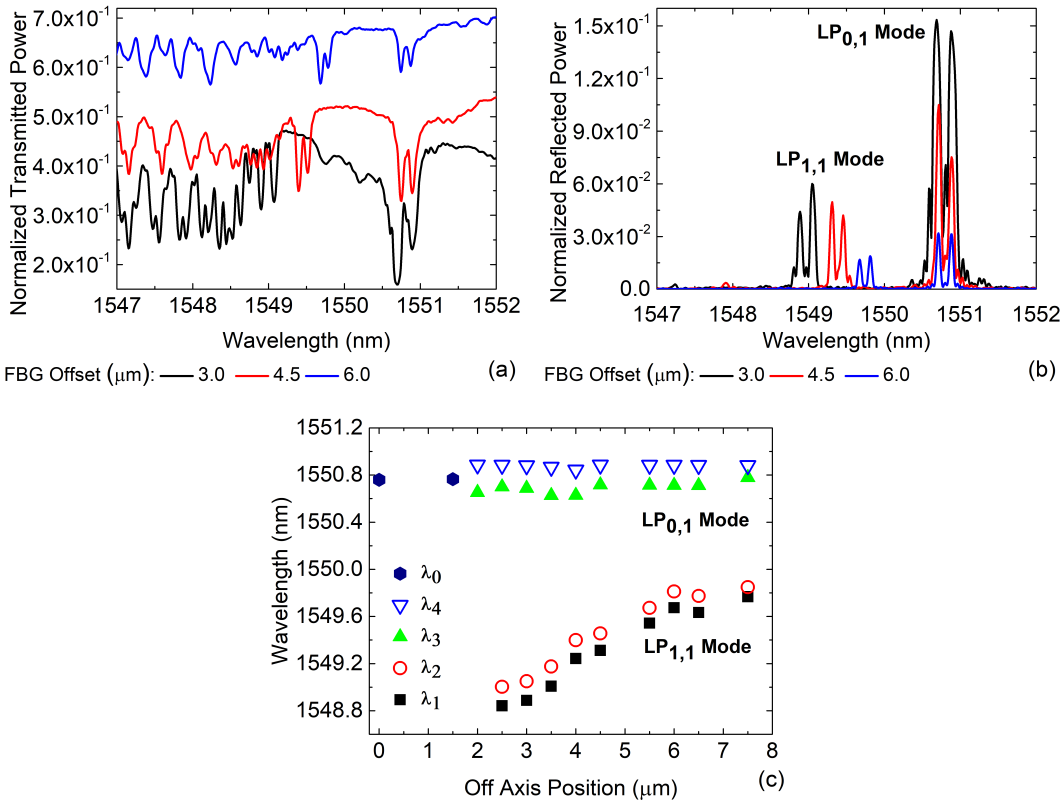


Figure 4.15. *Off-axis FBGs: (a) transmission and (b) reflection spectra, and (c) wavelength shift as a function of the grating inscription position from core center.*

To understand the effect of the off-axis FBGs inscribed in the SMF-28e fiber, lets consider the V-number that determines the number of modes supported by a fiber, the cutoff condition of the various modes and the respective propagation constants. This parameter is given by [127]:

$$V = \frac{2\pi a}{\lambda}\sqrt{n_{core}^2 - n_{clad}^2}, \tag{4.10}$$

where a is the core radius, and n_{core} and n_{clad} are the refractive indices of the core and cladding, respectively. When the V-number is lower than 2.405 only one mode ($LP_{0,1}$) can propagate along the fiber at a particular wavelength λ. In the wavelength region of interest ($\approx$ 1550 nm), the SMF-28e fiber only supports the fundamental mode $LP_{0,1}$, i.e. the fiber is single mode [84]. As can be seen from Figure 4.12 and Figure 4.14, when inscribing the off-axis grating, the core size and its

refractive index increases, which results in an increase of the V-number. If we take typical values (core index of $1.4440+0.0060$, cladding index of 1.4440, and core radius of the written section of 5.6 µm, for a grating inscription offset of 6.0 µm) we can estimate a V-number of ~ 2.991 at 1550.8 nm, which is above the cut-off condition. Therefore, the fiber section where the off-axis FBG is written turns into a two-mode fiber that can theoretically support the linearly polarized modes $LP_{0,1}$, and $LP_{1,1}$, explaining the additional resonance peak of the $LP_{1,1}$ mode observed in Figure 4.15 (b) [127]. With the increase of the offset from the core center, the grating reflectivity decreases, as can also be seen in Figure 4.15 (b). For the off-axis FBGs with greater offset, the reflectivity can be improved by increasing the grating length. The estimated V-number was utilized to calculate the effective refractive index, n_{eff} through the modal dispersion (i.e., bV) curves reported by Chen [127]. For a V-number of $\sim$2.991, the correspondent b value for the modes $LP_{0,1}$, and $LP_{1,1}$ are 0.65 and 0.15, respectively. Accordingly, the estimated n_{eff} for the modes, $LP_{0,1}$, and $LP_{1,1}$ are $\sim$1.4480 and $\sim$1.4450, respectively. The Bragg relation was also used to determine the effective refractive index of the guided modes, resulting in a n_{eff} for the modes $LP_{0,1}$, and $LP_{1,1}$ of $\sim$1.4470 and $\sim$1.4460, respectively. It was considered the Bragg wavelength of each mode for a grating period of 535.44 nm. Thus, the estimated n_{eff} values, calculated through the two methods, present a good approximation.

The theoretical calculation was supported through a 2D analysis of the optical fiber structure and the electromagnetic field modes using the mode analysis of the COMSOL Multiphysics®. A structure similar to the presented in the inset of Figure 4.14 (c) for the fabricated off-axis FBG with 6.0 µm from the core center was designed. The correspondent RI values were defined through the IFA measurements of the RI profile presented in Figure 4.12 (b). The electric field distribution, E_z, in 2D of the $LP_{0,1}$ and $LP_{1,1}$ modes in the core diameter at a wavelength of 1550 nm was evaluated, as shown in Figure 4.16 (a) and (b), respectively.

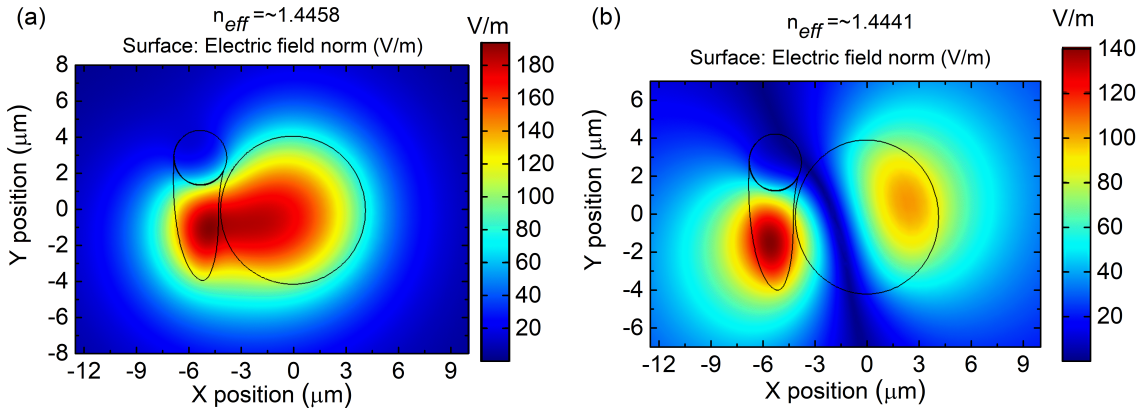


Figure 4.16. *Simulated mode profiles (electric field norm) at the core/structure for the: (a) $LP_{0,1}$ mode, and (b) $LP_{1,1}$ mode.*

The increase in core dimensions due to the off-axis FBG inscription affects the modal structure of the fiber, as observed in the intensity of the electric field for the $LP_{0,1}$ and $LP_{1,1}$ modes, yielding effective mode indices of $\sim$1.4458 and $\sim$1.4441, respectively. The results achieved with the COM-

SOL Multiphysics® allows confirmation of the multimode propagation in the fiber section where the off-axis FBG is inscribed.

Polarization Analysis

Similar to what was previously described, due to the asymmetric RI modification, the fs-laser writing process introduces birefringence to the SMF-28e, which causes the splitting of the Bragg resonance into two polarization modes [100]. Figure 4.17 shows the reflection spectra of the off-axis FBG with 4.5 µm offset measured with polarization control (a) and the birefringence (b) of the off-axis FBGs as a function of the offset distance. From Figure 4.17 (b), it is observed that for lateral shifts above 2.0 µm, the Bragg resonance (for each mode) presents two peaks due to laser-induced birefringence. Therefore, the lateral offset inscription process results in birefringent gratings, whereby the magnitude of birefringence mainly depends on the position of the modified zone in the core.

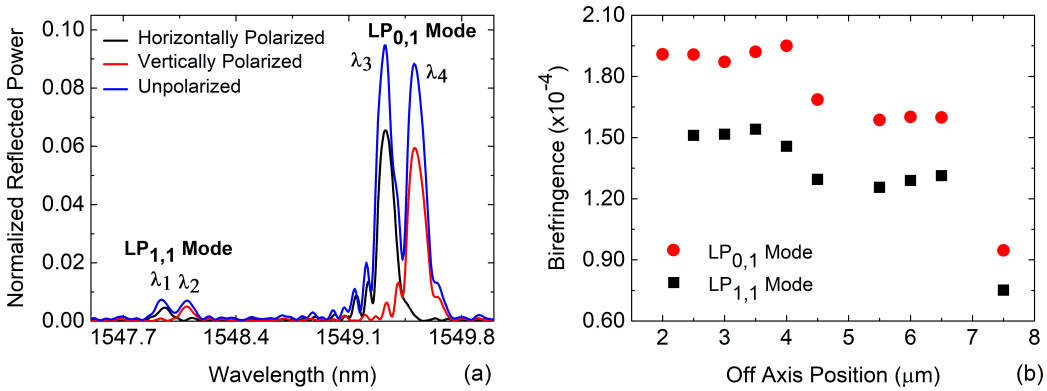


Figure 4.17. *(a) Reflection spectra of the off-axis FBG with 4.5 µm offset (measured with polarization control), and (b) birefringence, as a function of the grating inscription position from core center.*

For the FBG written with an offset of 4.5 µm, the two Bragg resonances of each mode ($LP_{1,1}$ and $LP_{0,1}$) are separated by 139 and 181 pm, yielding a birefringence value equal to 1.3×10^{-4} and 1.7×10^{-4}, respectively. It was also confirmed that vertically polarized incident light stimulates the Bragg resonances λ_4 and λ_2 from the $LP_{0,1}$ and $LP_{1,1}$ modes, respectively. In the case of horizontally polarized light, the corresponding Bragg resonances observed are λ_3 and λ_1 from the $LP_{0,1}$ and $LP_{1,1}$ modes, respectively. Figure 4.17 (b) also shows that, for the $LP_{0,1}$ mode, the birefringence decreases from a mean value of 1.91×10^{-4} to 1.62×10^{-4} (variation of 0.29×10^{-4}) when the offset distance increases from 2.5 to 6.5 µm. The birefringence of the $LP_{1,1}$ mode, decreases from 1.51×10^{-4} to 1.29×10^{-4} mean value (a difference of 0.22×10^{-4}). The birefringence value of the FBG with a 7.5 µm offset is lower compared with all the others. For an offset smaller than 2 µm the birefringence value is below the measurement resolution. These differences in the birefringence values may be due to small variations of the physical length and/or refractive index modulation of the grating, and also due to the differences in the strength of the gratings.

Off-axis FBGs for optical sensing

Three off-axis FBGs fabricated with 3.0, 4.5, and 6.0 µm offsets were characterized in strain, temperature, bending, and twist (only for the FBG written with an offset of 4.5 µm). The spectral characterization of the off-axis FBG was realized with customized setups composed of a broadband light source (model ASE2000) that was coupled to the fiber through an optical circulator. The spectrum was measured in reflection with an optical spectrum analyzer (OSA, model Yokogawa AQ6370D) with a resolution of 0.02 nm. The results of the spectral variations with each measurand and for each device are presented.

Strain measurements

Each off-axis FBG was subjected to mechanical strain, by gluing one extreme of the optical fiber to a micro-positioning stage, while the other side was glued to a fixed holder (Figure 4.18).

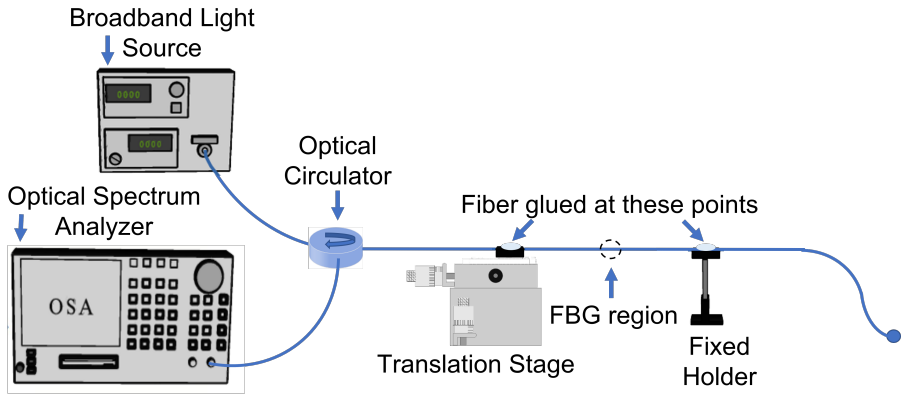


Figure 4.18. *Schematic illustration of the off-axis FBGs strain characterization setup.*

The off-axis FBGs were stretched from 0 to 522 µε in intervals of 43.5 µε; the measurements were made at room temperature (∼ 23 °C). Some of the acquired reflection spectra of the 6.0 µm offset FBG for different strain values are shown in Figure 4.19 (a).

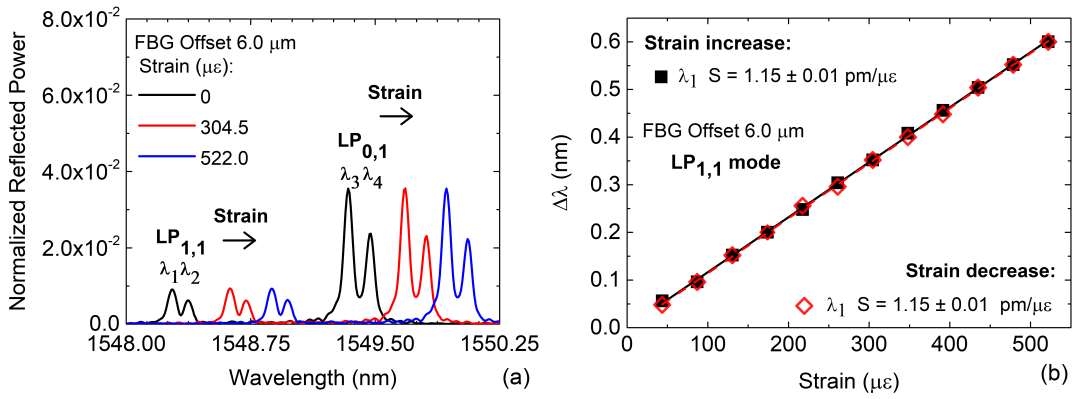


Figure 4.19. *Off-axis FBG with 6.0 µm offset from the core center: (a) reflection spectra for different strain values and (b) normalized wavelength shift (Δλ) as a function of strain.*

For this off-axis FBG, the reflection spectra evolution was recorded both during the fiber strain increase and decrease. When the fiber is stretched, there is a shift in the Bragg wavelength mainly due to changes in the grating period. For the FBG shown in Figure 4.19 (a), the two Bragg resonances of each mode ($LP_{1,1}$ and $LP_{0,1}$) red-shifted by $\sim$ 600 pm at the maximum applied strain, corresponding to a linear sensitivity of $\sim 1.15 \pm 0.01$ pm/$\mu\varepsilon$. In addition, no hysteresis was observed. Similar sensitivities of $\sim 1.13 \pm 0.01$ pm/$\mu\varepsilon$ and $\sim 1.16 \pm 0.01$ pm/$\mu\varepsilon$ were achieved for each Bragg resonance of the 3.0 and 4.5 µm off-axis FBGs, respectively. These results are summarized in Table 4.5. The strain sensitivities obtained, 1.15 pm/$\mu\varepsilon$ at 1550 nm, are similar to the sensitivities reported in the works [1, 92, 105, 137]. The amplitude of the two Bragg resonances of the two $LP_{1,1}$ and $LP_{0,1}$ modes are approximately constant with the applied strain for each off-axis FBG.

Table 4.5. *Strain sensitivities of the off-axis FBGs.*

FBGs offset	Strain Sensitivity (pm/µε)				Linearity (R^2)			
(µm)	λ_1	λ_2	λ_3	λ_4	λ_1	λ_2	λ_3	λ_4
3.0	1.13 ± 0.01	1.13 ± 0.01	1.13 ± 0.01	1.13 ± 0.01				
4.5	1.16 ± 0.01	1.16 ± 0.01	1.16 ± 0.01	1.16 ± 0.01		0.99		
6.0	1.15 ± 0.01	1.15 ± 0.01	1.16 ± 0.01	1.15 ± 0.01				

Temperature measurements

The temperature characterization of the three off-axis FBGs was performed simultaneously, with the corresponding optical fibers introduced in a tubular oven (Termolab) and subjected to a constant tension produced by a suspended weight of 5.8 g (Figure 4.20). The temperature of the oven was increased from 23 to 300 °C in steps of $\sim$ 20 °C, for a dwell time of 5 minutes each. The cooling process to room temperature was done following the same protocol.

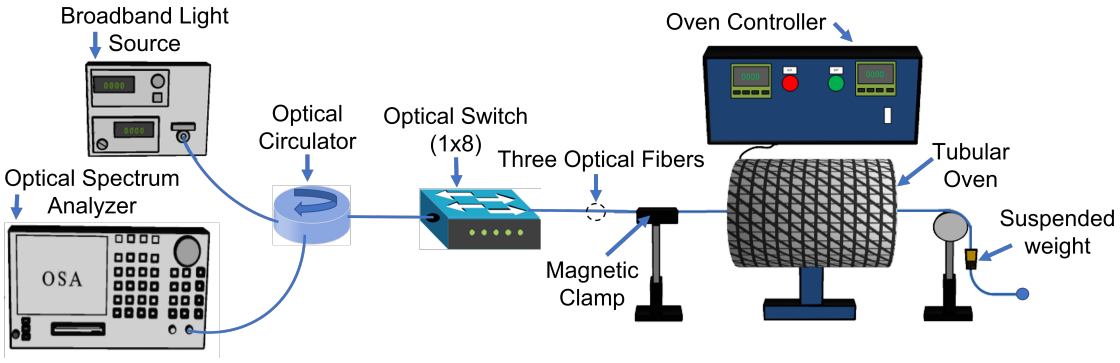


Figure 4.20. *Schematic illustration of the off-axis FBGs temperature characterization setup.*

During this procedure, the grating spectra were recorded and some of the acquired reflection spectra of the off-axis FBGs with 3.0 and 6.0 µm offset are shown in Figure 4.21.

The two Bragg resonances of each mode of the off-axis FBGs with 3.0 µm red-shifted by $\sim$ 3.3 nm when subjected to a maximum temperature of 300°C and showed a similar linear sensi-

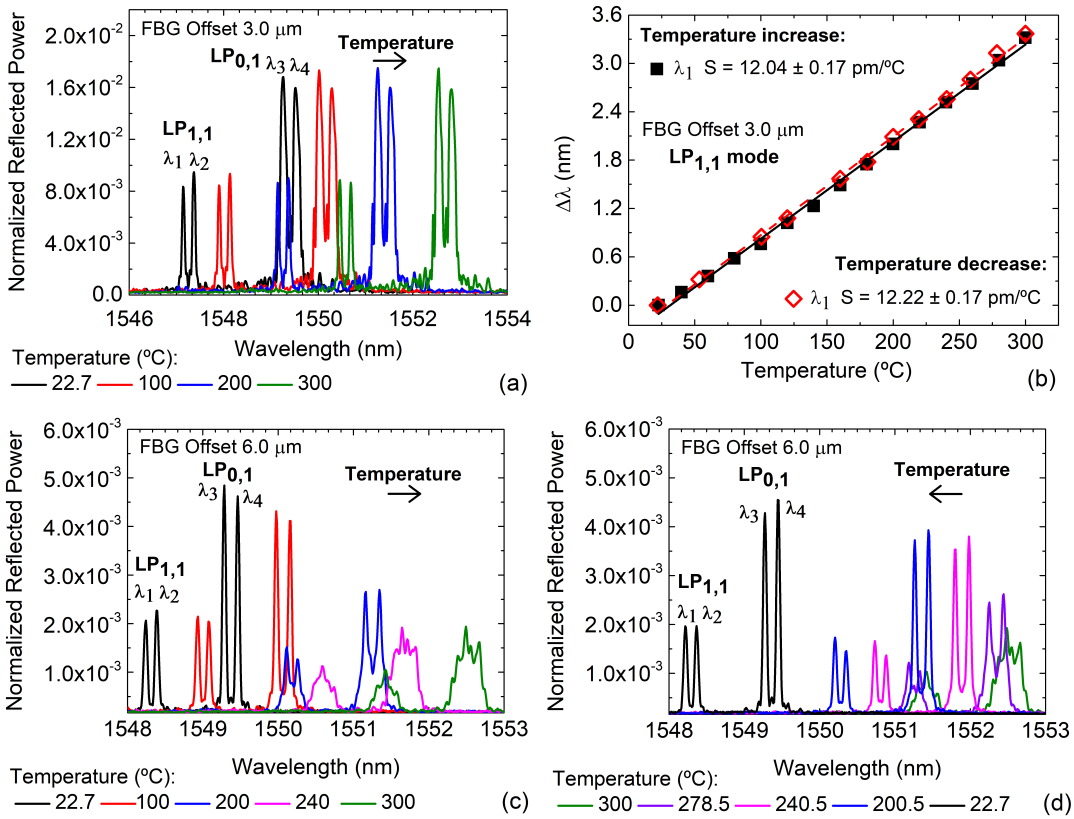


Figure 4.21. *Off-axis FBG with 3.0 μm offset: (a) reflection spectra for different temperature values and (b) normalized wavelength shift as a function of temperature; Off-axis FBG with 6.0 μm offset from the core center: (c) and (d) Reflection spectra for different temperature values.*

tivity of ~ 12 pm$/^{\circ}$C, as presented in Figure 4.21 (b). The measured sensitivities are presented in Table 4.6; in summary, a linear sensitivity of $\sim 12 \pm 0.2$ pm$/^{\circ}$C was achieved for each Bragg resonance of each off-axis FBGs characterized. In addition, negligible hysteresis was observed. For the sensitivity measurement of the off-axis FBG with a 6.0 μm offset, a temperature range from 22 to 200 $^{\circ}$C was utilized. These results are similar to the temperature sensitivity of the FBGs fabricated in the core of an SMF, which is 10.6 pm/$^{\circ}$C at 1550 nm wavelength, [1, 7, 92].

Table 4.6. *Temperature sensitivities of the off-axis FBGs.*

FBGs offset	Temperature Sensitivity (pm/ºC)				Linearity (R^2)			
(μm)	λ_1	λ_2	λ_3	λ_4	λ_1	λ_2	λ_3	λ_4
3.0	12.04 ± 0.17	12.07 ± 0.17	11.99 ± 0.16	12.01 ± 0.16	0.99			
4.5	11.94 ± 0.19	11.98 ± 0.19	11.94 ± 0.19	11.99 ± 0.19				
6.0	11.70 ± 0.16	11.65 ± 0.19	11.75 ± 0.18	11.76 ± 0.19	0.98			

For the off-axis FBG with 3.0 μm offset, the amplitude of the two Bragg resonances of both modes remain unchanged for the range of temperatures tested. For the off-axis FBG with a 4.5 μm offset, the results were very similar. Type I FBGs are known to be thermally stable up to ~ 300 $^{\circ}$C when written in the fiber core center, as previously demonstrated; off-axis FBG fabricated with a

3.0 µm offset have a similar behavior as can be seen in Figure 4.21 (a). However, in the case of the off-axis FBG with a 6.0 µm offset, the resonance amplitude decreases with the temperature increase, as can be seen in Figure 4.21 (c). When the temperature reaches 240 °C, the reflection spectra of the FBG become deformed, with the two Bragg resonances, for each mode, being poorly resolved. After heating up to 300 °C, the grating was cooled down to room temperature, and, during this process, the normalized reflected power increases as seen in Figure 4.21 (d) at a temperature of 278.5 °C. This effect can be associated with the position of the FBG relative to the fiber core and with the heating process. For the off-axis FBG with 6.0 µm offset, the majority of the RI modification was made in the cladding, leading to a smaller effective index modification when compared with the off-axis FBGs with 3.0 and 4.5 µm offsets. The decay in the grating reflectivity is thus associated with the decrease in the RI modulation of the grating. The reason for this is that the thermally activated defects induced by the fs-laser FBG cladding inscription are annealed out, leading to a different annealing process due to other defects being present. To make this off-axis FBG thermally stable it is necessary to perform a pre-annealing heat treatment at a higher temperature, typically at 700 ℃ [55]. However, with such treatment, the optical fiber becomes brittle, which for strain and curvature measurements is a disadvantage.

Curvature measurements

The characterization of the off-axis FBGs was also performed in curvature and curvature plane. The experimental characterization setup, presented in Figure 4.22, contains a custom-made aluminum step-like cylinder with diameters between 0.04 m and 0.025 m, corresponding to curvatures in the range of 50 to 80 m^{-1} respectively, which was mounted on a 3D translation stage.

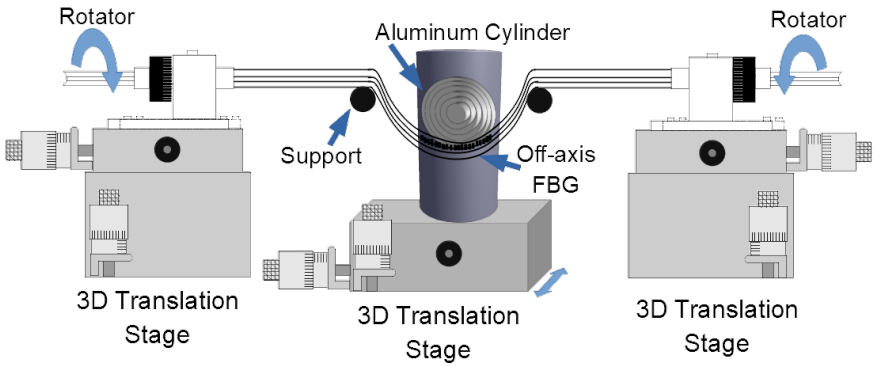


Figure 4.22. *Schematic illustration of the off-axis FBGs curvature characterization setup.*

The fiber was placed around the cylinder with the section where the grating was inscribed (0.015 m) in the middle of the curvature radius. The ends of the fiber were then mounted on two rotary fiber holders which were fixed on a pair of 3D translation stages and separated by 0.4 m, with the aluminum cylinder between the two stages. The applied curvature can be changed by displacing the cylinder to the desired radius, and by moving the translation stages in order to fit the fiber to the cylinder. Before adjusting the fiber for a specific curvature radius, the bending orientation can

be changed by simultaneously rotating and adding the two rotary fiber holders, so that the optical fiber can be rotated as a whole without inducing twist.

Some aspects were considered during the curvature measurements: the curvature plane is defined as the plane passing through the center of the fiber and orthogonal to the optical table, the twisting strain was avoided, and the room temperature ($\sim$ 23 °C) was kept constant. The difficulty of ensuring the same fiber orientation when the different fibers were moved from the fabrication to the characterization setup lead to the assignment of a random initial orientation angle θ. This angle remained constant during curvature measurements. The curvature was always performed on the same plane. During the curvature direction angle θ characterization, the fiber was rotated an angle θ around its axis and 50 m^{-1} curvature was applied again. Depending on the defined angle for the curvature measurement, the off-axis FBGs will be stretched (when located at the outer side of the bend) or compressed (when located at the inner side of the bend). Figure 4.23 shows the acquired reflection spectra of the $LP_{1,1}$ mode for the off-axis FBGs against the applied curvature at a random angle and the normalized reflected power variation (ΔNRP) as a function of curvature for the Bragg resonance (λ_1) of each off-axis FBG. When a curvature greater or equal to 50 m^{-1} was applied, the reflected optical power and the wavelength for both Bragg resonances of the $LP_{1,1}$ mode changed, as can be seen in Figure 4.23 (a), (b) and (c).

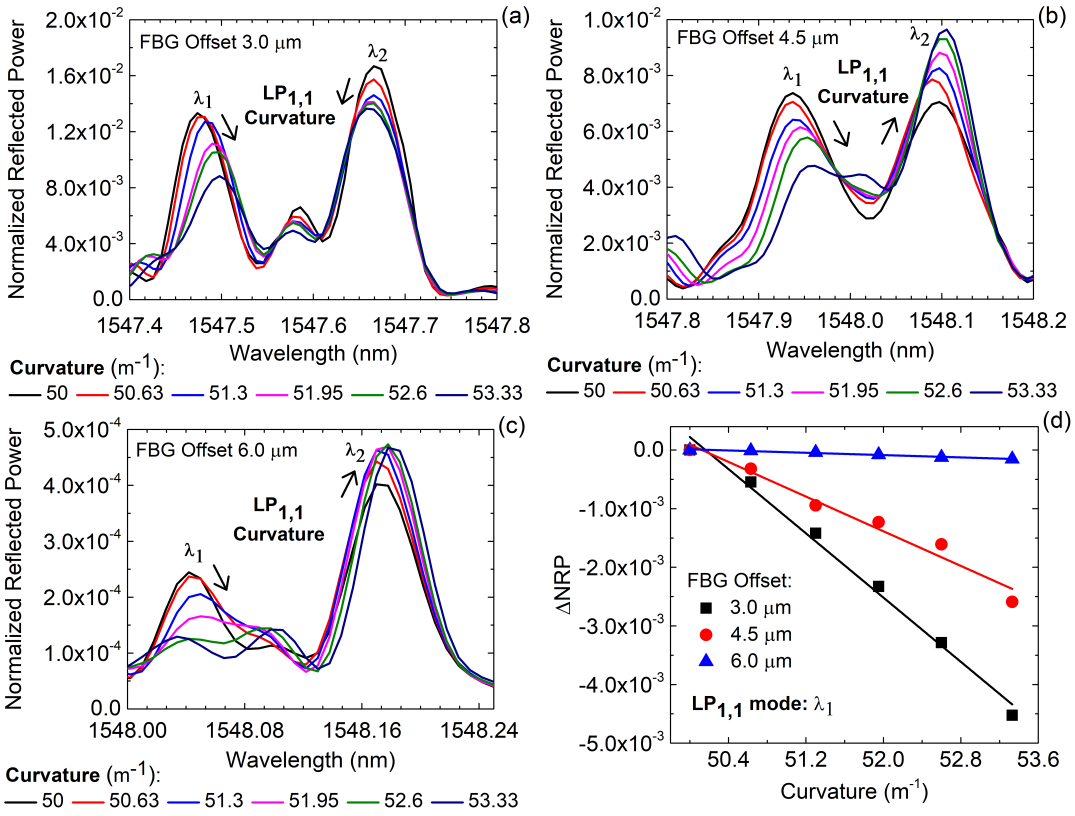


Figure 4.23. *Bragg resonances of the $LP_{1,1}$ mode (λ_1 and λ_2) of the three off-axis FBGs: reflection spectra under different curvature values at a random angle for the: (a) 3.0 μm, (b) 4.5 μm and (c) 6.0 μm off-axis FBGs, respectively. Also shown for the Bragg resonance of the $LP_{1,1}$ mode (λ_1) of each off-axis FBG: (d) the normalized reflected power variation as a function of curvature.*

The differences in the behavior of the intensity response of each resonance (see arrows in Figure 4.23 (a - c)) are associated to the angle θ used to measure the curvature. Figure 4.23 (d) shows the ΔNRP variation of the Bragg resonance (λ_1) of the $LP_{1,1}$ mode of each off-axis FBG. All devices display the same behavior for this resonance: the reflected power decreases as the curvature increases. Linear sensitivities of 1.37×10^{-3}, 7.39×10^{-4} and -4.94×10^{-5} $1/m^{-1}$ were obtained for the 3.0, 4.5 and 6.0 μm off-axis FBGs, respectively. Table 4.7 shows the curvature sensitivities of the off-axis FBGs tested. Maximum sensitivities were obtained for the off-axis FBGs with a 3.0 μm offset, due to the grating higher reflectivity. The sensitivity may be enhanced by a certain curvature direction angle θ, since the mode and off-axis FBG overlap is dependent on the curvature direction and the grating offset from the core center. Regarding the reflectivity of the off-axis FBGs, it was possible to conclude that the maximum grating reflectivity was achieved for the fabrication of the off-axis FBGs with a smaller offset from the core center. So, the sensitivities of the intensity to the curvature will be affected, decreasing for the off-axis FBGs with smaller reflectivity. The wavelength shifts of both Bragg resonances of the $LP_{1,1}$ mode (λ_1 and λ_2) shown in Table 4.7 present curvature sensitivities in the order of few pm/m^{-1} that are not enough to detect the curvature response. Regarding, the $LP_{0,1}$ mode, it was also observed that both Bragg wavelengths are stable during the curvature measurement. For this mode, the reflected optical power shows fluctuations, resulting in a nonlinear response to the applied curvature.

Table 4.7. *Wavelength and Optical Power sensitivities (curvature) of the off-axis FBGs.*

FBGs offset	**Wavelength Sensitivity (pm/m^{-1})**		**Linearity (R^2)**	
(μm)	λ_1	λ_2	λ_1	λ_2
3.0	7.48 ± 0.39	-1.81 ± 0.12	0.98	
4.5	7.53 ± 0.36	6.88 ± 0.22		
6.0	8.25 ± 0.52	1.69 ± 0.17	0.97	
FBGs offset	**Optical Power Sensitivity ($1/m^{-1}$)**		**Linearity (R^2)**	
(μm)	λ_1	λ_2	λ_1	λ_2
3.0	$(-1.37 \pm 0.07) \times 10^{-3}$	$(-0.90 \pm 0.14) \times 10^{-3}$	0.98	0.99
4.5	$(-0.74 \pm 0.06) \times 10^{-3}$	$(0.77 \pm 0.05) \times 10^{-3}$	0.97	0.98
6.0	$(-0.05 \pm 0.01) \times 10^{-3}$	$(0.02 \pm 0.01) \times 10^{-3}$	0.97	0.96

To characterize the curvature direction angle, a curvature of 50 m^{-1} was chosen for the three off-axis FBGs. The normalized wavelength shift and the ΔNRP of the two Bragg resonances of the $LP_{1,1}$ and $LP_{0,1}$ mode were recorded in steps of 30° and up to a complete rotation. Figure 4.24 presents, in polar coordinates, the results achieved for the off-axis FBGs.

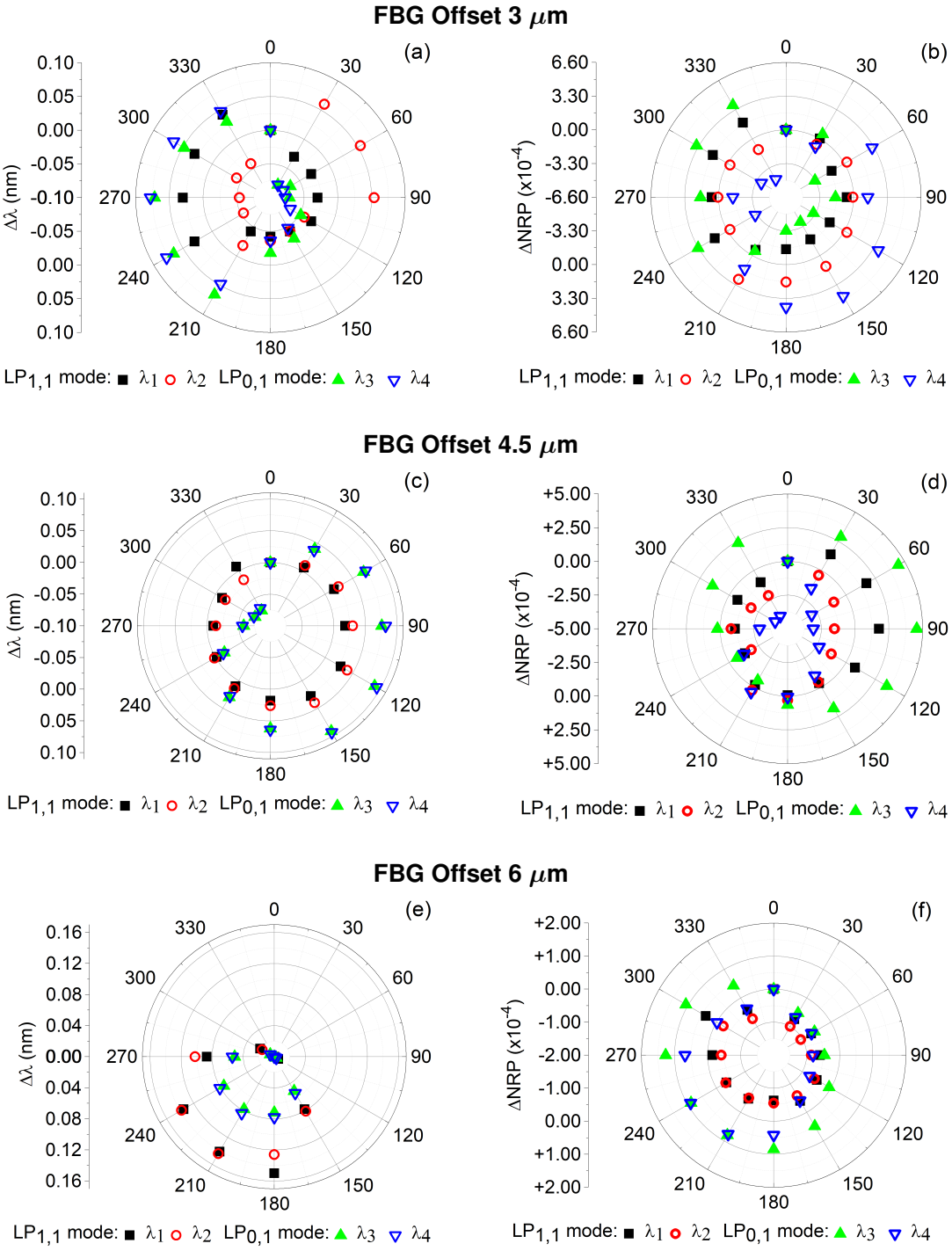


Figure 4.24. *Normalized wavelength shift and normalized reflected power variation as a function of the curvature direction angle (θ) under a curvature equal to 50 m^{-1} for the Off-axis FBGs with: 3.0 μm offset (a), (b), 4.5 μm offset (c), (d), and 6.0 μm offset (e), (f), respectively.*

In Figure 4.24 it is clearly seen that each resonance presents a strong orientation dependence in wavelength and intensity depending on the angle θ. Analyzing the data from the three off-axis FBGs, it is visible that the response, both in wavelength and in intensity, to the curvature direction response increases with the increase of the offset distance. The observed wavelength response to

the curvature's direction angle θ occurs because of the compression and stretching, resulting in a shift to shorter and longer wavelengths, respectively. From this information, it is possible to define the angle θ at which the off-axis FBGs were tested against the applied curvature. The angles used were 180°, 90° and 60° for the 3.0, 4.5 and 6.0 µm off-axis FBGs, respectively. Depending on the initially defined angle for the plane of curvature measurement, different curvature responses of each off-axis FBGs resonance are achieved, as observed in Figure 4.24. The maximum sensitivity was obtained when the angle θ is parallel to the grating axis, and the minimum with the angle θ orthogonal to the grating. This is due to the asymmetric refractive index distribution induced by the fs-laser inscription and by the position of the grating inscription.

To compare our curvature sensitivity results with the literature, the ΔNRP values were converted to a logarithmic scale and presented in Table 4.8. A curvature sensitivity of 1.93 dB/m^{-1} (curvature range: 0 to 2.5 m^{-1}), and - 0.21 dB/m^{-1} (curvature range: 25 to 80 m^{-1}) were reported for an off-axis ultraviolet written thin-core FBG [90], and for a two-mode FBG fabricated by UV laser [138], respectively. Compared to these curvature sensors based on the $LP_{1,1}$ mode resonance, the work presented here shows similar sensitivity for a curvature between 50 and 53.33 m^{-1}.

Table 4.8. *Curvature sensitivities of the off-axis FBGs.*

FBGs offset	**Optical Power Sensitivity (dB/m^{-1})**	
(µm)	λ_1	λ_2
3.0	-0.53 ± 0.04	-0.26 ± 0.04
4.5	-0.53 ± 0.06	0.40 ± 0.04
6.0	-1.33 ± 0.16	0.24 ± 0.02

In summary, the $LP_{0,1}$ mode is not sensitive to curvature, while the optical power of the $LP_{1,1}$ mode is affected by it. The analysis of both modes allows a self-referenced optical power measurement. It was observed that the temperature changes do not affect the reflected optical power of the $LP_{0,1}$ mode for the 3.0 and 4.5 µm off-axis FBGs. This enables simultaneous measurement of curvature and temperature through the measurements of the intensity variations of the $LP_{1,1}$ mode and wavelength shift of the $LP_{0,1}$ mode, respectively.

Twist measurements

For twisting measurements the fiber was clamped between a static and a rotary holder 4 cm apart, in a way that the 4.5 µm off-axis FBG was centered in the middle section, as shown in Figure 4.25. The rotatable holder was rotated up to 6.28 rad in steps of 0.52 rad, so the maximum twist step applied to the 4.5 µm off-axis FBG was 157.08 rad/m.

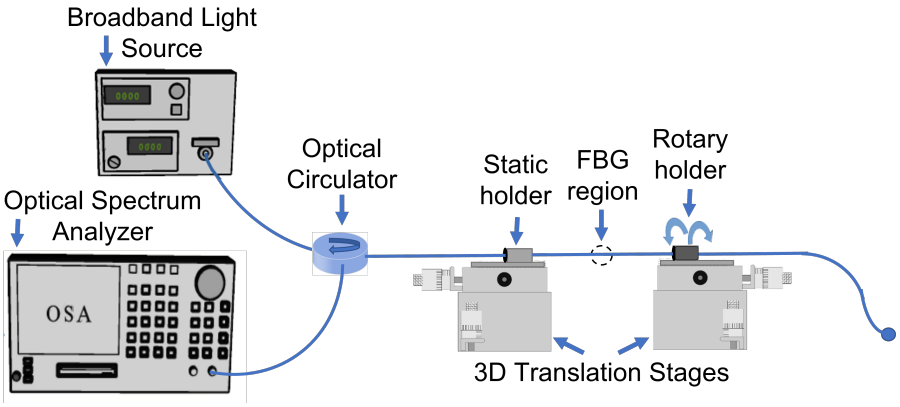


Figure 4.25. *Schematic illustration of the off-axis FBGs twist characterization setup.*

Twisting a fiber perturbs the refractive index profile non-uniformly over its cross-section, so the characterization of the off-axis FBG to twisting was performed, and the results presented in Figure 4.26.

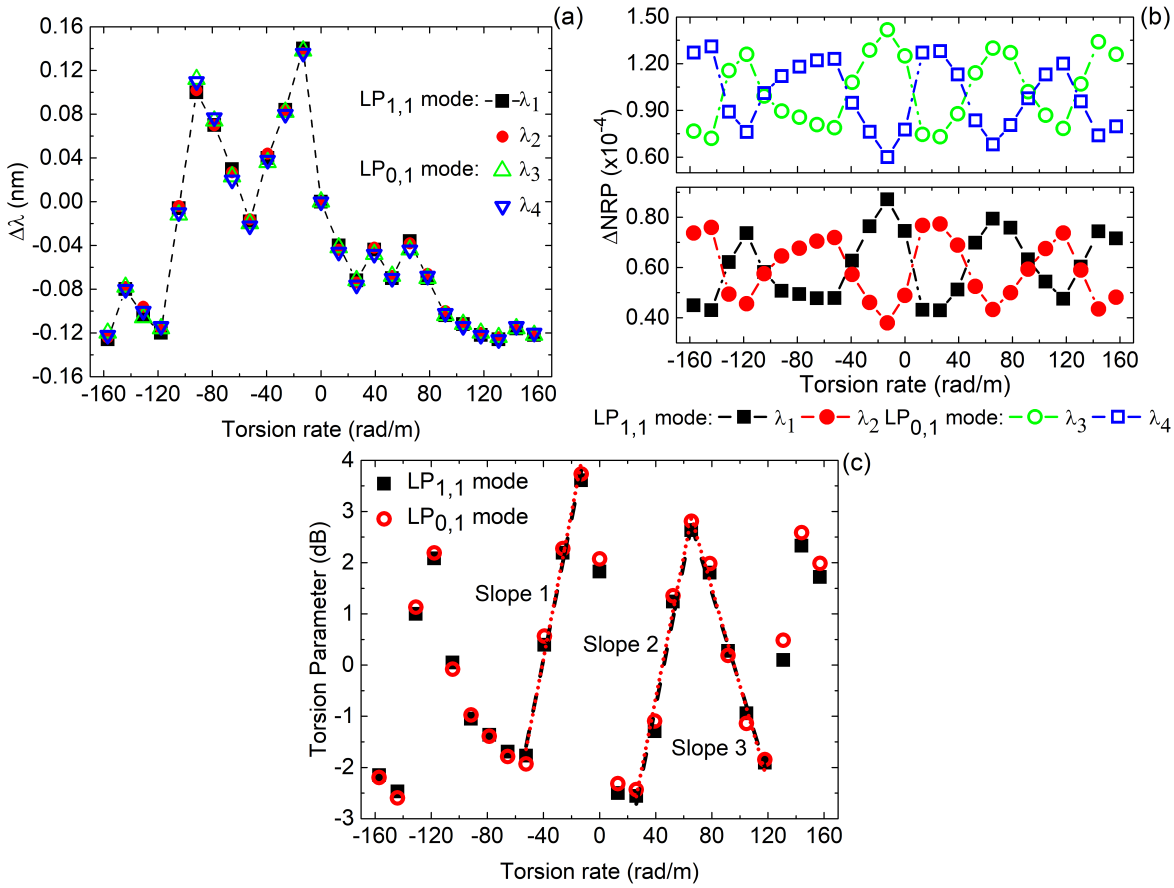


Figure 4.26. *4.5 µm off-axis FBG: (a) wavelength shift, (b) normalized reflected power, and (c) twist parameter as a function of the twist rate.*

As shown in Figure 4.26, when the fiber is twisted, the wavelength and the intensity response of both Bragg wavelengths of the $LP_{1,1}$ and $LP_{0,1}$ modes changed as the twist rate was applied. For the negative twist rate, anti-clockwise direction (from 0° to -360°), the wavelength shift is

superior compared to the wavelength shift of the clockwise direction. However, the wavelength shifts observed for each resonance of both modes are not enough to measure the twist response. Figure 4.26 (b) shows that the normalized reflected power intensities (I_{λ_1}, I_{λ_2}, I_{λ_3}, and I_{λ_4}) from the Bragg wavelengths of each mode ($LP_{0,1}$ and $LP_{1,1}$) interchange from one to another with the applied twist rate. Others already observed this effect for a high-birefringence (Hi-Bi) fiber torsion sensor demodulated using a Hi-Bi FBG [122]. The intensity variation was compensated by a twist parameter defined as $\eta = 10 \times \log\left(I_{\max(\lambda_1)}/I_{\min(\lambda_2)}\right)$ [122]. Hence, we utilize the twist parameter to simplify the relationship between the normalized reflected power and the twist rate and also compensate for the power intensity variations, as shown in Figure 4.26 (c). The intensity response of both modes is similar and presents three linear ranges defined as slope 1, 2, and 3 at specific twist rates. For the case of slope 1 and 2, both modes present a linear sensitivity of 0.140 $\pm$ 0.010 dB/(rad/m) in the range of -53.36 to -13.09 rad/m and 26.18 to 65.45 rad/m of the twist rate, respectively. The slope 3 presents a linear sensitivity of -0.092 $\pm$ 0.006 dB/(rad/m) in the range of 65.45 to 117.81 rad/m. The discrimination of the direction of twisting (clockwise and anticlockwise) is also possible due to the opposite intensity response.

The twist imposed on the 4.5 µm off-axis FBG fabricated in the SMF-28e fiber caused modulation of the intrinsic birefringence. This modulation is due to the geometric rotation of the principal axes of the optical fiber and the rotation due to circular birefringence related effects (i.e., optical activity) [109, 122].

4.1.4 Summary

In this work, a femtosecond laser direct writing system was developed to explore the fabrication of periodic structures, namely fiber Bragg gratings, in optical fibers. The optimum conditions to write FBGs in SMF-28e fiber were obtained with 63 nJ on-target pulse energy, 50 µm/s scan speed and a grating length of 10 mm. The possibility to write first- and second-order Bragg gratings in the same fiber with reflectivity's of 99.6 % and 59.3 %, respectively was demonstrated. The fabrication of several FBGs in the same fiber with different periods was demonstrated, which opens the possibility to explore different types of sensors configurations and multiplexing schemes. The fabrication of structures in a coreless fiber was also proven and, the written gratings were characterized in temperature. After annealing the FBGs at high temperature, only the femtoinscribed FBG in an SMF-28e fiber showed thermal stability at temperatures of 800 °C presenting a temperature sensitivity of 14.34 pm/°C. At these temperatures, UV-laser written gratings and gratings inscribed in a coreless fiber are erased. The fabricated FBGs can be classified as Type I.

The production of first order off-axis FBGs in an SMF-28e fiber through fs-laser direct writing was demonstrated. When inscribing the grating with a lateral shift above 2.5 µm from the core center, we found that it is possible to fabricate a multimode section in the SMF-28e that can support two separate fiber modes ($LP_{0,1}$ and $LP_{1,1}$), each split into two degenerate polarization modes. The grating structures break the cylindrical symmetry of the fiber and introduce a birefringence on the order of 10^{-4}, which also depends on the grating inscription offset.

The characterization of three off-axis FBGs fabricated with 3.0, 4.5 and 6.0 µm offsets from

the core center, was performed in strain, temperature, and curvature. The off-axis FBGs exhibit a similar strain and temperature sensitivities of $\sim$ 1.14 pm/$\mu\varepsilon$, and $\sim$12 pm/°C, respectively. For the off-axis FBG with a 6.0 µm offset, it was found that for temperatures above 240 °C the reflection spectra of the FBG becomes deformed and the two Bragg resonances poorly resolved, limiting the range of temperatures that can be sensed. The $LP_{0,1}$ and $LP_{1,1}$ modes of the three off-axis FBGs show a strong orientation dependence, in wavelength and intensity, to the plane of curvature. The Bragg resonance (λ_1) of the $LP_{1,1}$ mode present in the 3.0 µm offset off-axis FBG shows a maximum curvature sensitivity of 1.37×10^{-3} 1/m^{-1} at an angle of 180° for a curvature from 50 to 53.33 m^{-1}. The Bragg resonances of the $LP_{0,1}$ mode were not sensitive to curvature measurements. In addition, the different sensitivity of both modes to curvature enables the possibility to simultaneously measure curvature and temperature. The birefringent off-axis FBG potential for twist measurements was also explored and a maximum linear sensitivity of 0.140 $\pm$ 0.010 dB/(rad/m) in the range of -53.36 to -13.09 rad/m and 26.18 to 65.45 rad/m of the twist rate, respectively was achieved. Thus, the 4.5 µm off-axis FBG can simultaneously measure twist and discriminate the direction. The relatively low complexity and the robust nature of the fabricated device open the possibility to measure the twist and discriminate the twist direction in practical applications, such as structural health monitoring.

4.2 Long Period Fiber Gratings

Long period fiber gratings have been under continual investigation for at least forty years [139]. The fabrication of the LPFGs using several methods has been demonstrated, including exposure to UV and CO_2 laser radiation [140−143], electric arc discharge [144], laser ablation [145], mechanical pressure [130], and also fs-laser writing [146−150]. The LPFGs inscription in different optical fibers, such as photonic crystal fibers [151], standard single mode optical fibers [146, 150], polarization-maintaining fibers [152], and photosensitive fibers were also extensively explored [145, 152].

The resonance wavelength sensitivity of the LPFGs to external perturbations relies on the effective RI and the grating period, underlying to the propagation conditions in the core and cladding modes. The resonance wavelength shift caused by the changes in the effective RI and the grating period allows the measurement of several parameters such as temperature, strain, and refractive index [130, 139, 141, 146]. The LPFGs fabrication in standard SMF-28e fiber employing a fs-laser system and its sensing characteristics to temperature, external refractive index (RI), and strain have already been demonstrated [103, 148, 153, 154]. The fs-laser direct writing technique opens the possibility to inscribe LPFGs inside the core volume with high spatial resolution due to the underlying non-linear light-matter interaction [147−149, 153, 155]. This technique also shows excellent design flexibility and enables rapid change of the LPFGs parameters, such as length, bandwidth, or period, unlike other fabrication methods [103, 154−157].

Temperature sensitivity of 124 pm/°C at temperatures above 450 °C were reported [148]. However, the experiments reported so far only characterize the LPFGs thermal response and thermal

stability and do not describe in detail the spectral behavior of the LPFGs at room temperature after exposing it to a certain temperature. Temperature-induced spectral changes can be used to tune the resonant wavelength and to improve thermal sensitivity. A TAP LPFG having a single attenuation band in air, when immersed in a medium having a higher RI, or annealed at high temperature, causes the single resonance band to split into two resonances [130]. Consequently, the sensitivity of the TAP LPFGs is reduced. Therefore, properly addressing issues related to the TAP LPFG fabrication, such as the exact period to ensure the operation at the TAP at a specific external RI and, at the same time, to have thermal stability at higher temperatures, is fundamental to maintain the high sensitivity characteristics [131].

Regarding the LPFGs based RI sensors, they can be used efficiently in biological, chemical, and biochemical sensing applications [131, 158, 159]. The RI measure is defined by a shift of the resonance wavelength per RI Unit (RIU) [131]. The fabrication of LPFGs with high sensitivity to the surrounding refractive index (SRI) has been explored [158, 160, 161]. The methodologies reported include LPFGs operating in the turning around point (TAP) region, evanescent field enhancement by reducing cladding diameter, and mode transition (MT) [162] achieved by coating the LPFGs with a thin layer of material whose RI is higher than that of the cladding [158, 160, 161]. The high RI thin film coatings promote the transition between cladding guided modes in overlay guided modes inducing a re-distribution of the cladding modes, enhancing the evanescent wave interaction with the surrounding medium [158, 160, 161]. In addition, a combination of these methods by selecting a period very close to the TAP and making the fine tuning to operate precisely in the TAP by reducing the cladding diameter or by coating with a thin layer of material could further improve the SRI sensitivity of the LPFGs sensors [158, 160, 161].

The fabrication of LPFGs operating at the TAP without the use of post-fabrication techniques (i.e., chemical etching to fine tune the LPFGs operation around TAP) has proven to be a challenge, corroborated by the few manuscripts reported so far [140, 141, 150, 158, 163]. In addition, the fabrication of LPFGs operating at the TAP of asymmetric cladding modes for SRI sensing has not been discussed in detail; nevertheless, to our knowledge, fabrication of LPFGs allowing the coupling to asymmetric cladding mode was demonstrated in [144, 164, 165]. The SRI sensitivity of the LPFGs sensors could be further improved, selecting a high RI thin film, such as titanium dioxide (TiO_2). TiO_2 is non-toxic and biocompatible, exhibits low optical absorption, it is mechanically resistant, and supports high temperature and large electrical fields [158, 166]. Several optical fiber sensors based on LPFGs [158, 166−171], Mach-Zehnder Interferometers [172], and fiber Bragg gratings [173], mainly fabricated by exposure to UV and CO_2 laser radiation, and electric arc discharge, were coated with TiO_2 thin films given the advantages shown. However, the fs-laser fabrication of LPFGs operating in the TAP with coupling to asymmetric cladding modes and coated with TiO_2 thin films has not been systematically studied.

In this section, the entire fabrication process, including the thermal annealing to improve temperature stability, the coating with different TiO_2 film thicknesses, and characterization of LPFGs in SMF-28e fibers inscribed by fs-laser direct writing with periods set to couple to low and high order cladding modes, is described. The impact of the fabrication parameters in the

coupling behavior was studied in order to improve the coupling efficiency and obtain an LPFG in the TAP condition surrounded by air or water. The change in the effective RI of the asymmetric $LP_{1,12}$ cladding mode as a function of the TiO_2 film thicknesses was evaluated both with simulations and experimentally. The resonance wavelength sensitivity to the SRI of the uncoated and TiO_2 coated LPFGs operating at the TAP in air and water was evaluated and compared to the literature's reported works.

4.2.1 Theoretical Background

LPFGs consist of a periodic modulation of the RI along the longitudinal axis of an optical fiber with periods greater than 100 µm, that couple light from the core-guided mode (LP_{01} mode) into forward-propagating cladding-guided modes ($LP_{l,m}$, linearly polarized modes with azimuthal and radial integer indices l and m, respectively) at or near-resonant wavelengths [129, 141]. The interaction between the core mode and the co-propagating cladding modes, propagation constants $\beta_{0,1}$ and $\beta_{l,m}$ respectively, is described by [129, 141]:

$$\Delta\beta = \beta_{0,1} - \beta_{\mathrm{l,m}} - \frac{2\pi}{\Lambda}, \quad \beta_{0,1} = \left(\frac{2\pi}{\lambda}\right) n_{core}^{eff}, \quad \beta_{\mathrm{l,m}} = \left(\frac{2\pi}{\lambda}\right) n_{cl\ l,m}^{eff}, \tag{4.11}$$

where $\Delta\beta$ is the detuning factor, and Λ is the grating period. Under phase-matching condition ($\Delta\beta = 0$), the resonant wavelength λ_{res} of an LPFG is determined by [7, 129−131]:

$$\lambda_{res} = \left(n_{core}^{eff}(\lambda) - n_{cl\ l,m}^{eff}(\lambda)\right)\Lambda, \tag{4.12}$$

with n_{core}^{eff} as the effective RI of the propagating core mode at wavelength λ, and $n_{cl\ l,m}^{eff}$ the effective RI of the m^{th} cladding mode, respectively. Any change in the surrounding RI alters the effective indices of the cladding modes inducing changes in the wavelength position and the attenuation intensity at the resonance band. The grating's transmission spectrum is characterized by a set of transmission dips, corresponding to different cladding modes, at wavelengths that satisfy equation 4.12. Consequently, the expression to calculate the minimum transmission of the attenuation bands is defined as [7, 129, 130]:

$$T_m = 1 - \sin^2(k_m L)\ , \tag{4.13}$$

where k_m is the coupling coefficient for the m^{th} cladding mode and, L is the length of the LPFG. The coupling coefficient is determined by the overlap integral of the core and cladding mode and by the amplitude of the periodic modulation of the mode propagation constants. The wavelength dependence is determined by the material and waveguide dispersion [7, 129]. The material dispersion can be assumed to have the same overall effect on $n_{core}^{eff}(\lambda)$, as well as $n_{cl\ l,m}^{eff}(\lambda)$ [129]. Therefore, the waveguide dispersion is the dominant contributor to the grating spectra evolution and is given by [129]:

$$\gamma = \frac{\frac{d\lambda_{res}}{d\Lambda}}{\left(n_{core}^{eff}(\lambda) - n_{cl\ l,m}^{eff}(\lambda)\right)}. \tag{4.14}$$

The central wavelengths of the LPFGs attenuation bands are determined through the calculation of the RI of the core and cladding modes. The coupling strength and the form of the LPFGs spectrum are achieved with the calculation of the electric field mode profiles [129]. The effective RI of the propagating core mode of the fiber is generally determined using the weakly guided field approximation [141]. A sketch of the phase-matching curves of mode resonance wavelength against the grating period of an LPFG, is shown in Figure 4.27.

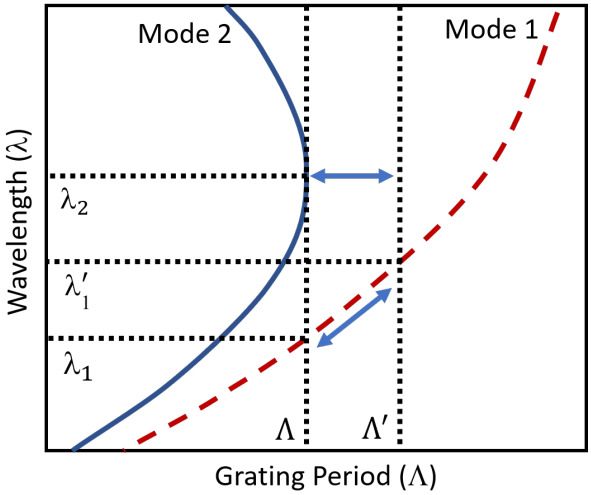


Figure 4.27. *Sketch of the phase-matching curves.*

The two phase-matching curves, shown in Figure 4.27, present different slope values according to the LPFG order mode. The slope value of the phase-matching curves increases from low- to high-order modes, and each one reaches a maximum at a specific TAP where $|d\lambda_{res}/d\Lambda| \rightarrow \infty$ [174]. The TAP occurs at longer wavelengths for lower order modes, shifting to shorter wavelengths as the mode order increases [131]. The fabrication of LPFGs with longer periods allows the coupling to lower-order modes (*e.g.*, mode 1), while shorter periods facilitate coupling to the higher-order cladding modes (*e.g.*, mode 2). According to the grating period, three types of LPFGs can be distinguished: positive linear-dispersion gratings for $\frac{d\lambda_{res}}{d\Lambda} > 0$ ($\lambda < \lambda_2$), negative linear-dispersion gratings for $\frac{d\lambda_{res}}{d\Lambda} < 0$ ($\lambda > \lambda_2$), and quadratic-dispersion grating for $\frac{d\lambda_{res}}{d\Lambda} = 0$ ($\lambda \approx \lambda_2$) [174].

A resonance with positive linear dispersion is presented by the coupling between the core mode and low-order cladding mode 1. A monotonic relationship between the LPFG period and the resonant wavelength occurs when the resonance shifts from λ_1 to $\lambda_1^{'}$ as the grating period shifts from Λ to Λ'. The turning point in the cladding mode 2 phase-matching curve occurs for a specific wavelength λ_2, and any deviation towards smaller periods gives origin to two attenuation bands. The high derivative around the turning point is what makes the TAP gratings very attractive.

The LPFGs fabricated with periods higher than Λ, results in different coupling condition, which makes the resonance vanish. The coupling between the core and cladding mode 2 changes its

character according to equation 4.11. Consequently, for increasing λ, it requires a substantial decrease of the cladding mode's index (especially pronounced for high-order cladding modes), resulting in a positive difference in the effective indices. However, a negative difference in the effective indices switches the sign of the slope of the phase-matching curve. The quadratic dispersion case occurs when the difference in the effective indices is exactly balanced. Therefore, at each turning point, $|d\lambda_{res}/d\Lambda| \to \infty$, which results in a waveguide dispersion value of $|\gamma| \to \infty$. As a result, for each cladding mode, the maximum sensitivity is determined by the turning point [174]. Thus, LPFGs with high sensitivity can be fabricated by selecting a cladding mode and a period that allows operating at, or very close to, a turning around point [131].

Temperature Sensitivity

The period of the LPFGs, the order of the cladding mode, and the composition of the optical fiber influence the sensitivity of LPFGs to temperature [130, 175]. As demonstrated in [130, 175], the LPFGs temperature sensitivity can be determined by differentiating equation 4.12:

$$\frac{\mathrm{d}\lambda^m}{\mathrm{d}T} = \frac{\mathrm{d}\lambda^m}{\mathrm{d}(\Delta n_{eff})} \left(\frac{\mathrm{d}n_{core}^{eff}}{\mathrm{d}T} - \frac{\mathrm{d}n_{cl\,l,m}^{eff}}{\mathrm{d}T} \right) + \Lambda \frac{\mathrm{d}\lambda^m}{\mathrm{d}\Lambda} \frac{1}{L} \frac{\mathrm{d}L}{\mathrm{d}T}, \tag{4.15}$$

where T is the temperature, Δn_{eff} is the difference in the effective indices ($\Delta n_{eff} = n_{core}^{eff} - n_{cl\,l,m}^{eff}$), and L is the length of the LPFG. The first term on the right-hand side (RHS) of equation 4.15 represents the material contribution. This is related to the change in the different RI of the core and cladding arising from the thermo-optic effect. The material contribution is strongly dependent upon the order of the cladding mode and also dependent on the fiber composition. The second term on the RHS of equation 4.15 represents the waveguide contribution, which results from changes in the LPFGs period and depends on the thermal expansion coefficient of the fiber [130, 175].

Refractive Index Sensitivity and Spectral Resolution

The wavelength sensitivity of an LPFG to the SRI is due to the dependence of the phase-matching condition upon the effective RI of the cladding modes. As a consequence, the effective refractive index of the cladding modes depends on the difference between the cladding and the surrounding medium [130, 139, 141]. Therefore, the central wavelengths of the LPFGs attenuation bands rely on the RI of the medium surrounding the cladding (provided that the cladding has the higher refractive index). Thus, the central wavelengths and the minimum transmission value of the LPFGs attenuation bands change as the SRI [130, 139, 141].

To assess the stability and repeatability of the sensing scheme, the spectral resolution was calculated based on the method reported in [176, 177]. The RI spectral resolution, R_{RI}, was estimated considering the following expression [176, 177]:

$$R_{RI} = \frac{\rho\sigma}{S_{RI}}, \tag{4.16}$$

where ρ represents the confidence interval (99.7%), σ is the standard deviation of a set of measurements performed in repeatable and reproducible conditions associated with a step variation of the external RI, and S_{RI} is the sensitivity linked with the SRI measurement range.

Strain Sensitivity

The LPFGs strain sensitivity can be determined by differentiating equation 4.12 [130, 175]:

$$\frac{\mathrm{d}\lambda^m}{\mathrm{d}\varepsilon} = \frac{\mathrm{d}\lambda^m}{\mathrm{d}(\Delta n_{eff})}\left(\frac{\mathrm{d}n_{core}^{eff}}{\mathrm{d}\varepsilon} - \frac{\mathrm{d}n_{cl\ l,m}^{eff}}{\mathrm{d}\varepsilon}\right) + \Lambda\frac{\mathrm{d}\lambda^m}{\mathrm{d}\Lambda} \tag{4.17}$$

where ε is the axial strain. The first term on the right-hand side (RHS) of equation 4.17 represents the material contribution. This is related to the change in the different RI of the core and cladding arising from the photo-elastic effect and the change in the optical fiber transverse dimensions arising from the Poisson's effect. Again, the material contribution is strongly dependent upon the order of the cladding mode and also dependent on the fiber composition. The second term on the RHS of equation 4.17 represents the waveguide contribution, which results from changes in the LPFGs period and depends on the slope $\mathrm{d}\lambda^m/\mathrm{d}\Lambda$ of the characteristic curve of the resonance band. Thus, attenuation bands with positive, negative, or zero sensitivity to strain will be achieved by selecting the proper grating period and fiber composition [130, 175].

4.2.2 Characterization of the LPFGs Writing process

Following the procedures described in the fabrication section 3.1.3, the LPFGs have been written on the SMF-28e Corning optical fiber. As mentioned earlier, the performance of the fs-laser system is subjected to environmental conditions (e,g., temperature, humidity, and dust). In addition, the LPFGs spectral proprieties are also influenced by environmental conditions. During the PhD work, the laser laboratory was improved to provide controlled environmental conditions. These changes affected the writing conditions and the spectral characteristics of the LPFGs. Therefore, in this section, the characterization of the LPFGs writing is divided into two groups. The first (second) group includes the characterization of the LPFGs fabricated before (after) the laboratory was equipped with an air conditioning system.

First Group [ambient temperature]

The LPFGs were written at a depth of 60 µm from the fiber surface, with a pulse energy of 130 nJ, a duty cycle of 50 %, 50 µm/s scan velocity, and with different lengths and modulation periods (depending on the desired resonance wavelength; as presented later in this section).

The spectral characteristics of the LPFGs were monitored in real-time during writing, by coupling a broadband light source to the fiber, while the other end was connected to an OSA (model ANDO AQ-6315B). The signal was measured without polarization control from 1000 to 1700 nm with a 10 nm resolution. All spectra were normalized to the transmitted spectrum of the light source, as already described in section 3.3.

The transmission spectra of two LPFGs fabricated with 372.5 and 390 µm RI modulation periods and 30.0 and 28.5 mm long, respectively, are shown in Figure 4.28.

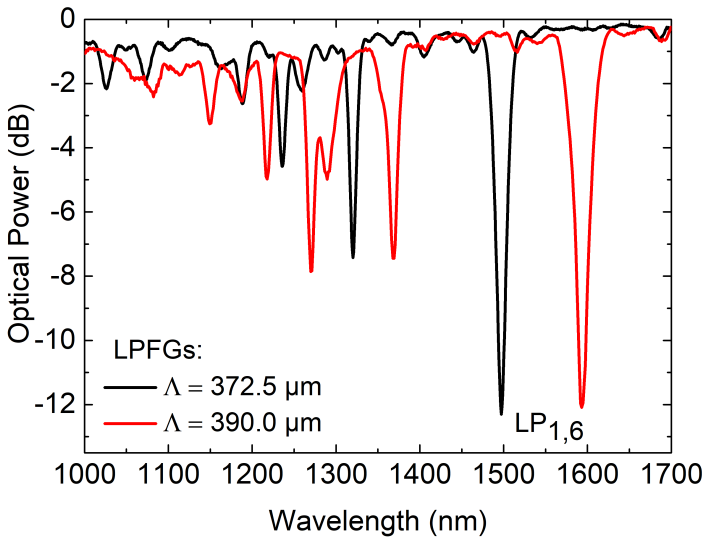


Figure 4.28. *Spectra of fs-laser direct written LPFGs in single mode fiber (SMF-28e).*

As can be seen in Figure 4.28, different periods with the same fabrication conditions lead to resonances at specific wavelengths; the position of the attenuation band shifts towards longer wavelengths ($\Delta\lambda$ = 95.64 nm) as the grating period increases from 372.5 to 390 µm. Furthermore, the grating strength increase, and the bandwidth decrease with the increase of the writing length.

To assess the symmetry of the perturbations in the fiber, the near fields of several cladding modes excited by the fs-laser gratings inscription were observed. One end of the fiber was coupled to a tunable laser (Santec TSL-210V), allowing wavelength scanning around the grating resonance, while the other end was cleaved just after the grating. The optical fiber is aligned using the Elliot Gold™ Professional Workstation (model: MDE881) with six independent axes of manipulation. The near field profile of the radiation emerging from the fiber was detected by an infrared camera (CCD, model: Point Grey Research CMLN-13S2M-CS). A 4x microscope objective was used to image the fiber cross-section at the grating end into the infrared camera, as illustrated in Figure 4.29.

The shape of the fs-laser induced RI modification was assessed by cleaving the optical fibers and inspecting the cross-sections of the structures with an optical microscope (Leica DM6000 M).

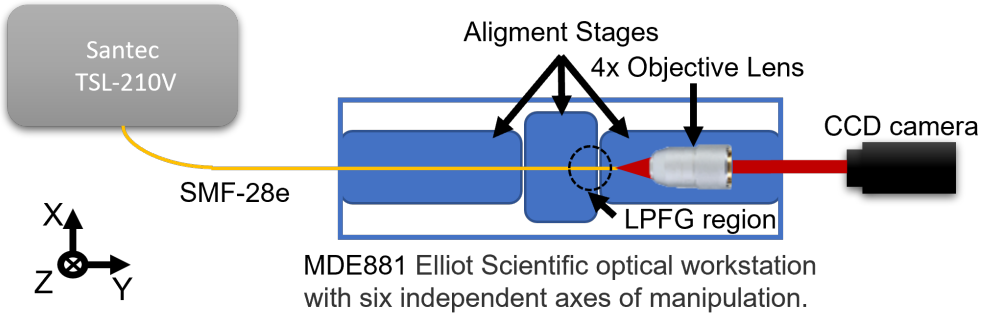


Figure 4.29. *Experimental setup for characterization of the near-field intensity distribution of several cladding modes excited by the fs-laser gratings inscription.*

Figure 4.30 shows a picture of the structure taken by the optical microscope (a) and the corresponding near-field intensity distribution acquired (b). The fs-laser induced RI modification presents a transversal inhomogeneous, asymmetric, elliptic shape which extends across the core center, inset of Figure 4.30 (a). Thereby, in the SMF-28e fiber, light is coupled to asymmetric $LP_{1,j}$ cladding modes of order j. Accordingly, the coupling strength is strongly influenced by the structure of the modified cross-section, including non-uniformity and localization. The intensity distribution presented in Figure 4.30 (b) shows that for a period of 390 µm coupling occurs to the asymmetric $LP_{1,6}$ cladding mode. Due to the asymmetrical shape of the RI modification, for shorter periods ($<$ 200 µm) coupling also occurs to asymmetric modes. For LPFGs written with short periods, the cladding mode identification was not possible through the near field intensity profile, because the resonances were out of the laser tuning range. The phase-matching curves for the LPFGs written in the SMF-28e fiber coupling to asymmetric cladding modes were already reported [144]. These simulated phase-matching curves do not fit precisely with the fs-laser gratings fabrication parameters. However, they can be used to claim that for periods between 175 and 200 µm coupling occurs to the asymmetric $LP_{1,12}$ cladding mode. In addition, the mode profile of the $LP_{1,12}$ mode was evaluated through a 2D analysis of the optical fiber structure and the electromagnetic field modes using the mode analysis of the COMSOL Multiphysics®, as will be discussed later.

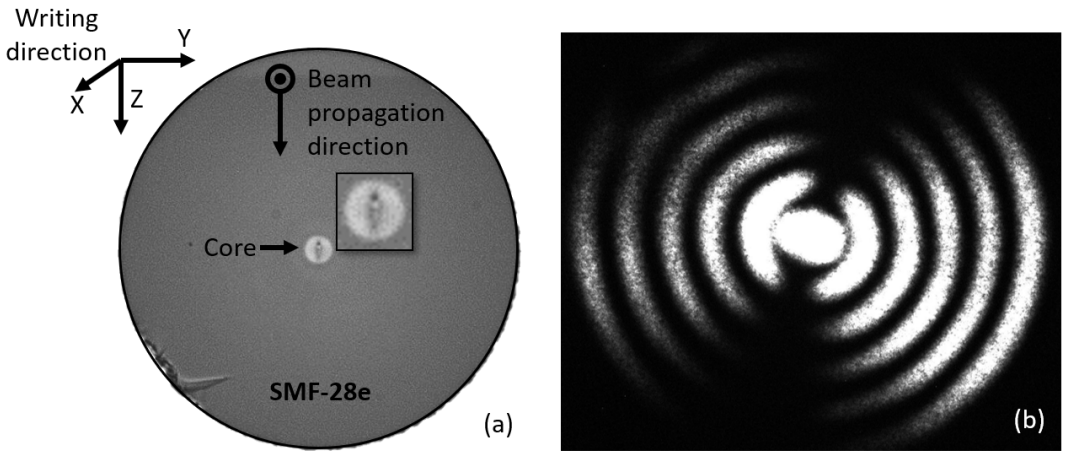


Figure 4.30. *Fs-laser inscribed LPFG in the SMF-28e fiber with a 8.2 µm core: (a) Optical microscope view of the cross-section, and (b) Near-field intensity distribution of the cladding mode $LP_{1,6}$ at 1592.7 nm (grating period of 390 µm).*

LPFGs with shorter periods (182.3, 182.5, and 182.7 µm) were also fabricated to study the behavior at, or very close to, a TAP in air. The length of the LPFGs was 19.0 mm. The transmission spectra in air, with and without applied tension, are shown in Figure 4.31.

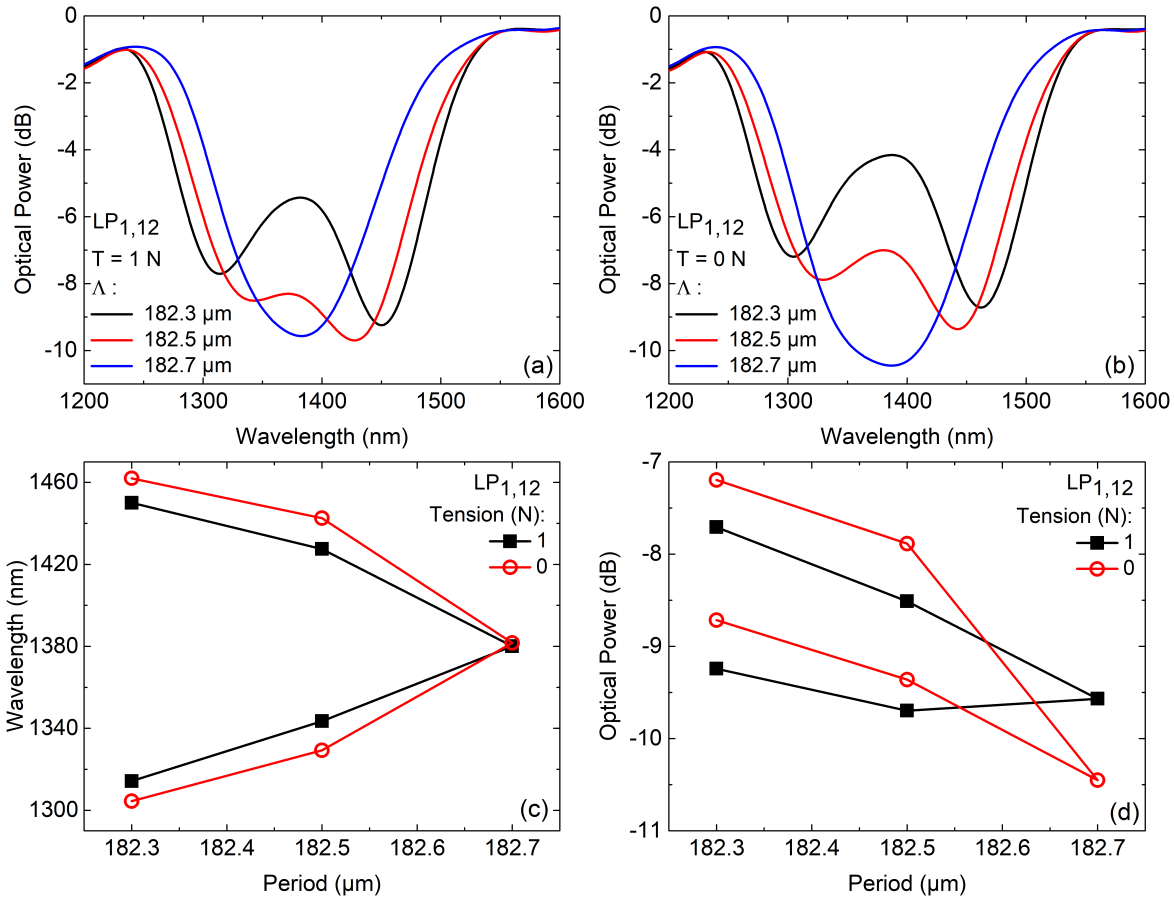


Figure 4.31. *Fs-laser TAP LPFGs cladding mode $LP_{1,12}$, inscribed in the SMF-28e fiber: (a) spectra under fabrication tension of 1 N, (b) spectra without tension, (c) resonance wavelengths versus grating period, and (d) optical power versus grating period.*

The transmission spectra presented in Figure 4.31 (a) exhibits two peaks (fiber surrounded by air and under tension) for periods of 182.3 and 182.5 µm. As can be seen in Figure 4.31 (b), relaxing the optical fiber increases the separation of the peaks, reaching a separation of 158.5 nm (blue-shift -10.8 nm, and red-shift +12.0 nm) and 113.3 nm (blue-shift - 14.3 nm, and red-shift +15.0 nm) for periods of 182.3 and 182.5 µm, respectively. Furthermore, the intensity of both resonances of each LPFG diminishes. It can also be seen that the increase of the inscription period to 182.7 µm causes the two resonance bands in the transmission spectrum to merge into one band, i.e., the 182.7 µm period coincides with the peak of the dispersion curve of the $LP_{1,12}$ cladding mode. Thus, the $LP_{1,12}$ cladding mode exhibits a turning point for a wavelength around 1380.0 nm, as shown in Figure 4.31 (c). The optical fiber relaxation with the 182.7 µm TAP LPFG results in a change in the coupling efficiency, but not in the wavelength, as shown in Figure 4.31 (c) and (d). The wavelength and intensity changes of the LPFGs resonance bands with the optical fiber relaxation are associated with the Poisson's effect (change in transverse dimensions), and to the waveguide contributions which depend on the slope of the characteristic curve of the resonance band [178].

Polarization Analysis

The polarization behavior of LPFGs, driven by birefringence, is critical for defining their operation and functionality. Birefringence introduces differences in the phase matching conditions for light polarized along vertical and horizontal axes. This asymmetry alters the coupling efficiency and can lead to resonance band splitting or polarization-dependent loss. By controlling birefringence, e.g., using the fs-laser direct writing technique, it is possible to tailor the coupling between modes for the design of optical devices used in applications such as strain and temperature sensing or polarization-selective optical filters [133, 179]. This control is achieved by adjusting fabrication parameters, such as pulse energy, writing velocity, duty cycle, and laser polarization. These adjustments allow birefringence to be introduced in a predictable and controlled manner, enabling precise refractive index modifications tailored to specific device needs. The fs-laser LPFGs exhibits considerable polarization dependence, and birefringence leads to the splitting of the resonance peak into two distinct ones. The different resonance peak associated with each polarization axis can be used as a means to determine the degree of birefringence using the following equation [179, 180]:

$$\Delta n = \frac{\lambda_2 - \lambda_1}{2\Lambda}. \tag{4.18}$$

The experimental setup shown in Figure 4.32 is used to measure the transmitted spectrum of the LPFGs with polarization control. In this configuration, the optical source is connected to an in-line polarizer (Thorlabs ILP1550PM-APC) to allow linearly polarized light to pass while blocking the orthogonal polarization from the unpolarized light source. Additionally, the output polarization of the polarization-maintaining fiber is adjusted using a manual paddle fiber polarization controller (Thorlabs FPC564), which modifies the polarization state of the light incident on the LPFG.

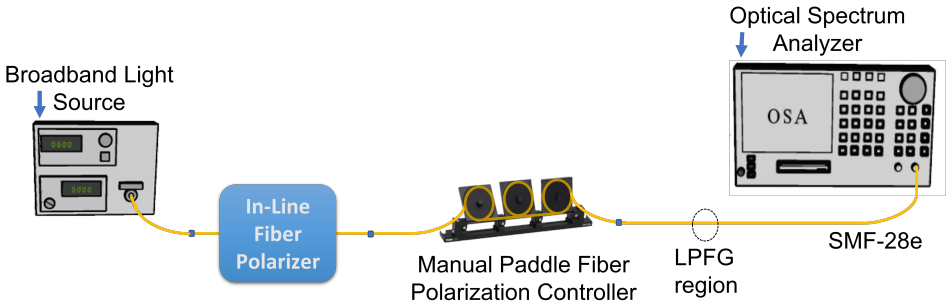


Figure 4.32. *Experimental setup for measurement of the LPFGs transmitted spectrum with polarization control.*

The LPFBGs fabricated by the fs-laser direct written system with different duty cycles and writing positions in the optical fiber, were explored to determine how changes in these parameters affect the grating's spectral response, i.e., wavelength, optical power, and birefringence. The Figure 4.33 shows the transmission spectra of the TAP LPFG measured with polarization control and without any applied tension (surrounded by air). The TAP LPFG was fabricated with a period of 182.7 µm at a depth of 60 µm with a pulse energy of 120 nJ and 19.0 mm long. An optical micrograph (bottom right corner) shows the cross-section of a single-mode fiber core with a RI modification written with the fs-laser beam incident from the top.

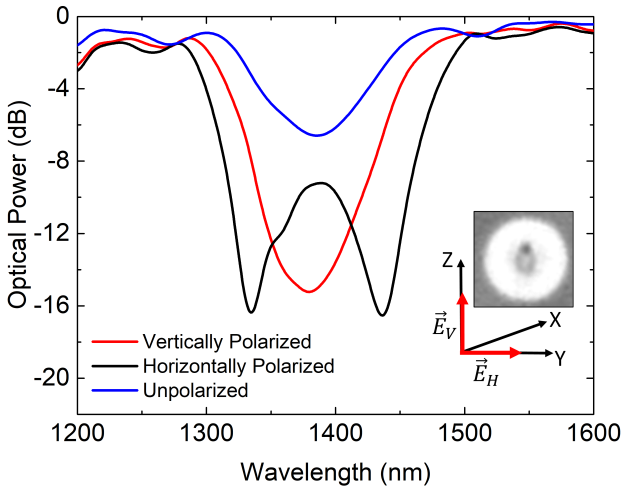


Figure 4.33. *Transmission spectra of the TAP LPFGs fabricated at a depth of 60 µm with pulse energy of 120 nJ, a duty cycle of 50 %, and 19.0 mm long (measured with polarization control). An optical micrograph (bottom right corner) shows the cross-section of a single-mode fiber core with a RI modification written with the fs-laser beam incident from the top. The $\vec{E}_V$ and $\vec{E}_H$ indicate the electric field orientation for Vertical, V, and Horizontal, H, grating polarization eigenmodes.*

The transmission spectra of the 182.7 µm TAP LPFG, shown in Figure 4.33, exhibit distinct polarization-dependent behavior. A single resonance peak is observed when measured without polarization control at ∼1388.0 nm and under vertical polarization at ∼1380.0 nm. Under horizontal polarization, the spectrum exhibits two resonances at ∼1334,8 and ∼1436.0 nm ($\Delta\lambda$ = 101.2 nm). Furthermore, the intensity of the resonance band increases from ~ -10 dB to ~ -16 dB when measured with controlled polarization. In summary, for the grating period of 182.7 µm, it was verified that the $LP_{1,12}$ mode exhibits a TAP at ∼1388.0 nm and ∼1380.0 nm when measured without polarization control and under vertical polarization, respectively. In addition, under horizontal polarization, the $LP_{1,12}$ mode exhibits two resonances around the TAP region at ∼1334,8 and ∼1436.0 nm, with a wavelength separation ($\Delta\lambda$) of 101.2 nm.

Figure 4.34 shown the transmission spectra of the LPFGs fabricated with a period of 380 µm, 28.5 mm long, a pulse energy of 120.0 nJ, 50 µm/s scan velocity, a fiber tension of 1 N, and with duty cycle of 20 %, 50 %, and 80 % (measured with polarization control). By analysing the transmission spectrum of the LPFGs to different duty cycles, it is observed that for all duty cycles, the wavelength and intensity of the resonance band, when subjected to polarization control, changes compared to the unpolarized state. When the LPFGs were analyzed under horizontal polarization, the resonance wavelength exhibited a blue shift (shorter wavelengths) and increased intensity loss. Conversely, under vertical polarization, the resonance wavelength exhibited a red shift (longer wavelengths) along with an increase in intensity loss, except a decrease in intensity loss noted at a 20 % duty cycle.

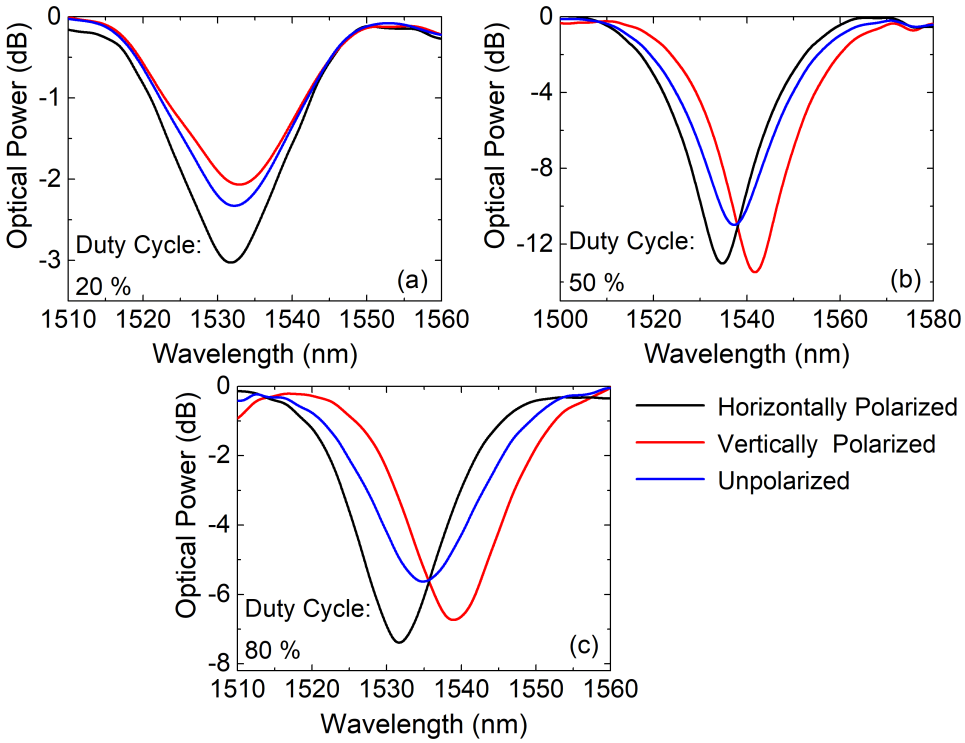


Figure 4.34. *Transmission spectra of the LPFGs fabricated with a duty cycle of (a) 20 %, (b) 50 %, and (c) 80 % with pulse energy of 120 nJ and 28.5 mm long (measured with polarization control).*

The spectral characteristics of the LPFGs fabricated with different duty cycles are summarized in Table 4.9.

Table 4.9. *Summary of the spectral characteristics of the LPFGs fabricated with different duty cycles.*

Duty Cycle (%)	λ_{res} (nm)	I_{res} (dB)	FWHM Bandwidth (nm)	Birefringence
20	1532.5	-2.4	17.8	3.2×10^{-6}
50	1537.4	-11.1	19.3	1.9×10^{-5}
80	1535.0	-5.6	16.1	2.0×10^{-5}

The intensity of the resonance band increases for a writing duty cycle of 50%, reaching a value of -11.1 dB. In addition, the widest bandwidth of 19.3 nm is observed at this duty cycle. Higher duty cycles, such as 80%, increase birefringence, which can be advantageous for applications requiring enhanced polarization sensitivity or birefringence-induced resonance band splitting. However, this increase in birefringence comes with a decrease in the intensity of the resonance band. In addition, lower duty cycles (20%) produce minimal birefringence and a resonance band with lower intensity, indicating inadequate writing condition for effective LPFG fabrication. The duty cycle is a fundamental parameter in fs-laser fabrication of LPFGs, directly influencing resonance wavelength, intensity, bandwidth, and birefringence. The results indicate a relationship between the resonance band intensity and birefringence, with 50% duty cycle identified as the optimal choice for most applications requiring high coupling efficiency. Higher duty cycles may be appropriate for applications that rely on birefringence effects.

Figure 4.35 shows the transmission spectra of LPFGs fabricated at different depths from the fiber surface and lateral offset. The LPFGs were written with a period of 380 µm, 28.5 mm long, a pulse energy of 12.0 nJ, a scan velocity of 50 µm/s, a fiber tension of 1 N, and a duty cycle of 50 %. The spectra were measured with polarization control to evaluate the influence of these parameters on the the spectral response of the LPFGs. By analysing the transmission spectrum of the LPFGs to different writing position, it is observed that for the 50% duty cycle, the wavelength and intensity of the resonance band, when subjected to polarization control, changes compared to the unpolarized state. When the LPFGs were analyzed under horizontal polarization, the resonance wavelength exhibited a blue shift (shorter wavelengths) and increased intensity loss. In addition, under vertical polarization, the resonance wavelength exhibited a red shift (longer wavelengths) along with an increase in intensity loss. The LPFGs spectral behaviour is similar to those presented for the LPFGs fabricated with different duty cycles. For an LPFG fabricated at a depth of 58 µm from the fiber surface, the resonance band presents a nonuniform transmition spectra for the different states of polarization, as shown in (Figure 4.35 (a)).

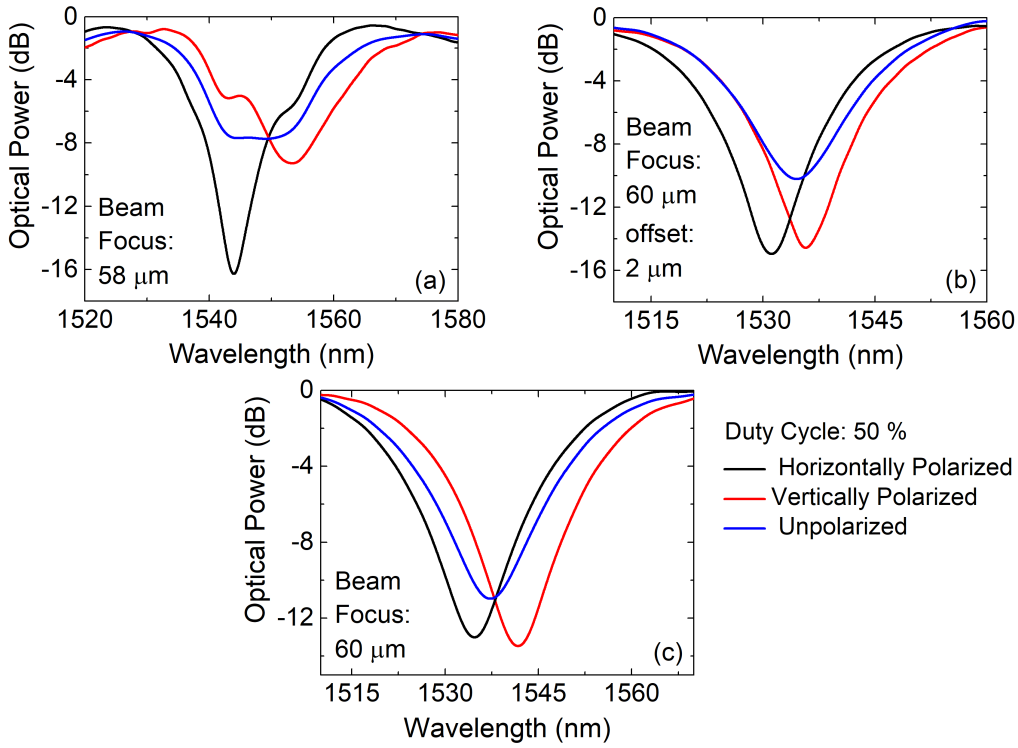


Figure 4.35. *Transmission spectra of the LPFGs fabricated at a depth from the fiber surface of (a) 58 µm, (b) 60 µm (and 2 µm lateral offset), and (c) 60 µm with pulse energy of 120 nJ and 28.5 mm long (measured with polarization control).*

The spectral characteristics of the LPFGs fabricated at different positions inside the SMF-28e fibers are summarized in Table 4.10.

Table 4.10. *Summary of the spectral characteristics of the LPFGs fabricated at different positions inside the SMF-28e fiber.*

Beam Focus	λ_{res} (nm)	I_{res} (dB)	FWHM Bandwidth (nm)	Birefringence
58 μm	1548.2	-7.7	20.7	2.5×10^{-5}
60 μm with 2 μm offset	1534.5	-10.2	16.5	1.3×10^{-5}
60 μm	1537.4	-11.1	19.3	1.9×10^{-5}

The resonance band's higher intensity loss (-11.1 dB) was observed at 60 µm depth for the fabrication without lateral offset. In addition, the lateral offset slightly weakens the coupling efficiency. Thus, the spectral performance of LPFGs is influenced by the fabrication condition. Birefringence in LPFGs manifests as a change in grating wavelength and attenuation in the transmission spectrum with changing polarization of incident light, [179].

Second Group [controlled temperature]

The fabrication parameters, namely for the TAP LPFGs writing, are dependent on environmental conditions. Therefore, the optimization of TAP LPFGs writing parameters can be realized by keeping the laser room in controlled environmental conditions (room temperature kept at $\sim 20\ ^{\circ}$C).

Two 40 mm long LPFGs with a period of 191.8 µm were fabricated at a depth of 60 and 57 µm from the top center position of the fiber cladding with pulse energies of 120 and 140 nJ, respectively. The shape of the fs-laser induced RI modification was also assessed, as previously detailed in First Group. Figure 4.36 shows a picture of the structures taken by the optical microscope.

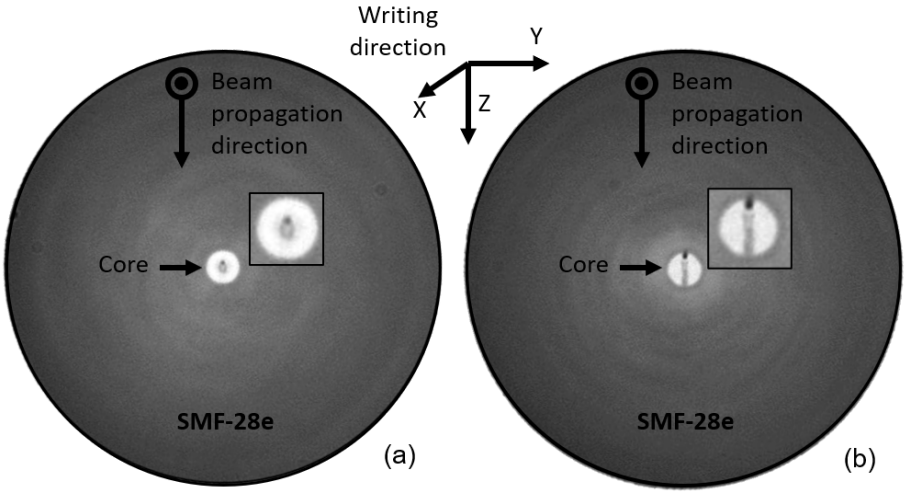


Figure 4.36. *Optical microscope views of the cross-sections of the fs-laser written LPFGs in the SMF-28e fiber (8.2 µm core diameter) at a depth from the fiber surface of (a) 60 µm with pulse energy of 120 nJ and (b) 57 µm with pulse energy of 140 nJ.*

Both types of fs-laser induced RI modifications are transversely inhomogeneous and asymmetric, resembling an elliptic and rectangular shape that extends across the core center, as shown in the insets of Figure 4.36 (a) and (b), respectively. Therefore, the coupling occurs to the asymmetric cladding modes, as previously addressed.

LPFGs with periods between 190 and 193 µm were inscribed with the fabrication parameters aforementioned, to study the spectral behavior at, or very close to, the TAP of the asymmetric $LP_{1,12}$ cladding mode, considering the LPFGs surrounded by air and water. The LPFGs transmission spectra in air and water for the two fabrication conditions are shown in Figure 4.37 (a) and (b), respectively.

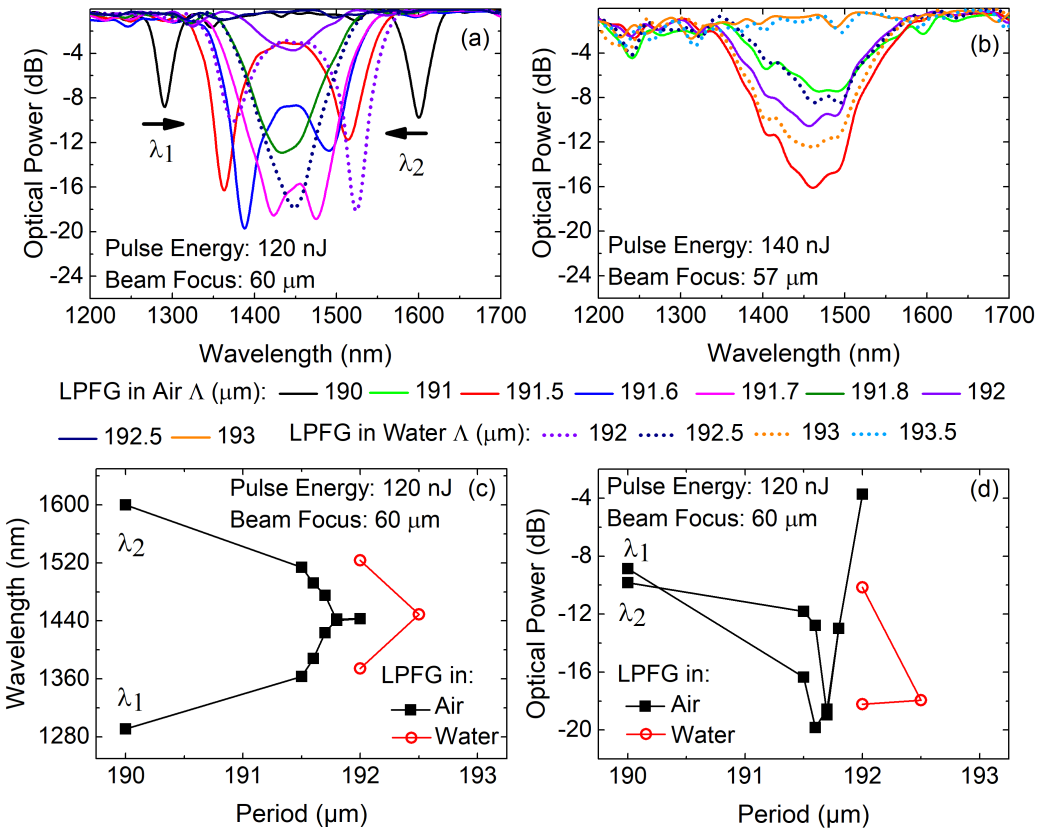


Figure 4.37. *Transmission spectra of the LPFGs fabricated at a depth of (a) 60 µm with pulse energies of 120 nJ and (b) 57 µm with pulse energies of 140 nJ; (c) resonance wavelengths; (d) optical power versus the grating period for fabrication at a depth of 60 µm with a pulse energy of 120 nJ.*

For the grating period of 190 µm, the $LP_{1,12}$ mode exhibits two resonances at ∼1290.8 and ∼1600.2 nm ($\Delta\lambda$ = 309.4 nm) in air, as shown in Figure 4.37 (a). When the grating inscription period increased from 190 to 191.7 µm, the two resonances approach, reaching a separation of 51.4 nm. As can be seen in Figure 4.37 (c), the 191.8 µm period matches the peak of the dispersion curve of the $LP_{1,12}$ cladding mode, where the two resonance bands in the transmission spectrum merge into one band at ∼1442.7 nm. Moreover, the increase of the inscription period to 192 µm results in a decrease of coupling efficiency, but not in wavelength, as shown in Figure 4.37 (c) and (d). For LPFGs fabricated with periods greater than 192 µm and surrounded by air, the resonance vanishes because the coupling occurs outside of the dispersion curve of the

$LP_{1,12}$ cladding mode. However, if the SRI increase, i.e., when the LPFGs are immersed in water, the coupling behavior changes, which induce a re-distribution of the cladding modes. Thus, for the LPFGs fabricated with 192 µm and immersed in water, the $LP_{1,12}$ mode exhibits two resonances around the TAP region at $\sim$1374.4 and $\sim$1523.7 nm ($\Delta\lambda$ = 149.3 nm). The LPFGs operation at the TAP in water was achieved with a grating inscription period of 192.5 µm. In summary, for the grating periods of 191.8 and 192.5 µm, it was verified that the $LP_{1,12}$ mode exhibits a TAP at $\sim$1442.7 and $\sim$1448.6 nm in air and water, respectively.

In order to improve the amplitude of the LPFGs attenuation band, the fs-laser pulse energy was increased to 140 nJ, and the laser beam focus adjusted at a depth of 57 µm from the top center position of the fiber cladding. This procedure allowed the RI modification across the entire core center, as shown in the inset of Figure 4.36 (b). The difference between the effective RIs of the core and cladding modes increased, and the underlying RI modification induced a change in the coupling behavior leading to a re-distribution of the cladding modes. For this writing condition, the LPFGs operation at the TAP was achieved with grating inscription periods of 192 µm in air and 193 µm in water, resulting in resonance wavelengths at $\sim$1451.1 and $\sim$1453.8 nm, respectively. In addition, the coupling efficiency was improved for the 192 µm LPFG in air, resulting in an -3.1 dB increase of the attenuation band, in comparison with the attenuation band value ($I_{res}= -13.0$ dB) of the 191.8 µm LPFG. However, as can be seen in Figure 4.37 (b), additional peaks appear on the LPFGs resonance for this writing condition. These additional peaks can be due to the coupling to the higher-order cladding modes, which rely on the sharp inhomogeneities as well as the position and asymmetrical shape of the induced RI modification. In [165], it was theoretically and experimentally determined that the additional peaks were mainly caused by decentered and homogeneous RI modifications induced in the fiber core. Alternatively, by performing the grating inscription with an offset of 0.8 µm on the X-axis, makes coupling occur to the asymmetric higher-order cladding modes, where additional peaks appear between the main resonances. The suppression of these additional peaks can be achieved inducing homogeneous and centered RI modifications in the fiber core, which results in the coupling to the symmetric cladding modes, as reported in [165, 181]. As can be seen in Figure 4.37 (a), the fabrication of TAP LPFGs without additional peaks in the transmission spectra and coupling to asymmetric modes was achieved due to the position, asymmetry, and elliptic shape of the induced RI modification, depicted in the inset of Figure 4.36 (a).

Reproducibility of the LPFGs fabrication

Several LPFGs were fabricated to optimize and assess the reproducibility of the fs-laser direct writing. Table 4.11 presents a comparison between a pair of LPFGs inscribed with a period of 372.5 µm.

Table 4.11. *Comparison between a pair of LPFGs.*

LPFG number	Cladding Mode	Λ (µm)	λ_{res} (nm)	I_{res} (dB)	FWHM Bandwidth (nm)
1	$LP_{1,6}$	372.5	1494.9	−11.9	23.9
2			1495.2	−11.7	25.3

As can be observed, a resonance wavelength difference of 0.07 nm, an intensity variation of 0.15 dB, and a full width at half maximum (FWHM) difference of 0.66 nm were achieved for the LPFGs fabricated with a period of 372.5 µm. Long-period fiber gratings inscribed in a standard SMF-28e optical fiber using the electric arc technique, with a grating period of 387 µm, exhibit a resonance wavelength corresponding to the asymmetric $LP_{1,6}$ cladding mode around 1480 nm. The full width at half maximum of the spectral bandwidth was measured to be approximately 13.4 nm, with an attenuation intensity around -12.0 dB, [156, 182]. Fs-laser-written LPFGs exhibit distinct spectral features compared to those fabricated through the electric arc technique. Despite utilizing comparable grating periods, fs-laser written LPFGs are characterized by a resonance wavelength of approximately 1495 nm, an attenuation intensity of -11.9 dB, and a broader full-width at half maximum of 24 nm. Conversely, LPFGs fabricated through the electric arc technique exhibit a resonance wavelength closer to 1480 nm, with a similar attenuation intensity of around -12.0 dB and a considerably narrower FWHM of 13.4 nm, [156, 182]. These differences underscore how the choice of inscription method influences the spectral properties of LPFGs, particularly in terms of resonance behaviour and bandwidth characteristics.

Figure 4.38 shows the transmission spectra of twelve LPFGs operating at the TAP in air and water fabricated with a period of 191.8 and 192.5 µm, respectively.

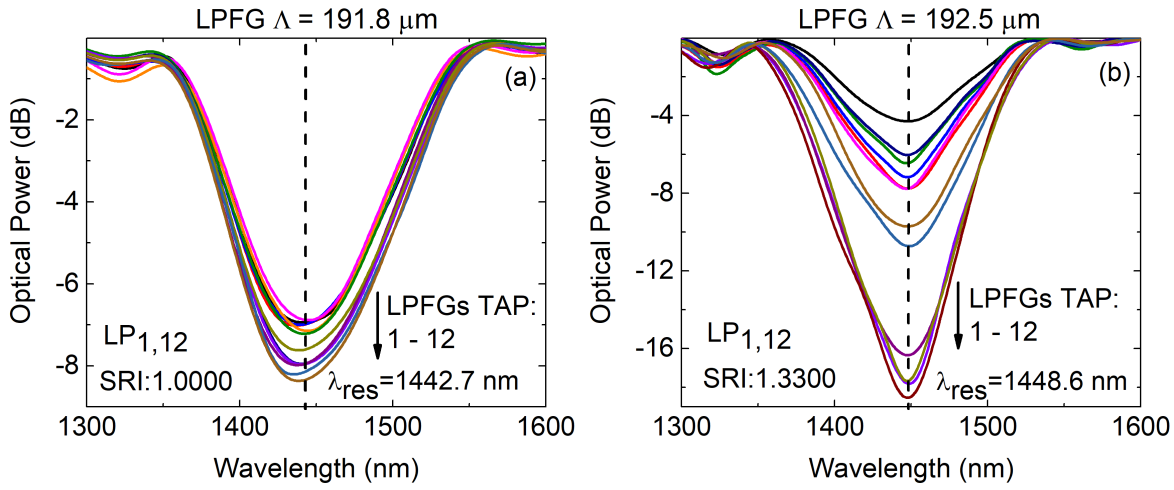


Figure 4.38. *Fs-laser TAP LPFGs inscribed with a period of (a) 191.8, and (b) 192.5 µm (numbered from 1 to 12).*

The wavelength, the intensity, and the full width at half maximum (FWHM) of the resonance bands are summarized in Table 4.12. Accordingly, it may be claimed the reproducibility of the fabrication process. The intensity reproducibility was the most challenging parameter to achieve, perceptible in the LPFGs operating at the TAP in water. These LPFGs operating at the TAP in water

were written without real-time monitoring of the spectral properties during the fabrication process. This constraint precludes the fine adjustment of the grating length or the coupling coefficient during the fabrication to obtain resonance bands with similar intensity, satisfying equation 4.13. However, the variation in intensity between devices is not critical for the temperature characterization and RI sensing. Precise fabrication of fs-laser LPFGs operating at the TAP relies on the fine control of several parameters such as: sub-micron period precision, pulse energy, the focal position of the laser beam, and fiber tension during fabrication.

Table 4.12. *Main characteristics of two sets of TAP LPFGs fabricated by fs-laser.*

Λ (µm)	Values	λ_{res} (nm)	Intensity (dB)	FWHM Bandwidth (nm)
191.8	Average	1442.7	−7.6	115.2
	Standard Deviation	1.0	0.4	3.5
192.5	Average	1448.6	−10.9	90.9
	Standard Deviation	1.0	5.3	9.5

4.2.3 Sensitivity Analysis of LPFGs

The LPFGs fabricated in standard SMF-28e fiber employing the fs-laser system and its sensing characteristics to temperature and external refractive index (RI) are addressed.

Characterization of Temperature Sensitivity

A characterization setup was mounted to measure the LPFGs spectrum at different surrounding mediums and temperatures. The setup consisted of a sliding tubular oven (Termolab), an acrylic chamber filled with water mounted on three-axis positioners (MBT616/M, Thorlabs), and an OSA (model Yokogawa AQ6370D). The optical fibers with the LPFGs were introduced in a horizontal tubular oven, being subjected to an axial tension produced by a suspended weight of 5.8 g, as illustrated in Figure 4.39.

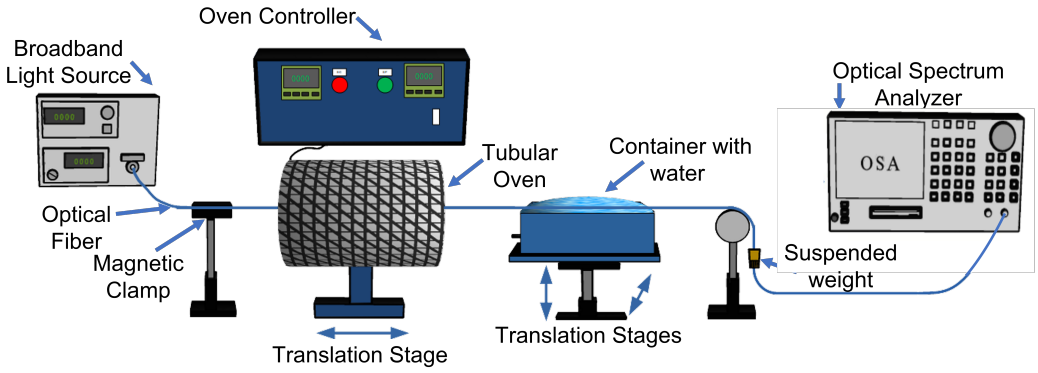


Figure 4.39. *Schematic illustration of the temperature characterization setup for LPFGs.*

The LPFGs spectra were recorded 5 min after the target temperature was reached. The fiber was then withdrawn from the oven after each temperature step, let cool down to room temperature, and then the spectra was measured again with the fiber in air and immersed in water (the latter was only done for the TAP LPFGs). Then, the temperature was increased, and the LPFGs were introduced again in the oven. This procedure was repeated for a temperature in the range of 100 to 600 °C in steps of 50 °C. The described thermal treatment was performed two times for the LPFG and once for the TAP LPFGs.

To reproduce and characterize the spectral responses of the LPFGs tested in this work, two broadband optical sources were used with an OSA. LPFGs were measured from 1450 nm to 1650 nm using a broadband amplified spontaneous emission (ASE) source (model ASE2000), with the OSA configured for a spectral resolution of 1 nm. TAP LPFGs were measured from 1000 nm to 1700 nm using a stabilized halogen lamp with broadband spectral emission, with the OSA configured for a spectral resolution of 2 nm.

Long Period Fiber Gratings

During the annealing procedure, the transmission spectra of the cladding mode $LP_{1,6}$ of a 372.5 µm LPFG were recorded and are shown in Figure 4.40.

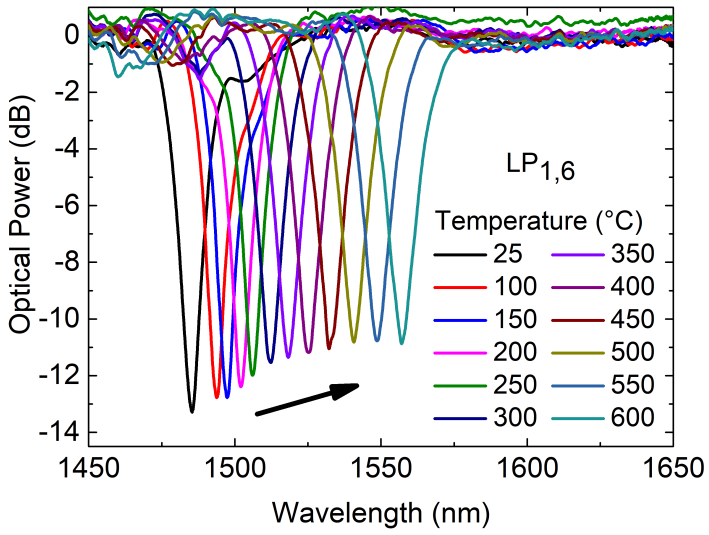


Figure 4.40. *Transmission spectra of the cladding mode $LP_{1,6}$ of a 372.5 µm LPFG at annealing temperature.*

As the temperature increases from 25 to 600 °C in steps of 50 °C, the resonance wavelength is gradually red-shifted, and the intensity loss decreases. The LPFG temperature response was recorded for two annealing cycles at the annealing and room temperature, as shown in Figure 4.41.

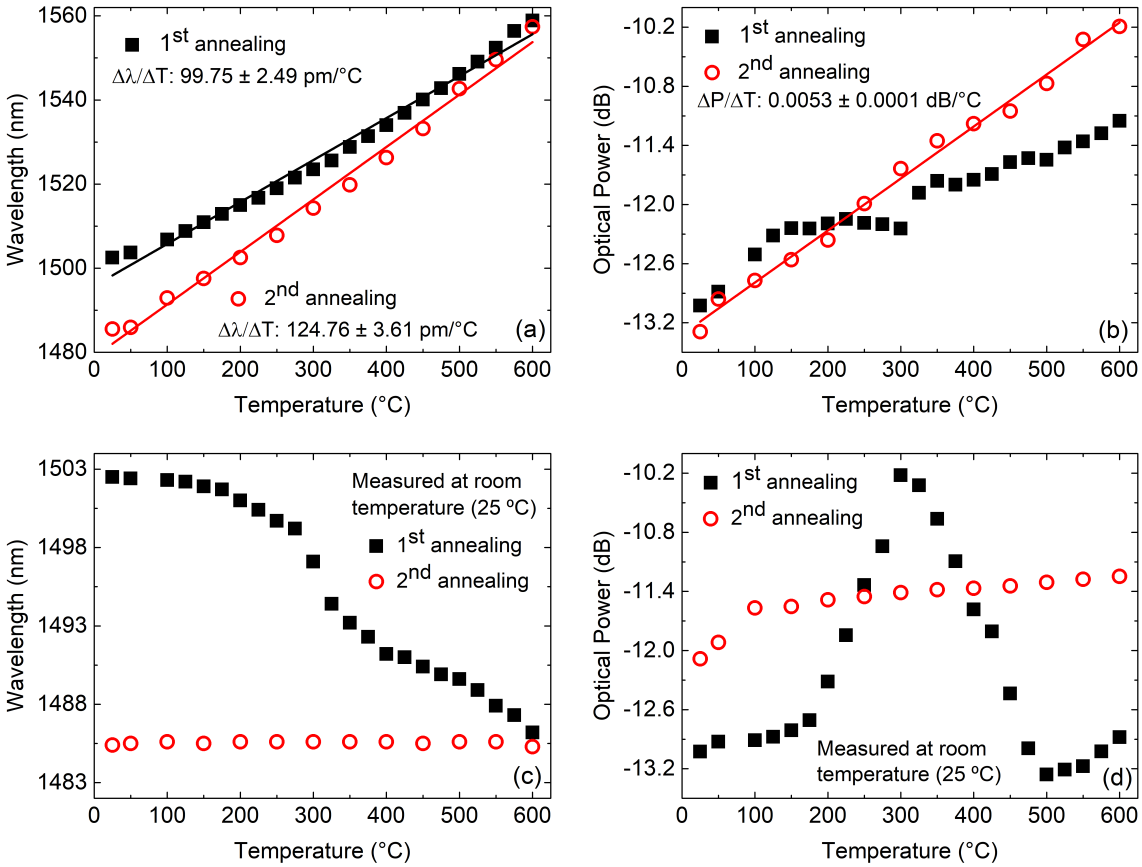


Figure 4.41. *Fs-laser LPFG inscribed with a period of 372.5 µm: (a) wavelength shift, and (b) strength of the peak attenuation, both* ***measured at the annealing temperature****; (c) wavelength shift, and (d) strength of the peak attenuation, both* ***measured at room temperature after annealing the grating at different temperatures.***

Figure 4.41 (a) shows for the first annealing cycle, a wavelength shift proportional to the temperature increase from 25 to 600 °C, at a rate of 99.75 ± 2.49 pm/°C (and $R^2 > 0.99$). The resonance optical power decreases non-uniformly with the annealing temperature, as shown in Figure 4.41 (b). The behavior of the LPFG was also recorded at room temperature after a dwell time of 5 min at each annealing temperature. A resonant wavelength blue-shift from 1502.51 to 1486.21 nm ($\Delta\lambda$ = 16.30 nm) was observed at the end of the first annealing, as shown in Figure 4.41 (c). As can be seen from Figure 4.41 (d), for the first annealing, the optical power decreased for the range from 100 to 300 °C, and then increased up to 500 °C. The optical power decreased again between 500 and 600 °C. The shift of the resonance to smaller wavelengths at the end of the annealing was mainly due to the change of the effective RI of the core mode [183]. This is because thermal activation of defects caused by the fs-laser inscription are annealed out, leaving a smooth and uniform RI modification between the structurally modified region and the unaffected region inside the core of the SMF-28e fiber [93, 103]. Accordingly, the LPFG exhibits poor thermal stability in their optical power because of the Type I RI changes produced by the fs-laser LPFG inscription [93]. The second annealing shows an improvement of the linearity of the wavelength temperature dependence with 124.76 ± 3.61 pm/°C (and $R^2 > 0.99$). Furthermore, the resonance optical power decreases uniformly with the annealing temperature, presenting a temperature dependence of

0.0053 $\pm$ 0.0001 dB/°C with linearity $R^2 > 0.99$ as shown in Figure 4.41 (b). At room temperature (25 °C), the resonance wavelength became essentially constant at 1485.54 nm, regardless of the annealing temperature. Concerning the resonance optical power, it was observed a decrease of around 0.52 dB up to 100 °C, followed by a reduction of 0.3 dB up to 600 °C. Thus, with the performed thermal treatment through short-term thermal exposure (5 min at each temperature), it is possible to enhance the fs-laser LPFGs thermal stability up to 600 °C. Furthermore, the temperature response presented in this work is higher compared to other high-temperature sensors based on LPFG fabricated in SMF 28 fiber [103, 148].

Turn Around Point Long-Period Fiber Gratings

The thermal treatment of the 182.7 µm TAP LPFG was performed, and the transmission spectra response at the annealing temperatures was recorded, as shown in Figure 4.42. From 25 to 300 °C, the TAP LPFG exhibits a single resonance that is wavelength-independent of temperature, as shown in Figure 4.42 (a). Furthermore, it is possible to see that the resonance optical power variation decreases (i.e., the coupling strength decrease) with the annealing temperature, leading to the resonance vanishing above the 300 °C. Figure 4.42 (b) shows a temperature dependence (normalized to the room temperature, 25 °C) of 0.0372 $\pm$ 0.0019 dB/°C with linearity of $R^2 > 0.98$.

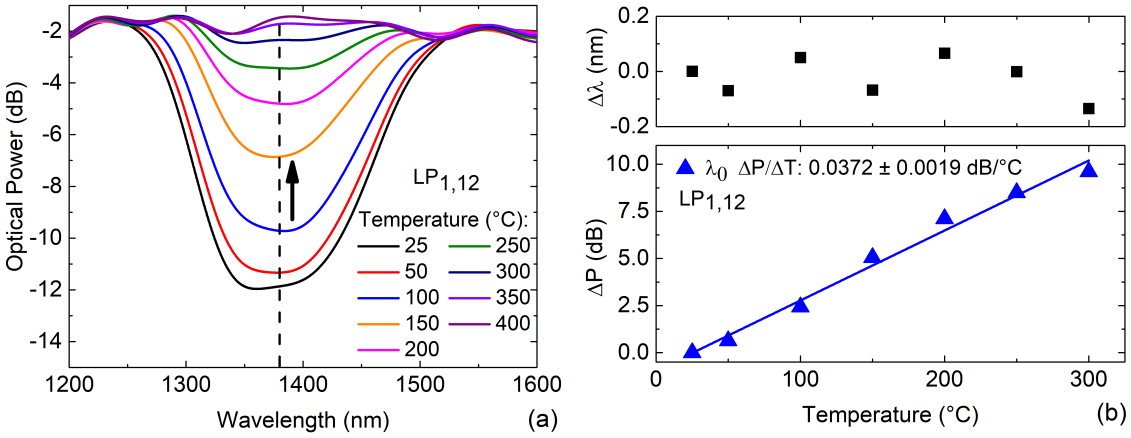


Figure 4.42. *Fs-laser TAP LPFG inscribed with a period of 182.7 µm: (a) transmission spectra at annealing temperature; (b) normalized wavelength shift (■) and optical power variation (▲) as a function of the annealing temperature.*

As the annealing temperature increased, the TAP LPFG transmission spectra response was also recorded in air and water at room temperature, as presented in Figure 4.43 (a) and (b), respectively. Figure 4.43 (a) shows the behavior of the TAP LPFG in air at room temperature where, for annealing temperatures higher than 250 °C, it is possible to see that the resonance peak bifurcates and separates into two resonances. The temperature dependence of the TAP LPFG immersed in water, leads to the appearance of two separated peaks, as shown in Figure 4.43 (b).

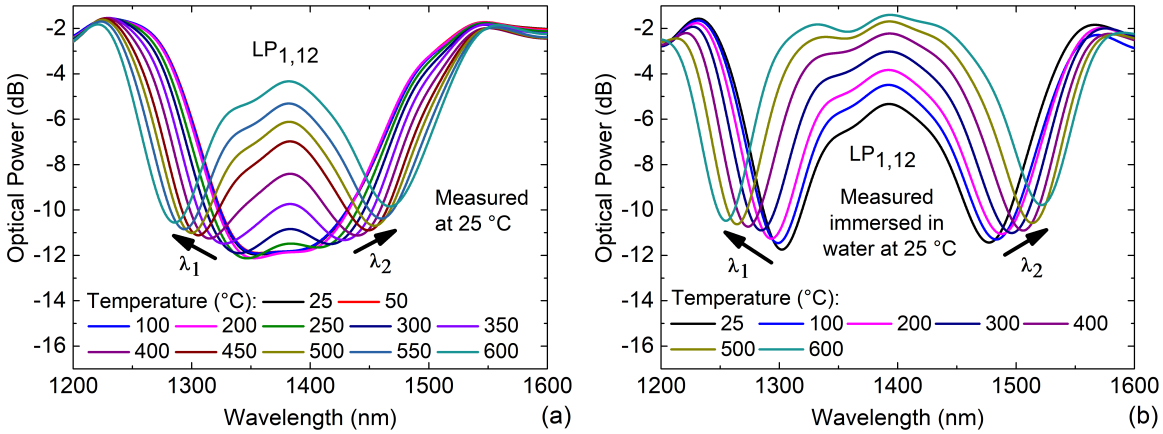


Figure 4.43. *Fs-laser TAP LPFG inscribed with a period of 182.7 µm: (a) transmission spectra at room temperature; (b) transmission spectra immersed in water at room temperature.* ***All measurements were acquired after annealing the grating at different temperatures****.*

Figure 4.44 shows the normalized wavelength shift and optical power variation measured of the TAP LPFG in air and water at room temperature, after a dwell time of 5 min at each annealing temperature.

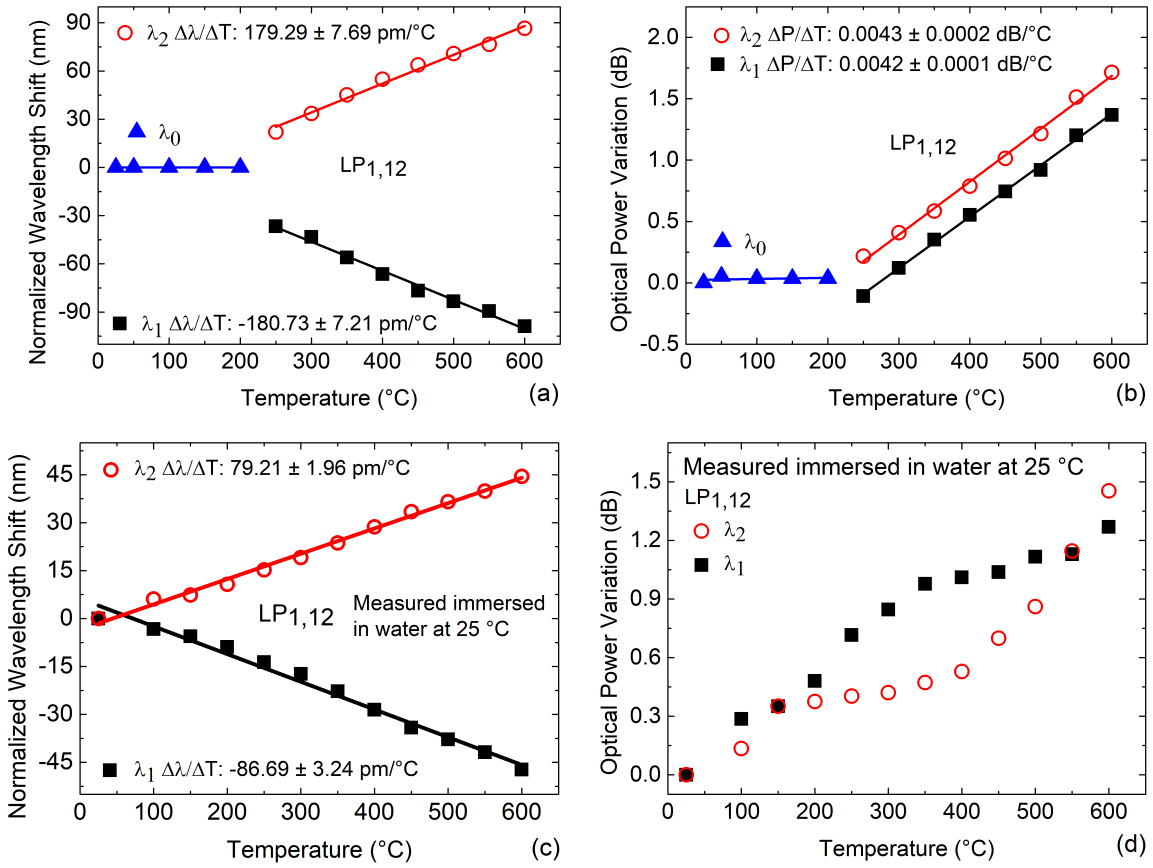


Figure 4.44. *Fs-laser 182.7 µm TAP LPFG: (a) normalized wavelength shift, and (b) normalized optical power variation in air at room temperature; (c) normalized wavelength shift, and (d) normalized optical power variation in water at room temperature.* ***All measurements were acquired after annealing the grating at different temperatures****.*

In the temperature range from 25 to 200 °C, the TAP LPFG in air exhibits a single resonance that is wavelength-independent of temperature, as shown in Figure 4.44 (a). At 250 °C, the resonance has bifurcated and presents two peaks separated by 58.67 nm (blue-shift -36.62 nm, and red-shift $+22.05$ nm normalized to the room temperature, 25 °C). The two resonances continue to separate with increasing temperature, reaching a separation of 185.47 nm (blue-shift -98.89 nm, and red-shift $+86.58$ nm) in air (25 °C) after annealing at 600 °C. The TAP LPFG in air after the annealing presents a temperature dependence of $-180.73\pm$ 7.21 pm/°C, and 179.29 $\pm$ 7.69 pm/°C, with linearity $R^2 > 0.99$ for both resonances λ_1 and λ_2, respectively.

In Figure 4.44 (b), the normalized optical power of the TAP LPFG measured in air (25 °C) after the annealing became essentially constant in the temperature range from 25 to 200 °C. Above 200 °C, the TAP LPFG normalized optical power reaches a temperature dependence (normalized to room temperature, 25 °C) of 0.0042 $\pm$ 0.0001 dB/°C, and 0.0043 $\pm$ 0.0002 dB/°C, with linearity $R^2 > 0.99$ for both resonances λ_1 and λ_2, respectively. These results demonstrate that the annealing changes the RI modifications inscribed with the fs-laser inside the core of the SMF-28e, as explained above for the cladding mode $LP_{1,6}$ of a 372.5 µm LPFG. For the $LP_{1,12}$ cladding mode with a TAP in its phase-matching curve for a wavelength around 1380 nm, the small changes in the coupling conditions caused by the annealing at temperatures higher than 200 °C split the resonance into two separate resonances, with positive and negative linear dispersions. The operation at the TAP for the 182.7 µm LPFG, with the performed thermal treatment, is ensured up to a temperature of 200 °C. To fabricate a TAP LPFG that is thermally stable at higher temperatures, it is necessary to increase the period of fabrication to values higher than 182.7 µm. Thus, with the performed thermal treatment through short-term thermal exposure (5 min for a given temperature), it is possible to operate around the TAP region with the 182.7 µm TAP LPFG fabricated by fs-laser.

Regarding the TAP LPFG immersed in water at 25 °C, the resonance presents two peaks separated by 175.15 nm (blue-shift -81.24 nm, and red-shift $+93.91$ nm normalized to the room temperature, 25 °C). As the annealing temperature increase, the two resonances continue to separate, reaching a separation of 266.84 nm (blue-shift -128.48 nm, and red-shift $+138.36$) in the water at room temperature after an annealing temperature of 600 °C. As shown in Figure 4.44 (c), temperature dependences of -86.69 ± 3.24 pm/°C, and 79.21 $\pm$ 1.96 pm/°C, with linearity $R^2 > 0.98$ and, $R^2 > 0.99$ were achieved for the λ_1 and λ_2 resonances, respectively. Figure 4.44 (d) shows that the optical power variation, normalized to the room temperature, increases non-linearly. This behavior is related to the waveguide dispersion, which depends upon the order ($LP_{1,12}$) of the cladding mode and the RI of the medium surrounding the cladding.

The thermal treatment of the 192.5 µm period LPFG operating at the TAP in water was also performed, and the transmission spectra response was recorded, as shown in Figure 4.45 (a).

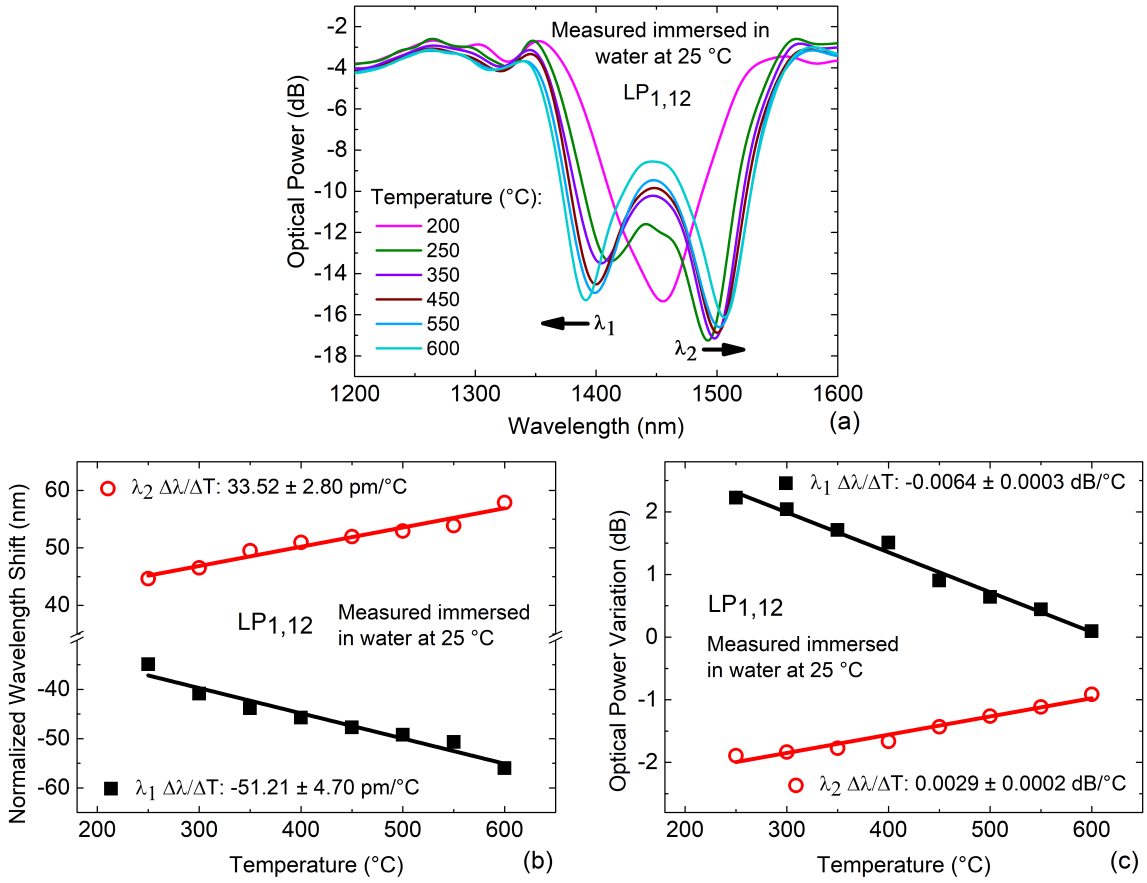


Figure 4.45. *Fs-laser TAP LPFG inscribed with a period of 192.5 µm, measured in water at 25 °C: (a) transmission spectra; (b) normalized wavelength shift; and (c) normalized optical power variation.* ***All measurements were acquired after annealing the grating at different temperatures****.*

As fabricated, this TAP LPFG exhibits a single resonance at ∼1448 nm. For annealing temperatures higher than 200 °C it is possible to see that the resonance peak bifurcates and separates into two resonances, reaching a separation of 113.90 nm (blue-shift of −56.01 nm, and red-shift of +57.89 nm) in water at room temperature after an annealing temperature of 600 °C. As shown in Figure 4.45 (b), temperature dependences of -51.21 ± 4.70 pm/°C and 33.52 ± 2.80 pm/°C, with linearity $R^2 > 0.94$ and $R^2 > 0.95$, were achieved for the λ_1 and λ_2 resonances, respectively. Figure 4.45 (c) shows that above 200 °C, the TAP LPFG normalized optical power reaches a temperature dependence (normalized to 200 °C) of 0.0064 ± 0.0003 dB/°C, and 0.0029 ± 0.0002 dB/°C, with linearity $R^2 > 0.98$ and $R^2 > 0.96$ for the resonances λ_1 and λ_2, respectively.

When comparing the annealing temperature results of the LPFGs with 372.5 and 182.7 µm, the highest temperature dependence was seen when the LPFG was chosen to operate near the TAP in air (182.7 µm period). The temperature dependence of the LPFGs relies on the material and waveguide contributions. For the LPFG with a period of 372.5 µm, the material effect dominates, which is related to the change in the differential RI of the core and cladding arising from the thermo-optic effect. The LPFGs with periods of 182.7 and 192.5 µm present a lower material contribution to the temperature dependence. In this case, the waveguide contribution, resulting from changes in the LPFG period, dominates. Thus, the choice of the LPFG period is important to balance the two

contributions to the temperature sensitivity and achieve a temperature-independent attenuation band and also to produce attenuation bands with temperature sensitivities (positive or negative) appropriate to specific applications. It was also verified that the spectral widths of the resonance peaks are broad when they are close to the turning points, and narrower when they are further away from them. The performed thermal treatment through short-term thermal exposure enables an optimization of the fabrication of the LPFGs, mainly at the TAP region (higher sensitivities). The LPFG period can be tuned through the annealing for a short time and also reach thermal stability up to the utilized annealing temperature. Furthermore, the LPFGs annealing procedure made before LPFGs functionalization with nano-assembled thin films is essential to ensure that the LPFG resonance wavelength and intensity remain unchanged with the temperatures used in the depositions procedures.

Long-Period Fiber Gratings: Titanium Dioxide Deposition System and Surrounding Refractive Index Characterization

The LPFGs sensitivity to the SRI could be further improved by selecting the optimum TiO_2 film thickness for a specific cladding mode. Therefore, the LPFGs were annealed, according to previously described procedure before the TiO_2 thin film coating, to ensure that the wavelength and the intensity of the resonance band remain unchanged with the temperature used in the deposition procedure. Titanium dioxide films of 10, 20, 30 and 60 nm thickness were deposited around the grating region by thermal evaporation of pure titanium in a controlled oxygen atmosphere using an electron beam evaporator Auto 306 (Edwards Ltd). The equipment is fitted with a homemade rotary system positioned in the vacuum chamber in order to rotate the LPFGs, as illustrated in Figure 4.46 (a).

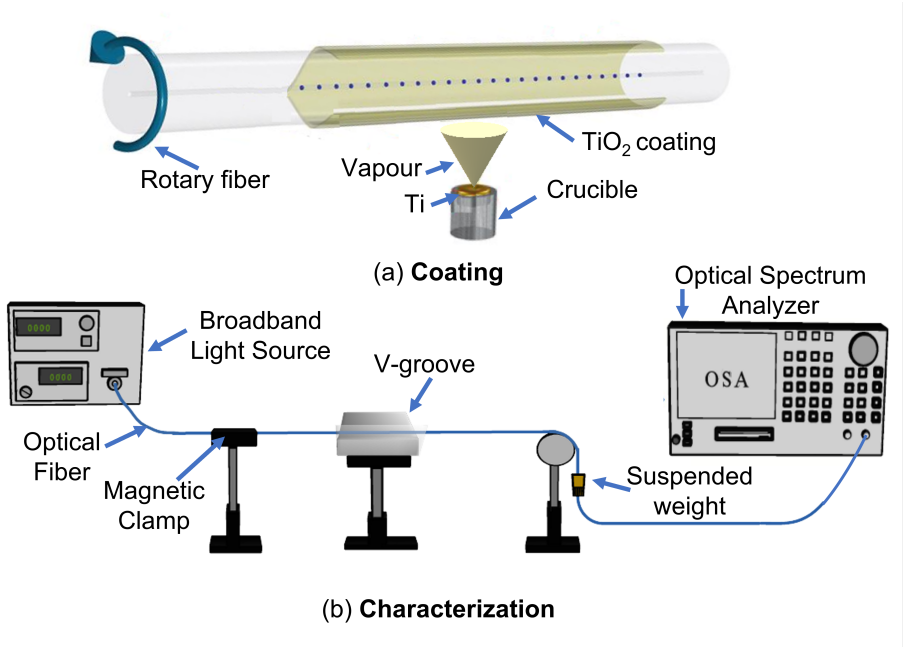


Figure 4.46. *Schematic illustration of the LPFGs: (a) coating, and (b) SRI characterization setups.*

The rotation velocity was set to 5 rpm, a value which was found to produce homogeneous thin films around the cylindrical fibers, for the range of TiO_2 thicknesses used in this work. A quartz microbalance model FTM5 (Edwards Ltd.) gives the value of film thickness deposited on a flat substrate in order to calibrate the deposition process [161, 162, 170]. The details of the deposition system, as well as the TiO_2 deposition and characterization protocols, are thoroughly described in Luís Coelho's doctoral dissertation (2016) [182].

A RI characterization setup was prepared to measure the LPFGs spectrum using different surrounding mediums. The LPFGs were characterized in the transmission mode, keeping the fiber stretched at a constant tension produced by a suspended weight of 5.8 g and measuring the normalized signal from the broadband light source with the OSA without polarization control from 1200 to 1700 nm with a 2 nm resolution. The LPFGs were introduced in a glass V-groove, parallel aligned to the fiber axis, and characterized with RI calibrated oils (Cargille-Sacher Laboratories Inc., U.S.A.), as illustrated in Figure 4.46 (b). The RI oils used belong to the series AAA ${n_D}^{25°C}$ = 1.3000 - 1.3950 $\pm$ 0.0002 and AA ${n_D}^{25°C}$ = 1.4000 - 1.4580 $\pm$ 0.0002 at 1550 nm. After each measurement, both LPFG and the V-groove were cleaned with acetone to avoid contamination of the next SRI oil. The measurements were performed in a temperature-controlled environment, monitoring the temperature during the characterization with a type K thermocouple thermometer (AMECaL ST-9612).

The behavior of the effective index of the asymmetric $LP_{1,12}$ cladding mode as a function of the TiO_2 film thicknesses was characterized through a 2D analysis of the optical fiber structure and the electromagnetic field modes using the mode analysis of the COMSOL Multiphysics®. The optical fiber structure (SMF-28e, Corning) with four concentric layers was simulated, and the parameters value are presented in Table 4.13.

Table 4.13. *Fiber parameters used in the simulation.*

Parameter	Core	Cladding	TiO_2 film thickness	SRI
Radius (µm)	4.1	62.5	$0.04 - 0.24$	200.0
RI	1.4515	1.4453	2.4567	1.0000

The Sellmeier coefficients for germanium-doped silica [184] and silica [185] were used to calculate the core and cladding RIs at 1442.7 nm, respectively, given by the Sellmeier relation reported in [184]. According to DeVore's empirical formula [186], the refractive index of TiO_2 film thickness at 1442.7 nm was determined.

The fs-laser induced RI variation (resembling an elliptic depicted in the inset of Figure 4.36 (a)), in relation to the core, of the reduced (located above) and increased (located under) RI regions were set to -0.025 and 0.009, respectively. These values were determined by the measurements of the RI profile at 980 nm with an IFA-100 (Interfiber Analysis) interferometric system. The dimension used in the structure design tried to represent as close as possible the fs-laser induce RI modification cross-section. The mode profiles of the $LP_{0,1}$ and $LP_{1,12}$ modes, at a wavelength of 1442.7 nm were evaluated, as shown in Figure 4.47 (a), yielding effective mode indices of $\sim$1.44599 and $\sim$1.43847, respectively. These values yield a grating period of 191.8 µm given by

equation 4.12, which was corroborated by the experimental results, where for the same inscription period, the coupling occurs to the asymmetric $LP_{1,12}$ cladding mode.

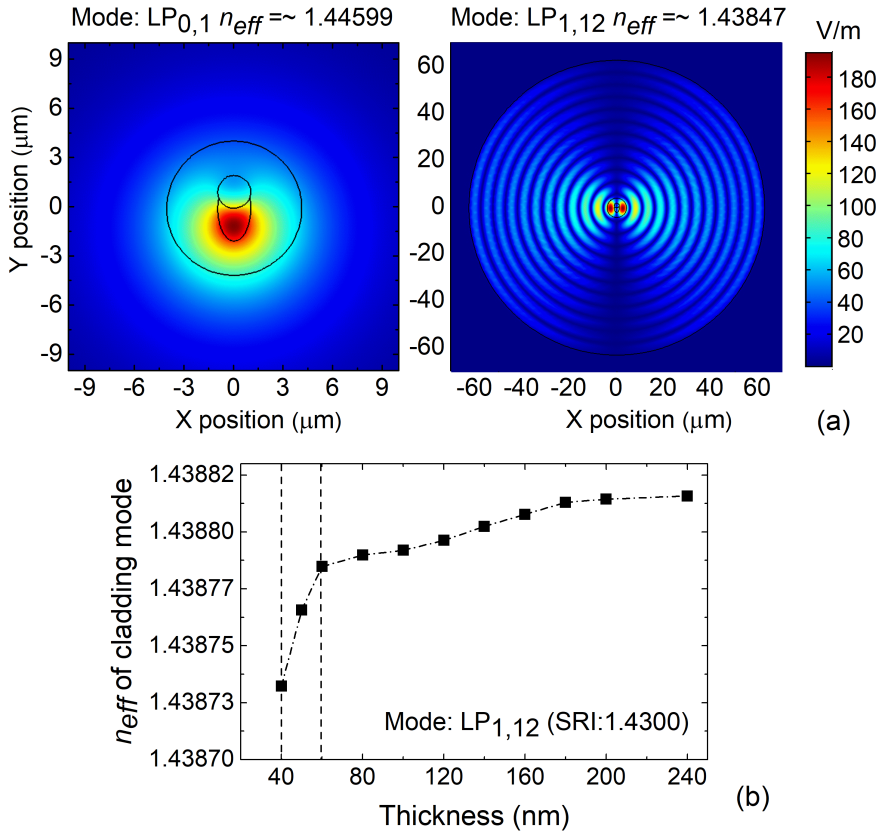


Figure 4.47. *Simulated, (a) mode profiles (electric field norm) for the $LP_{0,1}$ and $LP_{1,12}$ modes, respectively, considering the LPFG surrounded by air and (b) effective RI of the $LP_{1,12}$ cladding mode as a function of the TiO_2 film thickness for a SRI of 1.4300.*

Figure 4.47 (b) shows the variation of the effective RI of the $LP_{1,12}$ mode as a function of the TiO_2 film thickness for a SRI of 1.4300. The simulation was performed for a SRI closer to the cladding material to increase the interaction between the cladding mode and the external medium. The transition region occurs approximately in the range between 40 to 60 nm, as shown in Figure 4.47 (b). Otherwise, for TiO_2 film thicknesses above approximately 60 nm, the effective RI change stabilizes. However, in a more detailed analysis, the highest effective RI change as a function of the TiO_2 film thickness can be observed for a thickness between 40 to 50 nm. Therefore, for LPFGs fabricated with periods between 198.6 to 199.5 μm, and operating at the TAP in an SRI of 1.4300, the optimum TiO_2 film thickness is between 40 to 50 nm. The evolution of the effective RI as a function of TiO_2 film thickness observed is similar to the one reported in [166, 187, 188]. The behavior of the symmetric $LP_{0,10}$ cladding mode, as a function of the TiO_2 film thickness was verified by simulation and experimentally in [158], and the transition region is located between 60 to 80 nm. Thus, the transition regions depend on the grating fabrication period, the order of the coupling mode, and the SRI of interest underlying the film thickness [158, 166, 167]. The simulation (COMSOL Multiphysics® software, version 5.3a) for TiO_2 film thicknesses lower than 40 nm was hampered by compilation issues concerning the minimum mesh size. Consequently,

the experimental results demonstrated here could not be replicated theoretically. The mesh was defined by creating free triangular nodes with an extremely fine element size. However, this mesh does not adapt well to the curved geometry of the TiO_2 film for thicknesses lower than 40 nm, leading to inaccurate results (apparently, recent versions of the software used tackle this issue). Experimentally, the fabricated devices could use thicker TiO_2 films at a cost of a lower sensitivity since the resonances would move away from the TAP. Therefore, the devices can be optimized by increasing the film thickness and adjusting the grating period accordingly in order to maintain the grating very close to the TAP, thus ensuring high sensitivity.

The high RI of TiO_2 film coating promotes a quicker transition between cladding guided modes in overlay guided modes [189]. Therefore, LPFGs fabricated with periods to operate at TAP in air and in water were coated with TiO_2 thin films with a thickness of 10, 20, and 30 nm. The thickness of the coated LPFGs was selected to allow the operation very close to the TAP. This causes a coupling behavior change, which leads to a wavelength and intensity shift of the TAP LPFGs resonances. Table 4.14 presents the wavelength and intensity shifts for each LPFGs after coating. The resonance band split into two after coating, and the separation between the two resonances increases with the TiO_2 film thickness. Furthermore, a decrease of the attenuation band was observed when the TiO_2 thicknesses increased, more pronounced for the attenuation band ($I_{\lambda 1}$) of the 192.5 µm LPFG. The wavelength and intensity shifts also depend on the slope of the characteristic curve of the resonance band.

Table 4.14. *Summary of the spectral characteristics of the TiO_2 coated LPFGs operating very close to the TAP.*

SRI	Λ (µm)	λ_{res} (nm)	I_{res} (dB)	TiO_2 (nm)	$\Delta\lambda_{res}$ (nm)		ΔI_{res} (dB)	
					λ_1	λ_2	$I_{\lambda 1}$	$I_{\lambda 2}$
1.0000	191.8	1442.7	−10.6	10.0	−64.3	52.0	−1.3	1.9
				20.0	−77.0	63.9	−0.5	3.2
1.3330	192.5	1448.6	−15.6	10.0	−36.3	42.4	1.8	−1.9
				20.0	−55.6	58.3	2.8	−2.1
				30.0	−88.8	95.2	4.7	−0.4

Refractive Index Sensing

The wavelength sensitivity to the SRI, between 1.0000 and 1.4480, was assessed for the LPFGs fabricated with periods of 191.8 and 192.5 µm, uncoated (bare), and also coated with TiO_2 film thickness of 10, 20, and 30 nm. For clarity, only few of the acquired spectra are shown in Figure 4.48 (a) and (b) for the uncoated 191.8 and 192.5 µm LPFGs, and in Figure 4.48 (c) and (d) for the 191.8 and 192.5 µm LPFGs coated with 10 and 20 nm thick TiO_2 films, respectively. As can be seen in Figure 4.48, the separation between the two resonances increases with the increase of the TiO_2 thickness, and with the SRI. The LPFGs fabricated with a period of 192.5 µm allows the measurement of a broader RI range, which is restricted by the wavelength measurement range, in this case, up to SRI value of 1.4320 for both the uncoated LPFGs. For the coated LPFGs, the

dual-wavelength resonance measurement was restricted to SRI values lower than 1.4320. The increase of the coating thickness induces broader wavelength shift for a given SRI, which is more noticeable for the wavelength resonance, λ_2.

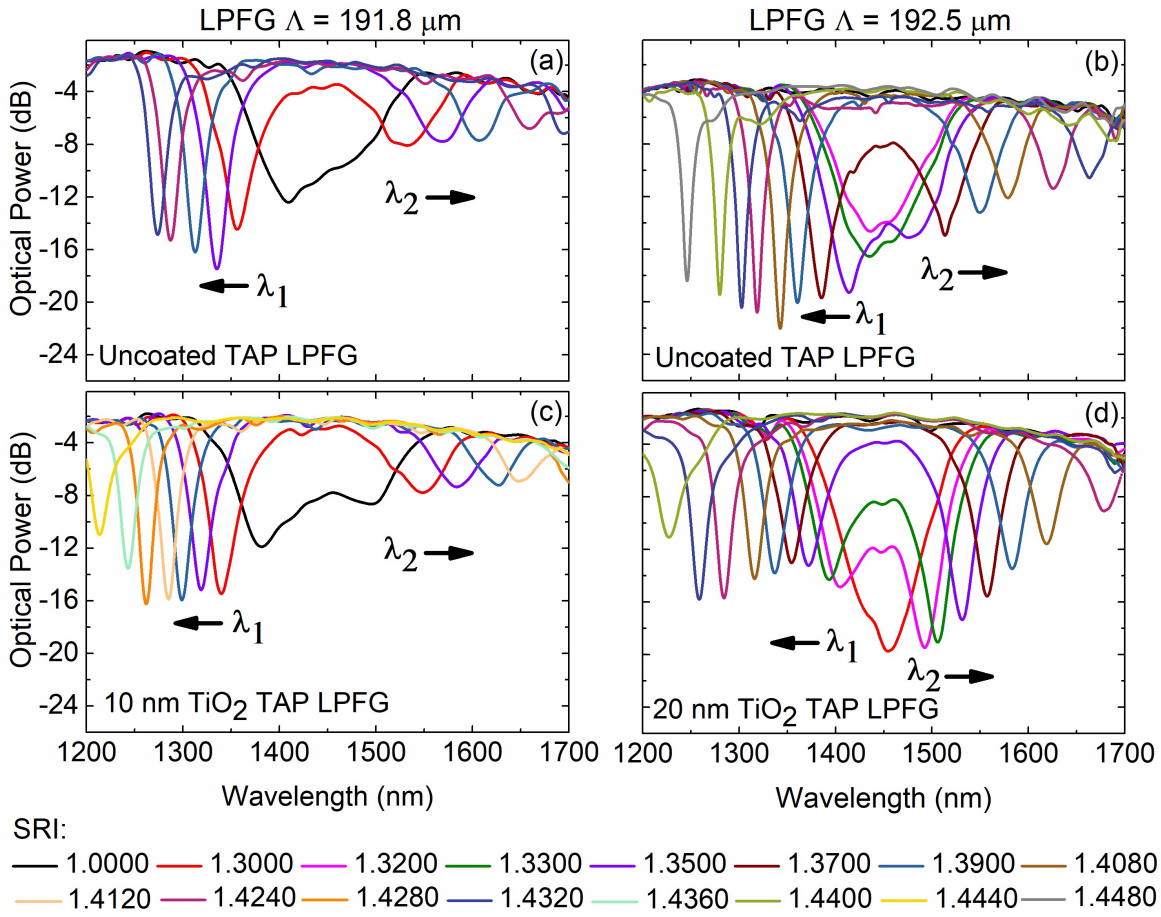


Figure 4.48. *Transmission spectra of LPFGs fabricated with a period of 191.8 and 192.5 μm, (a) and (b) uncoated and, (c) and (d) coated with 10 and 20 nm thick TiO_2 film, respectively for several values of the SRI.*

The normalized wavelengths shifts as a function of the SRI, from 1.3300 to 1.4480, are shown in Figure 4.49 (a) and (b) for the 191.8 and 192.5 μm LPFGs uncoated and TiO_2 coated, respectively. The wavelength response is not linear for this RI range. Thus, the first derivative of the data plotted in Figure 4.49 (a) and (b) were calculated to assess the wavelength sensitivity. In the RI range between 1.3700 to 1.4080, the 191.8 μm coated LPFGs presents a wavelength sensitivity increase to SRI, larger for thicker coating thicknesses. The dual-wavelength resonance measurement was defined as the total wavelength shift between the two resonances ($\Delta\lambda = \lambda_2 - \lambda_1$).

The LPFG coated with 20 nm TiO_2 thickness, presents a maximum wavelength sensitivity of -1583.5, and 2560.7 nm/RIU for the resonances λ_1 and λ_2, respectively. Therefore, a sensitivity value of 4144.2 nm/RIU was reached at a RI of 1.4040.

The 191.8 μm LPFG coated with 10 nm thick TiO_2 film, reached a wavelength sensitivity of 6351.1 nm/RIU (λ_1 = -1611.6, and λ_2 = 4739.5 nm/RIU) at a RI of 1.4200. However, the maximum wavelength sensitivity of 8169.8 nm/RIU (λ_1 = -2020.6, and λ_2 = 6149.2 nm/RIU) at a RI of 1.4320

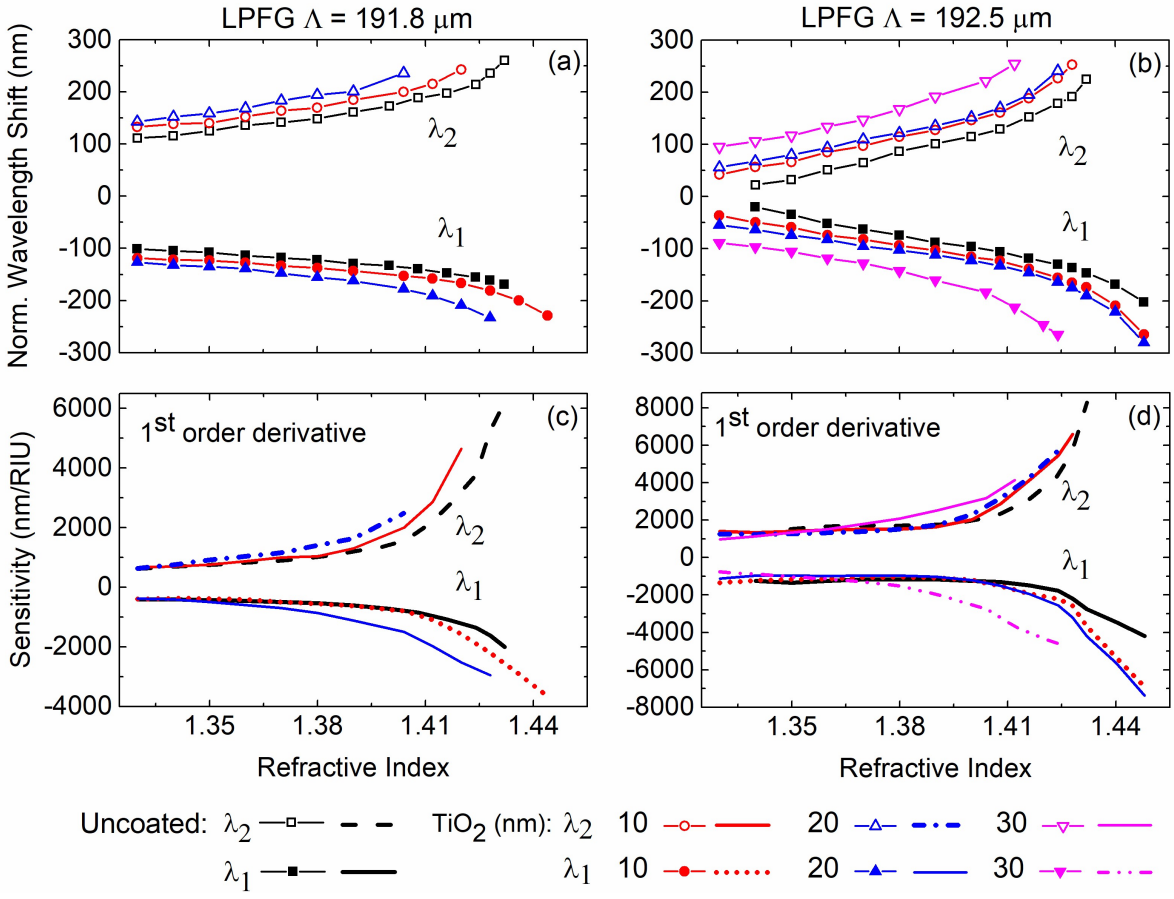


Figure 4.49. *Normalized wavelength shift (a) and (b), and wavelength sensitivity (c) and (d) of the uncoated LPFGs and coated with different TiO_2 films thickness fabricated with a period of 191.8 and 192.5 μm, respectively, as a function of the SRI.*

was found for the uncoated 191.8 μm LPFG. For the 192.5 μm LPFGs a maximum wavelength sensitivity value of 11257.5 nm/RIU (λ_1 = 2876.8, and λ_2 = 8380.7 nm/RIU) at a RI of 1.4320 was found for the uncoated LPFG. Therefore, it can be seen that the uncoated 192.5 μm LPFG sensitivity was improved by a factor of ∼1.4 in comparison to the 191.8 μm LPFG. However, for the 192.5 μm LPFG, it was seen a wavelength sensitivity decrease with the increase of the TiO_2 coating thickness for RI higher than 1.4120. This was due to the impossibility of dual-wavelength resonance measurement (resonance λ_2 outside of the measurement range). As such, the LPFG coated with 10 nm TiO_2 thickness, reached a wavelength sensitivity of 9117.1 nm/RIU (λ_1 = -2580.8, and λ_2 = 6536.3 nm/RIU) at a RI of 1.4280. Regarding the LPFG coated with 20 nm TiO_2 thickness, a wavelength sensitivity of 8347.4 nm/RIU (λ_1 = - 2553.4, and λ_2 = 5794.0 nm/RIU) at a RI of 1.4240 was achieved. In the RI between 1.3700 to 1.4120 (upper limit for dual-wavelength measurement) for all LPFGs, the maximum wavelength sensitivity of 8051.4 nm/RIU ($\lambda_1 = -3773.9$, and $\lambda_2 =$ 4277.5 nm/RIU) was achieved for the LPFG coated with 30 nm of TiO_2. It can be seen that the sensitivity enhancement depends on the fabrication period, which allows operating closer to the TAP region at a specific RI, where the sensitivity reaches maximum values. Furthermore, for SRI closer to the cladding RI of the SMF-28e fiber, i.e., $n_D{}^{25°C}$ = 1.4540, cladding modes interact more with the external medium, leading to the increase of the LPFG sensitivity. However, the increase of

the LPFG sensitivity for the RI range between 1.3700 - 1.4120, was mainly caused by the increase of the TiO_2 film thickness, which enhanced the evanescent wave interaction with the surrounding medium.

The normalized wavelengths shift to SRI in the range between 1.3300 to 1.3700 (i.e., around water-based solutions) was also determined, as depicted in Figure 4.50.

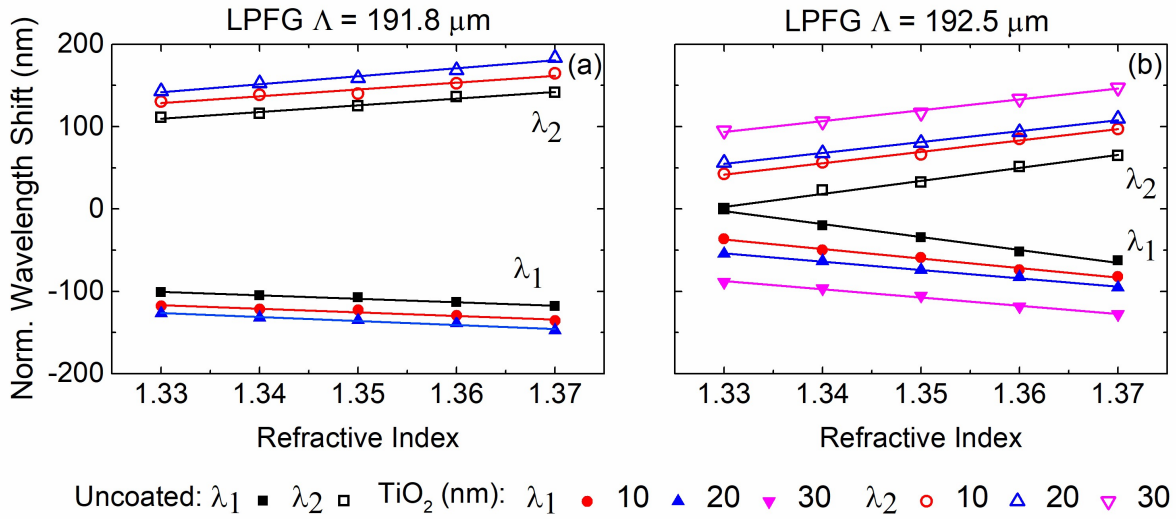


Figure 4.50. *Normalized wavelength shift (a) and (b) for the uncoated LPFGs and coated with different thick TiO_2 films fabricated with a period of 191.8 and 192.5 μm, respectively in the RI range of water-based solutions. Experimental data points were fitted to a linear equation.*

Although the wavelength response to the SRI presents a nonlinear trend, in a narrow SRI range it can be considered linear. Thus a linear fit was applied to the results in Figure 4.50 in order to assess the wavelength sensitivity (average $\pm$ standard deviation), presented in Table 4.15.

For the 191.8 μm LPFGs, the wavelength sensitivity in the RI range of water-based solutions was improved, being higher for larger TiO_2 film thickness. As such, a maximum average wavelength sensitivity of 1458.0 $\pm$ 137.2 nm/RIU (λ_1 = -487.0 $\pm$ 53.7, and λ_2 = 971.0 $\pm$ 85.6 nm/RIU) was achieved for the LPFG coated with 20 nm TiO_2 thickness. For the 191.8 μm LPFGs operation occurs far away from TAP for SRI around water solutions. In this zone of the phase-matching curve, it was found that the TiO_2 coating improves the wavelength sensitivity. Thus, the proper choice of the LPFGs period allows the tuning of the operation at the TAP, which improves the wavelength sensitivity of the bare and coated LPFGs. However, for the 192.5 μm LPFGs, it was found that the wavelength sensitivity decreases with the increase of the TiO_2 coating. Indeed, a maximum average wavelength sensitivity of 3151.8 $\pm$ 177.0 nm/RIU (λ_1 = -1571.9 $\pm$ 90.6, and λ_2 = 1579.9 $\pm$ 99.6 nm/RIU) was achieved for the bare 192.5 μm LPFG. In addition, considering a narrow RI between 1.3300 to 1.3400, the bare 192.5 μm LPFG reaches a wavelength sensitivity of 4294.5 nm/RIU (λ_1 = -2038.0, and λ_2 = 2256.5 nm/RIU).

Table 4.15. *Wavelength Sensitivity for Uncoated and TiO_2 coated LPFGs in the RI range of Water-based solutions.*

Λ (µm)	TiO_2 (nm)	Sensitivity (nm/RIU)		Linearity (R^2)	
		λ_1	λ_2	λ_1	λ_2
191.8	Uncoated	-421.4 ± 27.9	813.0 ± 57.4	0.99	
		$\Delta\lambda = 1234.4 \pm 72.2$			
	10.0	-437.6 ± 58.6	827.3 ± 84.8	0.95	
		$\Delta\lambda = 1264.9 \pm 173.4$		0.93	
	20.0	-487.0 ± 53.7	971.0 ± 85.6	0.96	0.98
		$\Delta\lambda = 1458.0 \pm 137.2$		0.97	
192.5	Uncoated	-1571.9 ± 90.6	1579.9 ± 99.6	0.99	
		$\Delta\lambda = 3151.8 \pm 177.0$			
	10.0	-1156.3 ± 56.3	1382.9 ± 70.4		
		$\Delta\lambda = 2539.2 \pm 177.7$			
	20.0	-1012.0 ± 39.5	1325.0 ± 54.8		
		$\Delta\lambda = 2337.0 \pm 91.2$			
	30.0	-1001.5 ± 50.8	1319.3 ± 65.7		
		$\Delta\lambda = 2320.8 \pm 115.4$			

The wavelengths sensitivity achieved for each LPFG relies on the TiO_2 coating thickness, which by changing the effective indices of the cladding modes induces a shift in the wavelength position of each TAP LPFG. Therefore, it causes the single resonance band to split into two distinct resonances and, consequently, the sensitivity of the TAP LPFGs decreases. The choice of a 192.5 µm fabrication period for an uncoated LPFG allowed the operation at the TAP for RI around water-based solutions, enhancing the wavelength sensitivity to the SRI. The fine-tuning of the LPFG fabrication period to values higher than 192.5 µm, in conjunction with an adequate choice of the TiO_2 film thickness, will allow the operation at TAP for SRI around water-based solutions.

The analysis of the spectral resolution was done as described in the section 4.2.1, and the data concerning the SRI step variations are shown in Figure 4.51.

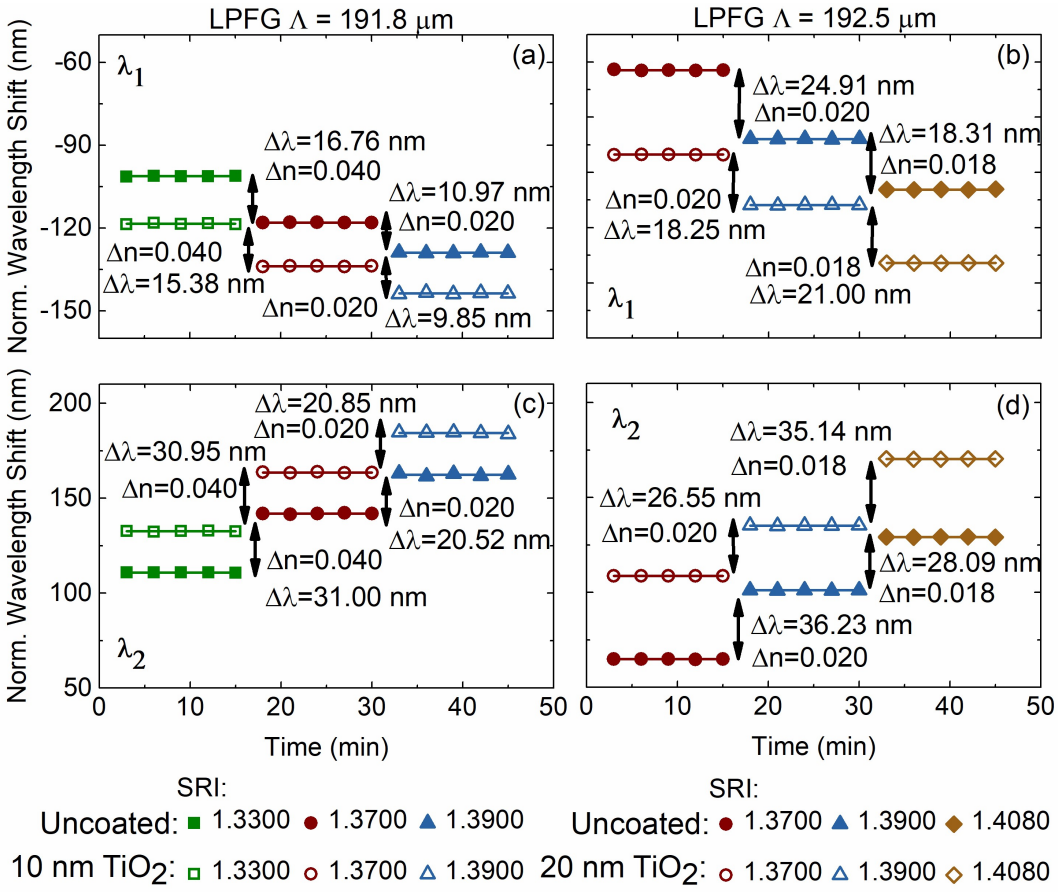


Figure 4.51. *Normalized wavelength shift as a function of time when the surrounding medium undertakes step variations for the resonance: (a) and, (b) λ_1 and (c) and, (d) λ_2 of the LPFGs fabricated with a period of 191.8 and 192.5 μm, respectively.*

Table 4.16 presents the calculated RI resolutions for the bare and TiO_2 coated LPFGs. Refractive index resolutions with magnitudes of 10^{-4} and 10^{-5} RIU were achieved for the LPFGs fabricated with a period of 191.8 and 192.5 μm, respectively.

Table 4.16. *RI Resolutions for the uncoated and TiO_2 coated LPFGs operating around TAP.*

Λ (μm)	TiO_2 (nm)	Step	RI Resolutions	
			λ_1	λ_2
191.8	Uncoated	1	1.7×10^{-4}	2.7×10^{-4}
		2	2.3×10^{-4}	5.9×10^{-4}
	10.0	1	5.7×10^{-4}	2.7×10^{-4}
		2	4.3×10^{-4}	3.1×10^{-4}
192.5	Uncoated	1	1.3×10^{-5}	4.3×10^{-5}
		2	8.2×10^{-5}	6.8×10^{-5}
	20.0	1	8.8×10^{-5}	8.2×10^{-5}
		2	6.9×10^{-5}	5.6×10^{-5}

Finally, a comparison between the LPFGs fabricated in SMF-28e fibers operating at the TAP reported in the literature and the ones developed in this work was realized and summarized in Table 4.17. Thus, among the few LPFGs fabricated in SMF-28e fibers reported operating at the TAP, the LPFGs fabricated on this work exhibited higher sensitivity in comparison to the LPFGs fabricated by electric-arc, fs-laser direct written and also excimer laser exposure.

Table 4.17. *Comparison between the sensitivity displayed by LPFGs operating around TAP reported in the literature and this work*[1].

Fabrication Process	Sensitivity (nm/RIU)	RI Range	Ref.
1. Excimer laser point by point exposure; 2. Chemical Etching.	6269.2	1.3300 – 1.3400	[190, 191]
1. Excimer laser and chromium amplitude mask; 2. Chemical Etching; 3. Coating with TiO_2.	6200.0 4300.0	1.3400 1.3600 – 1.4100	[166]
1. Excimer laser and chromium amplitude mask; 2. Chemical Etching; 3. Coating with diamond-like carbon.	22000.0 2000.0	1.3344 – 1.3355 1.3400 – 1.3560	[192]
Theoretical Work: 1. Chemical Etching; 2. Coating with thin-film.	3750.0 143000.0	1.3300 – 1.3500 1.3300 – 1.3310	[193]
1. Excimer laser point by point exposure; 2. Chemical Etching; 3. Coating with Poly Allylamine Hydrochloride/Poly Acrylic Acid.	5602.0	1.3700 – 1.4100	[194, 195]
1. Excimer laser point by point exposure; 2. Sol-gel-based titania-silica thin film overlay.	7075.3	1.3330 – 1.3340	[167]
1. Chemical Etching; 2. Coating with tin dioxide (SnO_2); 3. Periodic laser ablation.	6430.0	1.3740 – 1.3890	[145]
Electric arc discharges	590.0	1.3300 – 1.4200	[144]
Femtosecond laser direct written	930.0	1.3330 – 1.3980	[155]
1. Femtosecond laser direct written; 2. Coating with TiO_2.	3151.8 4294.5 **11257.5** **8051.4**	1.3300 – 1.3700 1.3300 – 1.3400 1.4320 1.3700 – 1.4120	This Work

[1]This comparison was restricted to the LPFGs operating around the TAP and fabricated in the SMF-28e fiber.

Nevertheless, the maximum sensitivity (i.e., 143000 nm/RIU for a very narrow RI range between 1.3300 to 1.3310, [193]) was theoretically achieved for the TAP LPFGs with reduced cladding diameter and coated with a thin film. Experimentally, a sensitivity over 22000 nm/RIU for a very narrow RI range between 1.3344 to 1.3355 was reported for the TAP LPFGs with reduced cladding diameter and coated with a diamond-like carbon thin film [192]. The demonstrated LPFGs sensitivity enhancement relies mainly on the evanescent interaction achieved by reducing the cladding diameter. However, this approach involves a complex fabrication process to tune the LPFG operation at the TAP and makes the optical fiber fragile and difficult to handling. The fabrication process proposed in this work allows optimizing the LPFGs sensitivity to the SRI without making the optical fiber fragile in comparison to the fabrication process using chemical etching.

Indeed, the increase of the LPFGs sensitivity for SRI closer to 1.4300, mainly caused by the increase of the TiO_2 film thickness, makes them suitable, for example, for the detection of fuel adulteration (kerosene in petrol), which leads to air pollution and the consequent effects on public health. The refractive index of pure petrol and kerosene are 1.4270 and 1.4420, respectively [173]. The LPFGs can also be coated with a polymer engineered to be sensitive to external parameters, and having a RI close to the value where the highest sensitivity was obtained, and that changes with the ambient humidity or the presence of a specific gas, for example [167]. LPFGs operating at the TAP inscribed by a CO_2 laser in B-Ge doped fiber for fuel adulteration detection was reported in [196]. Here, an average grating sensitivity of 1635.0 nm/RIU for SRI in the range between 1.3970 to 1.4372 has been demonstrated. Nevertheless, a maximum wavelength sensitivity value of 11257.5 nm/RIU at a RI of 1.4320 was reported in our work. Therefore, it can be seen that the LPFG sensitivity was improved by a factor of $\sim$6.9 in comparison to TAP inscribed by a CO_2 laser [196].

Spectral Tuning and Refractive Index Sensitivity of LPFGs

The fs-laser written LPFGs, as previously described, can be reliably used for various applications. However, temperature annealing is necessary to achieve the regime of spectral stability. The thermal treatment modifies the grating's spectral properties, affecting its sensitivity to SRI changes. Therefore, the spectral response of fs-laser LPFGs to variations in the surrounding refractive index was characterized before and after the annealing process. The results of the spectral variations at annealing temperatures ranging up to 950 °C, alongside an analysis of the SRI sensitivity before and after the annealing process, are presented.

A characterization setup was mounted to measure the spectrum of LPFGs at different surrounding mediums and temperatures, similar to what was illustrated in Figure 4.39. The setup consisted of a sliding tubular oven (Termolab), a glass V-groove parallel aligned to the fiber axis, and an OSA (model Yokogawa AQ6370D). The optical fibers with the fs-laser LPFGs, with a period of 372.5 µm and a length of 30 mm, were introduced in a tubular oven. The annealing process was realized at a constant temperature ranging from 25 °C to 950 °C in steps of 50 °C, for a period of 5 min in each step. The grating spectra were recorded after each annealing step, and subsequently after the grating cool down to room temperature. Following, the LPFGs were introduced in a glass V-

groove, parallel aligned to the fiber axis, and characterized with RI calibrated oils (Cargille-Sacher Laboratories Inc., U.S.A.), as illustrated in Figure 4.46 (b). The RI oils used belong to the series AAA $n_D^{25°C}$ = 1.3000 - 1.3950 ± 0.0002 and AA $n_D^{25°C}$ = 1.4000 - 1.4580 ± 0.0002 at 1550 nm. After each measurement, both LPFG and the V-groove were cleaned with acetone to avoid contamination of the next SRI oil. The measurements were performed in a temperature-controlled environment, monitoring the temperature during the characterization with a type K thermocouple thermometer (AMECaL ST-9612). The LPFGs were characterized in the transmission mode, with the optical fiber being subjected to an axial tension produced by a suspended weight of 5.8 g. The signal was measured without polarization control from 1350 to 1650 nm with a 1 nm resolution. All spectra were normalized to the transmitted spectrum of the ASE broadband light source (model ASE2000).

Figure 4.52 presents the LPFG measured transmission spectra, and wavelength shift at room temperature (25 °C) after annealing at each temperature.

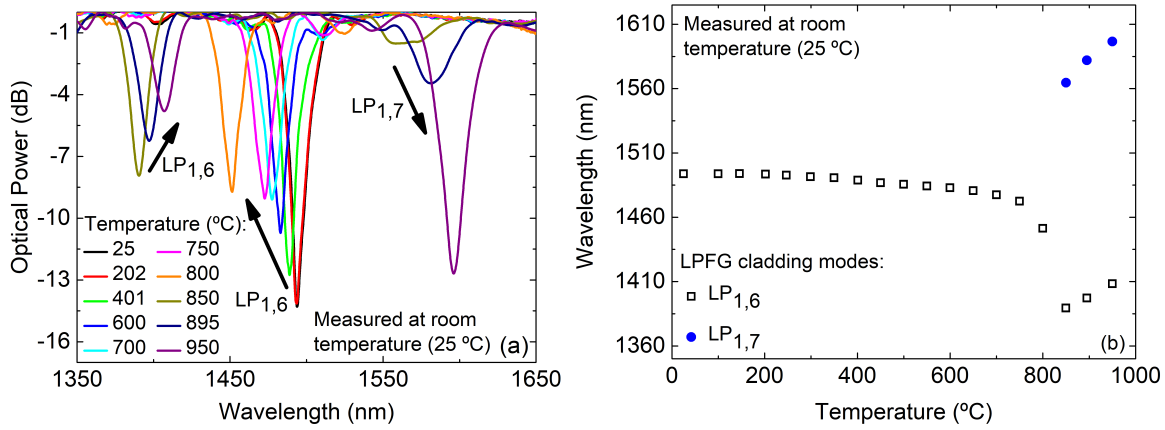


Figure 4.52. *Fs-laser LPFG inscribed with a period of 372.5 µm, measured at room temperature: (a) transmission spectra; (b) wavelength shift.* ***All measurements were acquired after annealing the grating at different temperatures****.*

The sensitivity to temperature of the LPFG is around 91 pm/°C for this type of fibers and a red shift of the wavelength resonance is observed [197]. The thermal annealing of femtosecond LPFGs allows the stabilization of the core modulation, with a small blue shift at room temperature after new temperature increase being observed. From Figure 4.52 this behavior is similar up to 750 °C with a shift of 21.2 nm where it starts to increase up to 850 °C with a larger blue shift of 83.2 nm. At this point the higher order mode $LP_{1,7}$ appear at 1560 nm. For temperatures above 850 °C, a red shift is observed for both modes: 11.16 nm for the mode $LP_{1,6}$ and 14.64 nm for the $LP_{1,7}$.

Figure 4.53 (a) and (b) present the measured transmission spectra (before and after annealing at 950 °C) corresponding to the $LP_{1,6}$ and $LP_{1,7}$ modes, for several values of the SRI. The normalized wavelength shifts to the initial state (RI = 1.000) as a function of the SRI, from 1.3000 to 1.4520, are shown in Figure 4.53 (c) for the $LP_{1,6}$ mode before and after annealing, and for the $LP_{1,7}$ mode after annealing. The first derivative of the data plotted in Figure 4.53 (c) was calculated to assess the wavelength sensitivity (Figure 4.53 (d)). The $LP_{1,6}$ and $LP_{1,7}$ cladding modes reached a wavelength sensitivity of 1400 nm/RIU and 2400 nm/RIU at a RI of 1.4400, respectively. Thus, the $LP_{1,7}$ mode exhibited higher sensitivity (i.e., a maximum sensitivity of

3200 nm/RIU) in comparison to the mode $LP_{1,6}$, which kept its average behavior before and after annealing.

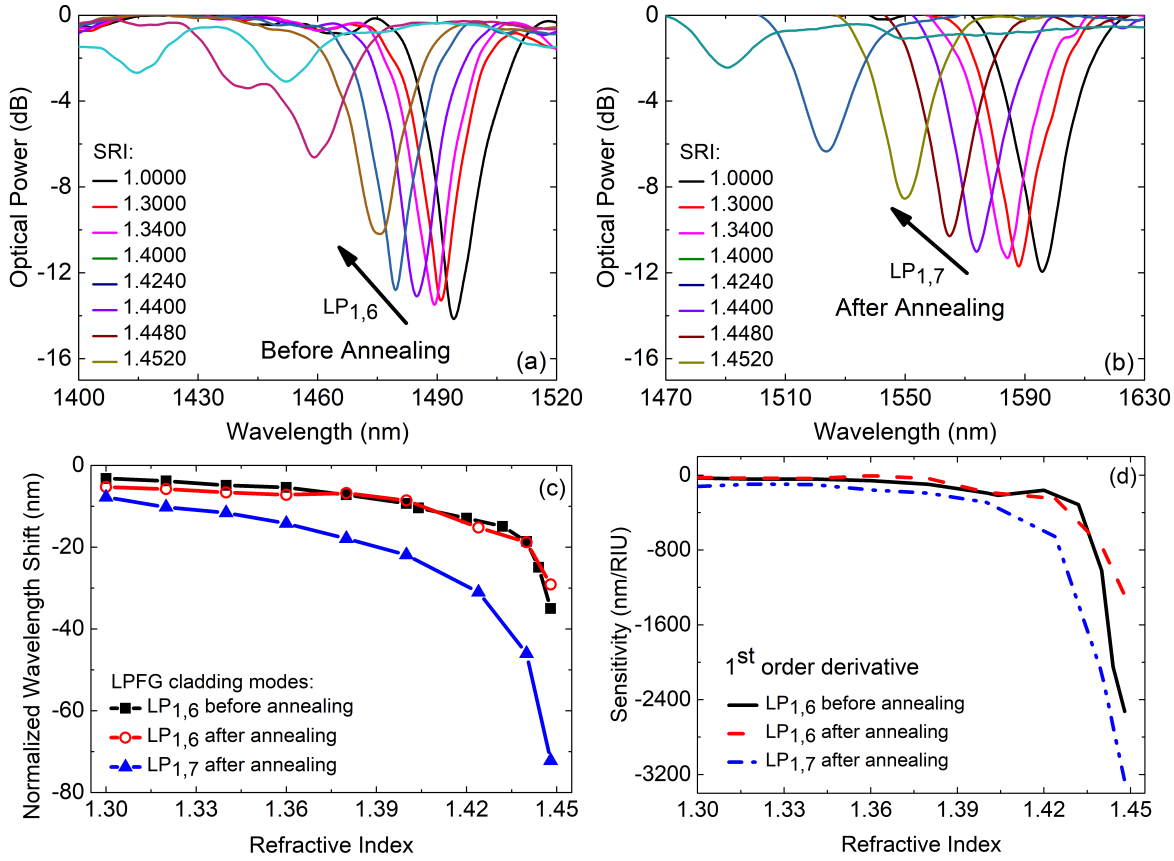


Figure 4.53. *Transmission spectra of the LPFG fabricated with a period of 372.5 µm for the (a) $LP_{1,6}$ mode before annealing, and (b) $LP_{1,7}$ mode after annealing; (c) Normalized wavelength shift, and (d) wavelength sensitivity for several values of the SRI.*

The analysis of the spectral resolution was done as described in the section 4.2.1, and the data concerning the SRI step variations are shown in Figure 4.54.

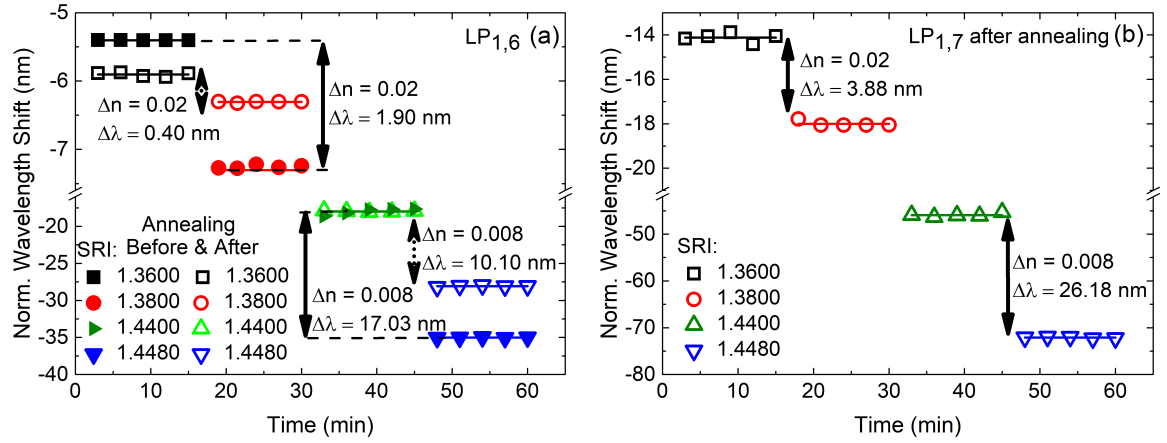


Figure 4.54. *Normalized wavelength shift as a function of time when the surrounding medium undertakes step variations for the (a) $LP_{1,6}$ and (b) $LP_{1,7}$ cladding modes .*

Table 4.18 presents the calculated RI resolutions for the $LP_{1,6}$ and $LP_{1,7}$ cladding modes. Refractive index resolutions with magnitudes of 10^{-3} were achieved for the $LP_{1,6}$ (before and after annealing) and $LP_{1,7}$ cladding modes.

Table 4.18. *RI Resolutions for the cladding mode $LP_{1,6}$ and $LP_{1,7}$.*

LPFG cladding mode	Annealing Process	Step	RI Resolutions
$LP_{1,6}$	Before	1	3.9×10^{-3}
		2	1.2×10^{-3}
	After	1	3.9×10^{-3}
		2	2.3×10^{-3}
$LP_{1,7}$	After	1	2.8×10^{-3}
		2	3.1×10^{-3}

LPFGs Coated with Titanium Dioxide Thin Films

The characterization of the bare LPFG has been completed. However, is still possible to enhance the sensitivity to the external mediums by coating the LPFG surface with different thin films of oxide with high-refractive-index, as TiO_2. The transmission spectra corresponding to the $LP_{1,6}$ cladding mode of three LPFGs, from 1425 to 1575 nm, uncoated (bare) and coated with a 30 and 60 nm thick TiO_2 films with air (RI = 1.000) as the SRI are shown in Figure 4.55.

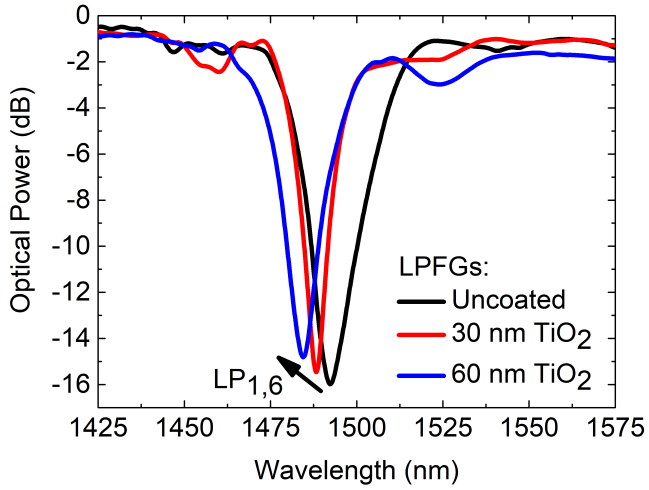


Figure 4.55. *Transmission spectra of the LPFGs, uncoated and coated with 30 and 60 nm thick TiO_2 films, in air (RI = 1.0000).*

The coating of the LPFGs with 30 and 60 nm thick TiO_2 films, leads to a shift to shorter wavelengths of the attenuation band of about 4.1 and 7.9 nm, respectively and a decrease of the resonance amplitude, as summarized in Table 4.19. This behaviour is consistent with the results presented in the literature, for the LPFGs fabricated by the electric arc technique SMF-28e fiber, and coated with TiO_2 [170]. The wavelength and amplitude of the attenuation band depends on the effective refractive index of the cladding modes, which in turn depends on the SRI. The thin film induces a

re-distribution of the cladding modes that leads to wavelength shift and amplitude intensity variation of the attenuation bands.

Table 4.19. *Summary of the spectral characteristics of the TiO_2 coated LPFGs.*

SRI	Λ (µm)	λ_{res} (nm)	I_{res} (dB)	TiO_2 (nm)	$\Delta\lambda_{res}$ (nm)	ΔI_{res} (dB)
1.0000	372.5	1492.1	−16.0	30.0	−4.1	0.5
				60.0	−7.9	1.2

The transmission spectra of a bare, 30 and 60 nm thick TiO_2 coated LPFGs were measured for SRI in the range 1.0000 to 1.6400, and the recorded spectra are presented in Figure 4.56 (a) and (b) for the $LP_{1,6}$ and $LP_{1,7}$ cladding modes. For clarity, only some of the acquired spectra are shown.

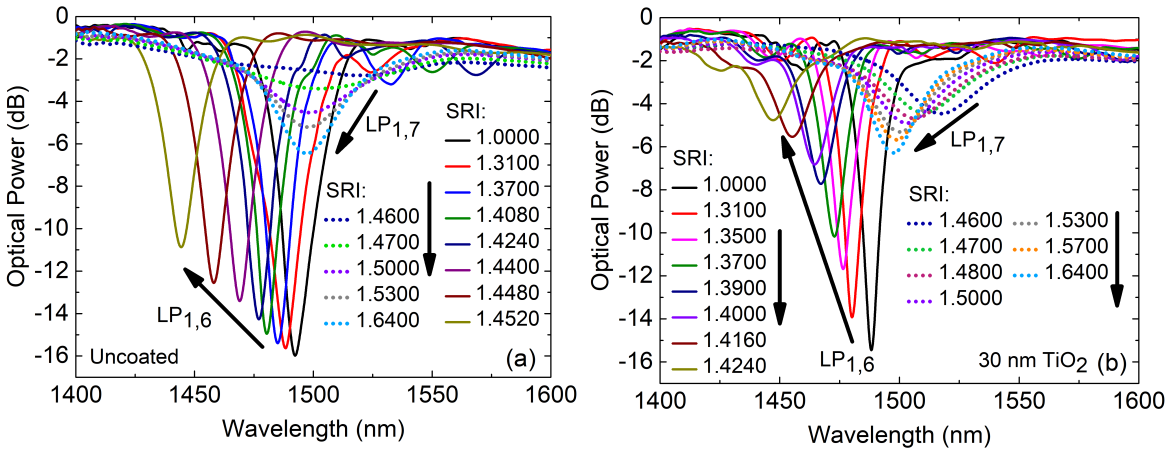


Figure 4.56. *LPFGs transmission spectra ($LP_{1,6}$ and $LP_{1,7}$ cladding modes) for several values of the SRI, for: (a) uncoated, and (b) coated with 30 nm thick TiO_2 film.*

As the SRI increases from 1.0000 to 1.4520, the resonance wavelength gradually blue-shift, and the intensity loss decreases. However, for SRI higher than the cladding refractive index (1.4570), the coated LPFG shows a resonance wavelength shift and intensity loss increase, while the bare LPFG only exhibits an intensity loss increase. The normalized wavelength shift, and the optical power variation to the initial values (RI = 1.000) as a function of the SRI, from 1.3000 to1.6400, are shown in Figure 4.57 (a) and (b), for the LPFGs uncoated and coated with 30 and 60 nm thick TiO_2 films, respectively. It must be noticed that for SRI values from 1.300 to 1.400, characteristic of many biological materials [170], the normalized wavelength shift is higher for the TiO_2 coated LPFGs. This is, the higher the film thickness, the higher is the wavelength shift. In this range, a bare LPFG provides very low sensitivity. In addition, for SRI greater than the cladding refractive index, the attenuation bands shifts to higher wavelengths, and an increase in the attenuation bands is observed. This behaviour is similar for bare and coated LPFGs. However, the wavelength shift with the SRI is much more noticeable for the coated LPFG due to the higher effective refractive index of the modified cladding layer. The bare LPFG is wavelength insensitive to SRI variations above the cladding refractive index, as demonstrated, [170].

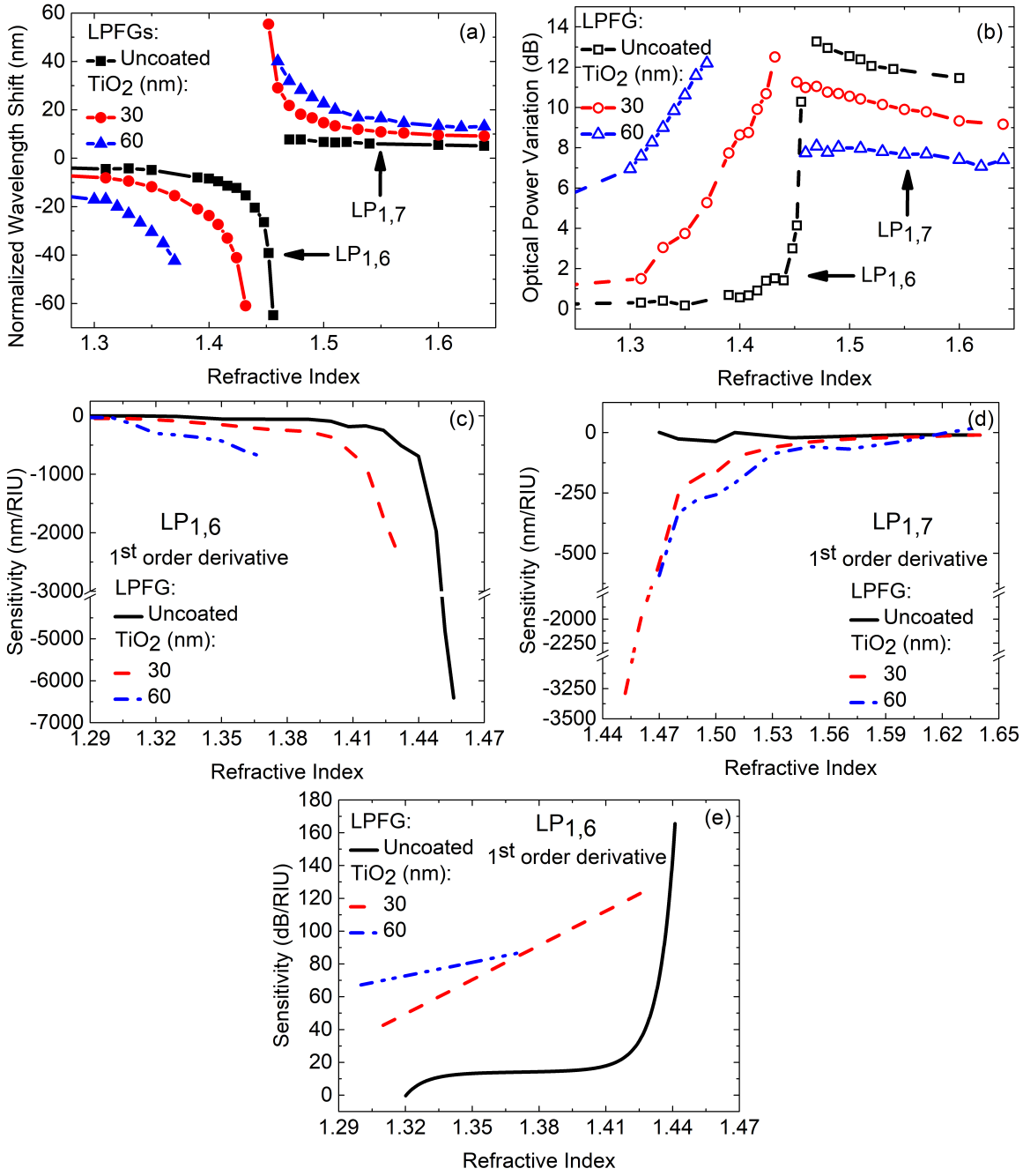


Figure 4.57. *LPFGs uncoated, and coated with 30 and 60 nm thick TiO_2 films: (a) normalized wavelength shift, (b) optical power variation; wavelength sensitivity for (c) $LP_{1,6}$ and (d) $LP_{1,7}$ cladding modes, and (e) optical power sensitivity as a function of the SRI.*

The first derivative of the data plotted in Figure 4.57 (a) and (b) were calculated, to assess the wavelength and intensity sensitivities shown in Figure 4.57 (c), (d), and (e). It was observed that the sensitivity increases for higher TiO_2 coating thickness being possible to choose the film thickness according to the SRI that needs to be measured. For example, from 1.3400 to 1.3700 RI range, the average normalized wavelength shift is lower than 60 nm/RIU for the bare LPFG, and ∼570 nm/RIU for the LPFG coated with 60 nm TiO_2, as shown in Figure 4.57 (a). For SRI values higher than the cladding refractive index, a sensitivity over ∼3000 nm/RIU was determined

for 30 nm of TiO_2 thick film, as shown in Figure 4.57 (b). From Figure 4.57 (c) it can be observed a region where a linear sensitivity behaviour was obtained for SRI smaller that the cladding refractive index, enabling the use of the intensity power variation to measure the SRI variation. For 30 nm of TiO_2, the LPFG is useful from 1.310 to 1.432, where the optical power variation is a quasi-linear function of the SRI, with a range of $\sim$10 dB. Additionally, as shown in Figure 4.57 (c), values of sensitivity as high as 50 dB/RIU at 1.320 and 120 dB/RIU at 1.420 can be achieved by selecting the appropriate film thickness. A limited range of SRI values can be accessed by using the optical power variation with a bare LPFG.

The analysis of the spectral resolution was done as described in section 4.2.1, and the data concerning the SRI step variations are shown in Figure 4.58.

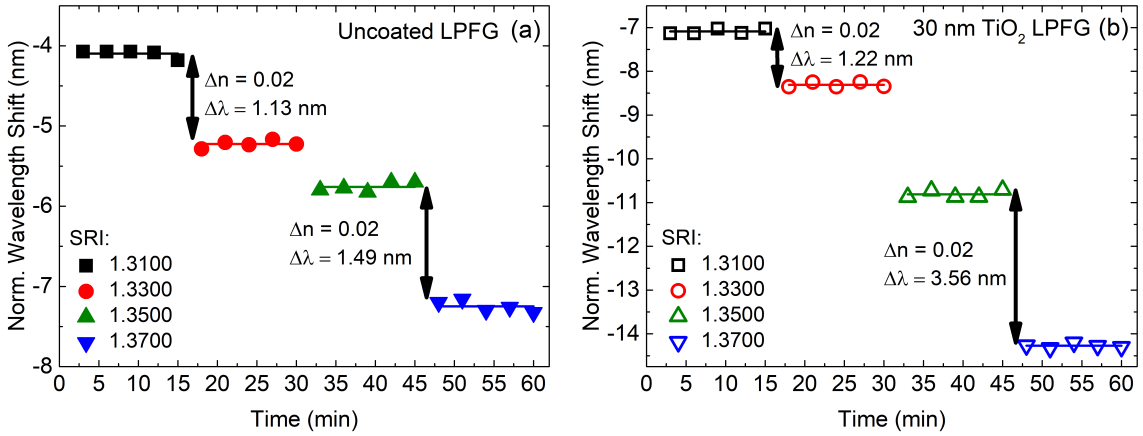


Figure 4.58. *Normalized wavelength shift as a function of time when the surrounding medium undertakes step variations for the LPFGs fabricated with a period of 372.5 µm, (a) uncoated and (b) coated with 30 nm thick TiO_2 film.*

Table 4.19 presents the calculated RI resolutions for the uncoated and TiO_2 coated LPFG. Refractive index resolutions with magnitudes of 10^{-3} and 10^{-4} RIU were achieved for the LPFGs uncoated, and coated with 30 nm thick TiO_2 film, respectively.

Table 4.20. *RI Resolutions of the LPFGs, uncoated and coated with 30 nm thick TiO_2 film.*

Λ (µm)	TiO_2 (nm)	Step	RI Resolutions
372.5	Uncoated	1	2.2×10^{-3}
		2	2.5×10^{-3}
	30.0	1	2.4×10^{-4}
		2	3.1×10^{-4}

Characterization of Strain Sensitivity

The fabricated LPFGs (with an RI modulation period of 369 µm and 191.8 µm) were subjected to mechanical strain, by gluing one extreme of the optical fiber to a micro-positioning stage, while the other side was glued to a fixed holder (Figure 4.59).

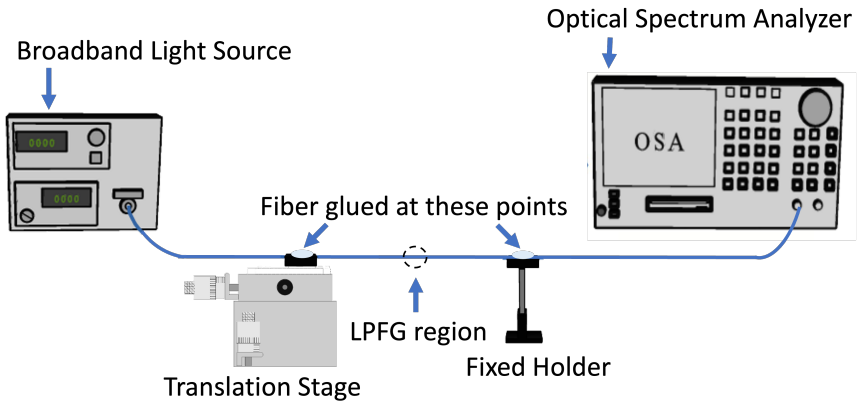


Figure 4.59. *Schematic illustration of the LPFGs strain characterization setup.*

The LPFGs were stretched from 0 to 1933.3 με in intervals of 66.7 με; the measurements were made at room temperature (∼ 23 °C). Some of the acquired transmission spectra of the 369 μm LPFG and 191.8 μm TAP LPFG for different strain values are shown in Figure 4.60 (a) and Figure 4.61 (a), respectively.

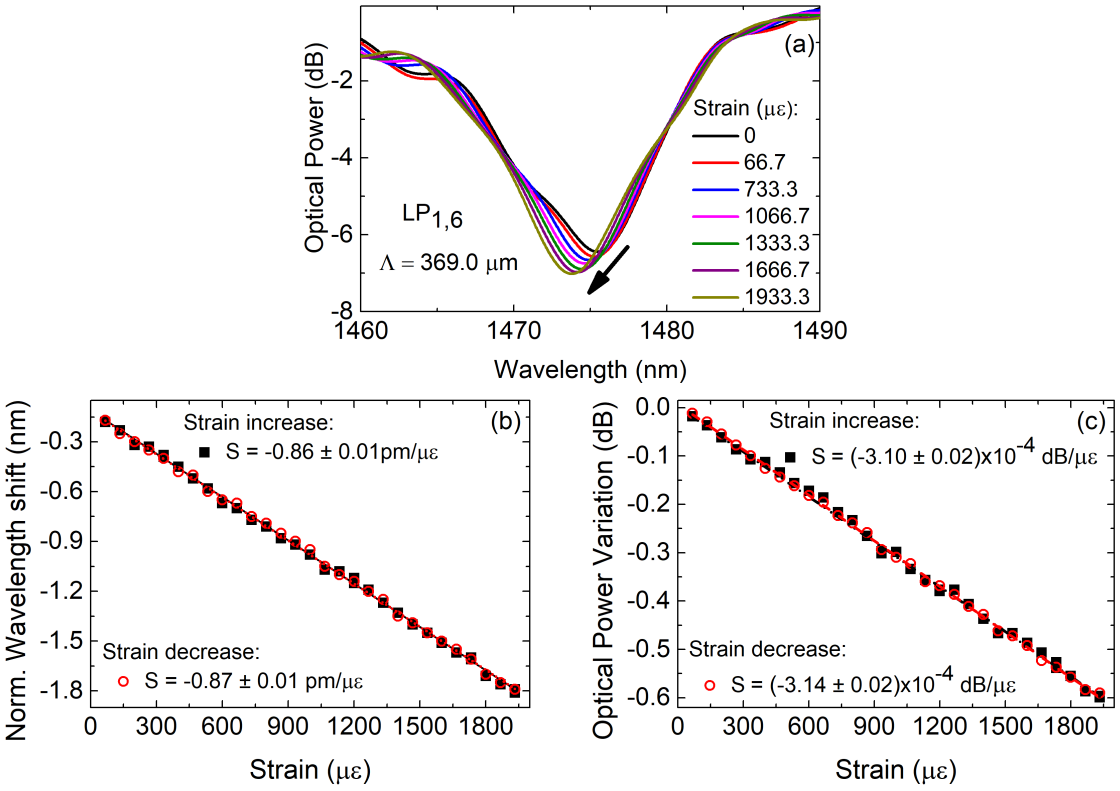


Figure 4.60. *Transmission spectra of the LPFG for different strain values (a), normalized wavelength shift (b), and normalized optical power variation as a function of strain (c).*

For these LPFGs, the transmission spectra evolution was recorded during both the increase and decrease of fiber strain. When the fiber is stretched, there is a shift in the resonance wavelength mainly due to changes in the grating period. The transmission spectra corresponding to the

resonance wavelength of the 369.0 µm LPFG ($LP_{1,6}$ mode) blue-shifted at the maximum applied strain, exhibiting a linear sensitivity of -0.87 ± 0.01 pm/µε (and $R^2 > 0.99$), Figure 4.60 (b). The normalized optical power increases uniformly with the applied strain, exhibiting a strain sensitivity of $(-3.14 \pm 0.02) \times 10^{-4}$ dB/µε with a linearity of $R^2 > 0.99$, as shown in Figure 4.60 (c). The transmission spectra corresponding to the resonance wavelength of the 191.8 µm TAP LPFG ($LP_{1,12}$ mode) red-shifted at the maximum applied strain, exhibiting a nonlinear sensitivity of 0.83 ± 0.01 pm/µε (and $R^2 > 0.99$), Figure 4.61 (b). The normalized optical power decreases uniformly with the applied strain, exhibiting a strain sensitivity of $(1.62 \pm 0.01) \times 10^{-3}$ dB/µε with a linearity of $R^2 > 0.99$, as shown in Figure 4.61 (c). Furthermore, no hysteresis was observed in the strain measurements for both LPFGs.

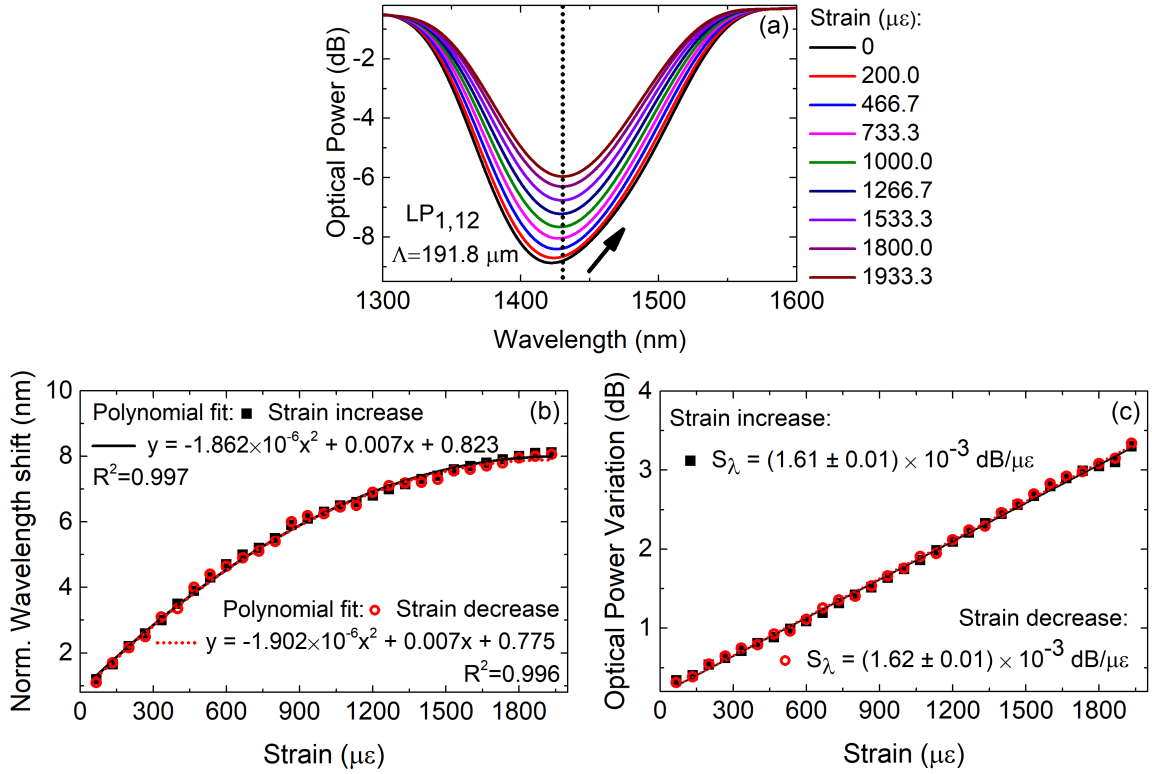


Figure 4.61. *Transmission spectra of the TAP LPFG for different strain values (a), normalized wavelength shift (b), and normalized optical power variation as a function of strain (c).*

The strain sensitivities obtained, approximately -0.87 pm/µε for the attenuation bands of the LPFGs with grating periods of 369 µm and 191.8 µm, are consistent to the sensitivities values reported in the works [130, 148, 175, 198, 199]. Thus, strain in LPFGs induces changes in both the refractive index, due to the photo-elastic effect, and the fiber dimensions, as a result of Poisson's effect. The influence of these factors is determined by the cladding mode order and the fiber composition and has a direct effect on the strain sensitivity of the device [130, 148, 175, 198, 199]. In addition, by selecting an appropriate fiber composition and grating period, attenuation bands can be fabricated to be insensitive to temperature or strain, allowing independent measurement of these parameters [130, 175, 200]. Alternatively, differential shifts in two or more resonance bands

of a single LPFG can be used to simultaneously and independently measure temperature and strain, leveraging their distinct sensitivities to these measurands [130, 175, 199, 200].

4.2.4 Summary

The fabrication of LPFGs in an SMF-28e fiber through fs-laser direct writing was demonstrated. The nonlinear nature of the absorption process of the fs-laser pulses, combined with the high precision and flexibility of the developed direct writing system allowed the fabrication of LPFGs with different cladding order modes (e.g., $LP_{1,6}$ and $LP_{1,12}$) by just selecting a particular period (e.g., 372.5 and 191.8 µm). The precise fabrication of LPFGs operating at the TAP in an SMF-28e fiber through fs-laser direct writing was demonstrated. The inscription of LPFGs with a clear spectrum without higher-order interference peaks was achieved by writing RI modification with a laser pulse energy of 120 nJ at a depth of 60 µm from the top center position of the fiber cladding. The LPFGs operating at the TAP of the asymmetric $LP_{1,12}$ cladding mode in air and water were fabricated with an RI modulation period of 191.8 and 192.5 µm, yielding a resonance wavelength at approximately 1442.7 and 1448.6 nm, respectively. It was demonstrated that the precise fabrication of the fs-laser LPFGs operating at the TAP requires a precise control on the fiber alignment, submicrometric control of the grating period, the focal position of the laser beam as well as the fiber tension during fabrication. The polarization behavior of LPFGs, driven by birefringence, is critical for defining their operation and functionality. The LPFGs fabricated by the fs-laser direct written system with different duty cycles and writing positions in the optical fiber, were explored to determine how changes in these parameters affect the grating's spectral response, i.e., wavelength, optical power, and birefringence. Thus, for the grating period of 182.7 µm, it was verified that the $LP_{1,12}$ mode exhibits a TAP at $\sim$1388.0 nm and $\sim$1380.0 nm when measured without polarization control and under vertical polarization, respectively. In addition, under horizontal polarization, the $LP_{1,12}$ mode exhibits two resonances around the TAP region at $\sim$1334.8 and $\sim$1436.0 nm, with a wavelength separation ($\Delta\lambda$) of 101.2 nm.

The experimental results show that the fabricated LPFGs must be annealed to stabilize their spectra. We demonstrated the fine-tuning of the resonance band's position and thermal stability up to 600 °C. The fabrication of LPFGs at the TAP, with thermal stability up to 200 °C was achieved, which holds on the high sensitivity characteristics. From 25 to 300 °C, the TAP LPFG exhibits a single resonance that is wavelength-independent of temperature and presents a temperature dependence of 0.0372 dB/°C. Furthermore, temperature dependences of -180.73 and 179.29 pm/°C were achieved for the λ_1 and λ_2 resonances, respectively, in the temperature range from 250 to 600°C. The temperature dependence of 124.76 pm/°C up to 600 °C was achieved for the 372.5 µm LPFG. Thus, it was demonstrated that an LPFG has attenuation bands with positive, negative, and independent wavelength responses to temperature. The temperature and strain dependence is associated with the LPFG period, the order of the cladding mode, and the composition of the optical fiber. The robust nature of the fabricated devices opens the possibility of high-temperature sensing with high sensitivity and also chemical and bio-chemical sensing with a thermally stable and temperature-independent attenuation band.

The LPFGs were coated with different TiO_2 film thickness to improve the sensitivity to SRI, and their spectral behavior around the TAP in air and water characterized. The wavelength sensitivity to the SRI was also assessed. Therefore, a maximum sensitivity of $\sim$8051.4 nm/RIU in the range between 1.3700 to 1.4120 was obtained for the 192.5 µm LPFG coated with 30 nm TiO_2 thickness. The maximum sensitivity in the RI range of water-based solutions was approximately 3151.8 nm/RIU, achieved for the uncoated 192.5 µm LPFG. The SRI sensitivity could be further improved, tuning the LPFG fabrication period to operate at the TAP accordingly to the TiO_2 film thickness. Another approach could be to tune the operation at TAP by reducing the cladding diameter and posterior coating with different TiO_2 film thickness. In addition, it was observed an increase of the wavelength and optical power sensitivities over broader ranges of SRI, including for values higher than the cladding refractive index. A limited range of SRI values can be accessed by using the optical power variation with a bare LPFG. Compared with the LPFGs fabricated by electric arc discharge, and coated with 60 nm of TiO_2, where a sensitivity of 525 nm/RIU at 1.3600 was reported [169, 170], the fs-laser fabricated LPFGs, and also coated with 60 nm of TiO_2 presented in this work has higher sensitivity, reaching values of $\sim$570 nm/RIU at 1.3600. For SRI values higher than the cladding refractive index, a sensitivity over $\sim$3000 nm/RIU was determined for 30 nm of TiO_2 thick film, a region where the bare LPFGs are useless. For 30 nm of TiO_2, the LPFG is useful from 1.3100 to 1.4320, where the optical power shift is a quasi-linear function of the SRI, with a range of $\sim$10 dB.

The LPFGs, showing the mode $LP_{1,6}$ at 1500 nm, were exposed to high-temperature annealing up to 950 °C. Modifications in the refractive index modulation are observed through a blue-shift in the LPFG attenuation bands and above 850 °C, the mode $LP_{1,7}$ appear at 1600 nm. The wavelength sensitivity to external RI from 1.300 to 1.452 was estimated for both modes before and after annealing. Greater sensitivity was found for the higher order mode in the entire range reaching 2400 nm/RIU around 1.440. After annealing the LPFG at high temperature, a higher cladding mode appears, which means that we can fine tune the grating position with thermal treatment instead of varying the period of the refractive index modulation. The LPFG with a period of 372.5 µm after annealing treatment shows RI sensitivity up to 3200 nm/RIU, for the cladding mode $LP_{1,7}$. Extensive work needs to be done in order to understand the effects of the annealing the femtosecond inscribed LPFG at higher temperatures.

4.3 Optical Fiber Interferometers

Optical interferometers are renowned for their ability to make precise measurements by utilizing the interference of light waves [201, 202]. When light from a single source is divided into two or more beams traveling along different optical paths, any changes, whether caused by physical displacement or changes in the refractive index of the medium, will result in corresponding shifts in the relative phase of the beams [201, 202]. These phase shifts appear as changes in the interference pattern, which can be accurately measured. The sensitivity of interferometric techniques is due to their ability to detect extremely small changes in optical path length through corresponding phase shifts [201, 202]. Based on this mechanism, optical fiber interferometers are utilized to measure a range of physical, chemical, and biological parameters (e.g., temperature, strain, pressure, refractive index, pH, etc.) [203−205]. The main optical fiber interferometer configurations used are Fabry-Perot interferometer (FPI) [63, 206], Mach-Zehnder interferometer (MZI) [64, 206], Michelson interferometer (MI) [65, 206], and Sagnac interferometer (SI) [206, 207].

The first part of this section presents the entire fabrication process, including the coating of different TiO_2 film thicknesses and the characterization of Mach-Zehnder interferometers inscribed in SMF-28e fibers using fs-laser direct writing. The wavelength sensitivity to the SRI of the uncoated and TiO_2 coated optical fiber Mach-Zehnder interferometers is evaluated and compared to the literature's reported works. The second part focuses on the fs-laser irradiation followed by chemical etching technique to fabricate Fabry-Perot interferometers in SMF-28e fibers. This technique is used to fabricate microchannels and cavities that facilitate the flow of samples in and out of the cavities. The preliminary results of the work realized to fabricate optical fiber Fabry-Perot interferometers, which are based on microchannels and cavities in an SMF-28e fiber, are presented herein. Two types of Fabry-Perot interferometers are proposed and evaluated: one with a single cavity and another with in-line dual cavities, both developed for gas pressure measurements.

4.3.1 Mach-Zehnder Interferometer

The fabrication of Mach-Zehnder interferometers in optical fibers has been explored using different techniques and configurations, including fs-laser micromachining [30, 208−212], electric arc discharge [172, 213−216], CO_2 laser writing [217−220], core-offset splicing [221−223], tapered structures [224−227], and multimode interference [228−230].

The versatility of the fs-laser writing technique allows a flexible configuration of MZIs for specific sensing applications. For instance, Li et al. demonstrated an in-fiber Mach−Zehnder interferometer for strain measurement [210]. Pallarés-Aldeiturriaga et al. designed an in-fiber Mach−Zehnder interferometer as a curvature sensor [212]. Sun et al. presented an in-line fiber MZI with a refractive index sensitivity of approximately -10^4 nm/RIU in the refractive index range of 1.332 to 1.352. The MZI consists of a micro V-shaped slit in the fiber core fabricated in a standard single-mode optical fiber by fs-laser micromachining followed by chemical etching. This method demonstrates the potential of hybrid fabrication techniques to achieve highly sensitive MZI structures suitable for applications in chemical, biological, and environmental monitoring [231]. The fs-laser direct writing

method has also been used to inscribe a straight waveguide in a coreless fiber spliced between two SMFs to form an in-line Mach−Zehnder interferometer [211]. In this work [211], the device exhibited a temperature sensitivity of -278.86 pm/℃ and a bending sensitivity of 0.28 nm/m^{-1} [211]. The work presented in [209] shows other Mach−Zehnder interferometer fabricated in the same SMF-coreless-SMF structure. Here, a straight waveguide was inscribed along the central axis of the coreless fiber (reference arm), and other curved waveguide (sensing arm) was inscribed bending toward the cladding interface to obtain a strong evanescent field sensitive to SRI. The fiber interface MZI exhibits an RI sensitivity of ∼3000 nm/RIU at the RI value of 1.432. Following, the work presented in [209], a fiber-interface directional coupler was fabricated for highly sensitive RI measurements. This device achieved a sensitivity as high as ∼8249 nm/RIU over an RI range of 1.440 - 1.450, due to strong evanescent fields excited in fiber-interface waveguides, as reported in [232]. A compact structure of a fiber in-line MZI fabricated by fs-laser micromachining, has also been reported in [233]. One of the interferometer arms contains a microcavity created by removing a part of the fiber core near the core and cladding interface, while the other arm is located in the remaining part of the fiber core. The interferometer exhibits a SRI sensitivity of -9370 nm/RIU in the RI range between 1.310 and 1.335 [233]. To improve the sensitivity of MZI sensors, various efforts have been employed, such as the use of tapered fibers [234, 235], offset fiber splicing [235, 236], and multi-core optical fibers [235, 237]. Multi-core optical fibers consist of multiple cores arranged together, allowing it to exceed the transmission capacity limitations of single-mode fibers in space division multiplexing optical communications. In addition, the presence of multiple cores enables the support of more transmission modes, which improves signal transmission efficiency and sensing performance while reducing the effects of mode interference. The well-designed multi-core fiber sensors can achieve higher sensitivity [235]. As a result, the development of an in-line MZI sensor using a four-core fiber showed significant improvements in curvature and strain sensitivity [235]. The sensor was fabricated by splicing a segment of four-core fiber between two no-core fibers. The two no-core fibers act as a splitter and a coupler, respectively. The self-focusing properties of the no-core fibers are used to couple light into all cores of the four-core fiber, which improves coupling efficiency, enables multi-path transmission, and also improves sensitivity. Thus, a curvature sensitivity of -78.04 dB/m^{-1} was achieved in a curvature range of 0.0104 to 0.1515 m^{-1}, and a strain sensitivity of -6.49 pm/με was achieved in the range of 0 to 600 με [235].

The Mach-Zehnder interferometer, formed by a pair of long period fiber gratings on a single mode fiber, was fabricated by the fs-laser point-by-point writing method and explored as surrounding refractive index sensors. In this work [238], the MZI achieved a high SRI sensitivity of 280.74 nm/RIU at 1437.74 nm in the range of 1.333 to 1.360. The work presented in [239] shows another Mach-Zehnder interferometer based on a pair of LPFGs, with a fiber taper between the two LPFGs to improve and tune the sensitivity of the sensor. In the SRI range of 1.333 to 1.360, the wavelength shift of the device exhibits a good linear response and the SRI sensitivities are about 267.02 nm/RIU at 1428.64 nm and 280.74 nm/RIU at 1437.74 nm [239]. Other LPFGs-based MZI fabricated by CO_2 laser showed an SRI sensitivity of 58.8 nm/SRI in the range of 1.334 to 1.364 [240].

The electric arc technique has emerged as an important method for the fabrication of in-line Mach-Zehnder interferometers, particularly for refractive index sensing applications [215, 241]. In addition, this method has been successfully employed in the fabrication of optical components, including fiber tapers [215, 241]. Mach-Zehnder Interferometers based on a pair of LPFGs fabricated by electric arc discharge and coated with titanium dioxide (TiO_2) have shown potential for SRI sensing due to their improved sensitivity and spectral resolution. For example, the work presented in [172] demonstrated a wavelength shift sensitivity of 216 nm/RIU, along with a spectral resolution of 1.1×10^{-4} RIU. This was achieved with a separation of 3 cm between a pair of LPFGs written in the fiber and coated with a 30 nm thick layer of titanium dioxide (TiO_2) [172]. The TiO_2 coating not only increases sensitivity, but also allows the sensor to operate effectively over a broader range of refractive indices, both lower and higher than the cladding refractive index, by adjusting the thickness of the TiO_2 layer [170].

Thus, this section presents the entire fabrication process, including the coating of different TiO_2 film thicknesses and the characterization of Mach-Zehnder interferometers inscribed in SMF-28e fibers using fs-laser direct writing. In addition, the wavelength sensitivity to the surrounding refractive index of both uncoated and TiO_2-coated optical fiber Mach-Zehnder interferometers is systematically evaluated, providing insight into their sensing performance.

Theoretical Background

The principle of operation of a Mach-Zehnder interferometer consists of splitting an incoming optical signal into two paths, referred to as arms, using beam-splitting components [201, 203, 204]. As the light travels along these separate paths, the reference and sensing arms, it may encounter different optical path lengths or different environmental medium conditions, resulting in a phase difference [201, 203, 204]. When the light beams are recombined at the second beam splitter, this phase difference manifests itself as an interference pattern containing regions of both constructive and destructive interference [201, 203, 204]. Long-period fiber gratings have improved the design of Mach-Zehnder interferometers by facilitating compact, in-line waveguide configurations that eliminate the requirement for physically separate reference and sensing arms [209, 215, 242]. Conventional Mach-Zehnder interferometers depend on the splitting of an optical signal into two distinct spatial paths, a process that can present challenges in terms of device size, alignment, and stability [209, 215, 242]. In contrast, LPFGs enable controlled coupling between the core and cladding modes within a single optical fiber [209, 215, 242]. Accordingly, one LPFG is used to couple a part of the light from the fundamental core mode of a single mode fiber into the cladding modes, whereas the remaining light continues to propagate in the fiber core. Subsequently, an identical LPFG then re-couples the light propagating as a cladding mode, back into the core mode. This coupling results in an interference fringe based on the different propagation constants of the modes, allowing separate arms to function as one within the unified structure [209, 215, 242]. Consequently, Mach-Zehnder interferometers based on a pair of long-period fiber gratings offer improved integration and reduced complexity while maintaining high sensitivity, making them particularly suitable for sensing applications [204, 209, 215, 242]. In additon, in an ideal Mach-Zehnder inter-

ferometers based on a pair of LPFGs, each LPFG exhibits a attenuation band of 3 dB, facilitating an equal power distribution between the core and cladding modes. Therefore, ensuring this balanced coupling can enhance the visibility of the interference fringe, thereby ensuring maximum fringe contrast and enhancing the interferometer's sensitivity to external perturbations [204, 209, 215, 242]. The optical intensity that propagates in the core functions as the reference signal (I_r), and the optical intensity in the cladding functions as the sensing signal (I_s). The intensity output of the Mach−Zehnder interferometer can be described as follows:

$$I = I_r + I_s + 2\sqrt{I_r I_s}\cos\left(\frac{2\pi\Delta(nL)}{\lambda}\right), \tag{4.19}$$

where λ is the wavelength and $\Delta(nL)$ is the optical path difference (OPD) between the two interferometer arms [204, 209, 215, 242]. The intensity dip manifests at the wavelength when the condition $\frac{2\pi\Delta(nL)}{\lambda} = (2m+1)\pi$ is met, where m denotes an integer [204, 209, 215, 242]. This results in the following relationship between the wavelength and the intensity dip:

$$\lambda_{\text{dip}} = \frac{2\Delta(nL)}{2m+1}. \tag{4.20}$$

The free spectral range (FSR) of the interference fringe dip of interest is determined by the OPD, $\Delta(nL)$, as follows:

$$\text{FSR} = \frac{\lambda^2}{\Delta(nL)}. \tag{4.21}$$

The output of the interferometer is given by equation 4.19. However, it is necessary to consider the transmission through the LPFG. The transmission factors for the core and cladding through the LPFG are given by the following equations:

$$T_{\text{core}} = \cos^2(\gamma L) + \frac{\Delta\beta^2}{\gamma^2}\sin^2(\gamma L), \tag{4.22}$$

$$T_{\text{clad}} = \frac{k^2}{\gamma^2}\sin^2(\gamma L), \tag{4.23}$$

where L is the length of the LPFG, k is the coupling coefficient constant, $\Delta\beta$ is the detuning factor and $\gamma = \sqrt{k^2 + \Delta\beta^2}$ [215, 242]. Accordingly, the terms I_r and I_s in equation 4.19 are replaced by the transmission factors T_{core} and T_{clad}, which are functions of the LPFG parameters. This dependence allows for the modulation of the interference fringe by controlling key fabrication parameters of the LPFG, such as the grating period and coupling coefficients [215, 242]. Furthermore, under the assumption of negligible losses in the LPFG, besides the attenuation band of 3 dB, equation 4.19 can be rewritten as follows:

$$I = 1 - 4T_{\text{core}}T_{\text{clad}}\sin^2\left(\frac{\pi\Delta n_{\text{eff}}L_{\text{cav}}}{\lambda}\right), \tag{4.24}$$

where Δn_{eff} is the effective refractive index difference between the core and the cladding modes, and L_{cav} is the physical length of cavity [215, 242].

Fabrication and Characterization of the MZIs

In-line Mach-Zehnder interferometers based on a matched pair of LPFGs were fabricated by the fs-laser direct writing system in an SMF-28e Corning optical fiber, following the procedures described in the fabrication Section 3.1.3. The MZI consists of two identical LPFGs, inscribed in-line such that an interferometer cavity whose length was set to 1.4 cm is formed between the two gratings, Figure 4.62 (a). The period of each LPFG was 380 µm, yielding a resonance wavelength at approximately 1.5 µm, related to the $LP_{1,6}$ asymmetric cladding mode. The visibility of the interference fringe of the MZIs is optimized based on the optical power coupled to the cladding mode. After the coating process, the attenuation band of the LPFG undergoes a blue shift and a reduction in amplitude, as previously demonstrated in Section 4.2. Therefore, three coated MZIs were fabricated with LPFGs whose attenuation band was set to approximately 4.5 dB, which was achieved for a length of 1.6 cm, Figure 4.62 (b). In addition, each pair of LPFGs was written in a single run to avoid rotations hat could induce a spectral mismatch. The MZIs were characterized in the transmission mode, keeping the fiber stretched at a constant tension produced by a suspended weight of 5.8 g and measuring the normalized signal from the broadband light source with the OSA without polarization control from 1400 to 1600 nm with a 1 nm resolution.

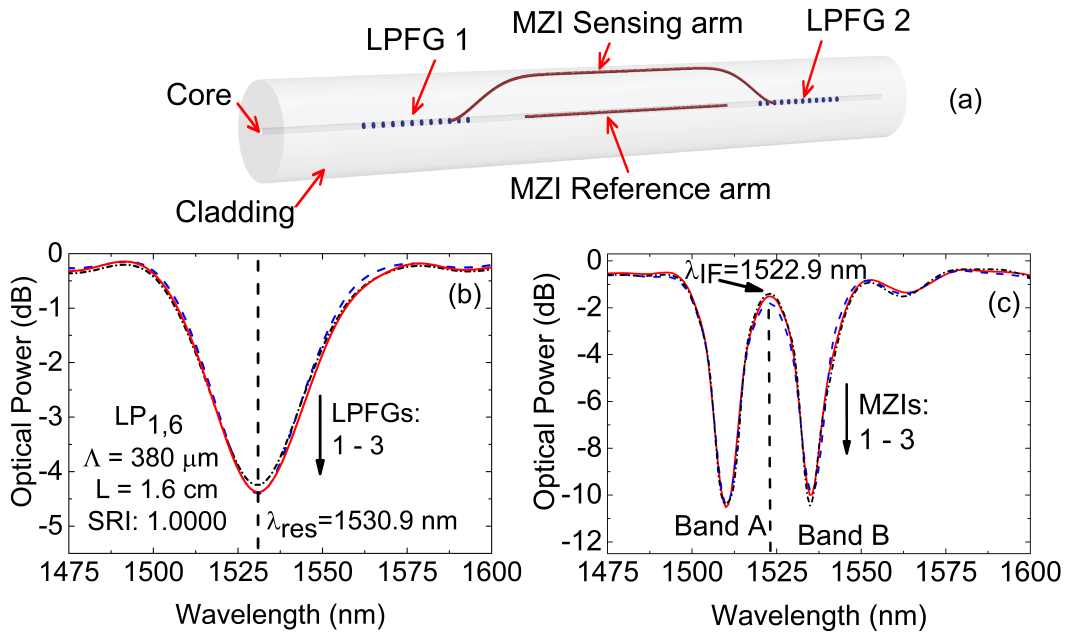


Figure 4.62. *In-line Mach−Zehnder interferometer based on a matched LPFG pair: (a) Schematic, and (b) and (c) Transmission spectra of the first single LPFG and MZI, respectively.*

For each MZI, the first LPFG was used to couple a part of the light from the fundamental core mode of a single mode fiber into the cladding modes, whereas the remaining light continues to propagate in the fiber core. Table 4.21 presents a summary of the spectral characteristics of the first set of fs-laser written LPFGs.

Table 4.21. *Summary of the spectral characteristics of the first LPFGs of the in-line MZI.*

LPFG number	Cladding Mode	Λ (µm)	λ_{res} (nm)	I_{res} (dB)	FWHM Bandwidth (nm)
1	$LP_{1,6}$	380.0	1530.9	-4.2	32.2
2			1530.9	-4.3	32.1
3			1530.9	-4.3	32.1

The second identical LPFG then re-couples the light propagating as a cladding mode, back into the core mode. This coupling results in an interference fringe with two leading bands, named Band A and Band B, based on the different propagation constants of the modes, Figure 4.62 (c). The summary of the spectral characteristics of the three in-line MZIs fabricated is shown in Table 4.22.

Table 4.22. *Summary of the spectral characteristics of the in-line MZIs.*

MZI number	λ_{res} (nm)		I_{res} (dB)		FWHM Bandwidth (nm)	
	Band A	Band B	Band A	Band B	Band A	Band B
1	1510.1	1536.2	-10.3	-10.5	-11.4	-11.9
2	1510.3	1536.1	-10.9	-10.4	-11.6	-11.8
3	1510.3	1536.3	-10.3	-9.9	-11.6	-11.9

In sensing applications one of the arms is used for reference and is kept free of perturbations while the other is exposed to the external medium and used for sensing. This type of MZIs has the same physical length in both arms, but the optical path lengths are different due to the lower effective refractive index of the cladding mode when compared with the one associated to the core mode.

Titanium dioxide films of 30, 40 and 50 nm thickness were deposited around the MZIs by thermal evaporation of pure titanium in a controlled oxygen atmosphere using an electron beam evaporator Auto 306 (Edwards Ltd), as previously described. In addition, the details of the deposition system, as well as the TiO_2 deposition and characterization protocols, are thoroughly described in [182]. The transmission spectra of the MZIs, from 1475 to 1575 nm, uncoated (bare) and coated with a 30 nm thick TiO_2 films with air (RI = 1.000) as the SRI are shown in Figure 4.63.

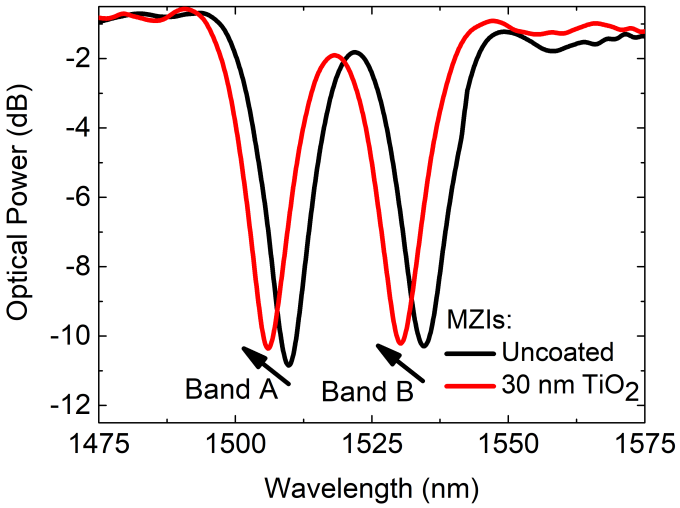


Figure 4.63. *Transmission spectra of the MZIs, uncoated and coated with 30 nm thick TiO_2 film, in air (RI = 1.0000).*

The coating of the MZI with 30 nm thick TiO_2 films leads to a shift to shorter wavelengths of the attenuation Bands A and B of about 4.6 and 4.9 nm, respectively and a decrease of the resonance amplitude, as summarized in Table 4.23. This behaviour is consistent with the results presented in the literature, for the MZIs fabricated by the electric arc technique in an SMF-28e fiber, and coated with TiO_2 [172, 182]. The wavelength and amplitude of the attenuation band depends on the effective refractive index of the cladding modes, which in turn depends on the SRI. The thin film induces a re-distribution of the cladding modes that leads to wavelength shift and amplitude intensity variation of the attenuation bands.

Table 4.23. *Summary of the spectral characteristics of the MZIs, uncoated and coated with 30 nm thick TiO_2 film.*

TiO_2 (nm)	λ_{res} (nm)		I_{res} (dB)		$\Delta\lambda_{res}$ (nm)		ΔI_{res} (dB)	
	Band A	**Band B**	**Band A**	**Band B**	**Band A**	**Band B**	**Band A**	**Band B**
Uncoated	1510.3	1536.1	−10.9	−10.4	−4.6	−4.9	0.5	0.2
30.0	1505.7	1531.2	−10.4	−10.2				

Surrounding Refractive Index

A RI characterization setup was prepared to measure the MZIs spectrum using different surrounding mediums. The MZIs were characterized in the transmission mode, keeping the fiber stretched at a constant tension produced by a suspended weight of 5.8 g and measuring the normalized signal from the broadband light source with the OSA without polarization control from 1400 to 1600 nm with a 1 nm resolution. The MZIs were introduced in a glass V-groove, parallel aligned to the fiber axis, and characterized with RI calibrated oils (Cargille-Sacher Laboratories Inc., U.S.A.), as illustrated in Figure 4.64. The RI oils used belong to the series AAA $n_D^{25^\circ C}$ = 1.3000 - 1.3950 $\pm$ 0.0002 and AA $n_D^{25^\circ C}$ = 1.4000 - 1.4580 $\pm$ 0.0002 at 1550 nm. After each measurement, both MZIs and the V-groove were cleaned with acetone to avoid contamination of the next

SRI oil. The measurements were performed in a temperature-controlled environment, monitoring the temperature during the characterization with a type K thermocouple thermometer (AMECaL ST-9612).

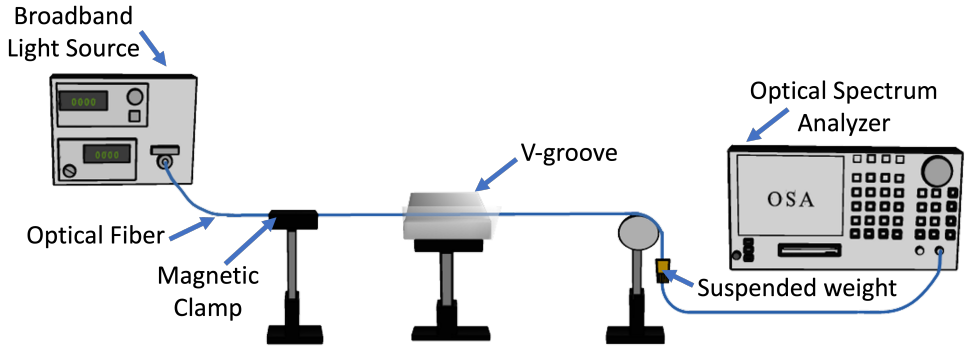


Figure 4.64. *Schematic illustration of the SRI characterization setup for MZIs.*

The measured transmission spectra, corresponding to the interference of the $LP_{1,6}$ cladding mode with the fundamental core mode, are presented in Figure 4.65 (a) and (b) for the uncoated and coated (30 nm TiO_2) MZI, respectively, for SRI values ranging from 1.3000 up to values lower than the cladding refractive index. For a cavity length of 1.4 cm between the LPFGs, all analyzed MZIs exhibited two dominant spectral bands.

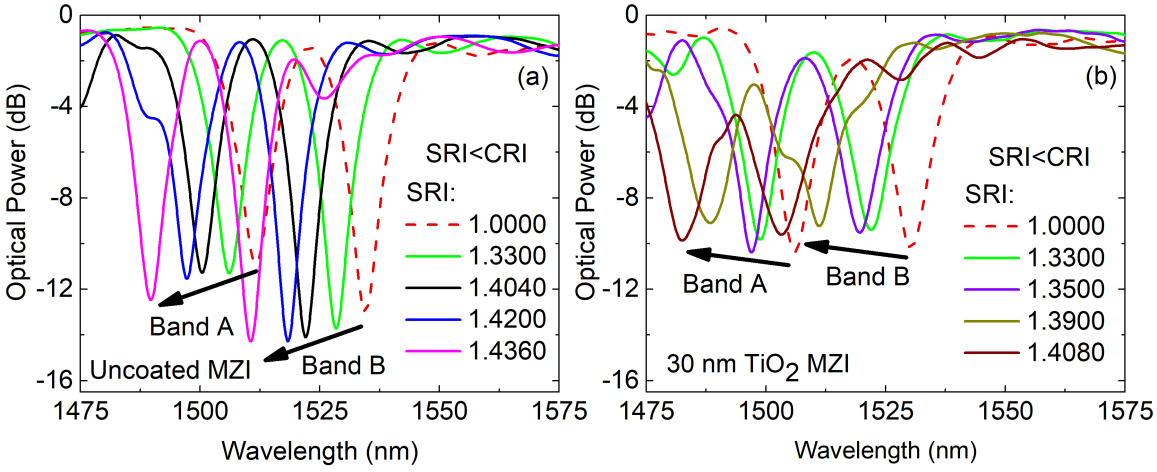


Figure 4.65. *Transmission spectra of an MZI: (a) uncoated and (b) coated with 30 nm thick TiO_2 film, for several values of the SRI.*

The normalized wavelength shift was determined using these bands, referred to as Band A and Band B, and is shown in Figure 4.66 (a) and (b) for MZIs uncoated and coated with 30, 40, and 50 nm of TiO_2. The sensitivity of the MZIs was determined by calculating the 1st order derivative of these curves and is presented in Figure 4.66 (c) and (d), for SRI lower and higher than the cladding refractive index, respectively.

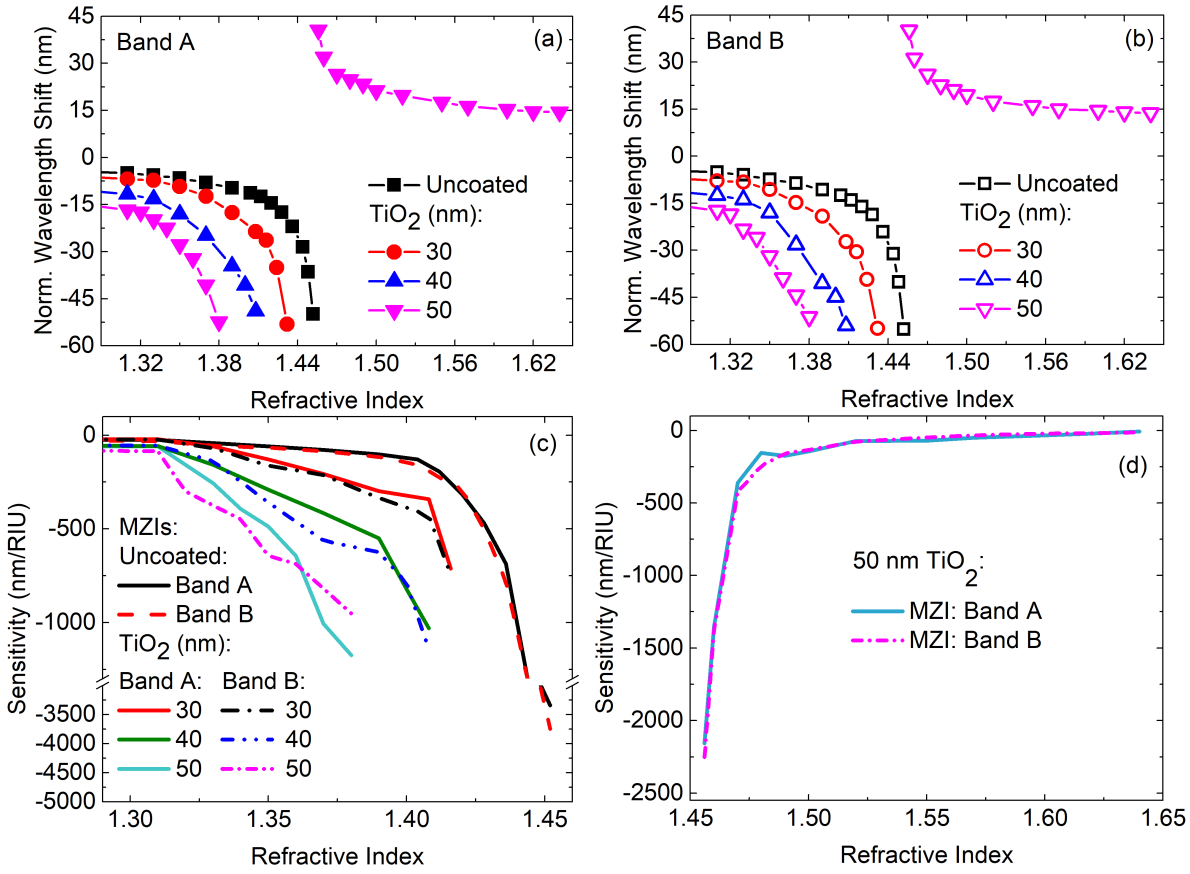


Figure 4.66. *Normalized wavelength shift as a function of the SRI for MZIs with a cavity of 1.4 cm, uncoated and coated with different TiO_2 films thickness: (a) Band A and (b) Band B. Wavelength sensitivity of the MZIs for SRI; (c) lower, and (d) higher than the cladding refractive index, respectively.*

The wavelength shift is higher for coated MZIs and increases with the thickness of the TiO_2 film, for both interferometric bands. This observation is consistent with the results presented in [172, 182] for TiO_2 coated LPFGs and MZIs. However, it is important to note that the calculated sensitivity, presented in Figure 4.66 (c) and (d), is higher than that determined for single LPFGs, whether bare or coated. As shown in Fig. 4.66 (c) and (d), no substantial difference in sensitivity between Bands A and B was observed within the experimental error. The wavelength sensitivity of both bands in the MZI coated with 50 nm of TiO_2 is higher than that of the single LPFG coated with 60 nm of TiO_2 for SRI values greater than the cladding refractive index. In addition, it was observed that the sensitivity increases for higher TiO_2 coating thickness being possible to choose the film thickness according to the SRI that needs to be measured. Wavelength sensitivities of 1175 nm/RIU at 1.3800 and over ∼2000 nm/RIU for SRI values higher than the cladding refractive index were determined for 50 nm of TiO_2 thick film, as shown in Figure 4.66.

The normalized wavelengths shift to SRI in the range between 1.3300 to 1.3700 (i.e., around water-based solutions) was also determined, as depicted in Figure 4.67.

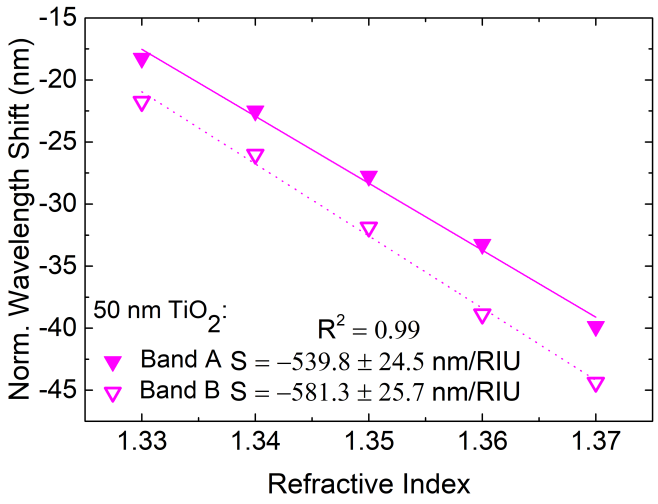


Figure 4.67. *Normalized wavelength shift for the MZI coated with 50 nm thick TiO_2 film in the RI range of water-based solutions. Experimental data points were fitted to a linear equation.*

Although the wavelength response to the SRI presents a nonlinear trend, in a narrow SRI range it can be considered linear. Thus a linear fit was applied to the results in Figure 4.67 in order to assess the wavelength sensitivity (average $\pm$ standard deviation). Therefore, a maximum sensitivity in the RI range of water-based solutions of -539.8$\pm$24.5, and -581.3$\pm$25.7 nm/RIU corresponding to Band A and Band B, respectively was achieved for the MZI coated with 50 nm TiO_2 thickness.

The analysis of the spectral resolution was done as described in section 4.2.1, and the data concerning the SRI step variations are shown in Figure 4.68.

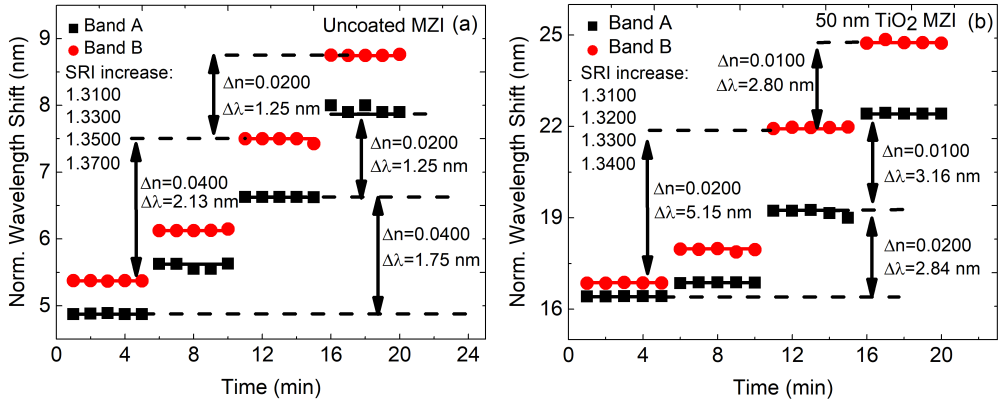


Figure 4.68. *Normalized wavelength shift as a function of time when the surrounding medium undertakes step variations for the interferometric bands of the MZIs: (a) uncoated and (b) coated with 50 nm thick TiO_2 film.*

Table 4.24 presents the calculated RI resolutions for the uncoated and TiO_2 coated MZIs. Refractive index resolutions with magnitude of 10^{-5} RIU were achieved for the MZIs uncoated, and coated with 50 nm thick TiO_2 film, respectively.

Table 4.24. *RI Resolutions for the uncoated and TiO_2 coated MZIs.*

TiO_2 (nm)	Step	RI Resolutions	
		Band A	Band B
Uncoated	1	3.3×10^{-5}	6.3×10^{-5}
	2	3.5×10^{-5}	6.1×10^{-5}
50.0	1	6.6×10^{-5}	3.9×10^{-5}
	2	6.4×10^{-5}	3.5×10^{-5}

Mach-Zehnder interferometers based on in-line LPFGs of 1.5 ± 0.5 cm length have been fabricated by the electric arc technique in an SMF-28e fiber and coated with TiO_2, [172]. The results presented demonstrate a measured wavelength sensitivity for the uncoated MZIs of 80.3 ± 2.5, 98.6 ± 2.7, and 116.4 ± 3.61 nm/RIU for sensing arms of 1 cm, 2 cm, and 3 cm length, respectively. Coating the interferometers with a 30 nm TiO_2 layer increased the wavelength sensitivity to 134.6, 141.8, and 215.9 nm/RIU for the corresponding sensing arm lengths within in the RI range of 1.3300 to 1.3700 RIU. Refractive index resolutions with magnitude of 10^{-5} RIU were achieved for the MZIs. The fs-laser written MZIs coated with 50 nm TiO_2 thickness and a sensing arm of 1.4 cm exhibits a maximum sensitivity of -581.3$\pm$25.7 nm/RIU in the RI range of 1.3300 to 1.3700 RIU. Table 4.25 presents a summary of the RI sensitivity of MZIs fabricated by the electric arc technique reported in [172] and this work.

Table 4.25. *RI sensitivity of MZIs fabricated by the electric arc technique reported in the literature and this work.*

MZI Fabrication Process	Sensitivity (nm/RIU)	RI Range	Ref.
Electric arc discharges and coated with 30 nm of TiO_2	215.9	$1.3300 - 1.3700$	[172]
Fs-laser direct written and coated with 50 nm of TiO_2	581.3		This Work

The results highlight the advantages of fs-laser written MZIs, particularly when coated with TiO_2. Although MZIs fabricated by the electric arc technique exhibit enhanced sensitivity with TiO_2 coatings, their RI wavelength sensitivity remains lower than fs-laser inscribed structures. The higher sensitivity observed in fs-laser written MZIs can be attributed to the precise delivery of optical energy to the irradiated medium through nonlinear absorption processes. This technique leads to localized modifications in the structural properties of the optical fiber. These controlled changes alter the refractive index characteristics, optimizing mode coupling and enhancing the interferometer's response to variations in the refractive index.

In conclusion, a preliminary study on the development of fs-laser-written Mach-Zehnder interferometers based on TiO_2 coated long period fiber gratings was presented. The proposed structure benefits from both the enhanced wavelength sensitivity of TiO_2 coated LPFGs and the improved spectral resolution provided by the interferometric configuration. Higher sensitivity and resolution were achieved with the MZI compared to single LPFGs. For the parameters tested in this study, the TiO_2 coated MZI exhibited a significant enhancement in wavelength sensitivity to refractive index

variations, along with an increase in spectral resolution by an order of magnitude. By optimizing the TiO_2 film thickness and the interferometric cavity length, further improvements in sensitivity can be expected while preserving spectral resolution. As demonstrated in the preliminary results presented here, a limited number of fs-laser-written Mach-Zehnder interferometers were fabricated and characterized. The limited sample size of the present work precludes a statistically rigorous evaluation of the reproducibility of fs-laser-written Mach-Zehnder interferometers. In future works, it is necessary to produce a larger batch of fs-laser-written Mach-Zehnder interferometers, fabricated and characterized under identical conditions, in order to obtain meaningful variability metrics.

4.3.2 Fabry-Perot Interferometer

Fabry-Perot interferometers fabricated in optical fibers have attracted significant research interest due to their wide range of applications in physical, chemical, and biological sensing [203, 243–245]. In particular, optical fiber gas pressure sensors have attracted interest for biomedical, structural, and aerospace applications, due to their compact structure, high sensitivity, and ease of integration [202, 204, 243, 246]. Various fabrication methods have been used to create Fabry-Perot interferometers, including fs-laser micromachining [202, 204, 243, 246], chemical etching [202, 203, 243], splicing or bonding of different types of fibers or tubes [202, 204, 243, 247], and focused ion beam milling [248–250]. There are typically two types of cavity structures: sealed and open cavities. FPIs based on the sealed cavities are generally used for the gas pressure measurements, and the modulation is based on the optical path difference of the FPI [202, 204, 243, 246]. However, FPIs based on open cavities become more interesting and valuable because the gaseous and liquid samples can easily flow in and out of the cavity [202, 204, 243, 246]. The change of RI can directly affect the OPD of the FPI. These FPIs are fabricated with a single cavity with two or three surface reflections, creating resonances that shift in response to changes in external parameters [202, 204, 243, 246].

The work presented in [246] showed an open-cavity FPI for gas pressure sensing, that has a fiber-tip structure, consisting of two tiny sections of fusion-spliced capillary tubes with different inner diameters. The sensor exhibits a gas pressure sensitivity of 4.147 nm/MPa in the range of 0 to 1.52 MPa. Tang et al., reported a gas pressure sensor based on FPI with a side-opened channel in hollow-core photonic bandgap fiber [251]. The FPI was formed by splicing a section of hollow-core photonic bandgap fiber between two sections of SMF. The side-opened hole was drilled using a fs-laser to introduce the compressed air into the hollow core. This structure enhanced the interaction between the gas and light signals in the FPI cavity (60 µm length). The sensor showed a gas pressure sensitivity of 4.24 nm/MPa in the range of 0 to 2.0 MPa. A three-dimensional printed miniature optical fiber FPI pressure sensor was developed using fs-laser direct writing through two-photon polymerization, as reported in [252]. The sensor consisted of an unsealed cylindrical column with a suspended polymer diaphragm directly printed on the tip of an SMF, forming an FP cavity. Two configurations were fabricated, each with different cavity lengths but with the same diaphragm thickness of 5 µm. Experimental results demonstrated that the device with a cavity length of 140 µm had a linear pressure sensitivity of 3.959 nm/MPa within the pressure range of 0 to 1100 kPa,

while the device with a 90 µm cavity length exhibited a sensitivity of 4.097 nm/MPa [252]. An ultra-compact fiber in-line cascaded FPI was fabricated using femtosecond laser micromachining, assisted by hydrofluoric etching [243]. The structure consists of two air cavities, each measuring 30 µm, connected by an unmodified fiber core that is 20 µm in length. The gas pressure sensitivity of this device was found to be 2.86 nm/MPa within a pressure range of 0 to 2.0 MPa [243].

One method to improve the sensitivity of the sensor is to use the optical Vernier effect [253, 254]. The Vernier effect is a technique that significantly increases the sensitivity and resolution of optical sensors by coupling two Fabry-Pérot interferometers with slightly different cavity lengths or free spectral ranges [253, 254]. When these two FPIs are combined, their interference patterns overlap, originates a beat between the two frequencies and producing a combined signal with an amplified response [253, 254]. This amplification occurs because the slight difference in the free spectral ranges causes the interference fringes to shift more noticeably in response to small changes in the measured parameters, such as pressure, temperature, or refractive index [253, 254]. As a result, the Vernier effect amplifies the response to small wavelength shifts by producing a large envelope shift due to interference between two mismatched resonators, allowing for higher resolution measurements and improved measurement sensitivity compared to the normal shift using a single FPI [253, 254]. FPI gas pressure sensors based on the Vernier effect have been proposed [255−259]. Pan et al. reported a parallel FPIs gas pressure sensor with UV glue sensitization based on the dual Vernier effect with a sensitivity of 131.88 nm/MPa [259]. The work presented in [255] describes a pressure sensor based on the Vernier effect, which consists of a cascaded FPI fabricated by fs-laser micromachining with another FPI formed by splicing of a capillary tube with SMF. The sensor exhibited a sensitivity of 303.65 pm/kPa. A gas pressure fiber probe with a side-opened microchannel and high sensitivity of 80.3 pm/kPa magnified by Vernier effect was also demonstrated in [256]. Yang et al. reported a highly sensitive gas pressure sensor based on a cascaded FPI and harmonic Vernier effect. The device was fabricated by fusion splicing two hollow silica capillaries and exhibited a sensitivity of 80.8 pm/kPa [257].

This section describes the fabrication of Fabry-Pérot interferometers in SMF-28e fibers using fs-laser irradiation followed by chemical etching. This method was used to fabricate microchannels and cavities that facilitate the flow of samples in and out of the cavities. This work presents preliminary results for two types of FPIs developed for gas pressure measurements: one with a single cavity and another with in-line dual cavities.

Theoretical Background

The Fabry-Pérot interferometer is an optical device that consists of an optical cavity formed by two parallel reflective surfaces [201, 202, 204, 260]. These surfaces can be either mirrors or interfaces with different refractive indices, which allow for multiple reflections and the formation of interference patterns [201, 202, 204, 260]. The interference pattern resulting from these processes is influenced by the optical path difference and the length of the cavity, making the FPIs highly sensitive to external factors such as temperature changes, strain, and variations in refractive index [201, 202, 204, 260]. In the case of the FPI, an incident light beam propagating through the

single-mode fiber core is partially reflected by the two reflective surfaces of the Fabry-Pérot cavity. These reflected beams recombine within the fiber core, generating an interference fringe pattern at the output [201, 202, 204, 260]. In the low-finesse regime ($R \ll 1$), a Fabry−Pérot cavity behaves as a two-wave interferometer. The light intensities of the beams reflected from the first and second cavity surfaces are denoted I_1 and I_2, respectively. The resulting interference signal intensity can be described as follows:

$$I = I_1 + I_2 + 2\sqrt{I_1 I_2}\cos\left(\frac{4\pi nL}{\lambda} + \phi_0\right), \tag{4.25}$$

where λ represents the wavelength of the incident light, n is the refractive index of the cavity medium, L denotes the cavity length, and ϕ_0 is the initial phase of the interference [201, 202, 204, 260]. At the positions of the interference fringe dips, the phase difference between the two reflected beams satisfies the condition:

$$\frac{4\pi nL}{\lambda_m} + \phi_0 = (2m+1)\pi, \tag{4.26}$$

where m is an integer, and λ_m corresponds to the wavelength of the m-th order interference dip [201, 202, 204, 260]. For the case where $\phi_0 = 0$, the wavelength at which an intensity dip occurs can be expressed as:

$$\lambda_{\text{dip}} = \frac{4nL}{2m+1}. \tag{4.27}$$

The free spectral range (FSR) of the interferometer, which represents the wavelength spacing between two consecutive transmission peaks, is given by:

$$\Delta\lambda = \frac{\lambda^2}{2nL}. \tag{4.28}$$

The quality of the interference signal is often quantified by the fringe visibility (or interference contrast). In general, high fringe visibility corresponds to a larger signal-to-noise ratio and improved measurement accuracy [201, 202, 204, 260]. The fringe visibility (V) of an interference signal can be determined as follows:

$$V = \frac{I_{\text{max}} - I_{\text{min}}}{I_{\text{max}} + I_{\text{min}}}, \tag{4.29}$$

where I_{max} and I_{min} represent the maximum and minimum intensity levels of the interference fringes, respectively [204, 243, 260, 261]. The FPI achieves maximum fringe visibility of 1 (or 100%) when the two reflected beams have equal intensities. However, in most practical scenarios, the second reflected beam has lower intensity than the first due to additional optical losses occurring as light propagates through the Fabry-Pérot cavity [204, 243, 260, 261]. In a low-finesse, air-gapped single-mode fiber extrinsic FPI, recoupling loss is the predominant loss mechanism. As the cavity length increases, beam divergence and misalignment reduce the efficiency of light recoupling into the fiber core, leading to a gradual decline in fringe visibility [204, 243, 260, 261]. This effect sets an upper limit on the maximum practical cavity length, beyond which the sensor's performance is significantly affected. In the case of an intrinsic FPI fabricated using the fs-laser chemical etching-

assisted technique, optical losses are primarily caused by scattering and mode mismatch at the etched hole interfaces [204, 243, 260, 261]. While this fabrication process creates a defined cavity within the fiber structure, surface roughness and refractive index variations at the etched interfaces contribute to scattering-induced losses, reducing interference contrast [204, 243, 260, 261]. As the cavity length increases, beam diffraction and lateral misalignment further degrade mode recoupling efficiency, leading to a progressive reduction in fringe visibility. These combined effects establish a limit on the maximum cavity length, beyond which the interference contrast weakens, affecting both sensor resolution and signal-to-noise ratio [204, 243, 260, 261].

Fabrication and Characterization of the FPIs

The schematic diagram shows the Fabry-Pérot interferometers (FPIs) fabricated in an SMF-28e optical fiber, depicting two configurations: (a) a single FP cavity and (b) an in-line dual FP cavity, with open channels, as illustrated in Figure 4.69. The single FP cavity consists of a single interferometric structure formed by two parallel reflective interfaces. Optical interference occurs between two beams, one reflected at the concave interface and another that is reflected at the convex interface and travels a round-trip through the cavity, Figure 4.69 (a). In addition, the in-line dual FP cavity consists of two FP cavities, with twice the number of reflective interfaces. These cavities are separated by a short unmodified fiber segment, Figure 4.69 (b).

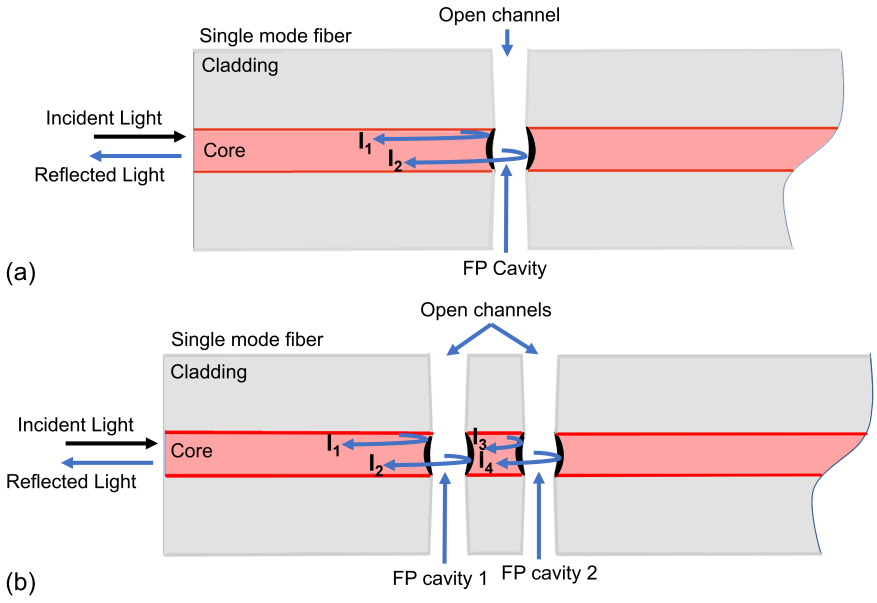


Figure 4.69. *Schematic of the proposed Fabry-Pérot interferometers in SMF-28e fiber: (a) single FP cavity and, (b) in-line dual FP cavities.*

FPIs with different cavity sizes were fabricated in SMF-28e fibers by using fs-laser micromachining assisted with hydrofluoric (HF) acid. This is made possible due to the high spatial resolution obtained from a nonlinear absorption process triggered by the fs-laser exposure. First, the fs-laser refractive index modified regions are written longitudinally from bottom to top by an fs-laser beam

that is focused with a 100× oil immersion lens. The fs-laser writing system is set up with a laser repetition rate of 500 kHz, a pulse energy of 160 nJ, a 10 µm/s scan velocity, and a fiber tension of 1 N. In the literature, it has been reported that for scanning velocities higher than 500 µm/s, the etching rate decrease [262−264]. In addition, an abrupt decrease in the etching rate is observed for laser pulse energies below 60 nJ [262−264]. Thus, the pulse energy and velocity employed allows a selective modification. The laser beam was linearly polarized orthogonal to the scanning direction, to take advantage of a maximum etch rate, [16, 263, 264]. Two regions with modified refractive indices, parallel to the fiber axis, were fabricated, with separation distances of 2 µm, 6 µm, 10 µm, and 20 µm, as shown in Figure 4.70.

Following fs-laser direct writing, a chemical etching process is realized to selectively remove the laser modified regions, thereby forming open micro channels and FP cavities within the optical fiber. The etching procedure involves immersing the optical fiber in a 40 mL solution of 10% HF acid, maintained at a temperature of $30 \pm 5^{\circ}$C [263, 264]. The reaction is carried out in an ultrasonic bath to enhance debris removal from the cavities and ensure uniform etching (Branson 2510 Ultrasonics Cleaner). This process facilitates the removal of laser modified material and progresses over a duration of 105 minutes, leading to the formation of the structures illustrated in Figure 4.70. Due to its highly corrosive and toxic nature, the handling of hydrofluoric acid requires strict adherence to safety protocols. Proper personal protective equipment (PPE), including chemical-resistant gloves, a Teflon apron, and safety goggles, must be worn to minimize the risk of exposure. To further ensure both personnel safety and process integrity, all etching procedures are carried out within an ISO (International Organization for Standardization) 6/7 cleanroom facility, providing a controlled environment that mitigates contamination and ensures compliance with laboratory safety standards. Following the etching process, the optical fiber diameter was reduced from 125 µm to 117 µm, corresponding to a total material removal of 8 µm. Therefore, the etching rate over a 105 minutes etching process is approximately 0.076 µm/min for the pristine fiber. Different FP cavities were developed in the fiber core region, resulting in open cavities with optical path lengths ranging from 10 µm to approximately 24 µm. The widening of the cavity within the fiber core is attributed to the presence of germanium dopants, which enhance the etch rate during chemical processing. In addition, the separation between the fs-laser modified regions also influenced the etching rate, thereby influencing the material removal efficiency. The measured etching rates were found to be approximately 0.095 µm/min and 0.229 µm/min for cavities with optical path lengths of $\sim$ 10 µm and $\sim$ 24 µm, respectively. This controlled material removal process leads to modification in the fiber geometry and influences its optical and mechanical properties.

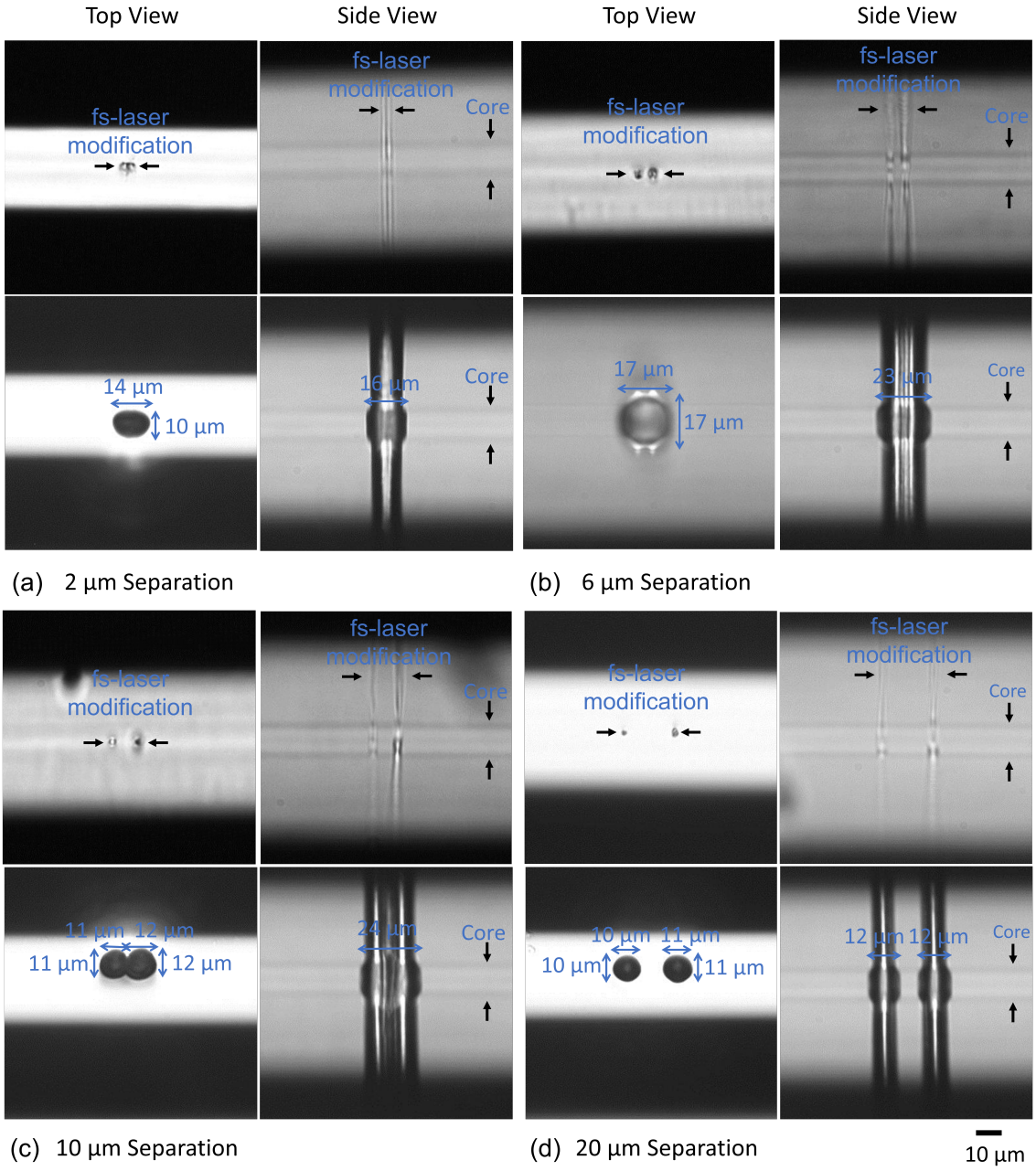


Figure 4.70. *Optical microscopy images of the fabricated structures: (a) and (b) single FP cavity before (on top) and after etching (at the bottom), fabricated with 2 µm and 6 µm separation, respectively; (c) and (d) in-line dual FP cavities before (on top) and after etching (at the bottom), fabricated with 10 µm and 20 µm separation, respectively (top views at the left and side views at the right).*

Among the fabricated FPIs, only the structures presented in Figure 4.70 (b) and (d) were characterized and evaluated for gas pressure measurement. The FPIs includes two configurations, a single cavity with $\sim$ 23 µm length and an in-line dual cavities with $\sim$ 12 µm length each, separated by $\sim$ 8 µm length of unmodified fiber core. Figure 4.71 shows reflection spectra of the single FP cavity and in-line dual FP cavities having air as SRI.

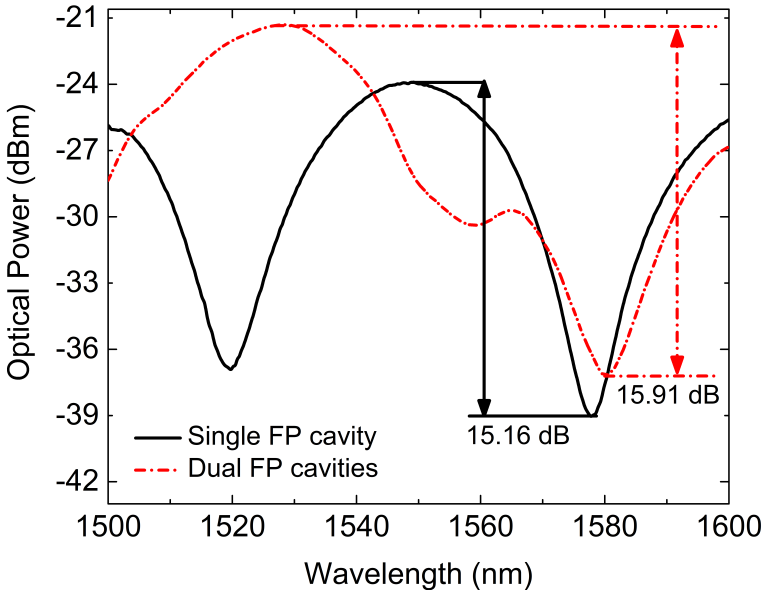


Figure 4.71. *Reflected spectra of the fabricated FPIs structures in air (RI = 1.0000).*

The fringe contrast in the single cavity is 15.16 dB, while the value increases to 15.91 dB in the in-line dual FP cavities. Table 4.26 presents the calculated FSR and fringe visibility, for both the single and dual FP cavities.

Table 4.26. *Comparison of FPIs structures*

FPI Configuration	Cavity Length (µm)	FSR (nm)	Fringe Visibility
Single FP Cavity	23	52	0.94
In-Line Dual FP Cavities	12	100	0.95

The in-line dual FP cavity exhibits a significantly larger FSR of 100 nm compared to the single FP cavity, which has an FSR of 52 nm. The FSR of an interferometer is inversely proportional to the length of the optical cavity, which explains the difference between the FSR of the single FP cavity and an in-line dual FP cavities. The FPIs achieve maximum fringe visibility of 1 (100%) when the two reflected beams have equal intensities, which ensures optimal interference contrast. As a result, fringe visibility is highly dependent on the surface quality of the fabricated structures. To enhance this parameter, it is essential to optimize the fabrication conditions, including pulse energy and scanning velocity. Doing so minimizes surface roughness and improves reflectivity, thereby maximizing the performance of the interferometer.

Gas Pressure Measurements

The spectral characterization of the FPIs was realized with customized setup composed of a broadband light source (model ASE2000) that was coupled to the fiber through an optical circulator, as shown in Figure 4.72. The spectrum was measured in reflection with an optical spectrum analyzer (OSA, model Yokogawa AQ6370D) with a resolution of 0.01 nm. The chamber is connected to an Edwards vacuum pump, which removes air from inside, cleans all the pipes in the system, and maintains the purity of the atmosphere. The FPIs were placed inside the chamber with a hermetic feedthrough that isolates the sensing device from the atmosphere. Prior to measurements, the gas or air in the chamber was evacuated using the vacuum pump, reducing the chamber pressure to vacuum. The gases used in the measurements were 100% nitrogen (N_2), and a gas mixture consisting of 50% methane (CH_4) and 50% nitrogen (N_2), both supplied by Linde Portugal, Lda.

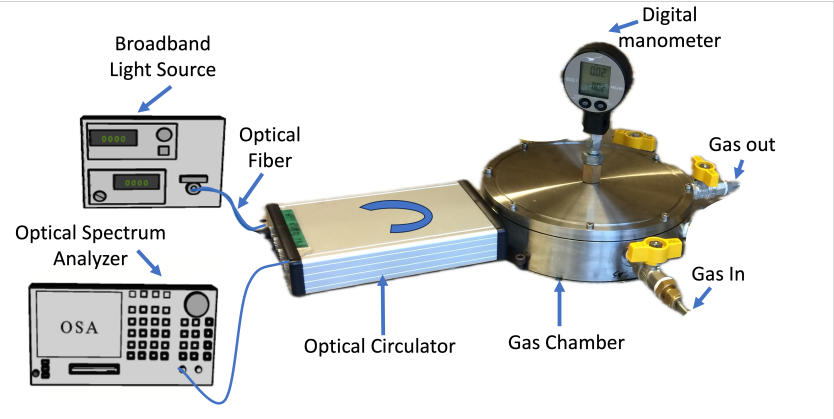


Figure 4.72. *Schematic illustration of the FPI experimental setup for gas pressure measurements.*

The gas pressure response of the single FP cavity and the in-line dual FP cavities structures were carried out with the chamber volume and temperature ($\sim 23\,^{\circ}C$) held constant. Pressure measurements were taken by incrementally introducing gas in steps of 0.1 MPa, monitored by a Keller ECO 1 digital manometer. Some of the acquired reflection spectra of the two FPI structures for different CH_4 and N_2 gas pressure values are shown in Figure 4.73. Figure 4.73 shows the reflection spectra at different pressure conditions, where it can be seen that as the pressure increases from vacuum to 1.0 MPa the resonance wavelength (λ) shifts towards the longer wavelength due to the increase in optical path difference caused by the increase in the gas refractive index induced by the pressure change. The fringe contrast of the single FP cavity remains constant with increasing CH_4 and N_2 gas pressure, as shown in Figure 4.73 (a) and (b). The measured fringe contrast remains stable at 15.16 dB, indicating that changes in gas pressure do not significantly affect the transmission through the cavity or the reflectivity of the cavity surfaces. In contrast, the in-line dual FP cavity exhibits a measurable increase in fringe contrast with increasing pressure, accompanied by an increase in the intensity of the resonance wavelength at around 1580 nm, as shown in Figure 4.73 (c) and (d). The fringe contrast increases from 15.91 dB at vacuum to 16.77 dB at 1.0 MPa in the presence of CH_4 and N_2, indicating that changes in gas pressure affect the optical properties of the in-line dual Fabry-Pérot cavities. This effect is mainly attributed to changes in the

refractive index or slight changes in the curvature of the middle surface, which increase the fringe contrast.

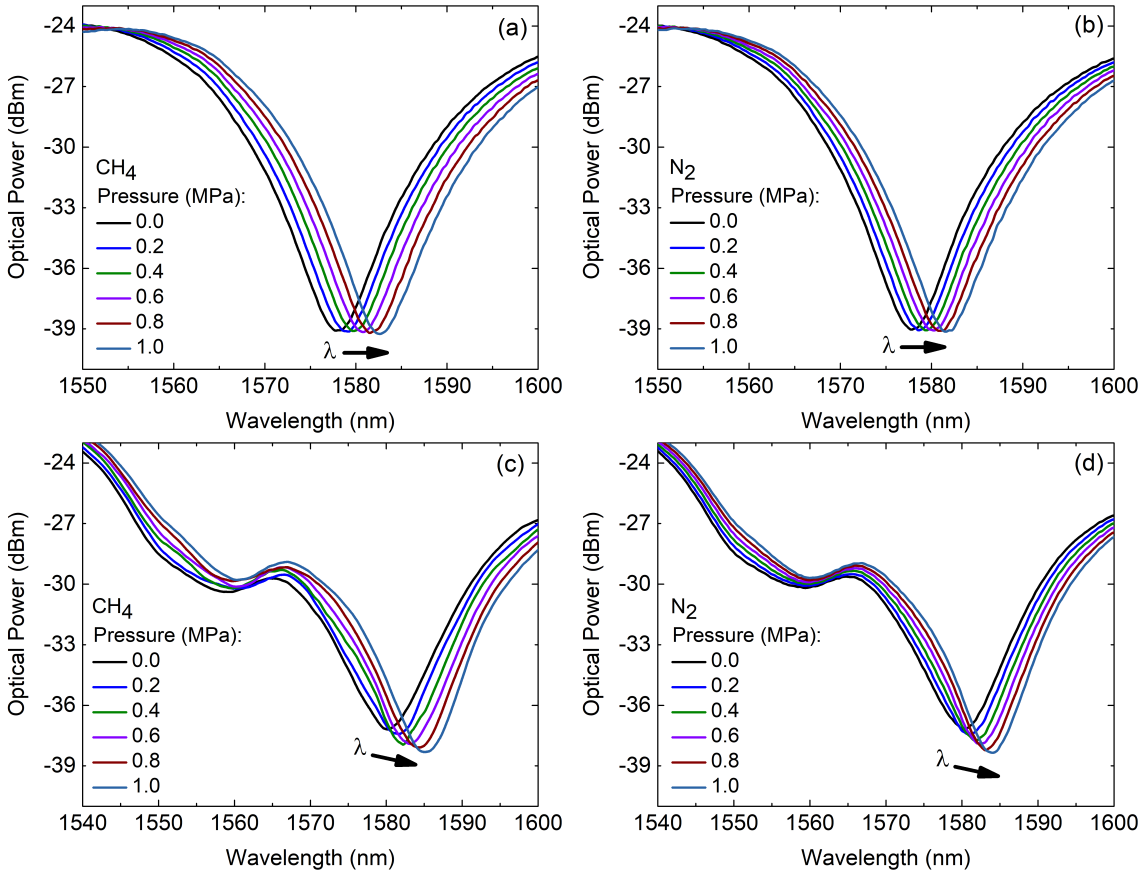


Figure 4.73. *Reflected spectra of the fabricated structures under different CH_4 and N_2 gases pressures, respectively: (a) and (b) single FP cavity; (c) and (d) in-line dual FP cavities.*

The normalized wavelength shift as a function of gas pressure increase ($\uparrow P$), and decrease ($\downarrow P$) for the single FP cavity and, in-line dual FP cavities are shown in Figure 4.74 (a) and (b), respectively.

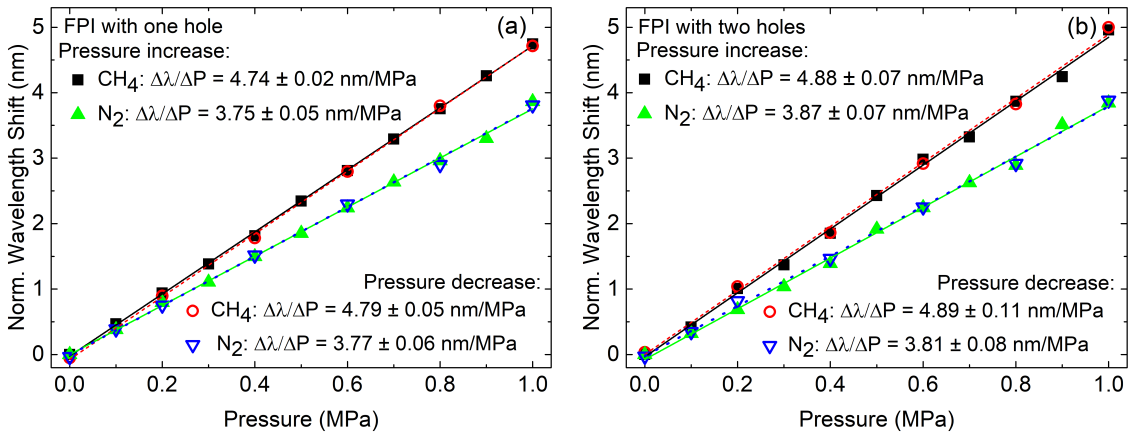


Figure 4.74. *Normalized wavelength shift as a function of gas pressure increase $\uparrow P$, and decrease $\downarrow P$: (a) single FP cavity and, (b) in-line dual FP cavities.*

The gas pressure sensitivity exhibited slight variations for the single FP cavity depending on the gas (CH_4 or N_2) and pressure direction. The gas pressure measured sensitivities are presented in Table 4.27.

Table 4.27. *Gas Pressure Sensitivities of the FPIs.*

FPIs	Gas	Pressure	Sensitivity (nm/MPa)	Linearity (R^2)
Single FP cavity	CH_4	$\uparrow P$	4.74 ± 0.02	0.99
		$\downarrow P$	4.79 ± 0.05	
	N_2	$\uparrow P$	3.75 ± 0.05	
		$\downarrow P$	3.77 ± 0.06	
Dual FP cavities	CH_4	$\uparrow P$	4.88 ± 0.07	0.99
		$\downarrow P$	4.89 ± 0.11	
	N_2	$\uparrow P$	3.87 ± 0.07	
		$\downarrow P$	3.81 ± 0.08	

In the presence of CH_4, a sensitivity of 4.74 ± 0.02 nm/MPa was achieved with increasing pressure and 4.79 ± 0.05 nm/MPa with the decreasing pressure. The sensitivity was lower in the presence of N_2 gas, with a sensitivity of 3.75 ± 0.05 nm/MPa achieved for increasing pressure and 3.77 ± 0.06 nm/MPa for decreasing pressure. The sensitivity of the in-line dual FP cavities was slightly higher than that of the single cavity configuration. In the presence of CH_4, the sensitivity was measured to be 4.88 ± 0.07 nm/MPa at increasing pressure and 4.89 ± 0.11 nm/MPa at decreasing pressure. For N_2, the sensitivity was 3.87 ± 0.07 nm/MPa at increasing pressure and 3.81 ± 0.08 nm/MPa at decreasing pressure. The in-line dual FP cavity structure shows slightly higher sensitivity than the single FP cavity, particularly in the presence of CH_4 gas as SRI. The higher sensitivity in the presence of CH_4 is probably due to its higher refractive index compared to N_2. In addition, no hysteresis was observed and a linearity of $R^2 = 0.99$ was obtained.

The analysis of the spectral resolution was done as described in section 4.2.1, and the data concerning the gases (CH_4 and N_2) pressure step variations are shown in Figure 4.75.

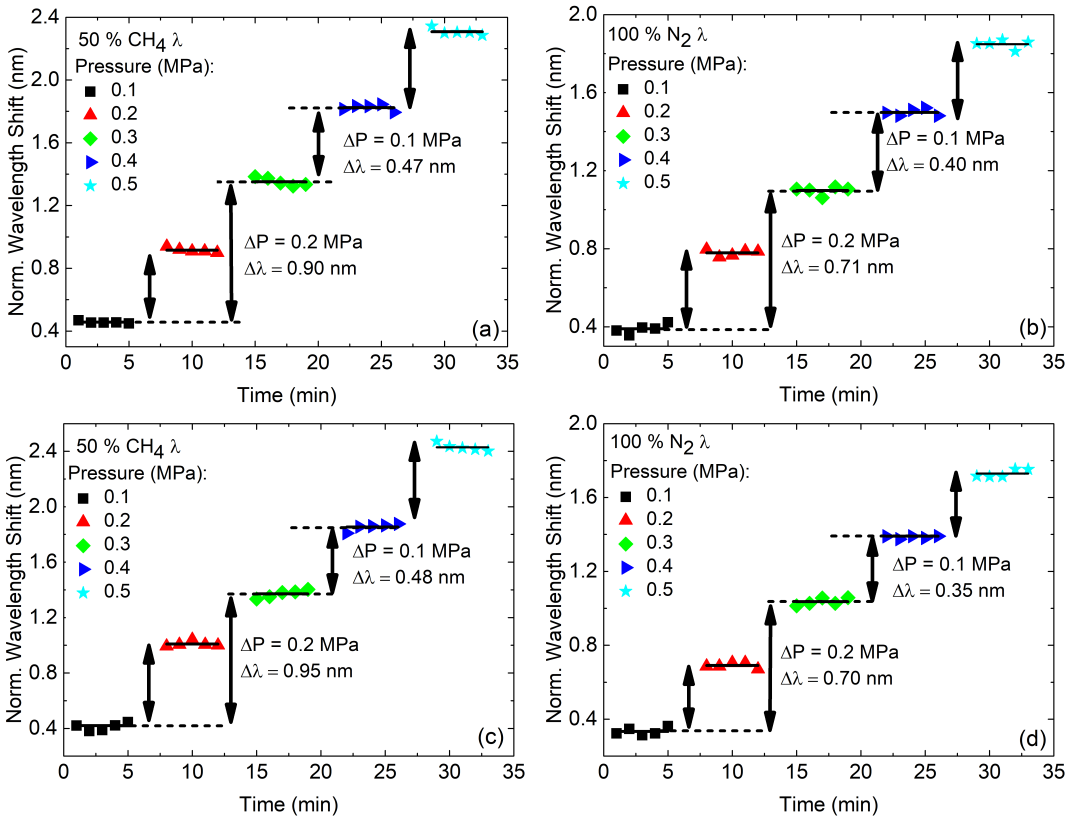


Figure 4.75. *Normalized wavelength shift of the FPIs resonance peak at approximately 1580 nm as a function of time when the gases (CH_4 and N_2) pressure undertakes step variations: (a) and (b) single FP cavity; (c) and (d) in-line dual FP cavities.*

Table 4.28 presents the calculated gas pressure resolutions for both the single and dual FP cavities. Gas pressure resolutions with a magnitude of 10^{-3} MPa were achieved for both the single and dual FP cavities.

Table 4.28. *Gas Pressure Resolutions of the FPIs.*

FPIs	Gas	Step	Gas Pressure Resolutions (MPa)
Single FP cavity	CH_4	1	5.2×10^{-3}
		2	4.9×10^{-3}
	N_2	1	5.9×10^{-3}
		2	5.0×10^{-3}
Dual FP cavities	CH_4	1	5.3×10^{-3}
		2	5.2×10^{-3}
	N_2	1	5.1×10^{-3}
		2	5.0×10^{-3}

Finally, a comparison between the FPIs reported in the literature and the ones developed in this work was realized and summarized in Table 4.29.

Table 4.29. *Gas pressure sensitivity of FPIs reported in the literature and this work.*

FPIs Structure	Sensitivity (nm/MPa)	Pressure Range (MPa)	Ref.
Open-cavity FPI with fiber-tip structure.	4.147	0.0 - 1.52	[246]
FPI with side-opened channel in hollow-core photonic bandgap fiber.	4.240	0.0 - 2.0	[251]
3D-printed FPI: cavity length of 140 µm.	3.959	0.0 - 1.1	[252]
3D-printed FPI: cavity length of 90 µm.	4.097		
Ultra-compact fiber in-line cascaded FPI. Two cavities of 30 µm long separated by a 20 µm unmodified fiber core.	2.860	0.0 - 2.0	[243]
Single FP cavity with $\sim$ 23 µm long.	**4.790**	0.0 - 1.0	This work
Dual FP cavities with $\sim$ 12 µm long, separated by $\sim$ 8 µm length of unmodified fiber core.	**4.890**		

The gas pressure sensitivity of the FPIs shows that the dual FP cavity configuration exhibits the highest sensitivity (4.890 nm/MPa), slightly exceeding that of the single FP cavity (4.790 nm/MPa). These values exceed those observed in other FPIs, such as ultra-compact fiber in-line cascaded FPIs (2.860 nm/MPa) and 3D-printed FPIs, which exhibit sensitivities ranging from 3.959 to 4.097 nm/MPa. Differences in sensitivity between FPIs result from differences in fabrication techniques and structures, highlighting the importance of fabrication parameters in improving gas pressure sensing. The Vernier effect improves sensitivity through the spectral overlap of two interferometric responses with slightly different free spectral ranges. However, this effect was not observed in the dual FP cavity configuration. Possible reasons for this include an insufficient mismatch between the free spectral ranges, improper phase alignment, or low interference contrast between the cavity responses. As a result, instead of the expected amplification, the system only showed a slight improvement in sensitivity compared to the single FP cavity. These results suggest that further optimization of the cavity lengths and reflective interfaces is necessary to achieve the Vernier effect and improve sensitivity.

4.3.3 Summary

This section presented the work developed in the fabrication of the optical fiber interferometers in SMF-28e fibers by the fs-laser system, focusing on the Mach-Zehnder interferometers (MZIs) and Fabry-Pérot interferometers (FPIs). It included a brief introduction to each type of interferometer, an explanation of their working principles, detailed fabrication procedures, and the experimental results related to the characterization of refractive index units (RIU) and gas pressure sensing. The first part of this work focused on the fabrication process, including the coating of different TiO_2

film thicknesses and the spectral characterization of MZIs formed by a pair of LPFGs inscribed in-line. The wavelength response to the SRI of the uncoated and TiO_2 coated MZIs was studied, exhibiting a maximum wavelength sensitivities of -539.8 $\pm$ 24.5 nm/RIU (Band A) and -581.3 $\pm$ 25.7 nm/RIU (Band B) for the MZI coated with 50 nm TiO_2 thickness in the RI range of water-based solutions. The results highlight the advantages of fs-laser written MZIs, particularly when coated with TiO_2. It is expected that by optimizing the TiO_2 thickness and cavity length, further sensitivity enhancements can be achieved while maintaining spectral resolution.

The second part of this work explored the fabrication of Fabry-Pérot interferometers through fs-laser irradiation followed by chemical etching, enabling the development of cavities within the fiber core and open channels to the sample access the sensing region, allowing the sample to in/out. The study focuses on two Fabry-Pérot interferometers: one composed by a single cavity, with a diameter of approximately 23 µm, and the other with an in-line dual cavity configuration, with cavities measuring approximately 12 µm in diameter and separated by approximately 8 µm of unmodified fiber core. The in-line dual FP cavities exhibited a higher free spectral range of 100 nm and fringe visibility of 0.95, compared to 52 nm and 0.94, respectively, in the single FP cavity. This increased FSR and enanhced fringe visibility contributes to an improved spectral resolution. All the configurations were tested under gas pressure variation, and when surrounded by 100% of N_2 and 50% of CH_4/N_2, sensitivities in the order of 3.870 nm/MPa and 4.890 nm/MPa were presented, respectively, in a pressure range of $0-1$ MPa. Gas pressure sensitivity measurements indicated that the dual-cavity FPI achieved a higher sensitivity (4.890 nm/MPa), slightly exceeding that of the single-cavity FPI (4.790 nm/MPa). Given the preliminary results presented, further research is necessary to improve the performance of such FPI sensors. This will involve the optimization of cavity sizes, surface roughness and form to achieve accurate refractive index measurements, which is still to be done, as well as a more thorough optical characterization.

The results demonstrate the feasibility and effectiveness of fs-laser direct writing in fabricating high-sensitivity optical fiber interferometers. The TiO_2 MZIs exhibit an improved refractive index sensitivity, while the dual-cavity FPIs demonstrate enhanced spectral response and gas pressure sensitivity.

4.4 Conclusions

This chapter presented a systematic research and development work on optical fiber sensors, mainly inscribed in SMF-28e fibers using femtosecond laser direct writing. The work focused on the development of fiber Bragg gratings (FBGs), long-period fiber gratings (LPFGs), and optical fiber interferometers, in particular Mach-Zehnder interferometers (MZIs) and Fabry-Pérot interferometers (FPIs). The chapter was structured according to the different sensor architectures, systematically detailing the fabrication methods used, followed by a characterization of their optical and sensing properties. Each sensor type was introduced with a brief overview of its underlying working principle, fabrication process and operating mechanisms. Experimental results were presented to evaluate their performance in various sensing applications.

The first part of this work explored the fabrication of FBGs using fs-laser direct writing, establishing optimal conditions for periodic structure inscription. The successful writing of first- and second-order Bragg gratings in SMF-28e fibers, achieving reflectivities of 99.6% and 59.3%, respectively, demonstrated the feasibility of the developed approach. Furthermore, the ability to inscribe multiple FBGs with different periods in the same fiber highlights the potential for sensor multiplexing and advanced sensing configurations. The thermal stability of fs-inscribed FBGs was evaluated, showing that only fs-written FBGs remained stable at 800°C, exhibiting a temperature sensitivity of 14.34 pm/°C, while UV-written gratings and gratings inscribed in coreless fibers were erased under similar conditions.

The pioner work on the fabrication of off-axis FBGs was also presented, confirming that a lateral inscription shift exceeding 2.5 µm from the fiber core center allows the formation of a multimode fiber section supporting $LP_{0,1}$ and $LP_{1,1}$ modes, each with two degenerate polarization states. The asymmetric grating structures introduced birefringence on the order of 10^{-4}, which was dependent on the inscription offset. The characterization of off-axis FBGs with 3.0, 4.5, and 6.0 µm offsets revealed their ability to simultaneously sense curvature and temperature, with a maximum curvature sensitivity of 1.37×10^{-3} m^{-1} recorded for a 3.0 µm offset. In addition, it was demonstrated the possibility of detecting twist magnitude and direction with the 4.5 µm offset FBG, with a maximum twist sensitivity of 0.140 ± 0.010 dB/(rad/m). These results confirm the feasibility of fs-laser inscribed off-axis FBGs as multi-parameter fiber sensors.

The second part of the work focused on the fabrication of LPFGs using fs-laser direct writing, demonstrating the ability to control mode coupling and spectral properties through the precise selection of grating period. The successful inscription of LPFGs operating at the turn-around point (TAP) was achieved, ensuring well-defined spectral features and suppression of higher-order interference peaks. It was demonstrated that the precise fabrication of the fs-laser LPFGs operating at the TAP requires a precise control on the fiber alignment, submicrometric control of the grating period, the focal position of the laser beam as well as the fiber tension during fabrication.

The thermal stability of fs-inscribed LPFGs was evaluated, showing that annealing was required to stabilize their spectra, with thermal stability confirmed up to 600°C. The TAP LPFGs maintained a temperature-independent resonance in the range of 25−300°C, exhibiting a temperature dependence of 0.0372 dB/°C. Additionally, for temperatures above 250°C, resonance peaks exhibited opposite temperature shifts (-180.73 pm/°C and 179.29 pm/°C), demonstrating their potential for temperature-compensated sensing applications. The results also indicated that high-temperature annealing (>850°C) resulted in the emergence of higher-order cladding modes ($LP_{1,7}$), enabling spectral tuning through thermal processing.

Titanium dioxide films of different thicknesses were deposited around the LPFGs to enhance their sensitivity to refractive index (RI) variations. The highest sensitivity, 8051.4 nm/RIU, was achieved for the 192.5 µm LPFG coated with 30 nm TiO_2 in the 1.3700−1.4120 RI range, while an uncoated LPFG exhibited a maximum sensitivity of 3151.8 nm/RIU in water-based solutions. Comparisons with electric arc fabricated LPFGs coated with 60 nm of TiO_2 showed higher sensitivity for fs-laser inscribed LPFGs, achieving a sensitivity of 570 nm/RIU at 1.3600 RI compared to

525nm/RIU for arc-fabricated LPFGs.

The final part of this study addressed the fabrication and characterization of optical fiber interferometers, specifically Mach-Zehnder interferometers (MZIs) and Fabry-Pérot interferometers (FPIs). The fs-laser written MZIs, formed by inscribing long-period fiber gratings (LPFGs) in-line, demonstrated enhanced refractive index (RI) sensitivity, with maximum sensitivities of -539.8 ± 24.5 nm/RIU (Band A) and -581.3 ± 25.7 nm/RIU (Band B) for MZIs coated with 50 nm TiO_2 thickness in the RI range of water-based solutions.

Fabry-Pérot interferometers were fabricated using fs-laser irradiation followed by chemical etching, enabling the development of cavities within the fiber core and open channels to the sample access the sensing region, allowing the sample to in/out. Two FPI configurations were developed: one composed by a single cavity, with a diameter of approximately 23 µm, and the other with an in-line dual cavity configuration, with cavities measuring approximately 12 µm in diameter and separated by approximately 8 µm of unmodified fiber core).

The in-line dual FP cavities exhibited a higher free spectral range of 100 nm and fringe visibility of 0.95, compared to 52 nm and 0.94, respectively, in the single FP cavity. This increased FSR and enanhced fringe visibility contributes to an improved spectral resolution. Gas pressure measurements demonstrated sensitivities of 3.870 nm/MPa (100% N_2) and 4.890 nm/MPa (50% CH_4/N_2), with the dual-cavity FPI achieving the highest sensitivity. These results indicate that femtosecond laser-inscribed Fabry-Pérot interferometers (FPIs) exhibit spectral characteristics suitable for gas pressure sensing and high-resolution optical interrogation.

This work has demonstrated the feasibility and advantages of fs-laser direct writing for fabricating high sensitivity optical fiber sensors, offering precise control over mode coupling, spectral response, and sensing characteristics. The results confirm that fs-laser inscribed LPFGs and MZIs exhibit higher sensitivity compared to conventional fabrication techniques, particularly in high-temperature applications and refractive index sensing with TiO_2 coatings. Additionally, the work shown annealing as a tool for spectral tuning, allowing for temperature stabilization and control over modal properties.

The successful fabrication of off-axis fiber Bragg gratings (FBGs) with controlled birefringence, curvature sensitivity, and twist detection, along with the development of long-period fiber gratings (LPFGs) optimized for thermal stability and enhanced refractive index (RI) sensitivity, provides a solid framework for the advancement of multi-parameter optical fiber sensing. These results indicate that by precisely tailoring the inscription parameters and structural modifications, it is possible to design fiber-based sensors capable of simultaneously measuring multiple physical parameters with high sensitivity and reliability.

CHAPTER 5

Conclusion

The main focus of this PhD program was the development of a femtosecond (fs) laser processing system for microfabrication of sensing structures in optical fibers. The foundation of this work is built upon three-dimensional (3D) micromachining using an fs-laser, leveraging its high precision and minimal heat-affected zone (HAZ) to optimize the fabrication of optical fiber sensors. The selection of this laser technology over other processing techniques is justified by its unique characteristics, including ultrashort pulse width, extremely high peak intensity, and high spatial resolution beyond the diffraction limit. These advantages facilitate the fabrication of intricate structures with enhanced performance, expanding the potential for optical fiber sensing applications. The developed direct writing system employs the fiber-amplified fs-laser Satsuma HP from Amplitude Systèmes, pulse controller, focusing optics, vision system, and sample positioning.

The research aimed to develop and optimize optical fiber sensor fabrication techniques, focusing on fiber Bragg gratings (FBGs), long-period fiber gratings (LPFGs), and optical interferometers, specifically Mach-Zehnder interferometers (MZIs) and Fabry-Pérot interferometers (FPIs). The objective was to enhance the precision, stability, and versatility of optical fiber sensors through femtosecond (fs) laser processing, while exploring novel fabrication methodologies and advanced characterization techniques.

One of the primary achievements of this research was the development of a cost-effective fs-laser fabrication system, designed to process various types of optical fibers with integrated fiber positioning, alignment, and pre-tensioning mechanisms. The system was designed to offer flexibility in fabrication by accommodating both oil-immersion and dry objective lenses. A significant aspect of this work was the optimization of fs-laser writing parameters, ensuring high precision, reproducibility, and long-term stability of the fabricated sensors. A systematic analysis was performed to understand the effects of scan velocity, writing pulse energy, and beam spot size, leading to refined fabrication techniques that enhance sensor performance.

To improve the reliability and applicability of these sensors in harsh environments, this study also investigated the thermal stability of FBGs and LPFGs, particularly through thermal annealing. This work established optimal annealing conditions, allowing the fabricated sensors to be effectively used in high-temperature sensing applications. Additionally, the research introduced the design and characterization of advanced optical fiber sensors, demonstrating improved performance across multiple optical modulation formats, including intensity, wavelength, phase, and polarization-based detection. These developments pave the way for high-sensitivity, multi-parameter sensing applications.

Beyond conventional fabrication techniques, this work also explored the integration of fs-laser irradiation with chemical etching, enabling the development of cavities within the fiber core and open channels to the sample access the sensing region, allowing the sample to in/out. This technique significantly expands the application scope of optical fiber sensors, particularly in biological, chemical, and biochemical sensing, by facilitating the measurement of refractive index variations in surrounding media.

This research led to the establishment of a technological platform for fs-laser-inscribed gratings, which not only contributed to fundamental scientific advancements but also fostered industrial collaborations with the Fraunhofer Institute for Manufacturing Engineering and Automation and EFACEC (Empresa Fabril de Máquinas Eléctricas, SARL). These collaborations highlight the industrial relevance and practical applicability of the developed sensors in real-world applications. Furthermore, this work played an important role in academic training and skill development by contributing to the Advanced Laboratories of the Integrated Master of Science in Physics Engineering at the Faculty of Sciences, University of Porto (FCUP).

This PhD research significantly advances fs-laser inscription techniques in optical fibers, offering new insights into sensor fabrication methodologies and expanding the range of applications for optical fiber based sensing technologies. The main contributions of this research include:

Fabrication of Off-Axis First-Order FBGs in SMF-28e Fibers:

- A minimum offset distance of 2.5 µm between the grating and fiber core center was determined, leading to the formation of a multimode section that supports two separate fiber modes ($LP_{0,1}$ and $LP_{1,1}$).
- The resulting structure introduces birefringence (10^{-4}), breaking the cylindrical symmetry of the fiber and creating polarization-dependent Bragg wavelengths.
- The multimode section was successfully tested for strain, temperature, curvature, and torsion sensing, demonstrating its robustness and potential for simultaneous multi-parameter detection.

Optimization of fs-Laser Inscribed LPFGs, Including Thermal Annealing and TiO_2 Coatings:

- A systematic fabrication and characterization study was conducted on LPFGs operating at the turn-around point (TAP) in SMF-28e fibers.
- The study evaluated grating periods, refractive index modification geometry, and TiO_2 film thickness for precise TAP operation in air and water, achieving asymmetric cladding mode coupling.
- Thermal annealing was found to be essential for spectral stability, and the fabricated LPFGs remained thermally stable up to 600 °C.
- The research demonstrated fine-tuning of resonance bands and significant enhancement in SRI sensitivity with TiO_2 coated LPFGs, surpassing previously reported values.

These innovative contributions significantly enhance the capabilities of fs-laser-inscribed optical fiber sensors, paving the way for high-sensitivity, multi-parameter sensing applications. Beyond

advancing scientific knowledge, this work has established a technology platform that is relevant to industry, demonstrating the feasibility of fs-laser-fabricated sensors for both commercial and applied research purposes.

5.1 Future Work

While this research has made significant advancements in fs-laser-based optical fiber sensor fabrication, several areas remain open for further exploration:

Enhancing Fabrication Precision and Repeatability:

- Future research should focus on refining the fs-laser inscription process to improve sensor uniformity and reproducibility.
- The integration of advanced beam-shaping techniques, such as spatial light modulators, astigmatic lenses, and water immersion objectives, could further enhance the quality of the focal volume and overall fabrication accuracy.
- The implementation of Position Synchronized Output (PSO) systems should be explored to ensure superior repeatability compared to the developed triggering method.
- Optimization of plane-by-plane inscription strategies may enable the precise fabrication of complex and slanted grating structures, enhancing both precision and design flexibility.

Expanding Sensor Applications and Multi-Parameter Sensing:

- The developed sensors could be optimized for simultaneous detection of temperature, strain, pressure, and refractive index variations.
- Hybrid sensing configurations, integrating different grating structures and interferometric techniques, should be explored.

Exploration of Different Fibers:

- Research should investigate fs-laser processing of special fibers, such as photonic crystal fibers, hollow-core fibers, multi-core fibers (MCFs), and high-birefringence (Hi-Bi) fibers.
- Extending micromachining capabilities to these fiber types could expand the range of detectable parameters and improve sensor performance.
- The concept of cladding functionalization, using the fiber surface as a functional substrate for novel sensing architectures, represents a promising direction for advanced sensor integration.

In the future, the integration of emerging technologies such as artificial intelligence, machine learning, and advanced data analytics could further improve the performance, scalability, and automation of fs-laser-inscribed optical fiber sensors.

5.2 Final Remarks

This PhD research marks a strategic advancement for the research group, nurturing new opportunities for international collaboration and reinforcing its potential for scientific innovation and commercialization. The results of this work will provide a foundation for further exploration of fs-laser microfabrication techniques, aiming to enhance optical fiber sensing technologies for a variety of scientific and industrial applications. This will lead to higher precision, broader applicability, and increased reliability in demanding sensing environments.

References

[1] G. Rajan, Optical Fiber Sensors: Advanced Techniques and Applications, 1st Edition, CRC press, 2015. doi:10.1201/b18074. [Cited on pages 1, 2, 3, 57, 59, 60, 61, 77, and 78.]

[2] L. Thevenaz, Advanced fiber optics: concepts and technology, EPFL press, 2011. doi:10.1201/b16404. [Cited on page 2.]

[3] L. A. Fernandes, J. R. Grenier, P. R. Herman, J. S. Aitchison, P. V. S. Marques, Stress induced birefringence tuning in femtosecond laser fabricated waveguides in fused silica, Optics Express 20 (2012) 24103−24114. doi:10.1364/OE.20.024103. [Cited on page 5.]

[4] K. M. Davis, K. Miura, N. Sugimoto, K. Hirao, Writing waveguides in glass with a femtosecond laser, Optics Letters 21 (1996) 1729−1731. doi:10.1364/OL.21.001729. [Cited on page 15.]

[5] R. Osellame, G. Cerullo, R. Ramponi, Femtosecond Laser Micromachining: Photonic and Microfluidic Devices in Transparent Materials, 1st Edition, Vol. 123 of Topics in Applied Physics Ser., Springer Berlin, Heidelberg, Berlin, Heidelberg, 2012. doi:10.1007/978-3-642-23366-1. [Cited on pages 15, 16, 17, 18, 19, 20, 21, 22, 23, 24, 25, 26, 27, 28, 60, and 61.]

[6] H. Xiao, L. Yuan, B. Cheng, Y. Song, All Optical Fiber Optofluidic or Ferrofluidic Microsensors Fabricated by Femtosecond Laser Micromachining, Springer Singapore, Singapore, 2019, pp. 2351−2388. doi:10.1007/978-981-10-7087-7_63. [Cited on pages 16, 17, 18, 19, 20, 21, and 22.]

[7] R. Kashyap, Fiber Bragg Gratings, 2nd Edition, Academic Press, 2010. doi:10.1016/C2009-0-16830-7. [Cited on pages 15, 20, 21, 28, 29, 30, 47, 57, 59, 60, 61, 69, 78, and 88.]

[8] R. R. Gattass, E. Mazur, Femtosecond laser micromachining in transparent materials, Nature Photonics 2 (2008) 219−225. doi:10.1038/nphoton.2008.47. [Cited on pages 16 and 27.]

[9] B. Rethfeld, K. Sokolowski-Tinten, D. von der Linde, S. I. Anisimov, Timescales in the response of materials to femtosecond laser excitation, Applied Physics A 79 (2004) 767−769. doi:10.1007/s00339-004-2805-9. [Cited on page 15.]

[10] M. Beresna, M. Gecevičius, P. G. Kazansky, Ultrafast laser direct writing and nanostructuring in transparent materials, Advances in Optics and Photonics 6 (2014) 293−339. doi:10.1364/AOP.6.000293. [Cited on pages 16, 17, 18, 23, and 24.]

[11] M. Ams, G. D. Marshall, P. Dekker, M. Dubov, V. K. Mezentsev, I. Bennion, M. J. Withford, Investigation of ultrafast laser−photonic material interactions: Challenges for directly written glass photonics, IEEE Journal of Selected Topics in Quantum Electronics 14 (2008) 1370−1381. doi:10.1109/JSTQE.2008.925809. [Cited on pages 16, 17, 18, and 19.]

[12] C. Hnatovsky, R. S. Taylor, P. P. Rajeev, E. Simova, V. R. Bhardwaj, D. M. Rayner, P. B. Corkum, Pulse duration dependence of femtosecond-laser-fabricated nanogratings in fused silica, Applied Physics Letters 87 (2005) 14104. doi:10.1063/1.1991991. [Cited on pages 18 and 19.]

[13] L. Shah, A. Y. Arai, S. M. Eaton, P. R. Herman, Waveguide writing in fused silica with a femtosecond fiber laser at 522 nm and 1 MHz repetition rate, Optics Express 13 (2005) 1999–2006. doi:10.1364/OPEX.13.001999. [Cited on pages 18, 19, and 43.]

[14] D. Pallarés-Aldeiturriaga, P. Roldán-Varona, L. Rodríguez-Cobo, J. M. López-Higuera, Optical Fiber Sensors by Direct Laser Processing: A Review, Sensors 20 (23) (2020) 6971. doi:10.3390/s20236971. [Cited on pages 18, 25, 26, 27, 28, 29, 30, 34, 35, 39, 69, and 70.]

[15] J. R. Grenier, M. Haque, L. A. Fernandes, K. K. C. Lee, P. R. Herman, Femtosecond Laser Inscription of Photonic and Optofluidic Devices in Fiber Cladding, Springer New York, New York, NY, 2015, pp. 67–110. doi:10.1007/978-1-4939-1179-0_4. [Cited on pages 18, 34, 35, 36, 37, 39, and 57.]

[16] C. Hnatovsky, R. S. Taylor, E. Simova, P. P. Rajeev, D. M. Rayner, V. R. Bhardwaj, P. B. Corkum, Fabrication of microchannels in glass using focused femtosecond laser radiation and selective chemical etching, Applied Physics A 84 (1–2) (2006) 47–61. doi:10.1007/s00339-006-3590-4. [Cited on pages 18, 19, 25, 26, 27, and 146.]

[17] D. N. Wang, Y. Wang, C. R. Liao, 14 - Femtosecond laser micromachining on optical fiber, in: J. Lawrence, D. Waugh (Eds.), Laser Surface Engineering, no. number 65 in Woodhead Publishing Series in Electronic and Optical Materials, Woodhead Publishing, Cambridge, England, 2015, pp. 359–381. doi:10.1016/B978-1-78242-074-3.00014-3. [Cited on pages 19, 27, 28, 30, 31, 32, 33, 34, 35, and 69.]

[18] S. Gross, M. J. Withford, Ultrafast-laser-inscribed 3D integrated photonics: challenges and emerging applications, Nanophotonics 4 (3) (2015) 332–352. doi:10.1515/nanoph-2015-0020. [Cited on pages 19 and 20.]

[19] K. Zhou, Y. Lai, X. Chen, K. Sugden, L. Zhang, I. Bennion, A refractometer based on a micro-slot in a fiber bragg grating formed by chemically assisted femtosecond laser processing, Optics Express 15 (2007) 15848. doi:10.1364/oe.15.015848. [Cited on pages 20, 26, and 35.]

[20] A. Saliminia, S. L. Chin, R. Vallée, Ultra-broad and coherent white light generation in silica glass by focused femtosecond pulses at 1.5 μm, Optics Express 13 (2005) 5731–5738. doi:10.1364/OPEX.13.005731. [Cited on page 21.]

[21] S. L. Chin, W. Liu, F. Théberge, Q. Luo, S. A. Hosseini, V. P. Kandidov, O. G. Kosareva, N. Aközbek, A. Becker, H. Schroeder, Some Fundamental Concepts of Femtosecond Laser Filamentation, Springer Berlin Heidelberg, 2008, pp. 243–264. doi:10.1007/978-3-540-73794-0_12. [Cited on pages 21 and 22.]

[22] J. Thomas, C. Voigtländer, R. G. Becker, D. Richter, A. Tünnermann, S. Nolte, Femtosecond pulse written fiber gratings: a new avenue to integrated fiber technology, Laser & Photonics Reviews 6 (6) (2012) 709–723. doi:10.1002/lpor.201100033. [Cited on pages 23, 24, 28, 30, 57, 69, and 70.]

[23] K. Sugioka, Y. Cheng, Femtosecond laser 3D micromachining for microfluidic and optofluidic applications, 2013. doi:10.1007/978-1-4471-5541-6. [Cited on pages 26, 27, and 35.]

[24] M. Haque, K. K. C. Lee, S. Ho, L. A. Fernandes, P. R. Herman, Chemical-assisted femtosecond laser writing of lab-in-fibers, Lab Chip 14 (2014) 3817–3829. doi:10.1039/C4LC00648H. [Cited on pages 27, 33, 35, 38, and 39.]

[25] K. Sugioka, Y. Cheng, Femtosecond laser three-dimensional micro-and nanofabrication, Applied Physics Reviews 1 (2014) 041303. doi:10.1063/1.4904320. [Cited on pages 27, 32, 33, and 35.]

[26] J. R. Grenier, L. A. Fernandes, P. R. Herman, Femtosecond laser inscription of asymmetric directional couplers for in-fiber optical taps and fiber cladding photonics, Optics Express 23 (2015) 16760−16771. doi:10.1364/OE.23.016760. [Cited on pages 28, 34, 35, 36, 37, 39, 57, and 58.]

[27] G. Marowsky, Planar waveguides and other confined geometries: Theory, technology, production, and novel applications, 1st Edition, Vol. 189, Springer, New York, NY, 2015. doi:10.1007/978-1-4939-1179-0. [Cited on pages 28, 30, 32, 33, 34, 35, 36, and 39.]

[28] T. Gissibl, S. Thiele, A. Herkommer, H. Giessen, Sub-micrometre accurate free-form optics by three-dimensional printing on single-mode fibres, Nature Communications 7 (2016) 11763. doi:10.1038/ncomms11763. [Cited on page 28.]

[29] Y.-J. Rao, Z.-L. Ran, Optic fiber sensors fabricated by laser-micromachining, Optical Fiber Technology 19 (6) (2013) 808−821. doi:10.1016/j.yofte.2013.07.016. [Cited on pages 28, 30, 31, and 32.]

[30] K. Kalli, C. Riziotis, A. Posporis, C. Markos, C. Koutsides, S. Ambran, A. S. Webb, C. Holmes, J. C. Gates, J. K. Sahu, P. G. R. Smith, Flat fibre and femtosecond laser technology as a novel photonic integration platform for optofluidic based biosensing devices and lab-on-chip applications: Current results and future perspectives, Sensors and Actuators B: Chemical 209 (2015) 1030−1040. doi:10.1016/j.snb.2014.12.003. [Cited on pages 28, 33, and 131.]

[31] J. He, B. Xu, X. Xu, C. Liao, Y. Wang, Review of Femtosecond-Laser-Inscribed Fiber Bragg Gratings: Fabrication Technologies and Sensing Applications, Photonic Sensors 11 (2021) 203−226. doi:10.1007/s13320-021-0629-2. [Cited on pages 28, 29, 30, 57, and 58.]

[32] K. Oi, F. Barnier, M. Obara, Fabrication of fiber bragg grating by femtosecond laser interferometry, in: LEOS 2001. 14th Annual Meeting of the IEEE Lasers and Electro-Optics Society (Cat. No.01CH37242), Vol. 2, 2001, pp. 776−777 vol.2. doi:10.1109/LEOS.2001.969045. [Cited on page 28.]

[33] A. Dragomir, D. N. Nikogosyan, K. A. Zagorulko, P. G. Kryukov, E. M. Dianov, Inscription of fiber bragg gratings by ultraviolet femtosecond radiation, Optics Letters 28 (2003) 2171−2173. doi:10.1364/OL.28.002171. [Cited on page 28.]

[34] S. J. Mihailov, C. W. Smelser, P. Lu, R. B. Walker, D. Grobnic, H. Ding, G. Henderson, J. Unruh, Fiber bragg gratings made with a phase mask and 800-nm femtosecond radiation., Optics letters 28 (2003) 995−997. doi:10.1364/OL.28.000995. [Cited on page 28.]

[35] M. Becker, J. Bergmann, S. Brückner, M. Franke, E. Lindner, M. W. Rothhardt, H. Bartelt, Fiber Bragg grating inscription combining DUV sub-picosecond laser pulses and two-beam interferometry, Optics Express 16 (2008) 19169. doi:10.1364/oe.16.019169. [Cited on page 28.]

[36] E. Ertorer, M. Haque, J. Li, P. R. Herman, Femtosecond laser filaments for rapid and flexible writing of fiber bragg grating, Optics Express 26 (2018) 9323. doi:10.1364/oe.26.009323. [Cited on pages 28 and 29.]

[37] A. Martinez, M. Dubov, I. Khrushchev, I. Bennion, Direct writing of fibre bragg gratings by femtosecond laser, Electronics Letters 40 (2004) 1170−1172. doi:10.1049/el:20046050. [Cited on pages 28, 29, and 57.]

[38] E. Wikszak, J. Burghoff, M. Will, S. Nolte, A. Tünnermann, T. Gabler, Recording of fiber bragg gratings with femtosecond pulses using a “point by point” technique, in: Conference on Lasers and Electro-Optics/International Quantum Electronics Conference and Photonic Applications Systems Technologies, Optical Society of America, 2004, p. CThM7. [Cited on page 28.]

[39] J. R. Grenier, L. A. Fernandes, P. V. S. Marques, J. S. Aitchison, P. R. Herman, Optical circuits in fiber cladding: Femtosecond laser-written bragg grating waveguides, in: CLEO:2011 - Laser Applications to Photonic Applications, Optical Society of America, 2011, p. CMZ1. doi:10.1364/CLEO_SI.2011.CMZ1. [Cited on pages 28, 29, and 57.]

[40] K. Zhou, M. Dubov, C. Mou, L. Zhang, V. K. Mezentsev, I. Bennion, Line-by-line fiber bragg grating made by femtosecond laser, IEEE Photonics Technology Letters 22 (2010) 1190–1192. doi:10.1109/LPT.2010.2050877. [Cited on pages 28 and 29.]

[41] B. Huang, X. Shu, Line-by-line inscription of phase-shifted fiber bragg gratings with femtosecond laser, in: J. Y. K. K. T. H. X. K. G. P. C Lu Luo, J., N. Wada (Eds.), Asia Communications and Photonics Conference 2015, Optical Society of America, 2015, p. ASu2A.60. doi:10.1364/ACPC.2015.ASu2A.60. [Cited on pages 28, 29, and 30.]

[42] A. Theodosiou, A. Lacraz, M. Polis, K. Kalli, M. Tsangari, A. Stassis, M. Komodromos, Modified fs-laser inscribed fbg array for rapid mode shape capture of free-free vibrating beams, IEEE Photonics Technology Letters 28 (2016) 1509–1512. doi:10.1109/LPT.2016.2555852. [Cited on pages 28 and 30.]

[43] P. Lu, S. J. Mihailov, H. Ding, D. Grobnic, R. Walker, D. Coulas, C. Hnatovsky, A. Y. Naumov, Plane-by-plane inscription of grating structures in optical fibers, 25th International Conference on Optical Fiber Sensors 10323 (2017) 103234M. doi:10.1117/12.2265793. [Cited on pages 28 and 30.]

[44] P. S. Salter, M. J. Woolley, S. M. Morris, M. J. Booth, J. A. J. Fells, Femtosecond fiber bragg grating fabrication with adaptive optics aberration compensation, Optics Letters 43 (2018) 5993. doi:10.1364/ol.43.005993. [Cited on page 29.]

[45] F. Ahmed, M. B. G. Jun, Filament-based fabrication and performance analysis of fiber bragg grating sensors using ultrashort pulse laser, Journal of Micro and Nano-Manufacturing 2. doi:10.1115/1.4027368. [Cited on page 29.]

[46] R. J. Williams, R. G. Krämer, S. Nolte, M. J. Withford, Femtosecond direct-writing of low-loss fiber bragg gratings using a continuous core-scanning technique, Optics Letters 38 (2013) 1918. doi:10.1364/ol.38.001918. [Cited on page 29.]

[47] P. R. Herman, H. Zhang, Ultrashort-pulsed laser direct writing of strong bragg grating waveguides in bulk glasses, OFC/NFOEC 2008 - 2008 Conference on Optical Fiber Communication/National Fiber Optic Engineers Conference 1 (2008) 8–10. doi:10.1109/OFC.2008.4528551. [Cited on pages 29 and 47.]

[48] S. Antipov, M. Ams, R. J. Williams, E. Magi, M. J. Withford, A. Fuerbach, Direct infrared femtosecond laser inscription of chirped fiber bragg gratings, Optics Express 24 (2016) 30. doi:10.1364/oe.24.000030. [Cited on pages 29 and 30.]

[49] H. Zhang, S. M. Eaton, P. R. Herman, Single-step writing of bragg grating waveguides in fused silica with an externally modulated femtosecond fiber laser, Optics Letters 32 (2007) 2559. doi:10.1364/ol.32.002559. [Cited on pages 29, 47, and 66.]

[50] J. Burgmeier, C. Waltermann, G. Flachenecker, W. Schade, Point-by-point inscription of phase-shifted fiber bragg gratings with electro-optic amplitude modulated femtosecond laser pulses, Optics Letters 39 (2014) 540. doi:10.1364/ol.39.000540. [Cited on page 30.]

[51] Y. X. Jin, C. C. Chan, X. Y. Dong, Y. F. Zhang, Temperature-independent bending sensor with tilted fiber bragg grating interacting with multimode fiber, Optics Communications 282 (2009) 3905−3907. doi:10.1016/j.optcom.2009.06.058. [Cited on pages 30, 58, and 59.]

[52] X. Fang, X. Y. He, C. R. Liao, M. Yang, D. N. Wang, Y. Wang, A new method for sampled fiber Bragg grating fabrication by use of both femtosecond laser and CO_2 laser, Optics Express 18 (2010) 2646. doi:10.1364/oe.18.002646. [Cited on pages 30 and 58.]

[53] R. J. Williams, C. Voigtländer, G. D. Marshall, A. Tünnermann, S. Nolte, M. J. Steel, M. J. Withford, Point-by-point inscription of apodized fiber bragg gratings, Optics Letters 36 (2011) 2988−2990. doi:10.1364/OL.36.002988. [Cited on page 30.]

[54] D. Grobnic, C. W. Smelser, S. J. Mihailov, R. B. Walker, Long-term thermal stability tests at 1000 c of silica fibre bragg gratings made with ultrafast laser radiation, Measurement Science and Technology 17 (2006) 1009. doi:10.1088/0957-0233/17/5/s12. [Cited on pages 30 and 58.]

[55] S. J. Mihailov, D. Grobnic, C. Hnatovsky, R. B. Walker, P. Lu, D. Coulas, H. Ding, Extreme Environment Sensing Using Femtosecond Laser-Inscribed Fiber Bragg Gratings, Sensors 17. doi:10.3390/s17122909. [Cited on pages 30, 58, 69, 70, and 79.]

[56] G. Brambilla, H. Rutt, Fiber bragg gratings with enhanced thermal stability, Applied Physics Letters 80 (2002) 3259−3261. doi:10.1063/1.1475366. [Cited on page 30.]

[57] T. Blanchet, A. Morana, S. Nehr, G. Laffont, E. Marin, A. Boukenter, Y. Ouerdane, S. Girard, Combined radiations and temperature effects on fbgs photo-inscribed by femtosecond laser in radiation-hardened optical fibers, in: Advanced Photonics 2018 (BGPP, IPR, NP, NOMA, Sensors, Networks, SPPCom, SOF), Optical Society of America, 2018, p. BM4A.5. doi:10.1364/BGPPM.2018.BM4A.5. [Cited on page 30.]

[58] W. Bao, N. Sahoo, Z. Sun, C. Wang, S. Liu, Y. Wang, L. Zhang, Selective fiber bragg grating inscription in four-core fiber for two-dimension vector bending sensing, Optics Express 28 (2020) 26461−26469. doi:10.1364/OE.398794. [Cited on page 31.]

[59] A. Donko, M. Beresna, Y. Jung, J. Hayes, D. J. Richardson, G. Brambilla, Point-by-point femtosecond laser micro-processing of independent core-specific fiber bragg gratings in a multi-core fiber, Optics Express 26 (2018) 2039−2044. doi:10.1364/OE.26.002039. [Cited on page 31.]

[60] K. C. Vishnubhatla, N. Bellini, R. Ramponi, G. Cerullo, R. Osellame, Shape control of microchannels fabricated in fused silica by femtosecond laser irradiation and chemical etching, Optics Express 17 (2009) 8685−8695. doi:10.1364/OE.17.008685. [Cited on page 31.]

[61] K. Zhou, L. Zhang, X. Chen, V. Mezentsev, I. Bennion, Microstructures made in optical fiber with femtosecond laser, International Journal of Smart and Nano Materials 1 (2010) 237−248. doi:10.1080/19475411.2010.529251. [Cited on page 31.]

[62] M. Haque, J. R. Grenier, K. K. C. Lee, L. A. Fernandes, P. R. Herman, Femtosecond laser 3d writing: from smart catheters to distributed lab-in-fiber sensing, SPIE Newsroom 8. doi:10.1117/2.1201505.005979. [Cited on pages 32, 34, 35, 36, and 39.]

[63] L. Yuan, J. Huang, X. Lan, H. Wang, L. Jiang, H. Xiao, All-in-fiber optofluidic sensor fabricated by femtosecond laser assisted chemical etching, Optics Letters 39 (2014) 2358–2361. doi:10.1364/OL.39.002358. [Cited on pages 32 and 131.]

[64] C. R. Liao, Y. Wang, D. N. Wang, M. W. Yang, Fiber in-line mach–zehnder interferometer embedded in fbg for simultaneous refractive index and temperature measurement, IEEE Photonics Technology Letters 22 (2010) 1686–1688. doi:10.1109/LPT.2010.2079924. [Cited on pages 32 and 131.]

[65] C. R. Liao, D. N. Wang, M. Wang, M. Yang, Fiber in-line michelson interferometer tip sensor fabricated by femtosecond laser, IEEE Photonics Technology Letters 24 (2012) 2060–2063. doi:10.1109/LPT.2012.2219517. [Cited on pages 32 and 131.]

[66] F. He, Y. Liao, J. Lin, J. Song, L. Qiao, Y. Cheng, K. Sugioka, Femtosecond Laser Fabrication of Monolithically Integrated Microfluidic Sensors in Glass, Sensors 14. doi:10.3390/s141019402. [Cited on pages 33 and 34.]

[67] C. R. Liao, D. N. Wang, Y. Wang, Microfiber in-line Mach-Zehnder interferometer for strain sensing, Optics Letters 38 (2013) 757–759. doi:10.1364/OL.38.000757. [Cited on page 33.]

[68] M. Consales, A. Ricciardi, A. Crescitelli, E. Esposito, A. Cutolo, A. Cusano, Lab-on-fiber technology: Toward multifunctional optical nanoprobes, ACS Nano 6 (2012) 3163–3170. doi:10.1021/nn204953e. [Cited on page 34.]

[69] J. Ma, A. Kos, W. J. Bock, X. Li, H. Nguyen, Z. Y. Wang, A. Cusano, Lab-on-a-Fiber Device for Trace Vapor TNT Explosive Detection: Comprehensive Performance Evaluation, Journal of Lightwave Technology 30 (2012) 1127–1133. doi:10.1109/jlt.2011.2170154. [Cited on page 34.]

[70] A. N. Chryssis, S. M. Lee, S. B. Lee, S. S. Saini, M. Dagenais, High sensitivity evanescent field fiber bragg grating sensor, IEEE Photonics Technology Letters 17 (2005) 1253–1255. doi:10.1109/LPT.2005.846953. [Cited on page 34.]

[71] S. Pevec, D. Donlagic, All-fiber, long-active-length Fabry-Perot strain sensor, Optics Express 19 (16) (2011) 15641–15651. doi:10.1364/OE.19.015641. [Cited on page 34.]

[72] Y. Gong, Y. Rao, Y. Guo, Z. Ran, Y. Wu, Temperature-Insensitive Micro Fabry–PÉrot Strain Sensor Fabricated by Chemically Etching Er-Doped Fiber, IEEE Photonics Technology Letters 21 (22) (2009) 1725–1727. doi:10.1109/LPT.2009.2032662. [Cited on page 34.]

[73] A. M. Vengsarkar, P. J. Lemaire, J. B. Judkins, V. Bhatia, T. Erdogan, J. E. Sipe, Long-period fiber gratings as band-rejection filters, Journal of Lightwave Technology 14 (1996) 58–65. doi:10.1109/50.476137. [Cited on page 34.]

[74] Y. Liu, S. Qu, Y. Li, Single microchannel high-temperature fiber sensor by femtosecond laser-induced water breakdown, Optics Letters 38 (2013) 335–337. doi:10.1364/OL.38.000335. [Cited on page 34.]

[75] S. Pissadakis, Lab-in-a-fiber sensors: A review, Microelectronic Engineering 217 (2019) 111105. doi:10.1016/j.mee.2019.111105. [Cited on pages 35 and 39.]

[76] C. Lin, C. Liao, Y. Zhang, L. Xu, Y. Wang, C. Fu, K. Yang, J. Wang, J. He, Y. Wang, Optofluidic gutter oil discrimination based on a hybrid-waveguide coupler in fibre, Lab Chip 18 (2018) 595–600. doi:10.1039/C8LC00008E. [Cited on page 35.]

[77] G. C. B. Lee, C. Mou, K. Zhou, K. Sugden, Optimization and characterization of femtosecond laser inscribed in-fiber microchannels for liquid sensing, 23rd International Conference on Optical Fibre Sensors 9157 (2014) 915743. doi:10.1117/12.2058315. [Cited on page 35.]

[78] J. C. Guo, Y. S. Yu, Y. Xue, C. Chen, R. Yang, C. Wang, Q. D. Chen, H. B. Sun, Compact long-period fiber gratings based on periodic microchannels, IEEE Photonics Technology Letters 25 (2013) 111−114. doi:10.1109/LPT.2012.2227701. [Cited on page 35.]

[79] Amplitude, Satsuma HP User Manual (2014). [Cited on page 41.]

[80] A. Dostovalov, S. Babin, M. Dubov, M. Baregheh, V. Mezentsev, Comparative numerical study of energy deposition in femtosecond laser microfabrication with fundamental and second harmonics of yb-doped laser, Laser Physics 22 (2012) 930−936. doi:10.1134/S1054660X12050064. [Cited on page 43.]

[81] Altechna, Watt Pilot Motorized Attenuator User Manual (2015). [Cited on page 43.]

[82] Olympus Corporation, 100× Plan Achromat Oil Immersion Objective, model PLN100XO: Data Sheet (2012). [Cited on page 44.]

[83] Newport, 40× Aspheric Objective Lens model 5722-A-H and Asphere Adapter, RMS Threaded model 5709: Data Sheets (2018). [Cited on page 44.]

[84] Corning Incorporated, Corning® SMF-28e® Optical Fiber Product Information Sheet (2014). [Cited on pages 50 and 73.]

[85] Thorlabs Inc, FG125LA - Coreless Termination Fiber, Ø125 μm Glass Rod Spec Sheet (2017). [Cited on page 50.]

[86] Cargille Laboratories, Fused Silica Matching Liquid, Code 06350: Data Sheet (2017). [Cited on page 51.]

[87] T. Erdogan, Fiber grating spectra, Journal of Lightwave Technology 15 (1997) 1277−1294. doi:10.1109/50.618322. [Cited on page 57.]

[88] Y. Wang, Z. Li, S. Liu, C. Fu, Z. Li, Z. Zhang, Y. Wang, J. He, Z. Bai, C. Liao, Parallel-integrated fiber bragg gratings inscribed by femtosecond laser point-by-point technology, Journal of Lightwave Technology 37 (2019) 2185−2193. doi:10.1109/JLT.2019.2899585. [Cited on page 57.]

[89] D. Feng, X. Qiao, J. Albert, Off-axis ultraviolet-written fiber bragg gratings for directional bending measurements, Optics Letters 41 (2016) 1201. doi:10.1364/ol.41.001201. [Cited on page 57.]

[90] L. Zhang, X. Qiao, Q. Liu, M. Shao, Y. Jiang, D. Huang, Off-axis ultraviolet-written thin-core fiber bragg grating for directional bending measurements, Optics Communications 410 (2018) 197−201. doi:10.1016/j.optcom.2017.09.061. [Cited on pages 57 and 83.]

[91] C. Koutsides, K. Kalli, D. J. Webb, L. Zhang, Characterizing femtosecond laser inscribed bragg grating spectra, Optics Express 19 (2011) 342. doi:10.1364/oe.19.000342. [Cited on page 57.]

[92] K. Chah, D. Kinet, C. Caucheteur, Negative axial strain sensitivity in gold-coated eccentric fiber bragg gratings, Scientific Reports 6 (2016) 1−6. doi:10.1038/srep38042. [Cited on pages 57, 58, 77, and 78.]

[93] S. J. Mihailov, Femtosecond Laser-Inscribed Fiber Bragg Gratings for Sensing Applications, Elsevier Inc., 2018. doi:10.1016/B978-0-12-803131-5.00006-4. [Cited on pages 57, 59, and 105.]

[94] J. Habel, T. Boilard, J.-S. Frenière, F. Trépanier, M. Bernier, Femtosecond FBG Written through the Coating for Sensing Applications, Sensors 17 (11) (2017) 2519. doi:10.3390/s17112519. [Cited on page 57.]

[95] Y. Zhang, D. Qiao, Y. Zhu, P. Jiang, High-order fiber bragg grating fabricated by femtosecond laser pulses for high-sensitivity temperature and strain sensing, Optik 222 (2020) 165423. doi:10.1016/j.ijleo.2020.165423. [Cited on page 57.]

[96] V. Maselli, P. R. Herman, Integrated optical circuits in fiber cladding by tightly focused femtosecond laser writing, in: W. Pfleging, Y. Lu, K. Washio, J. Amako, W. Hoving (Eds.), Laser-based Micro- and Nanopackaging and Assembly IV, Vol. 7585, SPIE, 2010, pp. 132–142. doi:10.1117/12.845431. [Cited on page 57.]

[97] J. R. Grenier, Femtosecond laser inscription of optical circuits in the cladding of optical fibers, Ph.D. thesis (2016). [Cited on page 57.]

[98] J. Thomas, N. Jovanovic, R. G. Becker, G. D. Marshall, M. J. Withford, A. Tünnermann, S. Nolte, M. J. Steel, Cladding mode coupling in highly localized fiber Bragg gratings: modal properties and transmission spectra, Optics Express 19 (1) (2010) 325–341. doi:10.1364/OE.19.000325. [Cited on pages 57 and 58.]

[99] J. U. Thomas, N. Jovanovic, R. G. Krämer, G. D. Marshall, M. J. Withford, A. Tünnermann, S. Nolte, M. J. Steel, Cladding mode coupling in highly localized fiber Bragg gratings II: complete vectorial analysis, Optics Express 20 (19) (2012) 21434. doi:10.1364/oe.20.021434. [Cited on page 57.]

[100] K. Chah, D. Kinet, M. Wuilpart, P. Mégret, C. Caucheteur, Femtosecond-laser-induced highly birefringent bragg gratings in standard optical fiber, Optics Letters 38 (2013) 594. doi:10.1364/ol.38.000594. [Cited on pages 58, 62, 71, and 75.]

[101] K. Chah, V. Voisin, D. Kinet, C. Caucheteur, Surface plasmon resonance in eccentric femtosecond-laser-induced fiber bragg gratings, Optics Letters 39 (2014) 6887–6890. doi:10.1364/OL.39.006887. [Cited on page 58.]

[102] C. Caucheteur, P. Megret, Demodulation technique for weakly tilted fiber bragg grating refractometer, IEEE Photonics Technology Letters 17 (2005) 2703–2705. doi:10.1109/LPT.2005.859411. [Cited on page 58.]

[103] J. Tang, C. Fu, Z. Bai, C. Liao, Y. Wang, Sensing characteristics of tilted long period fiber gratings inscribed by infrared femtosecond laser, Sensors 18 (9) (2018) 3003. doi:10.3390/s18093003. [Cited on pages 58, 86, 105, and 106.]

[104] J. Chen, Q. Liu, Z. He, High-Resolution Simultaneous Measurement of Strain and Temperature Using π-Phase-Shifted FBG in Polarization Maintaining Fiber, Journal of Lightwave Technology 35 (2017) 4838–4844. doi:10.1109/JLT.2017.2760343. [Cited on page 58.]

[105] L. Zhang, X. Qiao, W. Bao, Q. Liu, M. Shao, Strain and temperature discrimination using a fiber bragg grating with off-axis inscription, Optik 171 (2018) 941–946. doi:10.1016/j.ijleo.2018.06.128. [Cited on pages 58 and 77.]

[106] X. Chen, C. Zhang, D. J. Webb, K. Kalli, G. D. Peng, Highly sensitive bend sensor based on bragg grating in eccentric core polymer fiber, IEEE Photonics Technology Letters 22 (2010) 850–852. doi:10.1109/LPT.2010.2046482. [Cited on page 58.]

[107] D. Su, X. Qiao, F. Chen, Q. Rong, Higher order coupling mode for orientation-dependent bend measurement using an off-axis fbg inscription over few-mode fiber, IEEE Sensors Journal 19 (2019) 1368–1372. doi:10.1109/JSEN.2018.2881423. [Cited on page 58.]

[108] C. Caucheteur, T. Guo, J. Albert, Polarization-assisted fiber bragg grating sensors: Tutorial and review, Journal of Lightwave Technology 35 (2017) 3311–3322. doi:10.1109/JLT.2016.2585738. [Cited on page 58.]

[109] V. Budinski, D. Donlagic, Fiber-optic sensors for measurements of torsion, twist and rotation: A review, Sensors 17 (2017) 1–29. doi:10.3390/s17030443. [Cited on pages 58 and 85.]

[110] T. Wang, Y. Guo, X. Zhan, M. Zhao, K. Wang, Simultaneous measurements of strain and temperature with dual fiber bragg gratings for pervasive computing, in: 2006 First International Symposium on Pervasive Computing and Applications, IEEE, 2006, pp. 786–790. doi:10.1109/spca.2006.297530. [Cited on page 58.]

[111] Q. Rong, T. Guo, W. Bao, Z. Shao, G. D. Peng, X. Qiao, Highly sensitive fiber-optic accelerometer by grating inscription in specific core dip fiber, Scientific Reports 7 (2017) 1–9. doi:10.1038/s41598-017-12322-6. [Cited on page 58.]

[112] D. Feng, W. Zhou, X. Qiao, J. Albert, Compact optical fiber 3d shape sensor based on a pair of orthogonal tilted fiber bragg gratings, Scientific Reports 5 (2015) 1–7. doi:10.1038/srep17415. [Cited on page 58.]

[113] L. A. Fernandes, Birefringence and Bragg grating control in femtosecond laser written optical circuits, Ph.D. thesis (2012). [Cited on page 58.]

[114] W. Bao, Q. Rong, F. Chen, X. Qiao, All-fiber 3D vector displacement (bending) sensor based on an eccentric FBG, Optics Express 26 (2018) 8619. doi:10.1364/oe.26.008619. [Cited on page 58.]

[115] Y. Zhao, C. Wang, G. Yin, B. Jiang, K. Zhou, C. Mou, Y. Liu, L. Zhang, T. Wang, Simultaneous directional curvature and temperature sensor based on a tilted few-mode fiber Bragg grating, Applied Optics 57 (2018) 1671. doi:10.1364/ao.57.001671. [Cited on page 58.]

[116] Y. Wang, S. Liu, Z. Li, C. Liao, Y. Wang, J. He, Z. Tan, K. Yang, J. Zhou, K. Guo, Femtosecond laser inscription of fiber bragg grating in twin-core few-mode fiber for directional bend sensing, Journal of Lightwave Technology 35 (2017) 4670–4676. doi:10.1109/jlt.2017.2750407. [Cited on page 58.]

[117] J. He, Y. Wang, C. Liao, C. Wang, S. Liu, K. Yang, Y. Wang, X. Yuan, G. P. Wang, W. Zhang, Negative-index gratings formed by femtosecond laser overexposure and thermal regeneration, Scientific Reports 6 (2016) 23379. doi:10.1038/srep23379. [Cited on page 58.]

[118] W. Bao, X. Qiao, Q. Rong, N. Hu, H. Yang, Z. Feng, M. Hu, Sensing characteristics for a fiber bragg grating inscribed over a fiber core and cladding, IEEE Photonics Technology Letters 27 (2015) 709–712. doi:10.1109/LPT.2015.2389860. [Cited on page 58.]

[119] F. Chen, D. Su, X. Qiao, Q. Rong, Compact vector bend sensor using Dual-Off-Axis innermost Cladding-Type FBGs, IEEE Sensors Journal 18 (2018) 7476–7480. doi:10.1109/JSEN.2018.2849360. [Cited on page 58.]

[120] B. Huang, X. Shu, Highly sensitive torsion sensor with femtosecond laser-induced low birefringence single-mode fiber based Sagnac interferometer, Optics Express 26 (2018) 4563–4571. doi:10.1364/OE.26.004563. [Cited on page 58.]

[121] P. Zu, C. C. Chan, Y. Jin, T. Gong, Y. Zhang, L. H. Chen, X. Dong, A temperature-insensitive twist sensor by using low-birefringence photonic-crystal-fiber-based sagnac interferometer, IEEE Photonics Technology Letters 23 (2011) 920–922. doi:10.1109/LPT.2011.2143400. [Cited on page 58.]

[122] Y.-L. Lo, B.-R. Chue, S.-H. Xu, Fiber torsion sensor demodulated by a high-birefringence fiber Bragg grating, Optics Communications 230 (4–6) (2004) 287–295. doi:10.1016/j.optcom.2003.11.068. [Cited on pages 58 and 85.]

[123] C.-Y. Lin, L. A. Wang, G.-W. Chern, Corrugated long-period fiber gratings as strain, torsion, and bending sensors, Journal of Lightwave Technology 19 (2001) 1159–1168. doi:10.1109/50.939797. [Cited on page 58.]

[124] D. Tentori, A. Garcia-Weidner, C. Ayala-Díaz, Birefringence matrix for a twisted single-mode fiber: Photoelastic and geometrical contributions, Optical Fiber Technology 18 (2012) 14–20. doi:10.1016/j.yofte.2011.10.001. [Cited on page 58.]

[125] S. J. Mihailov, D. Grobnic, C. W. Smelser, P. Lu, R. B. Walker, H. Ding, Bragg grating inscription in various optical fibers with femtosecond infrared lasers and a phase mask, Optical Materials Express 1 (4) (2011) 754. doi:10.1364/OME.1.000754. [Cited on pages 59, 69, and 70.]

[126] C. Wu, Z. Liu, K. M. Chung, M. L. V. Tse, F. Y. M. Chan, A. P. T. Lau, C. Lu, H. Y. Tam, Strong LP_{01} and LP_{11} mutual coupling conversion in a two-mode fiber Bragg grating, IEEE Photonics Journal 4 (2012) 1080–1086. doi:10.1109/JPHOT.2012.2204735. [Cited on page 59.]

[127] C.-L. Chen, Foundations for guided-wave optics, John Wiley & Sons, 2006. [Cited on pages 59, 60, 61, 73, and 74.]

[128] D. Tosi, C. Molardi, Basic Detection Techniques, 2021, pp. 91–124. doi:10.1002/9781119534730.ch4. [Cited on page 59.]

[129] T. W. MacDougall, S. Pilevar, C. W. Haggans, M. A. Jackson, Generalized expression for the growth of long period gratings, IEEE Photonics Technology Letters 10 (1998) 1449–1451. doi:10.1109/68.720290. [Cited on pages 88 and 89.]

[130] S. W. James, R. P. Tatam, Optical fibre long-period grating sensors: characteristics and application, Measurement Science and Technology 14 (5) (2003) R49–R61. doi:10.1088/0957-0233/14/5/201. [Cited on pages 86, 87, 88, 90, 91, 128, and 129.]

[131] X. Shu, L. Zhang, I. Bennion, Sensitivity characteristics of long-period fiber gratings, Journal of Lightwave Technology 20 (2002) 255–266. doi:10.1109/50.983240. [Cited on pages 59, 87, 88, 89, and 90.]

[132] L. A. Fernandes, J. R. Grenier, P. V. S. Marques, J. S. Aitchison, P. R. Herman, Strong birefringence tuning of optical waveguides with femtosecond laser irradiation of bulk fused silica and single mode fibers, Lightwave Technology, Journal of 31 (2013) 3563–3569. doi:10.1109/JLT.2013.2284240. [Cited on pages 62 and 66.]

[133] N. Jovanovic, J. Thomas, R. J. Williams, M. J. Steel, G. D. Marshall, A. Fuerbach, S. Nolte, A. Tünnermann, M. J. Withford, Polarization-dependent effects in point-by-point fiber bragg gratings enable simple, linearly polarized fiber lasers, Optics Express 17 (2009) 6082–6095. doi:10.1364/OE.17.006082. [Cited on pages 62 and 95.]

[134] S. I. Younus, A. A. Al-Dergazly, A. K. Abass, Characterization of multimode interference based optical fiber, IOP Conference Series: Materials Science and Engineering 1076 (1) (2021) 012060. doi:10.1088/1757-899x/1076/1/012060. [Cited on page 66.]

[135] A. Heisterkamp, P. R. Herman, M. Meunier, S. Nolte (Eds.), Direct writing of fiber optic components in photonic crystal fibers and other specialty fibers, no. volume 9740 in Proceedings of SPIE, SPIE, Bellingham, Washington, 2016, teilkonferenz von: SPIE Photonics West (innerhalb der Teil-Konferenz: SPIE LASE). doi:10.1117/12.2213597. [Cited on page 71.]

[136] D. Choudhury, J. R. Macdonald, A. K. Kar, Ultrafast laser inscription: Perspectives on future integrated applications, Laser & Photonics Reviews 8 (2014) 827–846. doi:10.1002/lpor.201300195. [Cited on page 71.]

[137] L. A. Fernandes, M. Becker, O. Frazão, K. Schuster, J. Kobelke, M. Rothhardt, H. Bartelt, J. L. Santos, P. V. S. Marques, Temperature and strain sensing with femtosecond laser written bragg gratings in defect and nondefect suspended-silica-core fibers, IEEE Photonics Technology Letters 24 (2012) 554–556. doi:10.1109/LPT.2012.2183344. [Cited on page 77.]

[138] H. Yu, W. Gao, X. Jiang, H. Guo, S. Jiang, Y. Zheng, On-line writing of fiber Bragg grating array on a two-mode optical fiber for sensing applications, Materials 12. doi:10.3390/ma12081263. [Cited on page 83.]

[139] N. Jovanovic, A. Fuerbach, G. Marshall, M. Ams, M. Withford, Fibre grating inscription and applications, Vol. 123 of Topics in applied physics, 2012, pp. 197–225. doi:10.1007/978-3-642-23366-1_8. [Cited on pages 86 and 90.]

[140] X. Lan, Q. Han, J. Huang, H. Wang, Z. Gao, A. Kaur, H. Xiao, Turn-around point long-period fiber grating fabricated by CO_2 laser for refractive index sensing, Sensors and Actuators B: Chemical 177 (2013) 1149–1155. doi:10.1016/j.snb.2012.12.006. [Cited on pages 86 and 87.]

[141] X. Lan, Q. Han, T. Wei, J. Huang, H. Xiao, Turn-around-point long-period fiber gratings fabricated by CO_2 laser point-by-point irradiations, IEEE Photonics Technology Letters 23 (22) (2011) 1664–1666. doi:10.1109/LPT.2011.2166256. [Cited on pages 86, 87, 88, 89, and 90.]

[142] R. Y. N. Wong, E. Chehura, S. E. Staines, S. W. James, R. P. Tatam, Fabrication of fiber optic long period gratings operating at the phase matching turning point using an ultraviolet laser, Applied Optics 53 (2014) 4669–4674. doi:10.1364/ao.53.004669. [Cited on page 86.]

[143] R. M. Carter, R. R. J. Maier, P. Biswas, N. Basumallick, S. Bandyopadhyay, B. J. S. Jones, S. McCulloch, J. S. Barton, Experimental Difficulties with LPG Sensors Operating Close to the Phase Turning Points, Journal of Lightwave Technology 34 (2016) 3999–4004. doi:10.1109/JLT.2016.2593028. [Cited on page 86.]

[144] C. Colaço, P. Caldas, I. D. Villar, R. Chibante, G. Rego, Arc-induced long-period fiber gratings in the dispersion turning points, Journal of Lightwave Technology 34 (2016) 4584–4590. doi:10.1109/JLT.2016.2540678. [Cited on pages 86, 87, 93, and 119.]

[145] J. Ascorbe, J. M. Corres, I. Del Villar, I. R. Matias, Fabrication of Long Period Gratings by Periodically Removing the Coating of Cladding-Etched Single Mode Optical Fiber Towards Optical Fiber Sensor Development, Sensors 18 (6) (2018) 1866. doi:10.3390/s18061866. [Cited on pages 86 and 119.]

[146] F. Ahmed, H.-E. Joe, B.-K. Min, M. B. G. Jun, Characterization of refractive index change and fabrication of long period gratings in pure silica fiber by femtosecond laser radiation, Optics & Laser Technology 74 (2015) 119–124. doi:10.1016/j.optlastec.2015.05.018. [Cited on page 86.]

[147] Y. Kondo, K. Nouchi, T. Mitsuyu, M. Watanabe, P. G. Kazansky, K. Hirao, Fabrication of long-period fiber gratings by focused irradiation of infrared femtosecond laser pulses, Optics Letters 24 (1999) 646. doi:10.1364/ol.24.000646. [Cited on page 86.]

[148] Y. Zhang, P. Jiang, D. Qiao, Y. Xi, Y. Zhu, Q. Xu, C. Wang, Sensing characteristics of long period grating by writing directly in SMF-28 based on 800 nm femtosecond laser pulses, Optics & Laser Technology 121 (2020) 105839. doi:10.1016/j.optlastec.2019.105839. [Cited on pages 86, 106, and 128.]

[149] A. I. Kalachev, D. N. Nikogosyan, G. Brambilla, Long-period fiber grating fabrication by high-intensity femtosecond pulses at 211 nm, Journal of Lightwave Technology 23 (8) (2005) 2568–2578. doi:10.1109/JLT.2005.851335. [Cited on page 86.]

[150] D. Viveiros, J. M. M. M. de Almeida, L. Coelho, H. Vasconcelos, J. M. Maia, V. A. Amorim, P. A. S. Jorge, P. V. S. Marques, Temperature Stability and Spectral Tuning of Long Period Fiber Gratings Fabricated by Femtosecond Laser Direct Writing, Sensors 20 (14) (2020) 1–15. doi:10.3390/s20143898. [Cited on pages 86 and 87.]

[151] S. Liu, M. Luo, Q. Ji, Sensing characteristics of femtosecond laser-induced long period gratings by filling cladding holes in photonic crystal fiber, Journal of Lightwave Technology 32 (12) (2014) 2287–2292. doi:10.1109/jlt.2014.2323403. [Cited on page 86.]

[152] A. A. Wolf, A. V. Dostovalov, I. A. Lobach, S. A. Babin, Femtosecond laser inscription of long-period fiber gratings in a polarization-maintaining fiber, Journal of Lightwave Technology 33 (2015) 5178–5183. doi:10.1109/jlt.2015.2496355. [Cited on page 86.]

[153] D. Viveiros, J. M. M. M. de Almeida, L. Coelho, H. Vasconcelos, V. A. Amorim, J. M. Maia, P. A. S. Jorge, P. V. S. Marques, Spectral Tuning of Long Period Fiber Gratings Fabricated by Femtosecond Laser Micromachining through Thermal Annealing, in: Multidisciplinary Digital Publishing Institute Proceedings, Vol. 15, 2019, p. 4. doi:10.3390/proceedings2019015004. [Cited on page 86.]

[154] Y. Liu, S. Qu, Femtosecond laser pulses induced ultra-long-period fiber gratings for simultaneous measurement of high temperature and refractive index, Optik 124 (2013) 1303–1306. doi:10.1016/j.ijleo.2012.03.062. [Cited on page 86.]

[155] F. Shen, K. Zhou, L. Zhang, X. Shu, Long period fiber grating around the dispersion turning point fabricated with a femtosecond laser, in: 2017 Asia Communications and Photonics Conference (ACP), 2017, pp. 1–3. doi:10.1364/acpc.2017.su2a.104. [Cited on pages 86 and 119.]

[156] G. Rego, O. V. Ivanov, P. V. S. Marques, Demonstration of coupling to symmetric and antisymmetric cladding modes in arc-induced long-period fiber gratings, Optics Express 14 (2006) 9594. doi:10.1364/oe.14.009594. [Cited on page 102.]

[157] C. Zhang, L. Cheng, S. Fu, M. Tang, D. Liu, Long period fiber grating fabrication by two-step infrared femtosecond fiber laser exposure, IEEE Photonics Journal 9 (4) (2017) 1–7. doi:10.1109/JPHOT.2017.2711483. [Cited on page 86.]

[158] F. Zou, Y. Liu, C. Mou, S. Zhu, Optimization of refractive index sensitivity in nanofilm-coated long-period fiber gratings near the dispersion turning point, Journal of Lightwave Technology 38 (2020) 889–897. doi:10.1109/jlt.2019.2949373. [Cited on pages 87 and 112.]

[159] F. Chiavaioli, P. Biswas, C. Trono, S. Bandyopadhyay, A. Giannetti, S. Tombelli, N. Basumallick, K. Dasgupta, F. Baldini, Towards sensitive label-free immunosensing by means of turn-around point long period fiber gratings, Biosensors and Bioelectronics 60 (2014) 305–310. doi:10.1016/j.bios.2014.04.042. [Cited on page 87.]

[160] M. Śmietana, M. Koba, P. Mikulic, W. J. Bock, Towards refractive index sensitivity of long-period gratings at level of tens of μm per refractive index unit: fiber cladding etching and nano-coating deposition, Optics Express 24 (11) (2016) 11897–11904. doi:10.1364/oe.24.011897. [Cited on page 87.]

[161] T. K. Dey, S. Tombelli, P. Biswas, A. Giannetti, N. Basumallick, F. Baldini, S. Bandyopdhayay, C. Trono, Analysis of the lowest order cladding mode of long period fiber gratings near turn around point, Journal of Lightwave Technologydoi:10.1109/jlt.2020.2987795. [Cited on pages 87 and 111.]

[162] A. Cusano, A. Iadicicco, P. Pilla, L. Contessa, S. Campopiano, A. Cutolo, M. Giordano, Mode transition in high refractive index coated long period gratings, Optics Express 14 (2006) 19–34. doi:10.1364/opex.14.000019. [Cited on pages 87 and 111.]

[163] P. Pilla, C. Trono, F. Baldini, F. Chiavaioli, M. Giordano, A. Cusano, Giant sensitivity of long period gratings in transition mode near the dispersion turning point: an integrated design approach, Optics Letters 37 (19) (2012) 4152–4154. doi:10.1364/ol.37.004152. [Cited on page 87.]

[164] X. Liu, M. Yan, L. Zhan, S. Luo, Z. Zhang, Y. Xia, Controlling of symmetric and asymmetric mode coupling in long-period fiber gratings singe-side induced by long-pulse CO_2 laser, Optics Communications 284 (2011) 1232–1237. doi:10.1016/j.optcom.2010.11.027. [Cited on page 87.]

[165] M. Heck, G. Schwartz, R. G. Krämer, D. Richter, T. A. Goebel, C. Matzdorf, A. Tünnermann, S. Nolte, Control of higher-order cladding mode excitation with tailored femtosecond-written long period fiber gratings, Optics Express 27 (4) (2019) 4292–4303. doi:10.1364/oe.27.004292. [Cited on pages 87 and 101.]

[166] M. Smietana, M. Koba, E. Brzozowska, K. Krogulski, J. Nakonieczny, L. Wachnicki, P. Mikulic, M. Godlewski, W. J. Bock, Label-free sensitivity of long-period gratings enhanced by atomic layer deposited tio2 nano-overlays, Optics Express 23 (2015) 8441. doi:10.1364/oe.23.008441. [Cited on pages 87, 112, and 119.]

[167] F. Chiavaioli, P. Biswas, C. Trono, S. Jana, S. Bandyopadhyay, N. Basumallick, A. Giannetti, S. Tombelli, S. Bera, A. Mallick, Sol–gel-based titania–silica thin film overlay for long period fiber grating-based biosensors, Analytical chemistry 87 (2015) 12024–12031. doi:10.1021/acs.analchem.5b01841. [Cited on pages 87, 112, 119, and 120.]

[168] K. Krogulski, M. Śmietana, B. Michalak, A. K. Dębowska, Ł. Wachnicki, S. Gierałtowska, M. Godlewski, M. Szymańska, P. Mikulic, W. J. Bock, Effect of TiO_2 nano-overlays deposited with atomic layer deposition on refractive index sensitivity of long-period gratings, International Journal on Smart Sensing and Intelligent Systems 7 (5) (2014) 1. [Cited on page 87.]

[169] L. Coelho, J. L. Santos, D. Viegas, J. M. M. M. de Almeida, Fabrication and characterization of metal oxide-coated long-period fiber gratings, Journal of Lightwave Technology 34 (2016) 2533−2539. doi:10.1109/jlt.2016.2540358. [Cited on page 130.]

[170] L. Coelho, D. Viegas, J. L. Santos, J. M. M. M. D. Almeida, Enhanced refractive index sensing characteristics of optical fibre long period grating coated with titanium dioxide thin films, Sensors and Actuators B: Chemical 202 (2014) 929−934. doi:10.1016/j.snb.2014.06.035. [Cited on pages 111, 123, 124, 130, and 133.]

[171] L. Coelho, D. Viegas, J. L. Santos, J. M. M. M. D. Almeida, Optical sensor based on hybrid FBG/titanium dioxide coated LPFG for monitoring organic solvents in edible oils, Talanta 148 (2016) 170−176. doi:10.1016/j.talanta.2015.10.067. [Cited on page 87.]

[172] H. C. A. S. G. Vasconcelos, J. M. M. M. de Almeida, C. M. T. Saraiva, P. A. da Silva Jorge, L. Coelho, Mach−zehnder interferometers based on long period fiber grating coated with titanium dioxide for refractive index sensing, Journal of Lightwave Technology 37 (2019) 4584−4589. doi:10.1109/jlt.2019.2912829. [Cited on pages 87, 131, 133, 137, 139, and 141.]

[173] Y. Singh, M. T. I. Ansari, S. K. Raghuwanshi, Fuel adulteration detection system using etched clad based fiber bragg grating (fbg) sensor, in: Optical Sensing and Detection VI, Vol. 11354, International Society for Optics and Photonics, 2020, p. 113542T. doi:10.1117/12.2556814. [Cited on pages 87 and 120.]

[174] V. Grubsky, J. Feinberg, Long-period fiber gratings with variable coupling for real-time sensing applications, Optics Letters 25 (2000) 203. doi:10.1364/ol.25.000203. [Cited on pages 89 and 90.]

[175] V. Bhatia, Temperature-insensitive and strain-insensitive long-period grating sensors for smart structures, Optical Engineering 36 (1997) 1872. doi:10.1117/1.601379. [Cited on pages 90, 91, 128, and 129.]

[176] F. Chiavaioli, C. A. J. Gouveia, P. A. S. Jorge, F. Baldini, Towards a uniform metrological assessment of grating-based optical fiber sensors: From refractometers to biosensors, Biosensors 7 (2017) 23. doi:10.3390/bios7020023. [Cited on page 91.]

[177] F. Chiavaioli, A. Giannetti, F. Baldini, From Refractometry to Biosensing with Optical Fibres, 2021, pp. 331−366. doi:10.1002/9781119534730.ch10. [Cited on page 91.]

[178] I. D. Villar, O. Fuentes, F. Chiavaioli, J. M. Corres, I. R. Matias, Optimized strain long-period fiber grating (lpfg) sensors operating at the dispersion turning point, Journal of Lightwave Technology 36 (2018) 2240−2247. doi:10.1109/JLT.2018.2790434. [Cited on page 94.]

[179] B. L. Bachim, T. K. Gaylord, Polarization-dependent loss and birefringence in long-period fiber gratings, Applied Optics 42 (34) (2003) 6816−6823. doi:10.1364/AO.42.006816. [Cited on pages 95 and 99.]

[180] M. Dubov, T. D. P. Allsop, A. Martinez, V. Mezentsev, I. Bennion, Highly birefringent long period gratings fabricated with femtosecond laser, in: 2006 Optical Fiber Communication Conference and the National Fiber Optic Engineers Conference, 2006, pp. 3−. doi:10.1109/OFC.2006.215534. [Cited on page 95.]

[181] A. V. Dostovalov, A. A. Wolf, S. A. Babin, Long-period fibre grating writing with a slit-apertured femtosecond laser beam (λ= 1026 nm), Quantum Electronics 45 (2015) 235. doi:10.1070/qe2015v045n03abeh015647. [Cited on page 101.]

[182] L. Coelho, Research and development of optical fibre sensors based on thin film coating technology, Ph.D. thesis (Jan. 2016). [Cited on pages 102, 111, 136, 137, and 139.]

[183] P. G. Kryukov, Y. V. Larionov, A. A. Rybaltovskii, K. A. Zagorul'ko, A. Dragomir, D. N. Nikogosyan, A. A. Ruth, Long-period fibre grating fabrication with femtosecond pulse radiation at different wavelengths, Microelectronic Engineering 69 (2003) 248−255. doi:10.1016/S0167-9317(03)00304-6. [Cited on page 105.]

[184] A. Méndez, T. F. Morse, Specialty Optical Fibers Handbook, Elsevier, Burlington, 2011. [Cited on page 111.]

[185] I. H. Malitson, Interspecimen comparison of the refractive index of fused silica, Journal of the Optical Society of America 55 (10) (1965) 1205−1209. doi:10.1364/josa.55.001205. [Cited on page 111.]

[186] A. K. Sharma, G. J. Mohr, Theoretical understanding of an alternating dielectric multilayer-based fiber optic spr sensor and its application to gas sensing, New Journal of Physics 10 (2) (2008) 023039. doi:10.1088/1367-2630/10/2/023039. [Cited on page 111.]

[187] M. Smietana, W. J. Bock, J. Szmidt, Evolution of optical properties with deposition time of silicon nitride and diamond-like carbon films deposited by radio-frequency plasma-enhanced chemical vapor deposition method, Thin Solid Films 519 (19) (2011) 6339−6343. doi:10.1016/j.tsf.2011.04.032. [Cited on page 112.]

[188] E. Davies, R. Viitala, M. Salomäki, S. Areva, L. Zhang, I. Bennion, Sol−gel derived coating applied to long-period gratings for enhanced refractive index sensing properties, Journal of Optics A: Pure and Applied Optics 11 (2008) 15501. doi:10.1088/1464-4258/11/1/015501. [Cited on page 112.]

[189] I. D. Villar, I. R. Matías, F. J. Arregui, P. Lalanne, I. D. Villar, I. R. Matías, F. J. Arregui, P. Lalanne, Optimization of sensitivity in Long Period Fiber Gratings with overlay deposition, Optics Express 13 (2005) 56−69. doi:10.1364/opex.13.000056. [Cited on page 113.]

[190] P. Biswas, N. Basumallick, S. Bandyopadhyay, K. Dasgupta, A. Ghosh, S. Bandyopadhyay, Sensitivity enhancement of turn-around-point long period gratings by tuning initial coupling condition, IEEE Sensors Journal 15 (2014) 1240−1245. doi:10.1109/jsen.2014.2361166. [Cited on page 119.]

[191] T. Eftimov, M. Janik, M. Koba, M. Śmietana, P. Mikulic, W. Bock, Long-period gratings and microcavity in-line mach zehnder interferometers as highly sensitive optical fiber platforms for bacteria sensing, Sensors 20 (2020) 3772. doi:10.3390/s20133772. [Cited on page 119.]

[192] M. Śmietana, M. Koba, P. Mikulic, W. J. Bock, Combined plasma-based fiber etching and diamond-like carbon nanooverlay deposition for enhancing sensitivity of long-period gratings, Journal of Lightwave Technology 34 (2016) 4615–4619. doi:10.1109/JLT.2016.2528411. [Cited on pages 119 and 120.]

[193] I. Del Villar, Ultrahigh-sensitivity sensors based on thin-film coated long period gratings with reduced diameter, in transition mode and near the dispersion turning point, Optics Express 23 (7) (2015) 8389–8398. doi:10.1364/oe.23.008389. [Cited on pages 119 and 120.]

[194] Q. Ling, Z. Gu, K. Gao, Smart design of a long-period fiber grating refractive index sensor based on dual-peak resonance near the phase-matching turning point, Applied Optics 57 (2018) 2693–2697. doi:10.1364/AO.57.002693. [Cited on page 119.]

[195] Q. Ling, Z. Gu, X. Jiang, K. Gao, Design of long period fiber grating surrounding refractive index sensor based on mode transition near phase-matching turning point, Optics Communications 439 (2019) 187–192. doi:10.1016/j.optcom.2019.01.060. [Cited on page 119.]

[196] S. Kher, S. Chaubey, J. Kishore, S. M. Oak, Detection of Fuel Adulteration With High Sensitivity Using Turnaround Point Long Period Fiber Gratings in B/Ge Doped Fibers, IEEE Sensors Journal 13 (11) (2013) 4482–4486. doi:10.1109/JSEN.2013.2270312. [Cited on page 120.]

[197] B. Li, L. Jiang, S. Wang, H.-L. Tsai, H. Xiao, Femtosecond laser fabrication of long period fiber gratings and applications in refractive index sensing, Optics & Laser Technology 43 (2011) 1420–1423. doi:10.1016/j.optlastec.2011.04.011. [Cited on page 121.]

[198] S. Prashar, D. Engles, P. Singh, Effect of material and waveguide parameters on strain sensitivity of uniform long-period fiber grating, in: 2015 International Conference on Signal Processing and Communication (ICSC), IEEE, 2015, pp. 448–451. doi:10.1109/icspcom.2015.7150695. [Cited on page 128.]

[199] V. Bhatia, Applications of long-period gratings to single and multi-parameter sensing, Optics Express 4 (11) (1999) 457–466. doi:10.1364/oe.4.000457. [Cited on pages 128 and 129.]

[200] V. Bhatia, D. Campbell, R. O. Claus, A. M. Vengsarkar, Simultaneous strain and temperature measurement with long-period gratings, Optics Letters 22 (9) (1997) 648–650. doi:10.1364/ol.22.000648. [Cited on pages 128 and 129.]

[201] Y. J. Rao, D. A. Jackson, Principles of Fiber-Optic Interferometry, Springer US, Boston, MA, 2000, pp. 167–191. doi:10.1007/978-1-4757-6081-1_5. [Cited on pages 131, 133, 143, and 144.]

[202] P. Hariharan, Optical Interferometry, 2nd Edition, Elsevier Science & Technology, 2003. [Cited on pages 131, 142, 143, and 144.]

[203] A. R. Bahrampour, S. Tofighi, M. Bathaee, F. Farman, Optical Fiber Interferometers and Their Applications, IntechOpen, 2012, Ch. 1. doi:10.5772/34346. [Cited on pages 131, 133, and 142.]

[204] B. H. Lee, Y. H. Kim, K. S. Park, J. B. Eom, M. J. Kim, B. S. Rho, H. Y. Choi, Interferometric fiber optic sensors, Sensors 12 (2012) 2467–2486. doi:10.3390/s120302467. [Cited on pages 133, 134, 142, 143, 144, and 145.]

[205] Z. Wen, Z. Guan, J. Dong, H. Li, Y. Cai, S. Gao, A review of sensitivity enhancement in interferometer-based fiber sensors, Sensors 22 (2022) 2506. doi:10.3390/s22072506. [Cited on page 131.]

[206] M.-q. Chen, T.-y. He, Y. Zhao, Review of femtosecond laser machining technologies for optical fiber microstructures fabrication, Optics & Laser Technology 147 (2022) 107628. doi:10.1016/j.optlastec.2021.107628. [Cited on page 131.]

[207] Y. Liu, X. Jing, H. Chen, J. Li, Y. Guo, S. Zhang, H. Li, S. Li, Highly sensitive temperature sensor based on sagnac interferometer using photonic crystal fiber with circular layout, Sensors and Actuators A: Physical 314 (2020) 112236. doi:10.1016/j.sna.2020.112236. [Cited on page 131.]

[208] Y. Zhao, H. Zhao, R.-q. Lv, J. Zhao, Review of optical fiber Mach−Zehnder interferometers with microcavity fabricated by femtosecond laser and sensing applications, Optics and Lasers in Engineering 117 (2019) 7−20. doi:10.1016/j.optlaseng.2018.12.013. [Cited on page 131.]

[209] Y. Zhang, C. Lin, C. Liao, K. Yang, Z. Li, Y. Wang, Femtosecond laser-inscribed fiber interface mach−zehnder interferometer for temperature-insensitive refractive index measurement, Optics Letters 43 (2018) 4421−4424. doi:10.1364/ol.43.004421. [Cited on pages 132, 133, and 134.]

[210] W. W. Li, W. P. Chen, D. N. Wang, Z. K. Wang, B. Xu, Fiber inline Mach-Zehnder interferometer based on femtosecond laser inscribed waveguides, Optics Letters 42 (21) (2017) 4438−4441. doi:10.1364/ol.42.004438. [Cited on page 131.]

[211] W. W. Li, D. N. Wang, Femtosecond laser inscribed straight waveguide in no-core fiber for in-line Mach-Zehnder interferometer construction, Optics Letters 43 (2018) 3405−3408. doi:10.1364/OL.43.003405. [Cited on page 132.]

[212] D. Pallarés-Aldeiturriaga, L. Rodríguez-Cobo, A. Quintela, J. M. López-Higuera, Curvature sensor based on in-fiber Mach-Zehnder interferometer inscribed with femtosecond laser, Journal of Lightwave Technology 35 (2017) 4624−4628. doi:10.1109/jlt.2017.2756103. [Cited on page 131.]

[213] B. Li, L. Jiang, S. Wang, Q. C. M. Wang, J. Yang, A new Mach-Zehnder interferometer in a thinned-cladding fiber fabricated by electric arc for high sensitivity refractive index sensing, Optics and Lasers in Engineering 50 (2012) 829−832. doi:10.1016/j.optlaseng.2012.01.024. [Cited on page 131.]

[214] Y. Geng, X. Li, X. Tan, Y. Deng, Y. Yu, A cascaded photonic crystal fiber Mach-Zehnder interferometer formed by extra electric arc discharges, Applied Physics B 102 (3) (2010) 595−599. doi:10.1007/s00340-010-4238-9. [Cited on page 131.]

[215] P. Caldas, G. Rego, Optical fiber interferometers based on arc-induced long period gratings at INESC TEC, Sensors 21 (2021) 7400. doi:10.3390/s21217400. [Cited on pages 133 and 134.]

[216] M. Shao, X. Qiao, H. Fu, N. Zhao, Q. Liu, H. Gao, An in-fiber Mach-Zehnder interferometer based on arc-induced tapers for high sensitivity humidity sensing, IEEE Sensors Journal 13 (2013) 2026−2031. doi:10.1109/jsen.2013.2247591. [Cited on page 131.]

[217] Y. Tan, L.-P. Sun, L. Jin, J. Li, B.-O. Guan, Microfiber Mach-Zehnder interferometer based on long period grating for sensing applications, Optics Express 21 (1) (2013) 154−164. doi:10.1364/oe.21.000154. [Cited on page 131.]

[218] J. Dong, M. Sang, S. Wang, T. Xu, Y. Wang, T. Liu, A novel Mach-Zehnder interferometric temperature sensor based on a symmetrical double-grooved structure, IEEE Sensors Journal 20 (24) (2020) 14850−14856. doi:10.1109/jsen.2020.3010338. [Cited on page 131.]

[219] Y. Tan, L.-P. Sun, L. Jin, J. Li, B.-O. Guan, Long period grating-based microfiber Mach-Zehnder interferometer for sensing applications, in: M. Yang, D. Wang, Y.-J. Rao (Eds.), Fourth Asia Pacific Optical Sensors Conference, Vol. 8924, SPIE, 2013, pp. 449–452. doi:10.1117/12.2031249. [Cited on page 131.]

[220] J. Fu, C. Guan, Z. Zhu, M. Wang, P. Huang, P. Li, J. Shi, L. Yuan, In-Fiber M-Z Interferometer Based on Cascaded Long Period Gratings in Embedded-Core Fiber, IEEE Photonics Technology Letters 29 (21) (2017) 1876–1879. doi:10.1109/lpt.2017.2754503. [Cited on page 131.]

[221] Y. Zhao, X.-g. Li, L. Cai, A highly sensitive Mach–Zehnder interferometric refractive index sensor based on core-offset single mode fiber, Sensors and Actuators A: Physical 223 (2015) 119–124. doi:10.1016/j.sna.2015.01.006. [Cited on page 131.]

[222] Y. Zhao, X.-g. Li, L. Cai, Mach-Zehnder interferometer formed by a large core-offset splicing fiber for temperature and displacement measurement, Optics Communications 356 (2015) 54–58. doi:10.1016/j.optcom.2015.06.081. [Cited on page 131.]

[223] S. Gao, C. Ji, Q. Ning, W. Chen, J. Li, High-sensitive Mach-Zehnder interferometric temperature fiber-optic sensor based on core-offset splicing technique, Optical Fiber Technology 56 (2020) 102202. doi:10.1016/j.yofte.2020.102202. [Cited on page 131.]

[224] R. Yang, Y.-S. Yu, Y. Xue, C. Chen, Q.-D. Chen, H.-B. Sun, Single S-tapered fiber Mach-Zehnder interferometers, Optics Letters 36 (23) (2011) 4482–4484. doi:10.1364/ol.36.004482. [Cited on page 131.]

[225] V. Bhardwaj, K. Kishor, A. C. Sharma, Tapered optical fiber geometries and sensing applications based on Mach-Zehnder Interferometer: A review, Optical Fiber Technology 58 (2020) 102302. doi:10.1016/j.yofte.2020.102302. [Cited on page 131.]

[226] V. Ahsani, F. Ahmed, M. B. G. Jun, C. Bradley, Tapered fiber-optic Mach-Zehnder interferometer for ultra-high sensitivity measurement of refractive index, Sensors 19 (2019) 1652. doi:10.3390/s19071652. [Cited on page 131.]

[227] Q. Wang, W. Wei, M. Guo, Y. Zhao, Optimization of cascaded fiber tapered Mach-Zehnder interferometer and refractive index sensing technology, Sensors and Actuators B: Chemical 222 (2016) 159–165. doi:10.1016/j.snb.2015.07.098. [Cited on page 131.]

[228] R. M. Jenkins, R. W. J. Devereux, J. M. Heaton, A novel waveguide Mach-Zehnder interferometer based on multimode interference phenomena, Optics Communications 110 (3–4) (1994) 410–424. doi:10.1016/0030-4018(94)90445-6. [Cited on page 131.]

[229] L. Wang, L. Yang, C. Zhang, C. Miao, J. Zhao, W. Xu, High sensitivity and low loss open-cavity Mach-Zehnder interferometer based on multimode interference coupling for refractive index measurement, Optics & Laser Technology 109 (2019) 193–198. doi:10.1016/j.optlastec.2018.08.002. [Cited on page 131.]

[230] O. Frazão, J. Viegas, P. Caldas, J. L. Santos, F. M. Araújo, L. A. Ferreira, F. Farahi, All-fiber Mach-Zehnder curvature sensor based on multimode interference combined with a long-period grating, Optics Letters 32 (21) (2007) 3074–3076. doi:10.1364/ol.32.003074. [Cited on page 131.]

[231] X. Sun, X. Dong, Y. Hu, H. Li, D. Chu, J. Zhou, C. Wang, J. Duan, A robust high refractive index sensitivity fiber Mach-Zehnder interferometer fabricated by femtosecond laser machining and chemical etching, Sensors and Actuators A: Physical 230 (2015) 111–116. doi:10.1016/j.sna.2015.04.006. [Cited on page 131.]

[232] J. Han, Y. Zhang, C. Liao, Y. Jiang, Y. Wang, C. Lin, S. Liu, J. Wang, Z. Zhang, J. Zhou, Y. Wang, Fiber-interface directional coupler inscribed by femtosecond laser for refractive index measurements, Optics Express 28 (2020) 14263–14270. doi:10.1364/OE.390674. [Cited on page 132.]

[233] Y. Wang, M. Yang, D. N. Wang, S. Liu, P. Lu, Fiber in-line Mach-Zehnder interferometer fabricated by femtosecond laser micromachining for refractive index measurement with high sensitivity, Journal of the Optical Society of America B 27 (2010) 370–374. doi:10.1364/JOSAB.27.000370. [Cited on page 132.]

[234] L. Dong, T. Gang, C. Bian, R. Tong, J. Wang, M. Hu, A high sensitivity optical fiber strain sensor based on hollow core tapering, Optical Fiber Technology 56 (2020) 102179. doi:10.1016/j.yofte.2020.102179. [Cited on page 132.]

[235] X. Zhu, F. Chen, H. Zhuang, J. Qian, H. Liu, J. Cao, Y. Shi, X. Wang, W. Wu, A Novel MZI Fiber Sensor with Enhanced Curvature and Strain Sensitivity Based on Four-Core Fiber, Micromachines 15 (12) (2024) 1427. doi:10.3390/mi15121427. [Cited on page 132.]

[236] S. Xu, H. Chen, W. Feng, Fiber-optic curvature and temperature sensor based on the lateral-offset spliced SMF-FCF-SMF interference structure, Optics & Laser Technology 141 (2021) 107174. doi:10.1016/j.optlastec.2021.107174. [Cited on page 132.]

[237] R. Zhao, X. Shu, Curvature sensor based on femtosecond laser-inscribed straight waveguide in FMF, Optics & Laser Technology 152 (2022) 108154. doi:10.1016/j.optlastec.2022.108154. [Cited on page 132.]

[238] J. R. Zheng, Y. Q. Yu, Z. L. Ou, C. L. Du, P. G. Yan, J. S. Wang, High Sensitivity Refractive Index Sensor Based on Long Period Fiber Gratings in Line Mach-Zehnder Interferometer, Advanced Materials Research 658 (2013) 609–613. doi:10.4028/www.scientific.net/amr.658.609. [Cited on page 132.]

[239] J.-F. Ding, A. P. Zhang, L.-Y. Shao, J.-H. Yan, S. He, Fiber-taper seeded long-period grating pair as a highly sensitive refractive-index sensor, IEEE Photonics Technology Letters 17 (2005) 1247–1249. doi:10.1109/lpt.2005.847437. [Cited on page 132.]

[240] Y.-e. Fan, T. Zhu, L. Shi, Y.-J. Rao, Highly sensitive refractive index sensor based on two cascaded special long-period fiber gratings with rotary refractive index modulation, Applied Optics 50 (2011) 4604–4610. doi:10.1364/ao.50.004604. [Cited on page 132.]

[241] G. Rego, Fibre optic devices produced by arc discharges, Journal of Optics 12 (2010) 113002. doi:10.1088/2040-8978/12/11/113002. [Cited on page 133.]

[242] E. M. Dianov, S. A. Vasiliev, A. S. Kurkov, O. I. Medvedkov, V. N. Protopopov, In-fiber Mach-Zehnder interferometer based on a pair of long-period gratings, in: Proceedings of European Conference on Optical Communication, Vol. 1, 1996, pp. 65–68 vol.1. [Cited on pages 133 and 134.]

[243] P. Zhou, C. Liao, Z. Li, S. Liu, Y. Wang, In-fiber cascaded FPI fabricated by chemical-assisted femtosecond laser micromachining for micro-fluidic sensing applications, Journal of Lightwave Technology 37 (13) (2019) 3214–3221. doi:10.1109/jlt.2019.2912835. [Cited on pages 142, 143, 144, 145, and 153.]

[244] Y. Liu, S. Qu, Optical fiber Fabry-Perot interferometer cavity fabricated by femtosecond laser-induced water breakdown for refractive index sensing, Applied Optics 53 (3) (2014) 469–474. doi:10.1364/ao.53.000469. [Cited on page 142.]

[245] C. R. Liao, T. Y. Hu, D. N. Wang, Optical fiber Fabry-Perot interferometer cavity fabricated by femtosecond laser micromachining and fusion splicing for refractive index sensing, Optics Express 20 (20) (2012) 22813–22818. doi:10.1364/oe.20.022813. [Cited on page 142.]

[246] B. Xu, C. Wang, D. N. Wang, Y. Liu, Y. Li, Fiber-tip gas pressure sensor based on dual capillaries, Optics Express 23 (18) (2015) 23484–23492. doi:10.1364/oe.23.023484. [Cited on pages 142 and 153.]

[247] M. R. Islam, M. M. Ali, M.-H. Lai, K.-S. Lim, H. Ahmad, Chronology of Fabry-Perot interferometer fiber-optic sensors and their applications: a review, Sensors 14 (4) (2014) 7451–7488. doi:10.3390/s140407451. [Cited on page 142.]

[248] J.-l. Kou, J. Feng, L. Ye, F. Xu, Y.-q. Lu, Miniaturized fiber taper reflective interferometer for high temperature measurement, Optics Express 18 (13) (2010) 14245–14250. doi:10.1364/oe.18.014245. [Cited on page 142.]

[249] A. D. Gomes, M. Becker, J. Dellith, M. I. Zibaii, H. Latifi, M. Rothhardt, H. Bartelt, O. Frazão, Multimode Fabry-Perot interferometer probe based on Vernier effect for enhanced temperature sensing, Sensors 19 (3) (2019) 453. doi:10.3390/s19030453. [Cited on page 142.]

[250] W. Yuan, F. Wang, A. Savenko, D. H. Petersen, O. Bang, Note: Optical fiber milled by focused ion beam and its application for Fabry-Pérot refractive index sensor, Review of Scientific Instruments 82 (7). doi:10.1063/1.3608111. [Cited on page 142.]

[251] J. Tang, G. Yin, C. Liao, S. Liu, Z. Li, X. Zhong, Q. Wang, J. Zhao, K. Yang, Y. Wang, High-sensitivity gas pressure sensor based on Fabry-Perot interferometer with a side-opened channel in hollow-core photonic bandgap fiber, IEEE Photonics Journal 7 (6) (2015) 1–7. doi:10.1109/jphot.2015.2489926. [Cited on pages 142 and 153.]

[252] H. Wei, M. Chen, S. Krishnaswamy, Three-dimensional-printed Fabry-Perot interferometer on an optical fiber tip for a gas pressure sensor, Applied Optics 59 (7) (2020) 2173–2178. doi:10.1364/ao.385573. [Cited on pages 142, 143, and 153.]

[253] A. D. Gomes, H. Bartelt, O. Frazão, Optical Vernier Effect: Recent Advances and Developments, Laser & Photonics Reviews 15 (7) (2021) 2000588. doi:10.1002/lpor.202000588. [Cited on page 143.]

[254] X. Zhu, C. Jiang, H. Chen, Y. Wang, S. Sun, H. Zhang, P. Wang, H. Huang, Highly sensitive gas pressure sensor based on the enhanced Vernier effect through a cascaded Fabry-Perot and Mach-Zehnder interferometer, Optics Express 30 (2022) 34956–34972. doi:10.1364/oe.463396. [Cited on page 143.]

[255] Q. H. Wang, X. Liu, D. N. Wang, Ultra-sensitive gas pressure sensor based on vernier effect with controllable amplification factor, Optical Fiber Technology 61 (2021) 102404. doi:10.1016/j.yofte.2020.102404. [Cited on page 143.]

[256] Z. Li, Y.-X. Zhang, W.-G. Zhang, L.-X. Kong, T.-Y. Yan, P.-C. Geng, B. Wang, High-sensitivity gas pressure Fabry-Perot fiber probe with micro-channel based on Vernier effect, Journal of Lightwave Technology 37 (14) (2019) 3444–3451. doi:10.1109/jlt.2019.2917062. [Cited on page 143.]

[257] X. Yang, S. Wu, H. Cheng, J. Ma, S. Wang, S. Liu, P. Lu, Simplified highly-sensitive gas pressure sensor based on harmonic Vernier effect, Optics & Laser Technology 140 (2021) 107007. doi:10.1016/j.optlastec.2021.107007. [Cited on page 143.]

[258] X. Guo, W. Ye, C. Jiang, S. Sun, High sensitivity gas pressure sensor based on two parallel-connected Fabry-Perot interferometers and Vernier effect, Measurement Science and Technology 32 (12) (2021) 125124. doi:10.1088/1361-6501/ac2b73. [Cited on page 143.]

[259] R. Pan, W. Yang, L. Li, H. Wu, Y. Yang, L. Zhang, X. Yu, S. Yu, Parallel-structured Fabry-Perot interferometers gas pressure sensor with ultraviolet glue sensitization based on dual Vernier effect, Measurement 193 (2022) 110973. doi:10.1016/j.measurement.2022.110973. [Cited on page 143.]

[260] Y.-J. Rao, Recent progress in fiber-optic extrinsic Fabry-Perot interferometric sensors, Optical Fiber Technology 12 (2006) 227–237. doi:10.1016/j.yofte.2006.03.004. [Cited on pages 143, 144, and 145.]

[261] Y. Liu, D. N. Wang, W. P. Chen, Crescent shaped Fabry-Perot fiber cavity for ultra-sensitive strain measurement, Scientific Reports 6 (2016) 38390. doi:10.1038/srep38390. [Cited on pages 144 and 145.]

[262] S. Ho, P. R. Herman, J. S. Aitchison, Single-and multi-scan femtosecond laser writing for selective chemical etching of cross section patternable glass micro-channels, Applied Physics A 106 (2012) 5–13. [Cited on page 146.]

[263] J. M. Maia, V. A. Amorim, D. Viveiros, P. V. S. Marques, Femtosecond laser micromachining of an optofluidics-based monolithic whispering-gallery mode resonator coupled to a suspended waveguide, Scientific Reports 11 (1) (2021) 9128. doi:10.1038/s41598-021-88682-x. [Cited on page 146.]

[264] J. M. Maia, V. A. Amorim, D. Alexandre, P. V. S. Marques, Real-time optical monitoring of etching reaction of microfluidic channel fabricated by femtosecond laser direct writing, Journal of Lightwave Technology 35 (2017) 2291–2298. doi:10.1109/jlt.2017.2678604. [Cited on page 146.]